Electronic Thesis and Dissertation Repository

7-30-2021 10:30 AM

Investigation of Shocked Basalts from Vargeão Dome and Vista Alegre: Implications for the Search for Life on Mars

Nikol Posnov, *The University of Western Ontario*

Supervisor: Osinski, Gordon R., *The University of Western Ontario*
Co-Supervisor: Flemming, Roberta L., *The University of Western Ontario*
Co-Supervisor: Pontefract, Alexandra, *Georgetown University*
A thesis submitted in partial fulfillment of the requirements for the Master of Science degree in Geology
© Nikol Posnov 2021

Recommended Citation

Abstract

Impact craters represent excellent astrobiological targets for planetary exploration missions to Mars. The impact of an asteroid or comet into a crystalline, H_2O-bearing target may result in development of a hydrothermal system and increase the habitability of the substrate for the colonization of endolithic microorganisms. Given that Mars' surface is covered by cratered basaltic rock, this study investigated target rocks and impact breccias from Vargeão Dome and Vista Alegre impact structures that formed in basalt in the Paraná Basin of Brazil.

Utilizing petrography and micro-X-ray diffraction (µXRD), the degree of shock metamorphism in plagioclase was quantitively determined. Measuring the full-width-at-half-maximum of diffraction peaks reveals increased strain-related mosaicity. This is correlated with increased optical evidence of deformation. Density and porosity results reveal trends that support conclusions from previous work on different rock types, whereby, increased shock level appears to result in greater porosity.

Optical microscopy, electron microprobe analysis, and µXRD were used to investigate hydrothermal alteration in the Vista Alegre crater and differentiate between pre- and post-impact hydrothermalism. We confidently verify that shocked samples within the Vista Alegre impact structure are altered by impact-induced hydrothermal activity. This alteration is distinct from that occurring outside the impact structure.

Summary for Lay Audience

Impact craters present excellent targets for current and future life detection missions to Mars. Although the initial impact bombardment is often viewed as a destructive process, it may also provide a unique environment for early life to assemble and, therefore, impact craters are prime sites in the search for evidence of past life on Mars. Impact events into a water-bearing target can result in an active hydrothermal system, the extent of which depends on the size of the impact and the target rock composition. Shocked substrates favourably interact with water, presenting access to nutrients and energy. Additionally, impacts play a role in providing a thermal gradient, a fluid reservoir, and a high level of permeability within the rock, thus enhancing the habitability of a host rock and its ability to support microbial life.

Impact-induced porosity correlates strongly with the shock level of the target rock. Current classification systems of impact-shocked rocks are predominantly based on the alteration of quartz, which is excellent for terrestrial sedimentary rocks, but difficult to implement in quartz-poor basalts. Given that impact craters on Mars would have occurred primarily within basaltic rocks, Vargeão Dome and Vista Alegre basaltic impact structures were selected as terrestrial analogues corresponding to the Martian surface in order to investigate how shock metamorphism and hydrothermal alteration influence the habitability of the target substrate for microorganisms.

In this contribution we quantitively characterize the degree of shock in plagioclase grains from shocked target basalts and impact breccia samples utilizing petrography and micro-X-ray diffraction (μXRD). Density and porosity results reveal trends that support conclusions from previous work on different target rocks, whereby, increased shock state correlates with increased porosity. Additionally, shocked basalts offer a higher porosity, high surface area environment which could make viable habitats for rock-dwelling microorganisms. This study also presents the first investigation of hydrothermal alteration in the Vista Alegre impact structure. Optical microscopy, electron microprobe analysis, and μXRD were used to investigate and differentiate between pre- and post-impact hydrothermal alteration. The degree of shock metamorphism and hydrothermal

iv

alteration were used to investigate the potential for microbial colonization in shocked targets and, thus, may guide the site selection and instrumentation for future Mars sample return missions.

Keywords

Vargeão Dome, Vista Alegre, shock metamorphism, basaltic impact craters, Paraná basin, Mars analogue, density and porosity, micro-X-ray diffraction, strain-related mosaicity, plagioclase-feldspar, Guarani aquifer, impact-generated hydrothermal system, basalt, alteration, secondary mineralization, chlorite-smectite mixed clay, illite-montmorillonite mixed clay, heulandite-Ca, chabazite-Ca, clinoptilolite-Ca.

Co-Authorship Statement

Chapter 1 was written by Nikol Posnov with comments and editing provided by Gordon Osinski, Roberta Flemming and Alexandra Pontefract. Chapter 2 is written as a manuscript to be submitted to Meteoritics & Planetary Science. The manuscript was written by Nikol Posnov with comments and editing by Gordon Osinski, Roberta Flemming, Phil McCausland and Alexandra Pontefract. Chapter 3 and 4 were written by Nikol Posnov with comments and editing provided by Gordon Osinski, Roberta Flemming and Alexandra Pontefract. Samples were collected by co-supervisor Dr. Alexandra Pontefract, alongside Dr. Álvaro Crósta. Data collection (optical microscopy, scanning electron microscope, He-pycnometer, μXRD), analysis, and interpretation was conducted by Nikol Posnov.

Appendix A was written by Nikol Posnov with comments and edits provided by Alexandra Pontefract. The concept for this study came from previous work and suggestions by Alexandra Pontefract. Sample preparation, culturing, and the modification and execution of DNA extractions methods were performed at Georgetown University, Washington, DC, USA, by Nikol Posnov, under the supervision and guidance of Dr. Alexandra Pontefract.

Acknowledgments

Of the entire thesis, the acknowledgments are one of the toughest sections to write because my gratitude for all the people that assisted me in finishing this thesis is limited by the English vocabulary.

First and foremost, I acknowledge that Western University is located on the traditional lands of the Anishinaabek (Ah-nish-in-a-bek), Haudenosaunee (Ho-den-no-show-nee), Lūnaapéewak (Len-ahpay-wuk) and Attawandaron (Add-a-won-da-run) peoples, whose traditional lands we are gathered upon today. With this, I respect the longstanding relationships that Indigenous Nations have to this land, as they are the original caretakers.

I would like to thank my three incredible supervisors, Dr. Gordon "Oz" Osinski, Dr. Roberta Flemming, and Dr. Alexandra Pontefract. If it wasn't for Robbie encouraging me to apply for a Masters in Geology, Alex for helping me develop a project that truly expresses my passion for geomicrobiology, and Oz for providing me with the countless opportunities, endless support, and the tremendous freedom to become the scientist I am today, I would never have been able to experience this amazing journey of pursuing a Master's degree. I truly admire all of your academic successes and aspire to be as productive and effective as you guys are in my academic future.

I would like to thank all the amazing academic and support staff that helped me collect my data; Marc Beauchamp for the countless hours of electron microprobe analyses, Phil McCausland for training me on the Helium Pycnometer instrument and providing guidance with bulk and grain density and porosity measurements, Alexandra Rupert for never failing to answer my phone calls whenever I had problems with the X-ray diffractometer, Joseph Umoh for the Micro-CT scan services, and Tianqi Xie for guidance and assistance with Raman Spectroscopy.

I would like to acknowledge MITACS Globalink for providing funding for my research at the Johnson Biosignatures Laboratory at Georgetown University, Washington, DC. A special mention goes out to Dr. Sarah Johnson for generously accepting me into her lab group and supplying me with the space and facilities needed to perform my experiments.

The experience I gained at Georgetown University is invaluable, providing me with the skills and networking capabilities required to excel not only in this research field, but also throughout all aspects of my professional life.

Lastly, I must thank my friends and family for being my solid foundation; Nico, Russell, Steph, James, Matt, Ian, David, Chris, Jason, Jen, Lindsay, Ramen, Cassy, Greg, and many, many others; I could always count on you all for support and helping me unwind after a long week in the lab!!!

Alex, you have a very unique version of perfection, one that is filled with harmony and beauty. Although I am always surprised of the perfection you see in me, I am extremely lucky to have you in my support system. This time, I look up to you, little sis.

My best friend Stephen, you are the main reason I was able to stay sane throughout this entire process. You are so kind and your desire for a world with no stress or pain is inspiring. Simply your lovely presence provides me comfort.

My parents Nina and Sergei, you have always seen the potential in me! The lessons you taught me and the advice you provided have guided me my entire life. If it wasn't for you, I wouldn't even be here (obviously).

This experience has been far more than just the culmination of a thesis, but a development of myself as a member of the academic community and a person as a whole.

I did it!

Shalom, so long, and till next time.

Table of Contents

List of Tables

List of Figures

List of Appendices

Chapter 1

1   Introduction and Background

A large part of this research focuses on a specific material that is common between all known terrestrial planets: shocked basalts. Shocked basalts form as a result of the ubiquitous geological process known as impact cratering. What starts as an extremely destructive and devastating event that may endanger or extinguish life on Earth, leads to a favorable habitat that is potentially accommodating for microbial life to flourish on Earth and elsewhere in the Universe. By studying basaltic impact structures on Earth, we gain a better understanding of the most effective and efficient methodology and instrumentation to study basaltic impact structures and their potential to host life on other rocky planets, including Mars. In comparison to other impact lithologies on Earth, basalts have received little research attention in terms of their habitability, shock effects, and development of hydrothermal systems mainly due to the limited coverage on the terrestrial surface. The main goal of this thesis is to characterize shock metamorphism and hydrothermal alteration in basaltic impact structures in order to understand how these processes influence the habitability of the target substrate for endolithic microorganisms. The specific objectives of this thesis are to: (1) utilize the µXRD method developed by Pickersgill et al. (2015a) for measuring strain-related mosaic spread to quantify shock level in plagioclase, and adjust the technique to support basaltic lithologies; (2) investigate the influence of shock on the physical properties of basaltic rocks, with a particular focus on the effects of shock pressure on the density and porosity of the target rock; (3) investigate impact-induced hydrothermal alteration at the Vista Alegre impact structure; (4) differentiate between pre- and post-impact hydrothermal alteration within and outside of the impact structure; and (5) tie the results together to obtain a better understanding of the habitability of the shocked basalts and breccia from the Vargeão Dome and Vista Alegre impact structures for future investigations of colonization by endolithic microorganisms.

1.1   Impact Cratering

1.1.1   Impact Crater Formation

The development of impact craters can be considered in three continuous phases (Fig. 1-1). The first phase is the contact and compression stage where the collision between two objects results in a transfer of kinetic energy from the smaller impactor to the larger target rock. The projectile penetrates one to two times its diameter, instantaneously releasing all of its kinetic impact energy in the form of primary propagating shock waves and secondary reflecting rarefaction waves (Ahrens & O'Keefe, 1972; Kieffer & Simonds, 1980; O'Keefe & Ahrens, 1982). The immense energy released results in extremely high pressures and temperatures in both the projectile and in the target rocks.
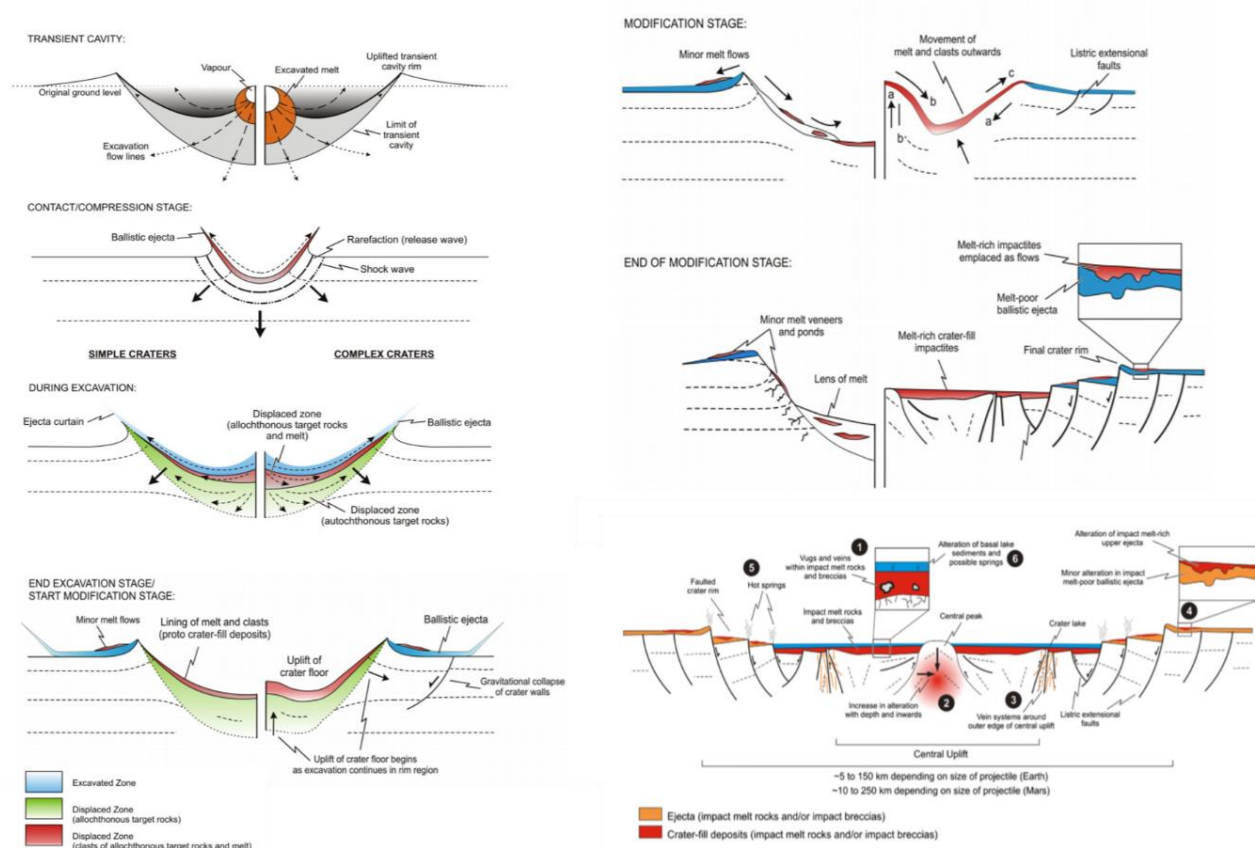
Figure 1-1. The first three stages of impact crater formation (Osinski et al., 2018), and the additional hydrothermal alteration modification stage (bottom right from Osinski et al., 2013).

The shock waves continue radiating into the target rock while the rarefaction wave returns to the impactor, melting and vaporizing it (Gault et al., 1968; Melosh, 1989; Osinski & Pierazzo, 2012). When the projectile stops contributing kinetic energy to the system, the crater structure begins to form (Osinski & Pierazzo, 2012). This is the second and defining stage of crater formation, the excavation stage. The shock wave and rarefaction wave result in shock melting, the formation of a near-surface zone of interference, and the excavation and displacement of target material (Ahrens & O'Keefe, 1972; Croft, 1980; Dense, 1968; Dense et al., 1977; Grieve et al., 1977; Grieve & Cintala, 1981; Melosh, 1989; Osinski & Pierazzo, 2012). Together these processes form a transient crater. Throughout the process, the top third of the transient crater is excavated, and the bottom two-thirds of the material is displaced (Stöffler et al., 1975). The extent of excavation is dependent on the target lithology and size of the projectile, while the diameter of the transient crater depends on the penetration depth of the impactor (Croft, 1985; French, 1998; Maxwell, 1977; Melosh, 1989; Melosh & Ivanov, 1999; Osinski & Pierazzo, 2012).

The third modification stage begins shortly after the crater expansion ceases and it has no strictly defined "end" point as the crater continues to be modified through geological time (French, 1998; Koeberl, 2014; Osinski & Pierazo, 2012). The size of the impactor, target lithology, and planetary gravitational field ultimately determine the final morphology of the crater dictating whether it becomes a simple crater, a complex crater (Fig. 1-1), or a multi-ring basin (French, 1998; Osinski & Pierazzo, 2012). Simple craters appear bowl shaped with only a minor uplift and negligible post-formation modification (Dence, 1965; French, 1998; Grieve et al., 1977; Melosh, 1989; Osinski & Pierazzo, 2012). Complex craters form as a result of the collapsed transient crater appearing as a shallow depression with a central uplift and concentric rings (French, 1998; Grieve, 1991; Osinski & Pierazzo, 2012; Quaide et al., 1965). In the central uplift, rocks from beneath the centre of the crater are uplifted and exposed (Dence et al., 1997; Grieve & Therriault, 2004; Melosh & Ivanov, 1999). Multi-ring basins are formed by very large impactors and are associated with very early stages of planetary accretion and cooling during the late heavy bombardment (LHB), and thus are uncommon on Earth in the present day. Such craters

can be seen on other planets and moons where weathering is less pervasive and structures are well preserved over geological time.

1.2   Shock Effects

Impact events dramatically change the physical properties of the target rocks. A topographic central uplift and concentric outer rim are the most obvious features visible in complex impact structures. Unfortunately, erosional processes and the active atmosphere and crustal recycling processes on Earth significantly complicate how readily we can study craters. Owing to the lack of pristine impact craters on Earth that exhibit such obvious complex morphologies, we must resort to studying craters by investigating the subsequent products that may have been preserved from the original impact event. The extremely high pressure and temperature conditions affect the mineral composition, density, porosity, and magnetic properties found at the site.

It has long been confirmed that the high pressures generated during an impact event affect the bulk physical structure of the target material. Pioneering work by Keiffer (1971, 1976) on the Coconino sandstone of Meteor Crater, Arizona, and further analysis by Cockell and Osinski (2007) and Osinski (2007) on carbonate-bearing sandstones from the Haughton impact structure revealed an increase in the porosity of sandstones with increasing shock level until the pore spaces collapse and the porosity decreases at pressures over ~35 GPa. Comparative analysis was completed by Cockell et al. (2002), Singleton et al. (2011), and Pontefract et al. (2014) on shocked gneisses from the Haughton impact structure revealing a similar trend; however, instead of a decrease in porosity due to pore space collapse, the porosity of these crystalline samples increases until whole rock melting occurs.

Also of importance to the understanding of impact craters is the generation of shock metamorphic features caused by shock waves. Target rocks and minerals develop distinctive micro- and macroscopic shock features such as shatter cones, undulatory extinction, mosaicism, planar fractures (PFs), planar deformation feature (PDFs), and diaplectic glass (Stöffler, 1972; Stöffler, 1974; Stöffler & Grieve, 2007). Within a sample, shock level can vary substantially from one grain to another based on grain size,

composition, orientation, surrounding minerals and heterogeneity in the shock wave (Dence, 2004; Robertson & Grieve, 1977). Jaret et al. (2014, 2018) has suggested that at high shock levels the distinctive features of shock becomes negligible, while at lower shock levels heterogeneity is much more pronounced. Based on the presence of characteristic shock metamorphic effects, the peak shock pressures experienced during impact can be estimated. Recorded peak shock pressures of rocks in the central uplift of smaller (~20 km) complex craters are ~25-30 GPa and larger ones are ~45-50 GPa (Grieve & Cintala, 1992; Grieve & Therriault, 2004; Melosh & Ivanov, 1999). Note that these estimated ranges are significantly less than the maximum pressure experienced at the surface during the contact and compression stages of crater formation (i.e. >100 GPa), and therefore represent material from the deep subsurface that has been stratigraphically uplifted in the form of ejecta during the modification phase (Melosh & Ivanov, 1999).

Most of our knowledge of shock effects are based on alterations found in quartz. Quartz is a well-studied shock level indicator mineral with diagnostic features such as PDFs and diaplectic glass, both of which are unique to specific shock pressures and temperatures (Carter, 1965; Stöffler, 1971). Unfortunately, apart from Earth, most impact target surfaces in our solar system are made of quartz-poor, feldspar-rich basalts.

1.2.1   Shock Metamorphism in Plagioclase Feldspar

Studies on shock effects in plagioclase feldspar have recently been receiving attention. Feldspars are a common framework silicate grouped into two solid solution series, plagioclase feldspar ($CaAl_2Si_2O_8$-$NaAlSi_3O_8$) and alkali feldspar ($NaAlSi_3O_8$- $KAlSi_3O_8$). Feldspar group minerals are extremely abundant on Earth, the Moon and other rocky planets; however, their diverse and complex crystal structure and susceptibility to weathering complicates the study of their shock effects. Feldspars display a range of microscopic shock effects, which (in order of progressing magnitude) appear as fracturing, kinking, undulatory extinction, mosaicism, planar deformation features (PDFs), amorphization and finally melting (Stöffler et al., 2018). Of these shock effects, fracturing, kinking, undulatory extinction and mosaic extinction can be produced by endogenic processes and should not be used as shock indicators outside of an impact

structure setting. Alternatively, planar deformation feature (PDFs), diaplectic glass, and high pressure polymorphs may be used as impact shock metamorphism indicators.

Planar deformation features (PDFs) in feldspars are considered to be a diagnostic shock feature but should be analyzed with care as feldspars have intrinsic characteristics that may be easily mistaken for PDFs (Pickersgill et al., 2015b; Pittarello et al., 2019). Plagioclase feldspars have two good cleavages and twinning is common (Nesse, 2004; Zoltai & Stout, 1984). Additional planar features result from planar fractures, exsolution concentrated along exsolution lamellae, and crystallographically oriented "clouded feldspar" (French and Short, 1968; Stöffler, 1967, 1972; French, 1998). Clouded feldspar is produced when dark inclusions, often oxides of transitions metals, concentrate around twin boundaries and cleavage planes (Poldervaart & Gilkey, 1954; Smith & Brown, 1988; Whitney, 1972). Feldspar PDFs form at ~8-35 GPa, around the same pressure as quartz PDFs (Stöffler, 1971). However, PDFs have only been reported in low-Ca plagioclase (<An_{30}) or K-feldspar because of the structural and compositional effects associated with the high symmetry of monoclinic minerals which encourage the development of PDFs (Gibson & Reimold, 2005; Jaret et al., 2014; Langenhorst et al., 1995; Nagy et al., 2018; Pickersgill et al., 2015b; Pittarello et al., 2013; Trepmann et al., 2003; Xie et al., 2020).

Partial or complete conversion to diaplectic glass is also a diagnostic product of shock. Diaplectic feldspar glass forms at 25-56 GPa depending on composition, porosity, grain size, and water content in the sample (Jaret et al., 2018). Nonporous experimentally shocked albite undergoes amorphization between 50–55.8 GPa, andesine between 28.4–29.4 GPa, and 25.5–27.0 GPa for bytownite. Complete amorphization occurs at >55 GPa for albite, ~47 GPa for andesine, and ~38 GPa for bytownite (Jaret et al., 2018). Natural samples exhibiting increased porosity, weathering and alteration are likely to convert to diaplectic glass at ~5–10 GPa lower than the experimentally shocked samples. Due to common misconceptions related to diapectic glass, characterization should be completed with care and confirmed with X-ray diffraction or Raman spectroscopic analysis. On Earth, diaplectic feldspar glasses are believed to be restricted to large (>20 km), crystalline craters that have experienced high shock pressures (Ferrière & Osinski, 2013).

Although not common in terrestrial impact craters, high pressure polymorphs with feldspathic compositions may also act as impact shock metamorphism indicators. $KAlSi_3O_8$ and $NaAlSi_3O_8$ hollandite have been synthesized and identified in chondrites, Martian meteorites, and terrestrial rocks (Dressler, 2003; El Goresy et al., 2000; Gillet et al., 2000; Liu, 1978; Langenhorst & Poirier, 2000; Ringwood et al., 1967; Tomioka et al., 2000). High pressure jadeite has also been documented in meteorites (Ohtani et al., 2004).

1.2.2   Measuring Shock in Plagioclase Feldspar

The first studies on shock effects in feldspar were conducted with optical petrography, which remains the most commonly used method for reporting shock (e.g., Chao, 1968; Engelhardt & Stöffler, 1968; Kieffer et al., 1976; Walawender, 1977). Based on trends in progression of optical shock features, several classification schemes have been developed and calibrated using experimentally shocked feldspars with known peak shock pressures (e.g., Short & Gold, 1996; Singleton et al., 2011; Stöffler et al., 1991, 2018). However, optical petrographic analysis is only capable of grouping shock stages into relatively large peak pressure ranges with poor precision (Bischoff & Stöffler, 1992; Kieffer et al., 1976; Stöffler, 1971). To help refine optical classifications, Raman spectroscopy, thermal infrared spectroscopy, cathodoluminescence, and X-ray diffraction (XRD) techniques have been developed to support optical observations and quantitively measure shock, crystallinity changes, and structural deformation (e.g., Fritz et al., 2005; Heyamann & Hörz, 1990; Johnson et al., 2002, 2003; Kayama et al., 2009; Pickersgill et al., 2015a; Reynard et al., 1999; Sims et al., 2019; Velde & Boyer, 1985; Velde et al., 1989). Raman studies measuring shocked feldspars result in band broadening and reduced intensity and peak shifting, while amorphization form a broad plateau in the spectra (e.g., Fritz et al., 2019; Jaret et al., 2018; Xie et al., 2020). Thermal infrared absorption shows a decrease in absorption band intensity, particularly for the Si-Si, O-T-O and Si-O bands. Amorphous feldspars (diaplectic glasses) show broad absorption bands near 1,000, 720, and 470 cm^{-1} (Arndt et al., 1982; Bunch et al., 1967; Lyon, 1963; Ostertag, 1983; Stöffler 1971, 1972; Stöffler & Hornemann, 1972). With increased shock level, cathodoluminescence studies display a peak shift to the lower wavelengths and an

increase in CL intensity. XRD results display a change in peak broadening with increased Bragg angle related to the strain of the crystal lattice until amorphization is reached and peaks can no longer be detected (Jenkins et al., 2019; Katama et al., 2012; Uchizono et al., 1999). Peak broadening due to crystallite size and lattice strain can be expressed as: $\beta = \frac{\lambda}{L}cos\theta + 4\varepsilon tan\theta + \beta_0$, whereby β is integral breadth in 2θ, λ is the wavelength, L is the crystal size, θ is the Bragg angle (half of the angle between incident and diffracted beams), ε is the strain, and β_0 is a constant related to the broadening (Williamson & Hall, 1953). With increasing shock pressure, line broadening increases in the 2θ direction, where broadening due to strain increases as a function of tanθ; this can be used to measure the degree of lattice strain within the shocked crystals of interest, helping to more accurately estimate the level of shock experienced (Hanss et al., 1978; Jenkins et al., 2019; Uchizono et al., 1999).

The effects of shock are also seen in XRD analyses of streaking along the Debye rings in the chi (χ) dimension (Fig. 1-2 A). This phenomenon has long been observed in Debye-Scherrer films where the length of streaks increases with increasing peak shock pressure (e.g. Hörz & Quaide, 1973), due to increasing mosaic spread of subgrain orientations within the non-uniformly strained crystal. Today, full-width-half-maximum (FWHM$_\chi$) can be measured quantitatively. The strain-related mosaicity method for quantifying shock in minerals using modern 2D Area Detectors was pioneered by Izawa et al. (2011) for enstatite, and modified by McCausland et al. (2010) and Vinet et al. (2011) for olivine, and by Pickersgill et al. (2015a) for plagioclase. It is important to note that this method is not designed to evaluate the shock level of the bulk rock as a whole, rather it is mineral specific. Thus, it is used in tandem with optical microscopic observations of the whole rock. Pickersgill et al. (2015a) developed their own shocked feldspar scheme (with reference to that of Stöffler et al., 1971) based on optical observation of shock effects within plagioclase minerals with two-dimensional X-ray diffraction (2D XRD). This scheme uses optical images, XRD GADDS images, and measurements of FWHM of peaks in the chi-dimension to study levels of shock in plagioclase. In this study, strain-related mosaicity (FWHM$_\chi$) of individual plagioclase grains was analyzed using X-ray diffraction following the procedure developed for plagioclase by Pickersgill et al. (2015a)

(Fig. 1-2). Using the relationship between FWHM$_\chi$ μXRD measurements, characteristics of 2D XRD diffraction spot images for plagioclase grains, and optical shock metamorphism features (Stöffler et al., 2018), these methods are applied here for the first time to study impact shocked basalts.

1.3   Hydrothermal Systems
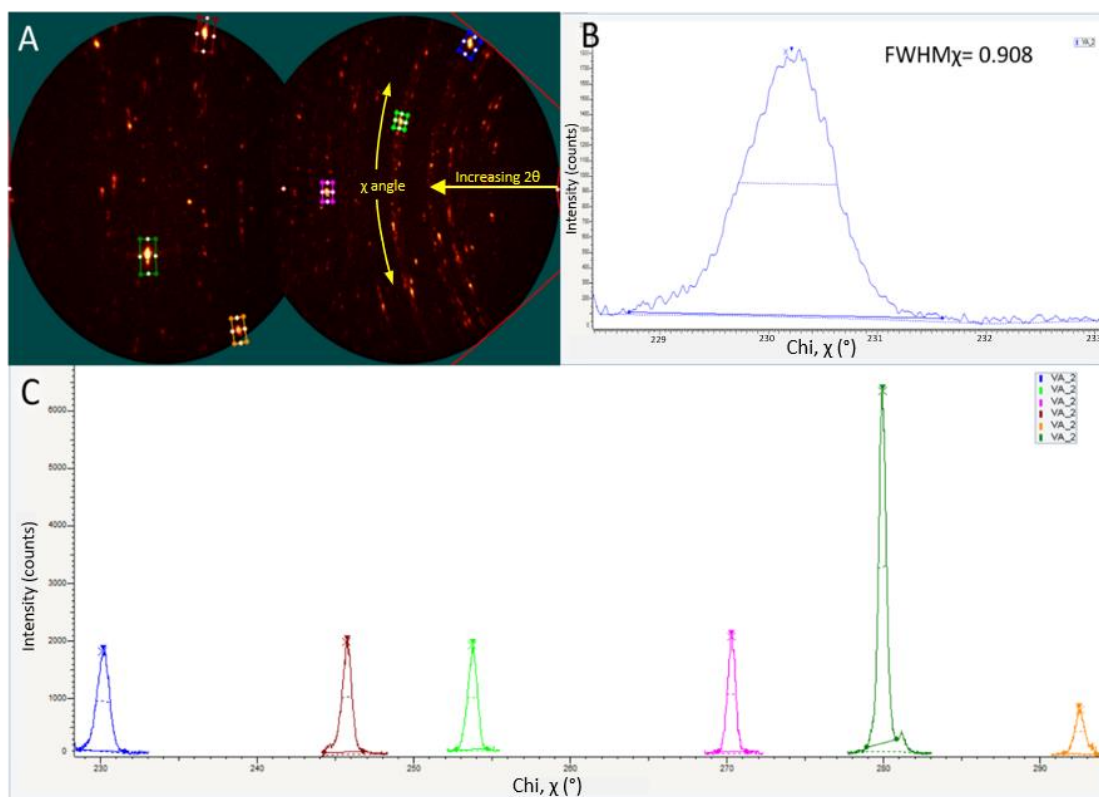
Figure 1-2. Example of strain-related mosaicity (FWHMχ) analyses of Vista Alegre sample VA-2017-2 using the method of Pickersgill et al. (2015a). A) GADDS image indicating spots selected for FWHMχ measurements of a plagioclase grain. B) Intensity versus χ plot of the blue spot with FWHMχ of 0.908°. C) Intensity versus χ plot of all spots.

A fourth stage of impact crater formation known as the alteration stage, has been proposed in addition to the three main phases described in Section 1.1.1. Hydrothermal alteration for example, is possible in both simple and complex craters if there is a sufficient source of water and heat (Abramov & Kring, 2004, 2005; Kirsimäe & Osinski, 2012; Osinski, 2005; Osinski et al., 2005; Osinski & Pierazzo, 2012, Osinski et al., 2013).

Hydrothermal alteration is defined as the chemical weathering of rocks through the redistribution of mass and energy by the movement of H_2O (Norton, 1984). Impact events are conducive to the development of hydrothermal systems because; (1) they provide an external source of energy that may not have been previously available, (2) they form shocked minerals which are more soluble and readily available and (3) they develop a porous environment favorable for transporting the elements.

Although a number of studies have looked at hydrothermal systems within impact structures on Earth, some very important parameters are still poorly understood: the source of the hydrothermal system, the role of the target lithology acting as the fluid reservoir, and the system's role in hosting microbial organisms. There is not much controversy surrounding the origin of these hydrothermal deposits, but a few questions remain hinging on the fact that it can be difficult to determine if hydrothermalism began prior to impact as a result of metamorphic or magmatic environments, or post-impact as a result of impact-induced hydrothermal conditions. To further complicate the matter, these processes are not mutually exclusive and may occur contemporaneously within the same impact structure.

1.3.1 Hydrothermal Alteration on Mars

Hydrothermal activity has been suggested to have occurred on Mars through spectroscopic data obtained with CRISM on the Mars Reconnaissance Orbiter (MRO) and ChemCam on the Curiosity rover (Nazari-Sharabian et al., 2020). Surface and subsurface material containing hydrous phyllosilicates (chlorite + smectites), zeolites and amorphous phases (e.g., silica glasses) are concentrated in heavily impacted areas of Mars (Carter et al., 2013; Ehlmann et al., 2011; Marzo et al., 2010; Murchie et al., 2009; Mustard et al., 2008). Mars currently has a source of solid H_2O, however it is not understood if the hydrated silicates formed as a result of impact-generated hydrothermal alteration on a colder and drier Mars, uplifted during impact from a pre-existing warmer and wetter climate material, or whether both processes contributed to the formation of these hydrous deposits (Osinski et al., 2013; Tornabene et al., 2013). The study of hydrothermal activity on Mars is currently restricted to using remote sensing data and rover data from very limited areas. Consequently, it is necessary to improve our current

understanding on the relationships between impacts and volatiles to better understand the remote data received from Mars by first learning to understand them on Earth. Hydrated silicates on Earth and Mars are very similar, with the most common alteration phases consisting of Mg-Fe phyllosilicates, Al-phyllosilicates, carbonates, zeolites, and oxides. Secondary clay minerals are particularly important for understanding hydrothermal deposits as they can act as a marker of water-rock interactions, giving insight into the temperature, longevity, pH, and reduction potential of the hydrothermal system (Inoue, 1995; Muttik et al., 2008).

1.3.2   Analysis of Clay Minerals

Identification and quantification of clay minerals remains a formidable challenge due to interference factors such as variable chemical compositions, tendency of preferred orientation, structural disorder, and the diversity involving different patterns of layer interstratification (Bergava & Lagaly, 2006; Brindley & Brown, 1980; Chen et al., 2019; Środoń, 2002; Środoń et al., 2001; Zwell & Danko, 1975). There are essentially two common approaches for carrying out the analysis of clays: 'clay fractionation' and 'whole-rock' techniques, of which fractionation followed by powder X-ray Diffraction (pXRD) is the dominant practice for identifying and quantifying mineralogy of clays (Hillier, 2003). pXRD is most effective when aided by other methods such as infrared (IR) spectroscopy, electron microscopy, oxygen isotope analysis and optical microscopy, which are important for validating the XRD method and for measuring bulk quantities, quantifying the mixed layering, determining the three-dimensional organization, and measuring particle sizes (Środoń, 2002).

Bragg's law ($n\lambda = 2d\sin\theta$) (Klug & Alexander, 1962) can be used to calculate the interplanar lattice d-spacing of minerals based on the observed 2θ value. Clay minerals produce low 2θ angle peak positions with d-spacings of 7 Å (kaolinite), 10 Å (illite), and 14 Å (smectite, chlorite) (Brindley & Brown, 1980). When compared to the more common pXRD method, µXRD is less frequently employed for clay minerals due to the difficulty of reaching the low 2θ angles (below 10–15° 2θ) that are characteristic to clay diffraction peaks. To circumvent this limitation, non-standard procedures must be developed for analysis of clays at angles as low as 4° 2θ, far lower than traditional µXRD

scans. The benefit of μXRD analysis is that it is completed *in situ*, non-destructively, and with significantly less sample preparation. Similar to pXRD, distinguishing the mineral types is qualitative (identification) or semi-quantitative.

1.4   Microbial Endolithy in Basalts

To guide the search for life on Mars, we first need to better understand microbial habitability on Earth. Like the majority of solid terrestrial planetary bodies in our solar system, Mars is predominantly basaltic in composition (e.g., Christensen et al., 2000; Christensen et al., 2001; Hamilton & Christensen, 2005; Sprague et al., 2009). For this reason, it is important to select an appropriate terrestrial basaltic analogue system. There is an extensive amount of literature on microorganisms in the terrestrial basaltic oceanic crust. Basaltic glasses within the oceanic crust have been documented to contain tubular and granular microbial alteration textures produced by etching of glass during microbial colonization (e.g., Benzerara et al., 2007; Bridge et al., 2010; Furnes et al., 2004; McLoughlin et al., 2009; Staudigel et al., 2008a; Walton, 2008). There is evidence of life surviving for up to ~3.5 Ga within these habitats developed from the water and basalt interactions (Schopf & Packer, 1987). However, the biodiversity of marine basalts may be heavily influenced by the ocean chemistry and plate tectonics, factors that do not exist on Mars.

The diversity of microbial communities inhabiting terrestrial volcanic glasses with implication to glass weathering has also been explored by Cockell et al. (2019a, 2019b) and Kelly et al. (2010). Results indicate that terrestrial volcanic glasses host diverse bacterial communities, heavily dominated by Actinobacteria. The role of organisms in rock weathering is not yet fully understood; however, Kelly et al. (2010) proposed that weathering of basaltic glasses increases the surface area for attachment and nutrient leaching of microbes. Beyond the studies mentioned above, very little is known about how these systems might translate to crustal basalt aqueous systems such as those found in impact craters.

Impact craters offer suitable environments for lithotrophic organisms by offering a localized reservoir of water, mobilization of minerals, increased porosity, and potentially

a diverse geochemical gradient (Cockell, 2006). An important link between impact cratering and the reactions necessary for life is the formation of secondary minerals, such as clays and zeolites in impact-generated hydrothermal systems. Post-impact hydrothermal deposits have been recognized as important potential templates for catalyzing and synthesizing prebiotic reactions (Ferris et al., 1988; Saladino et al., 2001; Zamarev et al., 1997). Under these conditions, it is also possible for microbes to liberate nutrients and gain chemical energy from redox reactions as an additional source of energy (Banerjee et al., 2008b). Fracture networks and pore spaces provide opportunities for microbial colonization in crystalline substrates that were initially limited in space. These endolithic environments provide a safe setting with protection from wind ablation and UV radiation, while also offering humidity regulation and temperature moderation. The fractures and pores serve as an environment for sediments and water to interact and form metabolically relevant elements (Cockell et al., 2005).

To date, microbial colonization studies within impact structures have been conducted in sandstones (Cockell et al., 2002; Cockell & Osinski, 2007), gneiss (Cockell et al., 2003; Fike et al., 2003; Pontefract et al., 2014), and one study in basaltic rocks (Antony et al., 2014). In that study, Antony et al. (2014) compared endolithic diversity between subaerial (i.e., exposed basalts on the crater wall) and subaqueous basalts (i.e., submerged basalts on the lake bed) at the Lonar impact structure, India, and revealed variations in the bacterial and archaeal communities colonizing crater-wall and lake-bed rocks.

The lack of microbial colonization studies in basaltic impact structures containing evidence of hydrothermal alteration is not altogether surprising. Of the six basaltic impact craters found on Earth, only two have been studied for hydrothermal alteration: Lonar crater (India) and the Vargeão Dome (Brazil) impact structure. However, impact structures that have undergone hydrothermal alteration have demonstrated great astrobiological potential through the ability to provide suitable conditions for the emergence of life by offering energy, nutrients and refugia, as well as protection against environments. In this contribution, two poorly studied basaltic impact structures with evidence of hydrothermal alteration were investigated to expand our understanding of the effects of impacts on basaltic lithologies, the resulting impact-induced hydrothermal

activity, and how both of these factors play a role in endolithic habitability potential. The impact structures used as Martian analogue systems in this study are Vargeão Dome and Vista Alegre.

1.5   Field Sites Background

1.5.1   Vargeão Dome and Vista Alegre Impact Structure

Vargeão Dome (12.4 km diameter, 123± 1.4 Ma) was first discovered by Paiva Filho et al. (1978) within the Serra Geral basalts of Brazil. Like most crater discoveries, it was first hypothesized to be an alkaline intrusion (Paiva Filho et al., 1978) or a volcanic crater (Barbour Jr. & Corrêa, 1981) before being accepted as having been formed by an impact event (Crósta, 1982; Hachiro & Coutinho, 1993). In 2004, Crósta et al. (2004) located the Vista Alegre impact structure (9.5 km diameter, 115± 4 Ma) ~100 km SE of Vargeão, with a similar diameter and geological context. The crater was named Vista Alegre after the rural village within the structure, meaning "Pleasant Sight" in Portuguese (Crósta et al., 2010). Both impact structures were first identified using satellite radar imagery (Crósta et al., 2004; Paiva Filho et al., 1979). Their well-preserved circular morphologies, central uplifts (measured from the outer rim to the bottom of the depression), and vertical fractures propagating radially from the centres of the structures are clearly visible in Landsat/ETM+ imagery (Crósta et al., 2010; Kazzuro-Vieira, 2004). Vargeão Dome and Vista Alegre are both complex impact craters exposing material from deep beneath the surface. Both Vargeão Dome and Vista Alegre have highly deformed and weathered sandstone boulders and polymict impact breccias present in their central uplifts that contain sandstones characteristic of the underlying Pirambóia (Triassic) and Botucatu (Jurassic) Formations. These sandstones usually sit 1,000 meters below the Serra Geral Formation, but were found in the center of both craters with no occurrences of them outside the structures (Kazzuo-Vieira et al., 2009). Although erosion may have played a role in exposing the sandstones at the present surface, the topographic gradients of the Vargeão Dome and Vista Alegre crater rims, 200 and 50 meters respectively, suggest that some of the original crater morphology is preserved (Crósta et al., 2004).

Figure 1-3. A) View of the Vargeão Dome crater along the NW crater rim, and the horizon is defined by the SE crater rim (Poulos, 2002). B) View of the Vista Alegre crater from the northern border, looking south (Crósta et al., 2011).

Shatter cones have been identified within sandstones and basalts in several locations within the two craters (Crósta & Viera, 2004; Pitarello et al., 2015). Shatter cones are the only distinctive shock feature that may be seen with the naked eye and are especially diagnostic of low shock pressures. Vista Alegre impact shatter cones are the only basaltic shatter cones that have been studied in detail (Pittarello et al., 2011). Multiple sets of PDFs were found in isolated quartz grains within breccias and sandstone samples; up to four different directions of PDF sets in Vargeão Dome samples and two sets in the Vista Alegre samples (Crósta et al., 2010; Crósta et al., 2011). The abundance and orientation of PDFs varies with shock pressure and target rock lithology (French, 1998; Grieve et al., 1996). Contrary to shatter cones, PDFs are indicative of higher shock pressures (7 to >30 GPa). Petrographic analysis revealed additional evidence of shock metamorphism in quartz, pyroxene and plagioclase such as undulatory extinction, mosaicism, planar features (PFs), kink banding, high-pressure polymorphs and shock melt occurrences (Crósta et al., 2004).

1.5.2   Basaltic Target Rocks

The volcanic-sedimentary rocks in this region are part of the São Bento Group (Fig. 1-4). The São Bento Group, from bottom to top, is made up of Pirambóia, Botucati and Serra Geral Formations (Crósta et al., 2011). Sedimentation began in the Triassic, followed by the large volcanic event in the Lower Cretaceous. The Pirambóia Formation has an accepted age of Upper Triassic/Lower Jurassic and is composed of aeolian sandstone and

alluvium (clays, silt) deposited by fluvial processes. This sedimentary unit contains both dry aeolian sands of the dune facies and wet aeolian sands of the interdune facies (Caetano-Chang & Wu, 1994). The Botucatu Formation is assigned to the interval between Early Jurassic to Early Cretaceous and is composed of a thick layer of dry-climate aeolian sandstone without the development of wet interdune facies. The upper stratigraphic unit of the Sao Bento Group, the Serra Geral Formation, was generated by volcanism which covered the Botucatu desert with thick basaltic flow between 137 and 127 Ma (Turner et al., 1994) (or 134 Ma, Scherer, 2000). Its formation began with the rifting of the Gondwana supercontinent which occurred in response to the heating of the mantle under the eruption of the Tristan (Tristão da Cunha) mantle plume during the Jurassic-Cretaceous transition (Peate et al. 1992; Turner et al. 1999a, 1999b). This led to the opening of the South Atlantic Ocean and fissure eruptions that split the continent (Ferreira et al., 2015). Strong tectonic control was produced in two main directions of sub-vertical faults: N45°–65°W and N50°–70°E (Zalán et al., 1990). The generated lava flow covered an area of more than 1,200,000 km^2 with thickness of up to 1700 m in the southeastern South America, forming one of the largest and most extensive flood basalt provinces on Earth, known as the present-day Parana Basin, Brazil (Milani et al., 2007).
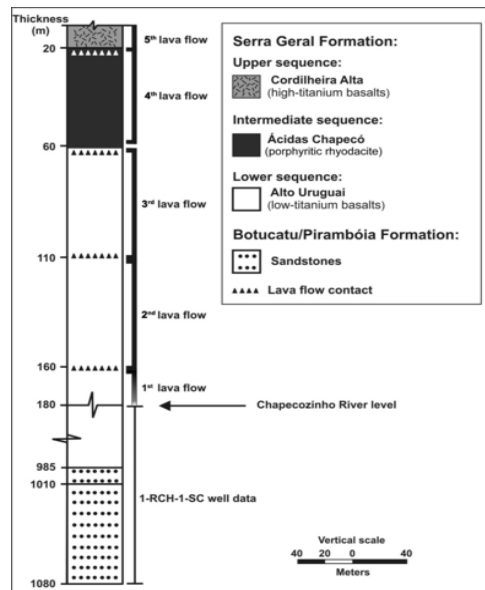
Figure 1-4. Stratigraphic column of the volcanic-sedimentary São Bento Group composed of the Serra Geral Formation and Botucatu/Pirambóia Formation. The upper volcanic sequence (Cordilheira Alta) does not occur at Vargeão Dome or Vista Alegre impact structures (Crósta et al., 2011).

Three-quarters of the total present-day Parana magmatic province belongs to the Serra Geral Formation, and consists of tholeiitic flood basalts (90 vol. %), tholeiitic andesine (~7 vol. %) and minor felsic volcanics such as dacites, rhyolites, thyodacites, and trachites (~3 vol.%) (Bellieni et al., 1984; Piccirillo & Melfi, 1988). The remainder of target rocks consists of sandstones from the Piramboia/ Botucatu Formations and calcite grains immersed in a fine-grained cataclastic matrix (Caetano-Chang et al., 1994).

1.5.3   Vargeão Dome and Vista Alegre Hydrothermal Systems

Below the 7500-meter-thick volcano-sedimentary Parana basin, lies one of the most important transboundary hydro-stratigraphic units in Southern Brazil, the Guarani Aquifer System (SAG, from the Spanish and Portuguese abbreviation) (Zalan et al., 1990). The Guarani Aquifer, also called the Mercosul aquifer system, is one of the largest water reservoirs in the world. With a surface area of 1.1 million km^2 and containing about 37,000 km^3 of water, it serves as an important source of fresh water for Brazil, Argentina, Uruguay and Paraguay (Araújo et al., 1999). Detailed water compositions from several wells in São Paulo state, Brazil can be found in Sracek and Hirata (2002) and are believed to be representative of the whole system.

Even prior to the impact events weakening and fracturing the target rock, the Parana basin was highly susceptible to hydrothermal alteration. The sedimentary characteristics of the host rock serves as an excellent reservoir for groundwater migration. The Cretaceous aeolian sandstones of the Botucatu Formation are well sorted and highly porous (average 19.5%, Gesicki, 2007). Parana basin basalts host secondary alteration phases which have been suggested to form as a result of low-grade metamorphism from continental spreading (Franco, 1952; Murata et al., 1987). Yokoyama et al. (2015) revealed evidence of post-impact hydrothermal alteration in the breccia veins of the Vargeão Dome impact structure and proposed that the impact triggered a hydrothermal system. Hydrothermalism within Vista Alegre has been mentioned by Pinto et al. (2011), but no formal detailed analysis has yet been conducted.

1.6   Introduction to thesis

This thesis is divided into four chapters. Chapter 1 provides an introduction to the work and the necessary background information about impact cratering, hydrothermal systems, and the biological habitability of basaltic impact craters. Chapter 2 is a manuscript (to be submitted to Meteoritics & Planetary Science) investigating shock deformation throughout the Vargeão Dome and Vista Alegre impact structures. Petrographic shock effects of impact target basalts and breccias from various locations within and around the impact structures are reported as results. This paper utilizes an effective, non-destructive, quantitative method to measure shock level in plagioclase feldspar grains and expands it to also include basaltic lithologies using micro X-ray diffraction (µXRD). Chapter 2 also reports the effect of impacts on the bulk physical characteristics of the target lithology, revealing that with increased shock level, porosity increases and bulk and grain density decreases. Chapter 3 characterizes the hydrothermal alteration in the Vista Alegre impact structure using optical microscopy, electron probe microanalysis (EPMA), and a novel µXRD technique optimized for clays and zeolites. The results suggest a differentiation between pre- and post-impact hydrothermal alteration within and outside the impact structure. Chapter 4 integrates the preceding chapters and frames this work within the context of searching for life beyond Earth with a particular focus on evaluating Martian conditions for life.

Appendix A provides an unfinished manuscript consisting of an introduction, detailed methods, and potential outcomes for a culture independent colonization experiment of shocked basalts. Sample culturing, DNA extraction, and bulk cell count preparation was completed before the COVID-19 pandemic began, but unfortunately 16S rRNA gene sequencing and bulk cell count results could not be obtained due to the ensuing pandemic. Additional appendices contain details about experimental methods and a complete set of results. These include all sample descriptions/petrology, µXRD General Area Diffraction Detection System (GADDS) images, diffraction patterns, chi plots and Full-Width-at-Half-Maximum measurements in chi (FWHMχ), EPMA analyses, Backscattered Electron (BSE) images and raw spectra from Raman analyses.

1.7   References

Abramov, O., & Kring, D. A. (2004). Numerical modeling of an impact-induced hydrothermal system at the Sudbury crater. *Journal of Geophysical Research, 109*, E10007.

Ahrens, T., & O'Keefe, J. (1972). Shock melting and vaporization of lunar rocks and minerals. *The Moon, 4*, 214–249.

Antony, C. P., Shimpi, G. G., Cockell, C. S., Patole, M. S., & Shouche, Y. S. (2014). Molecular characterization of prokaryotic communities associated with Lonar crater basalts. *Geomicrobiology Journal, 31*(6), 519–528.

Arndt, J., Hummel, W., & Gonzalez-Cabeza, I. (1982). Diaplectic labradorite glass from the Manicouagan impact crater; I, Physical properties, crystallization, structural and genetic implications. *Physics and Chemistry of Minerals, 8*, 230–239.

Barbour Jr., E., and Corrêa, W. A. G. (1981). Geologia da Estrutura de Vargeao, SC. *Relatório Técnico, Paulipetro, Consórcio CESP-IPT,* pp. 33.

Benzerara, K., Menguy, N., Banerjee, N. R., Tyliszczak, T., Brown, G. E. Jr., & Guyot, F. (2007). Alteration of submarine basaltic glass from the Ontong Java Plateau: a STXM and TEM study. *Earth Planetary Science Letters, 260*(1-2), 187–200.

Bergaya, F., & Lagaly, G. (2006). General introduction: Clays, clay minerals, and clay science. *Development in Clay Science*, *1*(1), 1–18.

G. W. Brindley, & G. Brown (Eds.) (1980). *Crystal Structures of Clay Minerals and Their X-Ray Identification* (pp. 125–195). Mineralogical Society, London, England.

Bunch, T. E., Cohen, A. J. & Dence, M. R. (1967). Natural terrestrial maskelynite. *American Mineralogist, 52*, 244–253.

Caetano-Chang, M. R., & Wu, F. T. (1994). Afloramento modelo da Formaçõ Pirambóia. *Geociências*, *13*(2), 371–385.

Carter, N. L. (1965). Basal quartz deformation lamellae-a criterion for recognition of impactites. *American Journal of Science*, *263*(9), 786–806.

Carter, J., Poulet, F., Bibring, J. P., Mangold, N. & Murchie, S. (2013). Hydrous minerals on Mars as seen by the CRISM and OMEGA imaging spectrometers: updated global view. *Journal of Geophysics Research: Planets, 118*(4), 831–858.

Chao, E. C. T. (1968). Pressure and temperature histories of impact metamorphosed rocks, based on petrographic observations. In B. French, N. M. Short (Eds.), *Shock metamorphism of natural materials* (pp. 135-158). Mono Book Corp., Baltimore, MD

Chen, Y., Wang, Q., & Han, Y. (2019). Crystallization variations in clay minerals with latitude in Jilin province, China: A climate perspective. *Clays, Clay Minerology, 67*, 507–517.

Christensen, P. R., Bandfield, R. N., Clark, R. N., Edgettt, K. S., Hamilton, V. E., Hoefen, H. H., Kieffer, R. O., Kuzmin, R. O., Lane, M. D., Malin, M. C., Morris, R. V., Pearl, R., Pearson, T. L., Roush, S. W., & Smith, M. D. (2000). Detection of crystalline hematite mineralization on Mars by the Thermal Emission Spectrometer: Evidence for near-surface water, *Journal of Geophysics Research*, *105*(E4), 9632– 9642.

Christensen, P. R., Bandfield, J. L., Hamilton, V. E., Ruff, S. W., Kieffer, H. H., Titus, T. N., Malin, M. C., Morris, R. V, Lane, M. D., Clark, R. L., Jakosky, B. M., Mellon, M. T., Pearl, J. C., Conrath, B. J., Smith, M. D., Clancy, R. T., Kuzmin, R. O., Roush, T., Mehall, G. L., Gorelick, N., Bender, K., Murray, K., Dason, S., Greene, E., Silverman, S., & Greenfield, M. (2001). Mars global surveyor thermal emission spectrometer experiment: Investigation description and surface science results. *Journal of Geophysics Research*, *106*(E10), *23*823–23871.

Cockell, C. S. (2006). The origin and emergence of life under impact bombardment. *Philosophical Transactions of the Royal Society B. Biological Sciences, 361*(1474), 1845–1856

Cockell, C. S., Lee, P., Osinski, G. R., Horneck, G., & Broady, P. (2002). Impact-induced microbial endolithic habitats. *Meteoritics & Planetary Science, 37*(10), 1287–1298.

Cockell, C. S., Lee, P., Broady, P., Lim, D. S. S., Osinski, G. R., Parnell, J., Koeberl, C., Pesonen, L., & Salminen, J. (2005). Effects of asteroid and comet impacts on habitats for lithophytic organisms —A synthesis. *Meteoritics & Planetary Science, 40*(12), 1901–1914.

Cockell, C. S., Olsson, K., Knowles, F., Kelly, L., Herrera, A., Thorsteinsson, T., & Marteinsson, V. (2009a). Bacteria in Weathered Basaltic Glass, Iceland. *Geomicrobiology Journal,* 26(7), 491–507.

Cockell, C. S., Olsson-Francis, K., Herrera, A., & Meunier, A. (2009b). Alteration textures in terrestrial volcanic glass and the associated bacterial community. *Geobiology, 7*(1), 50–65.

Cockell, C. S., & Osinski, G. R. (2007). Impact-induced impoverishment and transformation of a sandstone habitat for lithophytic microorganisms. *Meteoritics & Planetary Science, 42*(11), 1985– 1993.

Cockell, C., Rettberg, P., Horneck, G., Scherer, K., & Stokes, D. M. (2003). Measurements of microbial protection from ultraviolet radiation in polar terrestrial microhabitats. *Polar Biology*, *26*(1), 62-69.

Croft, S. K. (1980, March 17-21). *Cratering flow fields: Implications for the excavation and transient expansion stage of crater formation* [abstract]. 11th Lunar and Planetary Science Conference, Houston, TX.

Crósta A. P. (1982 Septemeber*). Estruturas de impacto no Brasil: Uma síntese do conhecimento atual* [abstract]. Anais do XXXII Congresso Brasileiro de Geologia, Salvador, Bahia.

Crósta, A. P. (1987). Impact structures in Brazil. In P. J. Wiesbaden (Ed.), *Research in terrestrial impact structures* (pp. 30-38). Friedrich Vieweg & Sohn.

Crósta, A. P., Kazzuo-Vieira, C., Pitarello, L., Koeberl, C., & Kenkmann, T. (2011). Geology and impact features of Vargeão Dome, southern Brazil. *Meteoritics & Planetary Science, 47*(1), 51–71.

Crósta, A. P., Kazzuo-Vieira, C., and Schrank, A. (2004, August 2-6). *Vista Alegre: A newly discovered impact crater in Southern Brazil* [abstact # 50501]. 67th Annual Meteoritics Society Meeting, Rio de Janeiro, Brazil.

Crósta, A. P., Koeberl, C., Furuie, R. A., Kazzuo-Vieira, C. (2010). The first description and confirmation of the Vista Alegre impact structure in the Paraná flood basalts of southern Brazil. *Meteoritics & Planetary Science*, *45*(2), 181–194

Dence, M. R.., Grieve, R. A. G., and Robertson, P. B. (1977). Terrestrial impact structures: Principal characteristics and energy consideration, in D. J. Roddy, R. O. Pepinn, and R. B. Merrill (Eds.), *Impact and exploration cratering* (pp. 247-275). Pergamon, New York.

Ehlmann, B. L., Mustard, J. F., Murchie, S. L., Bibring, J. P., Meunier, A., Fraeman, A. A., & Langevin, Y. (2011). Subsurface water and clay mineral formation during the early history of Mars. *Nature, 479*(7371), 53–60.

El Goresy, A., Chen, M., Gillet, P., & Dubrovinsky, L. S. (2000). Shock-induced high-pressure phase-transition of labradorite to hollandite "(Na47-Ca51-K2)" in Zagami and the assemblage hollandite "(Na80-Ca12-K8)" + jadeite in L chondrites: constraints to peak-shock pressures. *Meteoritics & Planetary Science Supplement, 35*, A51.

Engelhardt, W. von, & Stöffler, D. (1968). Stages of shock metamorphism in crystalline rocks of the Ries Basin, Germany. In B. M. French, and N. M. Short (Eds.), *Shock metamorphism of natural materials* (pp. 159-168). Mono Book Corp. Baltimore, MD.

Ferreira, J. C., Leite, E. P., Vasconcelos, M. A., & Crósta, A. P. (2019). 3D Gravity Modeling Of Impact Structures In Basaltic Formations In Brazil: Part I – Vargeão, Santa Catarina. *Revista Brasileira De Geofísica, 33*(2), 319-332.

Ferrière, L. & Osinski, G. R. (2013). Shock metamorphism. In G. R. Osinski, and E. Pierazzo (Eds.), *Impact cratering: Processes and products* (pp. 106-124). Oxford: Wiley-Blackwell.

Ferris, J. P., Huang, V. H., & Hagan, W. J. (1988). Montmorillonite: a multifunctional mineral catalyst for the prebiological formation of phosphate esters. *Origins of Life and Evolution of Biospheres, 18*(1-2), 121–133.

Fike, D. A., Cockell, C. S., Pearce, D., & Lee, P. (2003). Heterotrophic microbial colonization of the interior of impact-shocked rocks from Haughton impact structure, Devon Island, Nunavut, Canadian High Arctic. *International Journal of Astrobiology, 1*(4), 311–323.

Franco, R. R. (1952). Zeolitas dos basaltos do Brasil meridional (Genese e paragenese): Univ. Sao Paulo, Fac. Filos., Cien. e Letras, Bol. 150, *Mineralogia, 10*, 53.

French, B. M. (1998). *Traces of catastrophe, a handbook of shock-metamorphic effects in terrestrial meteorite impact structures* [LPI Contribution No. 954]. Lunar and Planetary Institute, Houston, TX.

Fritz, J., Assis Fernandes, V., Greshake, A., Holzwarth, A., & Böttger, U. (2019). On the formation of diaplectic glass: Shock and thermal experiments with plagioclase of different chemical compositions. *Meteoritics & Planetary Science, 54*(7), 1533– 1547.

Fritz, J., & Greshake, A. (2009). High-pressure phases in an ultramafic rock from Mars. *Earth and Planetary Science Letters, 288*(3), 619–623.

Fritz, J., Greshake, A., & Stöffler, D. (2005). Micro-Raman spectroscopy of plagioclase and maskelynite in Martian meteorites: Evidence of progressive shock metamorphism. *Antarctic Meteorite Research,* 18, 96–116.

Furnes, H., Banerjee, N. R., Muehlenbachs, K., Staudigel, H., & de Wit, M. (2004). Early life recorded in archean pillow lavas. *Science, 304*(5670), 578–581.

Gault, D. E., Quaide, W. L., & Oberbeck, V. R. (1968). Impact Cratering Mechanics and Structures. In B.M. French, and N. M. Short (Eds.), *Shock Metamorphism of Natural Materials* (pp. 87-99). Mono Book Corp., Baltimore, MD.

Gesicki, A. L. D. (2007). Evolucao diagenetica das formacoes Piramboia e Botucatu (Sistema Aquifero Guarani) no Estado de Sao Paula [Master's thesis, University of Sao Paulo]. Teses e Dissertações.

Gibson, R. L., & Reimold, W. U. (2005). Shock pressure distribution in the Vredefort impact structure, South Africa. In T. Kenkmann, F. P. Hörz, and A. Deutsch (Eds.), *Special Paper - Geological Society of America* (pp. 329-349). Geological Society of America, Boulder, CO.

Gillet, P., Chen, M., Dubrovinsky, L., & El Goresy, A. (2000). Natural NaAlSi3O8-hollandite in the shocked sixiangkou meteorite. *Science*, *287*(3), 1633–1636.

Grieve, R. A. F., & M. J. Cintala. (1981). *A method for estimating the initial impact conditions of terrestrial cratering events, exemplified by its application to Brent crater, Ontario* [abstract]. 12th Lunar and Planetary Science Conference, Houston, TX.

Grieve, R. A. F., & Cintala, M. J. (1992). An analysis of differential impact melt-crater scaling and implications for the terrestrial impact record. *Meteoritics, 27*(5), 526–538.

Grieve, R. A. F., Dence, M. R., & Robertson, P. B. (1977). Cratering processes: As interpreted from the occurrence of impact melts. In D. J. Roddy, R. O. Repin, and R. B. Merrill (Eds.), *Impact and Explosion Cratering* (pp. 791–814). New York: Pergamon Press.

Grieve, R. A., & Kring, D. A. (2007). The geologic record of destructive impact events on Earth. In *Comet/Asteroid Impacts and Human Society* (pp. 3-24). Springer, Berlin, Heidelberg.

Grieve, R. A. F., Langenhorst, F., & Stöffler, D. (1996). Shock metamorphism of quartz in nature and experiment: II. Significance in geoscience. *Meteoritics & Planetary Science*, *31*(1), 6-35.

Grieve, R. A., & Therriault, A. M. (2004). Observations at terrestrial impact structures: Their utility in constraining crater formation. *Meteoritics & Planetary Science, 39*(2), 199–216.

Hachiro, J., & Coutinho J. M. V. (1993). 3º Simp. Geol. Sudeste. *Brazilian Geological Society*, 276-283.

Hamilton, V. E., & Christensen, P. R. (2005). Evidence for extensive, olivine-rich bedrock on Mars. *Geology, 33*(6), 433–436

Hanss, R. & Montague, B. & Davis, M. & Galindo, Charles & Horz, F. (1978). *Pressure Distribution in Naturally and Experimentally Shocked Granodiorites* [abstract]. 9th Lunar and Planetary Science Conference, Houston, Texas.

Hillier, S. (2003). Quantitative analysis of clay and other minerals in sandstones by X-ray powder diffraction (XRPD). In R.H. Worden and S. Morad (Eds.), *Clay Mineral Cements in Sandstones* (pp. 213–251). Wiley Blackwell.

Hörz, F., & Quaide, W. L. (1973). Debye-Scherrer investigations of experimentally shocked silicates. *The Moon, 6*(1-2), 45–82.

Inoue, A., Lanson, B., Marques-Fernandes, M., Sakharov, B. A., Murakami, T., Meunier, A., & Beaufort, D. (2005). Illite-smectite mixed-layer minerals in the hydrothermal alteration of volcanic rocks: I. One-dimensional XRD structure analysis and characterization of component layers. *Clays: Clay Minerals, 53*(5), 423–439.

Izawa, M. R. M., Flemming, R. L., Banerjee, N. R., & McCausland, P. J. A. (2011). Micro-X-ray diffraction assessment of shock stage in enstatite chondrites. *Meteoritics & Planetary Science, 46*(5), 638–651.

Jaret, S. J., Johnson, J. R., Sims, M., Difrancesco, N., & Glotch, T. D. (2018). Microspectroscopic and Petrographic Comparison of Experimentally Shocked Albite, Andesine, and Bytownite. *Journal of Geophysical Research: Planets, 123*(7), 1701–1722.

Jaret, S. J., Kah, L. C., & Harris, R. S. (2014). Progressive deformation of feldspar recording low-barometry impact processes, Tenoumer impact structure, Mauritania. *Meteoritics and Planetary Science*, *49*(6), 1007– 1022.

Johnson, J. R., Hörz, F., Lucey, P. G., & Christensen, P. R. (2002). Thermal infrared spectroscopy of experimentally shocked anorthosite and pyroxenite; implications for remote sensing of Mars. *Journal of Geophysical Research*, *107*(E5), 14.

Johnson, J. R., Hörz, F., & Staid, M. I. (2003). Thermal infrared spectroscopy and modeling of experimentally shocked plagioclase feldspars. *American Mineralogist 88*(10), 1575–1582.

Kayama, M., Gucsik, A., Nishido, H., Ninagawa, K., & Tsuchiyama, A. (2009). Cathodoluminescence and Raman spectroscopic characterization of experimentally shocked plagioclase. *AIP Conference Proceedings, 1163*, 86.

Kazzuo-Vieira, C., Crósta, A. P., Gamboa, F., & Tygel, M. (2009). Characterização geofisoca da estrutura de impacto do Domo de Vargeão, Brasil. *Revista Brasileira de Geofisica, 27*(3), 375-388.

Kelly, L. C., Cockell, C. S., Piceno, Y. M., Andersen, G. L., Thorsteinsson, T., & Marteinsson, V. (2010). Bacterial Diversity of Weathered Terrestrial Icelandic Volcanic Glasses. *Microbial Ecology, 60*(4), 740–752.

Kieffer, S. W. (1971). Shock metamorphism of the Coconino Sandstone at Meteor Crater, Arizona. *Journal of Geophysical Research, 76*(23), 5449–5473.

Kieffer, S. W., Phakey, P. P., & Christie, J. M. (1976b). Shock processes in porous quartzite: Transmission electron microscope observations and theory. *Contributions to Mineralogy and Petrology*, *59*, 41–93.

Kieffer, S. W., Schaal, R. B., Gibbons, R., Horz, F., Milton, D. € J., &Dube, A. (1976a, March 15-19). *Shocked basalt from Lonar Impact Crater, India, and experimental analogues* [abstract]. 7th Lunar Science Conference, Houston, TX.

Kieffer, S. W., & Simonds, C. H. (1980). The role of volatiles and lithology in the impact cratering process. *Review of Geophysics and Space Physics, 18*(1), 143–181.

Kirsimäe, K., & Osinski, G. R. (2012). Impact-Induced Hydrothermal Activity. In G. R. Osinski, and E. Pierazzo (Eds.), *Impact cratering: Processes and products* (pp. 76–89). Wiley Blackwell.

Klug H. P. & Alexander L. E. 1962. X‑ray diffraction procedures for polycrystalline and amorphous materials. New York: Wiley.

Koeberl, C. (2004). The Late Heavy Bombardment in the Inner Solar System: Is There Any Connection to Kuiper Belt Objects? *The First Decadal Review of the Edgeworth-Kuiper Belt, 92*, 79–87.

Langenhorst, F., & Dressler, B. (2003). *First observation of silicate hollandite in a terrestrial rock* [abstact 4046]. Lunar Plantary Institute Contribution 1167.

Langenhorst, F., Joreau, P., & Doukhan, J. C. (1995). Thermal and shock metamorphism of the Tenham chondrite: A TEM examination. *Geochimica et Cosmochimica Acta, 61*(4), 1835– 1845.

Langenhorst, F., & Poirier, J. P. (2000). Anatomy of black veins in Zagami; clues to the formation of high-pressure phases. *Earth and Planetary Science Letters, 184*(1), 37–55.

Liu, L. G. (1978). High-pressure phase transformations of albite, jadeite and nepheline. *Earth and Planetary Science Letters, 37*(3), 438–444.

Lyon, R. J. P. (1963). *Evaluation of infrared spectrophotometry for compositional analysis of lunar and planetary soils* [NASA Technical Note D-1871]. Stanford Research Institute; Contract NASA-49 (04).

Marzo, G. A., Davila, A. F., Tornabene, L. L., Dohm, J. M., Fairn, A. G., Gross, C., Kneissl, T., Bishop, J. L., Roush, T. L., & McKay, C. P. (2010). Evidence for hesperian impact-induced hydrothermalism on mars. *Icarus, 208*, 667–683.

McCausland, P. J. A., Flemming, R. L., & Izawa, M. R. M. (2010, December*). Quantitative shock stage assessment in olivine and pyroxene bearing meteorites via in situ microXRD* [abstract #P14C-03]. American Geophysical Union Fall Meeting 91, San Francisco, California.

McLoughlin, N., Furnes, H., Banerjee, N. R., Muehlenbachs, K., & Staudigel, H. (2009). Ichnotaxonomy of microbial trace fossils in volcanic glass. *Journal of Geological Society, 166*(1), 159–169.

Melosh, H. J. (1989). *Impact Cratering: A Geologic Process.* New York: Oxford University Press.

Melosh, H. J., &Ivanov, B. A. (1999). Impact crater collapse. *Annual Review of Earth and Planetary Science*s, *27*(1), 385–415.

Milani, E.J., Melo, J.H.G., Souza, P.A., Fernandes, L.A., França, A.B. (2007). Bacia do Paraná. *Boletim de Geociências da Petrobras, 15*(2), 265–287.

Murata, K. J., Formoso, M. L., & Roisenberg, A. (1987). Distribution of Zeolites in Lavas of Southeastern Parana Basin, State of Rio Grande Do Sul, Brazil. *The Journal of Geology, 95*(4), 455–467.

Murchie, S. L., Mustard, J. F., Ehlmann, B. L., Milliken, R. E., Bishop, J. L., McKeown, N. K., Dobrea, E. Z. N., Seelos, F. P., Buczkowski, D. L., Wiseman, S. M., Arvidson, R. E., Wray, J. J., Swayze, G., Clark, R. N., Marais, D. J. D., McEwen, A. S., & Bibring, J. P. (2009). A synthesis of Martian aqueous mineralogy after 1 Mars year of observations from the Mars Reconnaissance Orbiter. *Journal of Geophysics Research*, *114*, E00D06.

Mustard, J. F., Murchie, S. L., Pelkey, S. M., Ehlmann, B. L., Milliken, R. E., Grant, J. A., Bibring, J. P., Poulet, F., Bishop, J., Dobrea, E. N., Roach, L., Seelos, F., Arvidson,

Muttik, N., Kirsimäe, K., Somelar, P., & Osinski, G. R. (2008). Post-impact alteration of surficial suevites in Ries crater, Germany: Hydrothermal modification or weathering processes? *Meteoritics & Planetary Science, 43*(11), 1827–1840.

Nagy, S., Gucsik, A., Berczi, S., Ninagawa, K., Nishido, H., Kereszturi, A., Hargitai, H., & Okumura, T. (2008, March). *Kfeldspar and biotite as shock indicator minerals from Bosumtwi impact crater* [abstract #1144]. 39th Lunar and Planetary Science Conference, League City, TX.

Nazari-Sharabian, M., Aghababaei, M., Karakouzian, M., & Karami, M. (2020). Water on Mars—a literature review. *Galaxies*, *8*(2), 40.

Nesse, W. D. (2004). *Introduction to Optical Mineralogy* (3rd ed.). New York: Oxford University Press.

Ohtani, E., Kimura, Y., Kimura, M., Takata, T., Kondo, T., & Kubo, T. (2004). Formation of high-pressure minerals in shocked L6 chondrite Yamato 791384: constraints on shock conditions and parent body size. *Earth and Planetary Science Letters,* 227, 505–515.

Osinski, G. R. (2005). Hydrothermal activity associated with the Ries impact event, Germany. *Geofluids, 5*(3), 202–220.

Osinski, G. R. (2007). Impact metamorphism of CaCO3-bearing sandstones at the Haughton structure, Canada. *Meteoritics & Planetary Science, 42*(11), 1945–1960.

Osinski, G. R., Grieve, R. A., Bleacher, J. E., Neish, C. D., Pilles, E. A., & Tornabene, L. L. (2018). Igneous rocks formed by hypervelocity impact. *Journal of Volcanology and Geothermal Research*, *353*, 25-54.

Osinski, G. R., Lee, P., Parnell, J., Spray, J. G., & Baron, M. (2005). A case study of impact-induced hydrothermal activity: The Haughton impact structure, Devon Island, Canadian High Arctic. *Meteoritics & Planetary Science, 40*(12), 1859–1877.

Osinski, G. R., & Pierazzo, E. (2012). *Impact Cratering: Processes and Products*. Wiley-Blackwell.

Osinski, G. R., Tornabene, L. L., Banerjee, N. R., Cockell, C. S., Flemming, R., Izawa, M. R. M., McCutcheon, J., Parnell, J., Preston, L., Pickersgill, A. E., Pontefract, A., Sapers, H. M., & Southam, G. (2013). Impact-generated hydrothermal systems on Earth and Mars. *Icarus*, *224*(2), 347–363.

Ostertag, R. (1983). Shock experiments on feldspar crystals. *Journal of Geophysical Research, 88*, 364–B376.

Paiva Filho, A., Andrade, C. A. V. de., & Scheibe, L. F. (1978). Uma janela estratigra´fica no oeste de Santa Catarina: O Domo de Vargea˜o. 30! Congresso Brasileiro de Geologia, Recife, Brazil: *Sociedade Brasileira de Geologia*, 408–412.

Peate, D. W., Hawkesworth, C. J. & Mantovani, M. S. M. (1992). Chemical stratigraphy of the Parana lavas (South America): classification of magma types and their spatial distribution. *Bulletin of Volcanology, 55*(1-2), 119–139.

Piccirillo, E. M., Comin-Chiaramonti, P., Melfi, A. J., Stolfa, D., Bellieni, G., Marques, L. S., Giaretta, A., Nardy, A. J. R., Pinese, J. P. P., Raposa, M. I. B. & Roisenberg, A. (1988). Petrochemistry of continental flood basalt–rhyolite suites and related intrusives from the Paraná basin (Brazil). In E. M. Piccirillo, & A. J. Melfi (Eds.), *The Mesozoic Flood Volcanism of the Paraná Basin: Petrogenetic and Geophysical Aspects* (pp. 94–106)*. São Paulo: University of São Paulo.

Pickersgill, A. E., Flemming, R. L., & Osinski, G. R. (2015a). Toward quantification of strain-related mosaicity in shocked lunar and terrestrial plagioclase by in situ micro-X-ray diffraction. *Meteoritics & Planetary Science, 50*(11), 1851–1862.

Pickersgill, A. E., Osinski, G. R., & Flemming, R. L. (2015b). Shock effects in plagioclase feldspar from the Mistastin Lake impact structure, Canada. *Meteoritics & Planetary Science, 50*(9), 1546–1561.

Pinto, V. M., Hartmann, L. A., & Wildner, W. (2010). Epigenetic hydrothermal origin of native copper and supergene enrichment in the Vista Alegre district, Paraná basaltic province, southernmost Brazil. *International Geology Review, 53*(10), 1163–1179.

Pittarello, L., Nestola, F., Viti, C., Crósta, A. P., & Koeberl, C. (2015). Melting and cataclastic features in shatter cones in basalt from the Vista Alegre impact structure, Brazil. *Meteoritics & Planetary Science, 50*(7), 1228–1243.

Poldervaart, A., & Gilkey, A. K. (1954). On clouded plagioclase. *American Mineralogist, 39*, 75–91.

Pontefract, A., Osinski, G. R., Cockell, C. S., Moore, C. A., Moores, J. E., & Southam, G. (2014). Impact-Generated Endolithic Habitat Within Crystalline Rocks of the Haughton Impact Structure, Devon Island, Canada. *Astrobiology, 14*(6), 522–533.

Quaide, W. L., Gault, D. E., & Schmidt, R. A. (1965). Gravitative effects on lunar impact structures. *Annals of the New York Academy of Science*, *123*(2), 563–572.

Reynard, B., Okuno, M., Shimada, Y., Syono, Y., & Willaime, C. (1999). A Raman spectroscopic study of shock-wave densification of anorthite (CaAl2Si2O8) glass. *Physics and Chemistry of Minerals, 26*(6), 432–436.

Ringwood, A. E., Reid, A. F., & Wadsley, A. D. (1967). High pressure transformation of alkali aluminosilicates and aluminogermanates. *Earth and Planetary Science Letters, 3*, 38–40.

Robertson, P. B., & Grieve, R. A. F. (1977). Shock attenuation at terrestrial impact structures. In D. J. Roddy, R. O. Peppin, and R. B. Merrill (Eds.), *Impact and explosion cratering* (pp. 687–702). New York: Pergamon Press.

Saladino, R., Crestini, C., Costanzo, G., Negri, R., & Di Mauro, E. (2001). A possible prebiotic synthesis of purine, adenine, cytosine, and 4(3H)-pyrimidinone from formamide: implications for the origin of life. *Bioorganic & Medicinal Chemistry, 9*(5), 1249–1253.

Scherer, C.M. (2000). Eolian dunes of the Botucatu Formation (Cretaceous) in southernmost Brazil; morphology and origin; *Sedimentary Geology, 137*(1–2), 63–84.

Schopf, J. W. & Packer, B. M. (1987). Early Archean (3.3-billion to 3.5-billion-year-old) microfossils from Warrawoona Group, Australia. *Science, 237*(4810), 70–73.

Short, N. M., & Gold, D. P. (1996). Petrography of shocked rocks from the central peak at the Manson impact structure. In C. Koeberl, and R. R. Anderson (Eds.), *Special Paper - Geological Society of America* (pp. 245–265). Geological Society of America (GSA), Boulder, CO.

Singleton, A. C., Osinski, G. R., McCausland, P. J. A., & Moser, D. E. (2011). Shock induced changes in density and porosity in shock-metamorphosed crystalline rocks, Haughton impact structure, Canada. *Meteoritics & Planetary Science, 46*, 1774– 1786.

Sims, M., Jaret, S. J., Carl, E., Rhymer, B., Schrodt, N., Mohrholz, V., Smith, J., Konopkova, Z., Liermann, H. P., Glotch, T. D., & Ehm, L. (2019). Pressure-induced amorphization in plagioclase feldspars: A time-resolved powder diffraction study during rapid compression. *Earth and Planetary Science Letters, 507*, 166–174.

Smith, J. V, & Brown, W. L. (1988). *Feldspar Minerals* (2nd ed.). Berlin: Springer-Verlag.

Sracek, O., & Hirata, R. (2002). Geochemical and stable isotopic evolution of the Guarani Aquifer System in the state of São Paulo, Brazil. *Hydrogeology Journal, 10*(6), 643–655.

Środoń, J. (2002). Quantitative mineralogy of sedimentary rocks with emphasis on clays and with applications to K-Ar dating. *Mineralogical Magazine, 66*(5), 677–687.

Środoń, J., Drits, V. A., McCarty, D. K., Hsieh, J. C., & Eberl, D. D. (2001). Quantitative X-ray diffraction analysis of clay-bearing rocks from random preparations. *Clays and Clay Minerals*, *49*(6), 514-528.

Staudigel, H., Furnes, H., McLoughlin, N., Banerjee, N. R., Connell, L. B., & Templeton, A. (2008). 3.5 billion years of glass bioalteration: volcanic rocks as a basis for microbial life? *Earth Science Reviews, 89*(3), 156–176.

Stöffler, D. (1967). Deformation und Umwandlung von Plagioklas durch Stoßwellen in den Gesteinen des Nördlinger Ries. *Contributions to Mineralogy and Petrology, 16*, 51–83.

Stöffler, D. (1971). Progressive metamorphism and classification of shocked and brecciated crystalline rocks at impact craters. *Journal of Geophysical Research, 76*(23), 5541–5551.

Stöffler, D. (1972). Deformation and transformation of rock-forming minerals by natural and experimental shock processes: I. Behavior of minerals under shock compression. *Fortschritte der Mineralogie, 49*, 50–113.

Stöffler, D. (1974). Deformation and transformation of rock-forming minerals by natural and experimental shock processes: II. Physical properties of shocked minerals. *Fortschritte der Mineralogie, 51*, 256–289.

Stöffler, D., Gault, D. E., Wedekind, J., & Polkowski, G. (1975). Experimental hypervelocity impact into quartz sand: Distribution and shock metamorphism of ejecta. *Journal of Geophysical Research, 80*(29), 4062–4077.

Stöffler, D., & Grieve, R. A. F. (2007). Impactites. In D. Fettes, and J. Desmons (Eds.), *Metamorphic Rocks: A Classification and Glossary of Terms, Recommendations of the International Union of Geological Sciences* (pp. 82-92). Cambridge, UK: Cambridge University Press.

Stöffler, D., Hamann, C., & Metzler, K. (2018). Shock metamorphism of planetary silicate rocks and sediments: Proposal for an updated classification system. *Meteoritics & Planetary Science, 53*, 5– 49.

Stöffler, D., & Hornemann, U. (1972). Quartz and feldspar glasses produced by natural and experimental shock. *Meteoritics,* 7(3), 371–394.

Stöffler, D., Keil, K., & Scott, E. R. D. (1991). Shock metamorphism of ordinary chondrites. *Geochimica et Cosmochimica, 55*(12), 3845–3867.

Tomioka, N., Mori, H., & Fujino, K. (2000). Shock-induced transition of NaAISi308 feldspar into a hollandite structure in a L6 chondrite. *Geophysical Research Letters, 27*(40), 3997–4000.

Tornabene, L. L., Osinski, G. R., McEwen, A. S., Wray, J. J., Craig, M. A., Sapers, H. M., & Christensen, P. R. (2013). An impact origin for hydrated silicates on Mars: A synthesis. *Journal of Geophysical Research E: Planets*, *118*, 994–1012.

Trepmann, C., Whitehead, J., & Spray, J. (2003, November). *Shock effects in target rocks from the Charlevoix impact structure, Quebec, Canada* [abstract 7-17]. 38th annual Geological Society of America Meeting, Seattle, Washington.

Turner, S., Kirstein, L., Hawkesworth, C., Peate, D., Hallinan, S. & Mantovani, M. (1999*a*). Petrogenesis of an 800 metre lava sequence in Eastern Uruguay: insights into magma chamber processes beneath the Paraná flood basalt province. *Journal of Geodynamics, 28*, 471–487.

Turner, S., Peate, D., Hawkesworth, C. & Mantovani, M. (1999b). Chemical stratigraphy of the Paraná basalt succession in western Uruguay: further evidence for the diachronous nature of the Paraná magma types. *Journal of Geodynamics, 28*, 459–469.

Turner, S., Regelous, M., Kelley, S., Hawkesworth, C., & Mantovani, M. (1994). Magmatism and continental break-up in the South Atlantic: high precision 40Ar39Ar geochronology. *Earth and Planetary Science Letters*, *121*(3-4), 333–348.

Velde, B., & Boyer, H. (1985). Raman microprobe spectra of naturally shocked microcline feldspars. *Journal of Geophysical Research, 90*, 3675–3682.

Velde, B., Syono, Y., Kikuchi, M., & Boyer, H. (1989). Raman microprobe study of synthetic diaplectic plagioclase feldspars. *Physics and Chemistry of Minerals, 16*, 436–441.

Vinet, N., Flemming, R. L., & Higgins, M. D. (2011). Crystal structure, mosaicity and strain analysis of Hawaiian olivines using *in situ* X-ray diffraction. *American Mineralogist*, *96*(4), 486–497.

Walawender, M. J. (1977). Shock-produced mosaicism in plagioclase, Charlevoix Structure, Quebec. *Canadian Journal of Earth Sciences, 14*(1), 74–81.

Walton, A. (2008). Microtubules in basalt glass from Hawaii scientific driling project #2 phase 1 core and Hilina slope, Hawaii: evidence of the occurrence and behavior of endolithic microorganisms. *Geobiology, 6*, 351–364.

Whitney, P. R. (1972). Spinel inclusions in plagioclase of metagabbros from the Adirondack Highlands. *American Mineralogist, 57*(9-10), 1429–1436.

Williamson, G. K., & Hall, W. H. (1953). X-ray line broadening from filed aluminium and wolfram. *Acta metallurgica*, *1*(1), 22-31.

R. E., Wiseman, S., Green, R., Hash, C., Humm, D., Malaret, E., McGovern, J. A., Seelos, K. … Wolff, M. (2008). Hydrated silicate minerals on Mars observed by the Mars Reconnaissance Orbiter CRISM instrument. *Nature*, *454*, 305–309.

Yokoyama, E., Nèdèlec, A., Baratoux, D., Trindade, R. I. F., Fabre, S., & Berger, G. (2015). Hydrothermal alteration in basalts from Vargeão impact structure, south Brazil, and implication for recognition of impact-induced hydrothermalism on Mars. *Icarus, 252*, 347–365.

Zalán, P. V., Wolff, S., Astolfi, M. A. M., Vieira, I. S., Conceição, J. C. J., Appi, V., Santos Neto, E. V., Cerqueira, J. R., & Marques, A. (1990). The Paraná Basin, Brazil. *American Association of Petroleum Geologists Memoir, 51*, 681–708

Zamaraev, K. I., Romannikov, V. N., Salganik, R. I., Wlassoff, W. A., & Khramtsov, V. V. (1997). Modelling of the prebiotic synthesis of oligopeptides: silicate catalysts help to overcome the critical stage. *Origins of Life and Evolution of Biospheres, 27*, 325–337.

Zoltai, T., & Stout, J. H. (1984). *Mineralogy: concepts and principles*. Minneapolis: Burgess Publishing Company.

Zwell, L., & Danko, A. W. (1975). Applications of X-ray diffraction methods to quantitative chemical analysis. *Applied Spectroscopy Reviews, 9*, 167–221.

Chapter 2

2   Mineral Deformation and Porosity Development in Shocked Basalts from Vargeão Dome and Vista Alegre Impacts, Brazil

2.1   Introduction

Meteorite impact craters are formed as a result of a hypervelocity impact, a naturally occurring geological process that is common on all solid planetary bodies within our solar system. The immense temperatures and pressures that are induced as the energy from the impactor is transferred to the surface produce a variety of deformation products collectively termed as impactites (Stöffler & Grieve, 2007; Grieve & Therriault, 2013). Impactites exhibit a variety of distinct deformation and shock metamorphic effects that range from microscopic to macroscopic in scale. Common shock effects include shatter cones in the target rock, as well as microscopic effects such as planar features [planar fractures (PFs) and planar deformation features (PDFs)], undulatory extinction, mosaicism, the formation of diaplectic glass, and shock melting in the host minerals (e.g., Chao, 1968; Ferriere & Osinski 2013; French & Koeberl, 2010; von Engelhardt & Stöffler, 1968, and references therein). Different features appear as a function of the target lithology and relative distance from the epicentre, ultimately defining the peak level of shock experienced by the target rock (French, 1998).

The most widely employed technique to determine the degree of progressive shock metamorphism is optical microscopy, which allows for visual identification of textural properties and deformation features associated with shock metamorphism. The current shock classification system based on optical features (Stöffler et al., 2018) has been recently extended to cover most rocks and sediment classes. Shock level is assigned based on the microscopic appearance of shock effects in the commonly occurring constituent minerals (quartz, plagioclase and pyroxene), and potential change in textures. Lots of new modern analytical techniques such as X-ray diffraction (e.g., Sims et al. 2019), transmission electron microscopy (e.g., Langenhorst et al., 1999), Raman

spectroscopy (e.g., Fritz et al., 2005) or thermal infrared (IR) analyses (e.g., Johnson et al., 2002, 2003) can be applied to increase our understanding of the pressure and temperature conditions created by an impact event, and the influence it had on the target rocks. Micro-X-ray diffraction is of particular interest in this study because it is a versatile, non-destructive method with little sample preparation required to investigate the crystalline phases as indicators of shock level in rock samples or thin sections. X-ray diffraction methods have been developed and applied to analyze mineral textures, grain size, and quantify strain, shock level and peak shock pressure using crystalline material (Bramble et al., 2015; Flemming, 2007; Hörz & Quaide, 1973; Izawa et al., 2011; Jenkins et al., 2019; McCausland et al., 2010a; Pickersgill et al., 2015; Rupert et al., 2020; Sims et al., 2019; Uchizono et al., 1999).

The majority of research concerning shock effects on minerals to date has been performed on quartz, which is excellent for Earth's quartz-rich crustal lithology but becomes difficult to implement for quartz-limited basaltic surfaces such as the Moon, Mars, and asteroids. When target rocks are shocked, mineral composition and proportion, grain size, variable porosity and density are all influenced. Previous research has investigated changes in porosity in carbonate-bearing sandstone and gneisses from the Haughton impact structure (Canada) as a result of the impact event (Cockell & Osinski, 2007; Pontefract et al., 2014; Singleton et al., 2011). While sedimentary rock experiences a collapse of pore space at pressures over ~35 GPa, crystalline rocks such as gneiss increase porosity proportionally until reaching their temperature of vaporization (Cockell & Osinski, 2007). This trend is caused by the fracturing and disruption of mineral structures and differential mineral melting and/or vaporization during the dispersion of the massive amount of energy from the initial impact shock wave (e.g., French & Short, 1968; Melosh, 1989; Osinski & Pierazzo 2013; Singleton et al., 2011; Stöffler, 1971, and references therein). The potential effects of shock on the porosity and density of basalts have not yet been studied in this capacity.

The current understanding on the effects of shock on basaltic rocks is based on the foundational work by Kieffer et al. (1976) on shocked basalts from Lonar impact structure, India, and additional experimental analogue studies comparing experimentally

shocked Lonar basalts to lunar samples (Schaal & Hörz, 1977). A major mineral component of these basalt-dominated bodies is plagioclase feldspar. Despite its complex mineral structure and rapid weathering, plagioclase feldspar has been found to effectively preserve shock levels via its degree of plastic deformation (e.g., Pickersgill et al., 2015a,b; Xie et al., 2020). Current understanding of shock features in plagioclase are derived from petrographic evidence of impact deformation (Pickersgill et al., 2015b; Singleton et al., 2011; Stöffler, 1971; Stöffler et al., 1991, 2018), spectral studies of internal mineral structure changes using micro-Raman (Fritz et al., 2005; Heymann & Hörz, 1990; Reynard et al., 1999; Velde & Boyer, 1985; Velde et al., 1989; Yin & Dai, 2020; Xie et al., 2017; Xie et al., 2020), thermal infrared spectroscopy (Johnson et al., 2002, 2003), XRD (Pickersgill et al., 2015a; Sims et al., 2019), and comparison of co-occurring shock features among different mineralogical phases (Jaret, 2017). Previous work of this nature has focused almost exclusively on high-pressure regimes because they are most apparent through PDFs and diaplectic glass that are produced and preserved in these environments, whereas evidence of low-pressure deformation is commonly lost to secondary chemical alteration (Jaret et al., 2014).

The aim of this research is two-fold. First, we seek to investigate the changes in the density and porosity of basaltic rocks with increasing shock pressure. Second, we intend to quantify the shock level of these same target rocks by investigating plagioclase using a combination of optical microscopy and *in situ* micro-X-ray diffraction measurements of strain-related mosaicity or bending. This research will reveal the effects of impacts on the bulk physical characteristic of basaltic target lithology, as well as verify the effectiveness of micro-X-ray diffraction when used as a technique for measuring shock level of planetary materials, and its pertinence to other lithologies such as basalts.

2.2   Methods

A total of 27 samples of basaltic target rocks and breccias were collected within Vargeão Dome and Vista Alegre in 2017 by one of the co-authors (AP). Vargeão Dome samples were collected at various distances from and within the centre of the structure, recognized

by the central uplift (Fig. 2-1). Seven Vista Alegre samples were collected within the crater at locations VA-1, 2, and 3; five of which were collected at a small abandoned quarry (VA-2017-1B, C, D, E, and E4), 2.8 km NW from the crater centre (Fig. 2-1). Two samples were collected outside the craters at location VA5, as representative of unshocked basement basalts of the Paraná Basin. Vargeão Dome and Vista Alegre crater samples used in this study are comprised of polymict and monomict breccias and basaltic target rock (Fig. 2-1), and characterization of the samples was obtained using a variety of methods, as described in the following sections.
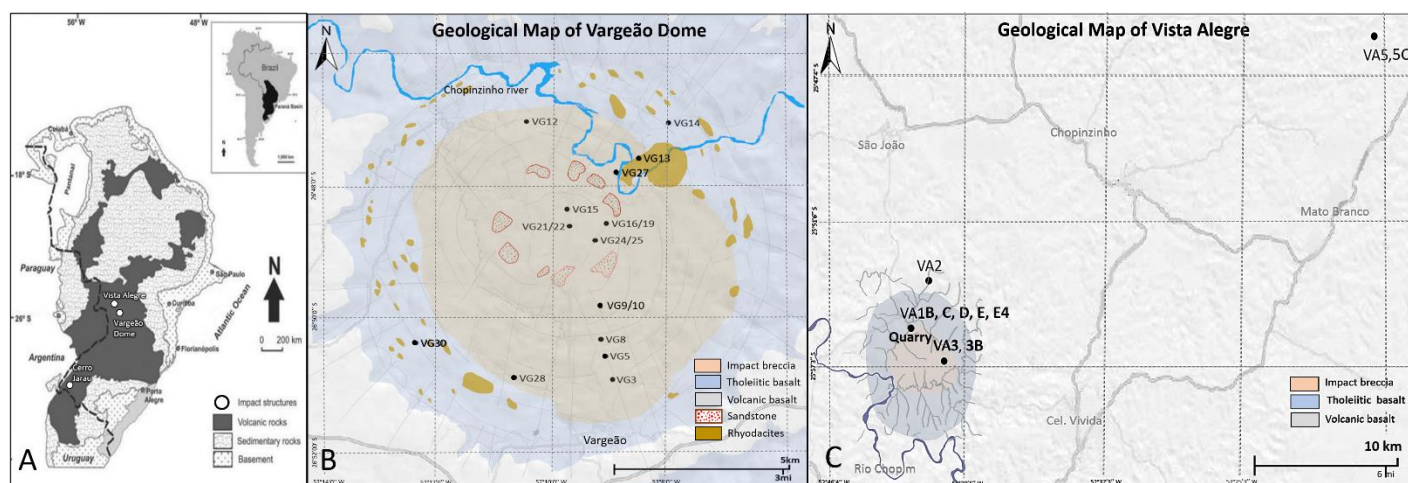
Figure 2-1. Maps showing the locations of the Vargeão Dome and Vista Alegre impact structures as well as sample location points. A) Location map of Paraná Basin and its impact structures (Crósta et al., 2010). B-C) Geological maps of Vargeão Dome (modified from Crósta et al., 2010) and Vista Alegre (modified from Crósta et al., 2011) impact structures with sample location points, respectively.

2.3   Geological Setting of Study Sites

Terrestrial basaltic impact craters act as excellent analogue sites for studying impacts on Mars, given the largely basaltic surface of that planet (Bandfield et al., 2000). To date, there are six confirmed impact structures on Earth occurring within basaltic targets: Lonar crater, India (Kieffer et al., 1976), Lochanga crater, Russia (Feldman et al., 1983), Pantasma crater, Nicaragua (Rochette et al., 2019), and Vargeão Dome, Vista Alegre, and Cerro do Jarau, Brazil (Crósta et al., 2010, 2011; Vasconcelos et al., 2010). Of these, Vargeão Dome (26° 49.0' S, 52° 10.0' W) and Vista Alegre (25° 57.0' S, 52° 41.5' W) are

two of the best-preserved basaltic impact sites, yet they also remain the most poorly studied. The digital elevation models (DEMs) of Vargeão Dome and Vista Alegre impact structures (Fig. 2-2) clearly illustrate crater morphology displaying a pertinent circular outline where the interior is topographically depressed in comparison to the surrounding terrain.
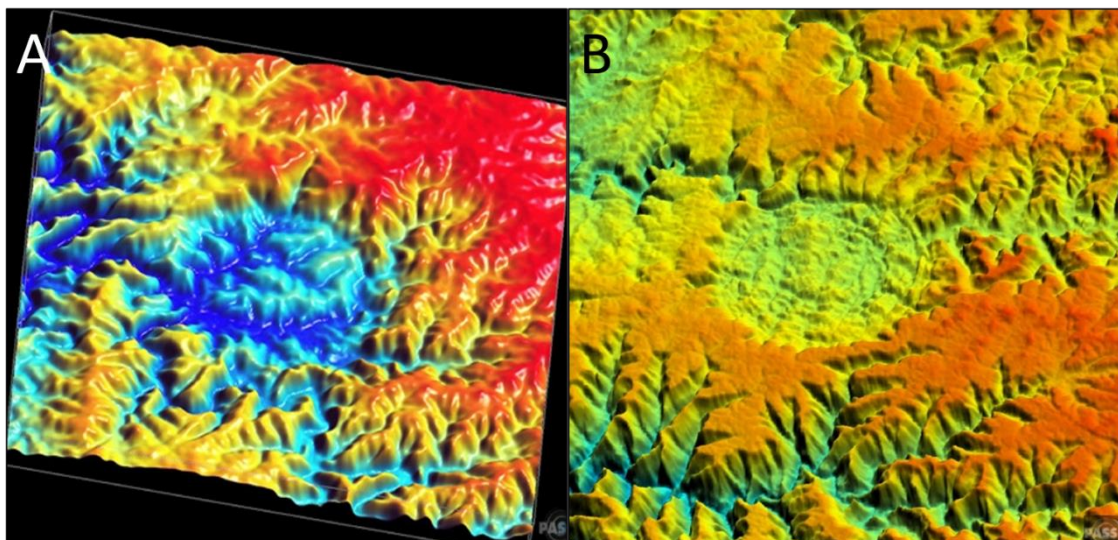
Figure 2-2. Digital elevation models (DEMs) from the Shuttle Radar Topographic Mission (SRTM) illustrating crater morphology. A-B) DEMs of Vista Alegre and Vargeão Dome impact structures, respectively. Elevated areas are red and less elevated areas are blue. (Crósta et al., 2010; www.unb.ca/passc/ImpactDatabase-- courtesy of Alvaro P. Crósta).

Vargeão Dome (12.4 km in diameter) and Vista Alegre (9.5 km in diameter) are complex impact craters located ~100 km apart in the Paraná Basin flood basalts of Central-West Brazil (Crósta et al., 2010; Yokoyama et al., 2015). The breakup of Gondwana resulted in extensive continental volcanism in south-eastern South America, forming the top stratigraphic layer of the Parana Basin called the Serra Geral Formation (Peate, 1997; Stewart et al., 1996). It is one of the largest and thickest tholeiitic flood basalt provinces on Earth, covering an area of ~1,500,000 km^2 and reaching a maximum thickness of 1.7 km (Crósta et al., 2010; Mantovani et al., 1995; Milani et al., 2007). The nature of the Formation suggests two peak periods of volcanic activity, the more recent of which has been dated to ~139–135 Ma (Renne et al., 1992; Turner et al., 1994).

Before being overlain by the thick basaltic flows of the Serra Geral Formation, Pirambóia (Triassic) and Botucatu (Jurassic) Formation sandstones were deposited under arid climatic conditions (Pinto et al., 2011). The sandstone units are, on average, 700–800 m below the present basaltic surface; however, boulders of sandstone have been found uplifted hundreds of meters above their original stratigraphic level as part of the central uplift in these craters (Crósta et al., 2010). It is unknown whether the excavated sandstones belong to the Botucatu or Pirambóia Formations owing to the high levels of deformation and recrystallization that prevents definitively differentiating the nearly identical Formations (Crósta et al., 2011; Kazzuo-Vieira, 2009). Although the original crater morphologies are relatively well preserved (Fig. 2-2) [i.e., majority of both crater rims remaining intact and only the western portion of the border of Vargeão Dome intersected by the Chopim River (Crósta et al., 2010; Kazzuo-Vieira et al., 2004)], the current sub-tropical supergene environment has resulted in the heavy weathering and dense vegetation coverage of surface outcrops (Crósta et al., 2010; Pinto et al., 2011).

Both impact structures are known to have impact breccias; Vargeão Dome structure contains monomict, polymict (Crósta et al., 2011) and melt-bearing breccias (Nédélec et al., 2013; Yokoyama et al., 2015), and Vista Alegre has polymict and melt-bearing breccias (Crósta et al., 2010). In both, breccia clasts are composed of Pirambóia and Botucatu volcanic rocks and sandstones (Crósta et al., 2010; Crósta et al., 2011). Impact breccias are generally only found within and around the central uplift, however in the case of Vista Alegre, the best exposure of polymict breccia is found in a small quarry near the village (located at 25°56007 S and 52°42021 W) (Crósta et al., 2010; Pittarello et al., 2015). Sandstones are concentrated in the centre of the structure, whereas other target rocks are found throughout the impact region. This study will investigate target rock basalts and polymict and monomict breccias containing sandstone fragments.

2.3.1   Optical microscopy and electron probe microanalysis

Polished thin sections were characterized for shock metamorphism using a Nikon Eclipse LV100POL compound petrographic microscope based on shock stage schemes developed by Stöffler et al. (2018). A JXA-8350F Field Emission Electron Probe Microanalyzer (FE-EPMA) in the Earth and Planetary Materials Analysis Laboratory

(EPMA Lab) at the University of Western Ontario, London, Canada, was used to determine the micro-textures in the Vargeão Dome and Vista Alegre samples using backscattered electron (BSE) imagery and energy dispersive X-ray spectrometry (EDS). The mineral chemistry of plagioclase was acquired with the FE-EPMA using wavelength dispersive spectroscopy (WDS). The operating conditions used were an accelerating voltage of 15 kV, beam current of 20 nA, and a spot size of 5 µm. The mineral standards used for calibration include Si, Al, Na – Albite (Amelia County, VA, USA), Ca, Mg – Diopside (Smithsonian, USNM 117733- Natural Bridge, NY, USA), Fe- Hematite (Harvard 92649) and K- Orthoclase (C.M. Taylor).

2.3.2   Bulk Density (Specific Gravity)

Bulk density is defined as the ratio of the mass of a sample to its total volume, including internal voids and cracks (Consolmagno & Britt, 1998). To establish the bulk density of these samples, we are using a standard specific gravity method, which is defined as the density of the sample relative to the density of a reference liquid, at a specified temperature. As oppose to the Archimedean bead method which utilizes microscopic glass beads to simulate Archimedean fluid (Consolmagno & Britt, 1998; McCausland et al., 2011), the total volume was measured by weighing the dry sample suspended on a sling and then again while submerged in a beaker of distilled water at approximately room temperature. Water was used as the reference media because at room temperature, the specific gravity of water equals the volume of one cubic centimetre (Crawford, 2013). The observed weight difference in apparent mass represents the volume of water displaced by the sample, and therefore the total volume of the sample. The mass of each sample was obtained (in grams) using a top-loading analytical balance to a precision of $\pm$ 0.0001 g. The total volume was measured using the standard specific gravity method.

Grain density is defined as the intrinsic (or "grain") volume of only the solid matter (excluding voids and cracks) in the sample. Grain density was measured via helium ideal-gas pycnometry using a Quantachrome Ultrapyc Multipycnometer at Western. Helium gas is preferred because it is chemically inert and can easily penetrate voids and cracks in the sample (Consolmagno et al., 2008). Using two sealed chambers with temperature invariance and known volumes and pressures, the sample was introduced into one

chamber and two separate pressure measurements were obtained. With this data, Boyle's Law equation (1) could be employed to measure the absolute volume of the sample, and therefore the grain density. This equation assumes atmospheric pressure conditions.

$$V_s = V_{cell} - \left[V_{ref} \left(\frac{P_1}{P_2} - 1 \right) \right] \qquad (1)$$

Within the Boyle's Law equation (1), V_s is the unknown intrinsic volume of the rock sample, V_{cell} is the known calibrated volume of the empty sample cell, V_{ref} is the known volume of the reference cell, P_1 is the measured maximum pressure of the reference cell, and P_2 is the measured pressure of both cells together once the valve between the sample and reference cells has been opened (Singleton et al., 2011). Measurement pressurization cycles were carried out five times to enable adequate averaging, avoiding potentially inaccurate results that may arise as a result of contamination or instrumental variability. The average intrinsic volume across the five measurements were used to obtain the grain density (density=sample mass/volume).

2.3.3   Micro-Computated Tomography

Of the 16 samples used for porosity analysis, five samples (VG-2017- 13b/15/21/24/30b) ranging in mass from 25.8 to 90.7 g were too fragile for either water or bead volume analysis methods. To accommodate these limitations, the samples were imaged using X-ray Micro-Computated Tomography (µCT) on the GEHC eXplore speCZT Micro-CT scanner at the Robarts Imaging Institute at Western.

Similar to a clinical Computed Tomography (CT) scanner, a laboratory-based µCT functions to non-destructively reconstruct X-ray attenuation images of the interior of objects. Through using smaller detector pixels, a more focused X-ray source and a higher dose of photons, µCT produces very high-resolution images with sub-0.1 mm resolution (Edey et al., 2019). Using custom tailored acquisition parameters, µCT has proven itself to be an accurate and reliable, non-destructive approach to obtain quantitative data regarding bulk volume, internal density, surface area and dimensional information of meteorites and terrestrial rocks (Edey et al., 2019; McCausland et al., 2010b; Melanson et al., 2012). In addition, micro-CT may provide qualitative visualization products for

determination of material density contrast or void space and aid in sample investigation and curation (McCausland et al., 2010b; Melanson et al., 2012).

Scans were acquired using 120 kV (peak) energy and 20 mA current, every five minutes to obtain 900 separate radiographs over one full 360° rotation about the long axis of the sample (McCausland et al., 2010b). 2-D images were collected from the total X-ray attenuations through the sample and reconstructed into a 3-D volume with an isotropic voxel size of 50 µm displayed in greyscale Hounsfield units (HU) (McCausland et al., 2010b; Edey et al., 2019). X-ray incident beams are more attenuated when propagating through materials with greater electron densities (e.g., metals) and thus appear brighter than thinner portions in the tomographic reconstructed image (McCausland et al., 2010b). This effect causes artifacts such as the beam hardening effect, complicating the analysis of Micro-CT data (Edey et al., 2019; Melanson et al., 2012). The beam hardening correction protocol described by Edey et al. (2019), was implemented, making the determination of interior information possible.

2.3.4   Porosity by Density

Porosity (P) refers to the voids and cracks in the sample, and it is important to note that for all porosity calculations, densities rather than volumes are used because of slight changes in sample mass between the applications of methods, especially in fragile samples susceptible to chipping and fracturing. If bulk density $\rho_b = M/V_b$ (where M is the mass of the sample and V_b is the bulk volume) and grain density $\rho_g = M/V_g$ (where V_g is the grain volume) are determined, porosity (2) is calculated as follows:

$$P = \left(1 - \frac{\rho_b}{\rho_g}\right) \times 100\% \qquad (2)$$

2.3.5   Micro-X-Ray Diffraction

Using a Bruker D8 Discover micro-diffractometer in the Powder X-ray Diffraction and Micro X-ray Diffraction Laboratory, Department of Earth Sciences at the University of Western Ontario, micro-X-ray diffraction (µXRD) analyses (Flemming, 2007) were performed on polished thin sections of each Vargeão Dome and Vista Alegre sample with

previously assigned petrographic shock levels. The diffractometer was operated with a sealed Cobalt anode source (CoKα_1 radiation, λ=1.78897 Å), generated at 35 kV accelerating voltage and 45 mA beam current. The instrument was equipped with a Göbel mirror parallel optics system and a 300 µm pinhole collimator, yielding a nominal beam diameter of 300 µm. The nominal 300 µm-diameter spot size analyzed is represented in Figure 2-3 by a red circle. Diffracted X-rays were detected with a Vantec-500 two-dimensional area detector with General Area Diffraction Detection System (GADDS) software. The θ-θ geometry of the diffractometer enabled the source and detector to rotate independently (omega scan mode) while the sample remained horizontal and stationary. Target plagioclase phenocrysts (basalt) and/or clasts (breccia) were located in situ using a microscope and laser system to position the samples via a movable XYZ stage.

The µXRD data for phase identification and strain-related mosaicity measurement of plagioclase grains was collected using omega scan geometry. Omega scanning of coarse-grained samples (grains $\geq$ 300 µm), which rotates the optics, generates more diffracted spots of more crystal lattices for a particular mineral phase in comparison with the equivalent stationary coupled scan. During an omega scan, both the source and detector are simultaneously rotated clockwise by a defined angle (ω), maintaining a constant 2θ position at the centre of the detector (where $\theta_1 + \theta_2 = 2\theta$) (Flemming, 2007). For frame 1, a θ_1 of 14.5° and a θ_2 of 25.5° were used, with an omega rotation of 10°. For frame 2, a θ_1 of 40° and a θ_2 of 40° was used, with a rotation of 10°. Data collection time of target grains was 60 minutes for frame 1 and 90 minutes for frame 2. Long collection times were employed to maximize the signal to noise ratio in all cases (Jenkins et al., 2019). The two GADDS frames were combined and integrated to generate a conventional intensity versus 2θ diffraction pattern spanning 90° 2θ from 15–105 ° 2θ. A 2θ angular range of ~25° to ~49° was generally used for mineral identification and plagioclase Miller indexing for subsequent strain-related mosaicity measurements because 2θ values outside that range often provided diffraction peaks with intensity (counts) too low to measure usefully. The integrated intensity versus 2θ diffraction patterns (Fig. 2-3) were best-matched to standard cards of various mineralogical compositions in the International

Centre for Diffraction Data (ICDD) database using the Bruker DiffracPlus EVA software package and the ICDD PDF-4 Database.
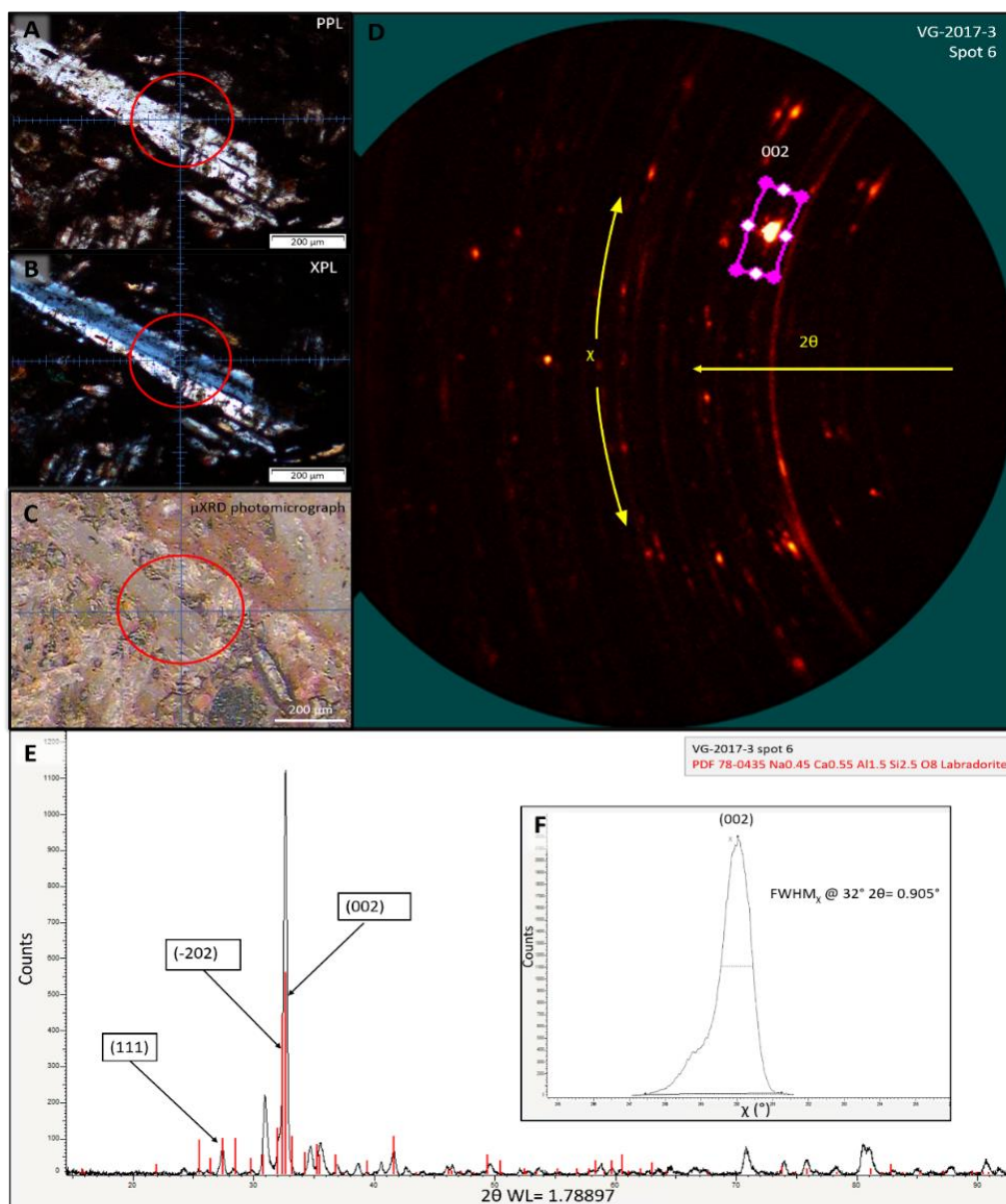
Figure 2-3. Optical petrography and µXRD analysis of sample VG-2017-3 spot 6. A-C) Plagioclase feldspar grains in XPL, PPL, and picture taken with the µXRD instrument, respectively. Red circles indicate the 300 µm-wide spot size analyzed. D) GADDS image of the corresponding plagioclase grain. Arrows indicate the 2θ and χ directions. Pink box surrounding a spot at ~32° 2θ, with Miller index of (002). E) Diffraction pattern of the labradorite grain. F) Strain-related mosaicity measurement of peak (002) corresponds to a FWHMχ of 0.905°.

After phase identification and Miller indexing of suitable plagioclase diffraction lines, the two-dimensional General Area Detector Diffraction System (GADDS) images were analyzed for evidence of strain-related mosaic spread and subsequently quantified via measuring its streak length along the Debye rings or chi dimension (Fig. 2-3). This was achieved by measuring the streak's FWHM intensity when plotted along chi. This technique was employed to study the 2θ peaks characteristic of plagioclase that produced intensity readings of 500 counts or greater.

2.3.6   Raman Spectroscopy

Raman spectroscopy analysis was performed on four Vargeão Dome and Vista Alegre target basalt and breccia samples (VG-2017-3, VG-2017-21, VA-2017-1E4 and VA-2017-3B). Areas with potential diaplectic glass within the polished thin sections were targeted using a Renishaw InVia Reflex Raman Spectrometer at Surface Science Western. The instrument is equipped with a 514 nm emission argon-ion laser, 6 mW nominal power, and a spot size of ~2 μm. Each spectrum collection was acquired using 50x (0.75 N.A) and 100x (0.90 N.A) objective lenses, collecting spectra from 126 to 2000 cm^{-1}.

2.4   Results

2.4.1   Petrography

Petrographic observations and shock effects of representative samples from Vargeão Dome and Vista Alegre impact sites are described in Table 2-1 and 2-2, and shown in Figures 2-4, 2-5 and 2-6. Shock features of interest in plagioclase, pyroxene, and quartz in shocked target basalts and breccias include undulatory extinction, mosaicism, planar fractures (PFs), feather features, planar deformation features (PDFs), and deformed feldspar twins (bent, kinked, offset features).

Table 2-1. Sample whole rock description and microscopic shock features in target rock basalts (VA= Vista Alegre) (VG= Vargeão Dome).

Sample Name	Rock Type	Rock Description	Plagioclase Shock Metamorphism Features							Other Mineral Shock Features
			Deformed twins (bent, kinked, offset features)	Fractures (irregular and PFs)	Undulatory extinction	Mosaicism	PDFs	Diaplectic feldspar glass (partial)	Diaplectic feldspar glass (complete)	
VA1E4	Target Basalt	Brownish-grey fine-grained basalt with macroscopic evidence of shatter cones	X	X		X				Irregular fractures and mosaicism in pyroxene.
VA2	Target Basalt	Black fine-grained basalt with brown weathering on the external, exposed surface.		X	X					Loss of grain boundary, undulatory extinction and mosaicism in quartz. Fracturing and mosaicism in pyroxene.
VA5	Unshocked Basalt	Dark coloured aphanitic lava basalt with large/medium-sized vesicles infilled with secondary alteration minerals.	Missing information							
VA5C	Unshocked Basalt	Aphanitic, dark brown basalt.	X	X						Irregular fractures in pyroxene.
VG8	Target Basalt	Brown basalt with elongated plagioclase phenocrysts and	X	X						Heavily fractured pyroxene with

Table 2-1 (Cont.)

		calcite/quartz alteration on surface								mosaicism and undulatory extinction. Heavily fractured quartz.
VG9	Target Basalt	Fine grained, light steel grey basalt with a calcite alteration crust	X	X						Fractured pyroxene with mosaicism.
VG10	Target Basalt	Brown fine grained basalt with black oxidation and green alteration on the surface	X	X		X				Fractured pyroxene with mosaicism and feather features in plagioclase.
VG12	Target Basalt	Very fine grained, black porphyritic basalt with tiny white elongated plagioclase crystals.	X	X	X	X				Mosaicism in pyroxene. Feather features in plagioclase.
VG13b	Target Basalt	Dark brown basalt with green (chlorite) alteration crust, displaying dendritic growth		X		X				Matrix heavily altered. Pyroxene displays light fractures and mosaicism.
VG14	Target Basalt – impact melt rock	Dark basaltic matrix with large fractured xenocrysts of plagioclase, pyroxene, calcite and glass mineral fragments.		X	X					
VG21	Target Basalt	Reddish-brown fine-grained basalt with dark pseudotachylitic veins	X			X				Heavily altered. Mosaicism in pyroxene

Table 2-1 (Cont.)

VG22	Target Basalt	Grey/brown basalt with white plagioclase laths and black pyroxene and melt spots.	X	X						Fracturing, mosaicism and undulatory extinction in pyroxene
VG24	Target Basalt	Heavily weathered light brown basalt.	X	X						Fracturing, undulatory extinction and mosaicism in pyroxene
VG27	Target Basalt	Basalt with red melt bearing veins. The plastically deformed basalt shows flow textures.	X	X		X				Vitric veins.
VG28	Target Basalt	Red fine-grained, basaltic matrix containing calcite, zeolite, quartz and plagioclase-filled veins and vesicles.	Missing information							Highly altered, and recrystallized. Fractures and mosaicism in pyroxene. Secondary quartz, calcite, zeolite, and clays.
VG30b	Target Basalt	Very fine-grained red basalt intruded by hydrothermal quartz and calcite veins. Vitric glass surrounding some veins.	X	X						Large quartz vein running through the sample. Heavily altered.

Table 2-2. Sample whole rock description and microscopic shock features in impact breccias (VA= Vista Alegre) (VG= Vargeão Dome).

Sample Name	Rock Type	Rock Description	Plagioclase Shock Metamorphism Features							Other Mineral Shock Features
			deformed twins (bent, kinked, offset features)	Fractures (irregular and PFs)	Undulatory extinction	Mosaicism	PDFs	Diaplectic feldspar glass (partial)	Diaplectic feldspar glass (complete)	
VA1B	Polymict breccia	Poorly sorted breccia with angular to sub-rounded lithic rock fragments (light), glassy fragments (dark) and calcite mineral fragments (white) in a brownish-grey clastic matrix. Some glassy fragments contain small, irregular feldspar microlites.	X	X		X				PDFs in pyroxene.
VA1C	Polymict Breccia	Poorly sorted breccia with rounded lithic rock fragments (light), large glassy fragments (dark) and calcite mineral fragments (white) in a brownish-grey clastic matrix.	X	X		X	X			Feather features in plagioclase.

Table 2-2 (Cont.)

VA1D	Polymict breccia	Poorly sorted breccia with sub-rounded lithic rock fragments (light) and small glassy fragments (dark) in a brownish clastic matrix.	X	X		X	X			PDFs in pyroxene, feather features in plagioclase, flow features, and multiple generations of calcite.
VA1E	Polymict breccia	Poorly sorted breccia with angular to sub-rounded lithic rock fragments (light) and glassy fragments (dark) in a brownish clastic matrix. Some glassy fragments contain small, irregular feldspar microlites.	X			X				
VA3	Polymict breccia	Poorly sorted brown breccia with rounded to sub-angular lithic rock fragments (light) and tiny glassy fragments (black). Displays contact between a target basalt and the polymict breccia.	X	X	X	X				PDFs in pyroxene and feather features in plagioclase.
VA3B	Polymict breccia	Poorly sorted light brown breccia with rounded to sub-angular lithic rock fragments (light), glassy fragments	X	X		X	X			PDFs in pyroxene

Table 2-2 (Cont.)

		(black) and calcite mineral fragments (white/clear). Displays contact between a target basalt and the polymict breccia.								
VG3	Monomict breccia	Breccia containing large, angular clasts of basaltic rock and a brownish—red melt matrix with no distinctive flow pattern	X		X	X	X			
VG5	Monomict breccia	Dark brown, aphanitic basalt with tiny vesicles infilled with quartz and calcite (white).	X	X	X		X			
VG15	Monomict sandstone breccia	Coarse grained pink sandstone on the outside surface. Inside surface appears darker with melt vein separating sandstone fragments.	Missing information							PDFs, undulatory extinction, mosaicism, and planar features in quartz.
VG19	Monomict breccia	Lithic basaltic clasts of various sizes immersed in a fine-grained, red melt matrix.	Missing information							Mosaicism in quartz, and vitric veins

2.4.1.1   Impact Breccias

Vargeão Dome Monomict Breccias

The Vargeão Dome sample set contains predominantly monomict brecciated volcanic rocks and one sandstone breccia. The majority of monomict breccias consist of centimetre-sized, poorly sorted, angular and fractured lithic and vitric clasts. Melt-free matrix with fine-grained basalt fragments (plagioclase and pyroxene), clays, zeolites, and altered glass surround the breccia clasts. The matrix is heavily oxidized and red in colour. The Vargeão Dome sample set also contains one sandstone monomict breccia from the central uplift of the impact structure. The sandstone breccia (VG-2017-15) is pink and contains cm-sized sandstone clasts (Fig. 2-4 B). In thin sections, quartz grains of ~500 µm in diameter and smaller locally display shock metamorphic features including fracturing (Fig. 2-4 C), decrease in birefringence (Fig. 2-4 C), mosaicism (Fig. 2-4 D), PFs, and FDFs with feather features (Fig. 2-4 E).

Vista Alegre Polymict Impact Breccias

Polymict impact breccias are only found in the Vista Alegre sample set. The clasts in the breccias range in size (mm-cm) and are composed of basalt (plagioclase and pyroxene), euhedral calcite clasts, and vitric clasts (Fig. 2-5). The term "vitric" here is used to describe the altered clasts that were originally glass but are now completely devitrified and altered, still preserving their original morphologies. Altered glass is abundant in all of the Vista Alegre polymict breccias (e.g., Fig. 2-5 F), indicating impact melt breccias. Clasts are suspended in a fine-grained matrix containing phenocrysts of plagioclase, pyroxene, clays, and zeolites. Vista Alegre impact breccias exhibit textures and temporal relationships evident of pre- and post-impact hydrothermal alteration including replacement of basaltic minerals by clays and zeolites, infilling and lining textures by secondary phases, and altered zeolite and calcite veins cross-cutting shocked breccia clasts and basaltic minerals. The main secondary phases are carbonates (calcite), Fe-Mg clays (smectite, chlorite, celadonite, and glauconite), Al-clays (montmorillonite/illite), zeolites (heulandite-Ca, chabazite-Ca, stilbite, analcime, and mordenite), quartz, and Fe-

oxides (ulvöspinel and ilmenite). Chapter 3 provides a detailed analysis of the hydrothermal alteration in the Vista Alegre impact structure.
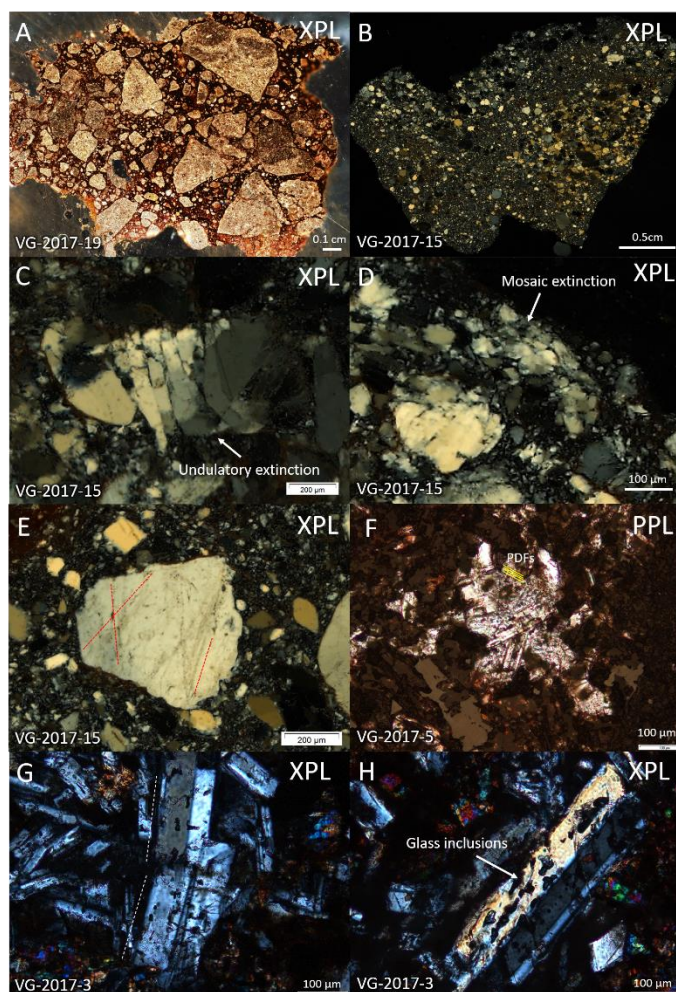
Figure 2-4. Petrography and shock effects in monomict breccias from Vargeão Dome. A) Basaltic impact monomict breccia with a mosaic of microporphyritic clasts in a heavily oxidized red matrix. Clasts are composed of mainly plagioclase and pyroxene varying in size from <100 μm to 0.5 cm. B) A typical sandstone monomict breccia from the central uplift of Vargeão Dome, showing sub-rounded to sub-angular grains, ~0.2–0.5 mm. C) Quartz grain exhibiting fractures and undulatory extinction. D) Quartz displaying evidence of mosaic extinction. E) Quartz grain displaying three sets of PFs (dotted red lines). F) Plagioclase grain with PDFs. Yellow dotted lines display the direction of the PDFs. G) Kinked twins in plagioclase showing optical evidence of non-uniform strain. Dotted lines indicate the kink. Pyroxene in the bottom left displays evidence of mosaicism. H) Reduced birefringence between albite twins. Several glass inclusions are present within the twins. Surrounding pyroxene exhibits mosaic extinction.
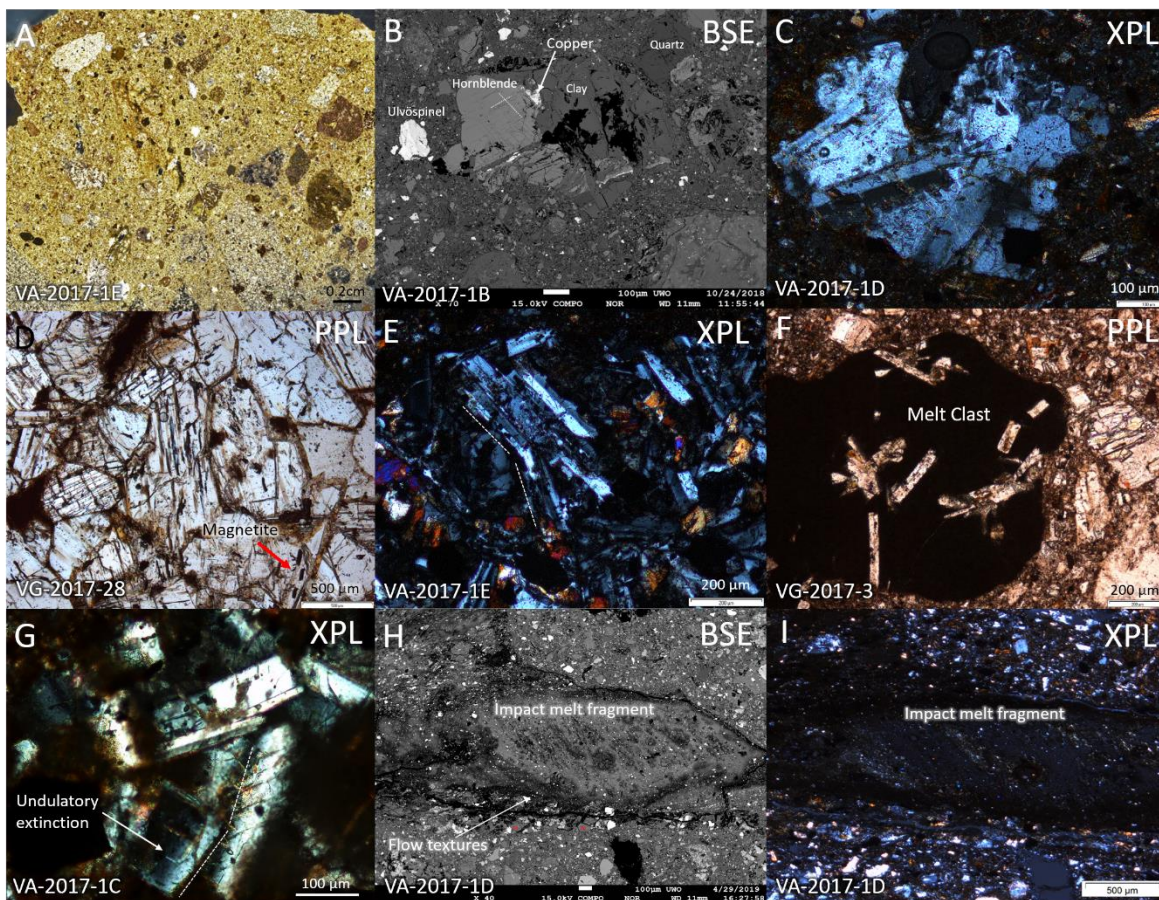
Figure 2-5. Petrography and shock effects in polymict impact breccias from Vargeão Dome and Vista Alegre impact structures. A) Polymict breccia with fragments consisting of lithic basalts, diabase, and mineral clasts, and varying in size from 0.1–0.7cm. B) Hornblende crystal with planar fractures along its cleavage, surrounded by clay. Copper is found infilling fractures. Quartz and ulvospinel grains are also immersed in the fine-grained matrix. C) Feldspar grain showing mosaic extinction. D) Interlocking texture of plagioclase and pyroxene grains. Plagioclase and pyroxene grains both exhibit planar features and opaques along cleavage lines. Note the rod-shaped, opaque magnetite grains at the bottom right corner (red arrow). E) Plagioclase displaying albite twinning and kinking. Nearby pyroxene grains are fractured and display mosaicism. F) Plagioclase laths within a melt clast displaying bending, fracturing and twinning. G) Plagioclase crystals displaying deformation and bending in the original polysynthetic albite twinning (light/dark bands). Plagioclase exhibits well-developed undulatory extinction. H-I) Heavily altered impact melt fragment from an impact melt-bearing breccia. Melt clast is very fine-grained, displaying some flow textures. Microphotographs obtained in BSE and XPL, respectively.

2.4.1.2   Target Basalts

Vargeão Dome:

Vargeão Dome basaltic target rocks are aphanitic to sub-ophitic or hypocrystalline in texture (Fig. 2-6 B, E) and consist of ~50% plagioclase, ~30% clinopyroxene (augite and pigeonite), 10-15% opaque minerals (e.g., ulvöspinel, hematite, magnetite) and 3–5% quartz. WDS spectroscopy reveals that the plagioclase of intermediate composition or labradorite ($An_{56–70}$) makes up 57% of the plagioclase minerals, plus ~23% albite (An_2), ~9% bytownite ($An_{70–77}$), ~4% anorthite (An_{99}). Approximately ~7% orthoclase is also present throughout the target rock (Fig. 2-7 and Table 2-3). No clear trends are seen for the samples containing feldspars with different compositions than the majority of the basalts (i.e., albite and K-rich feldspars). The matrix is fine-grained and varying in colour from red, to black, to grey (Fig. 2-6 B). The target basalts within the impact structure display cm-sized breccia veins filled with lithic clasts and secondary phases such as calcite, phyllosilicates, quartz and zeolites. In agreement with Yokoyama et al. (2015), these breccia veins exhibit crosscutting relationships and phases associated with hydrothermal alteration (see Chapter 3).
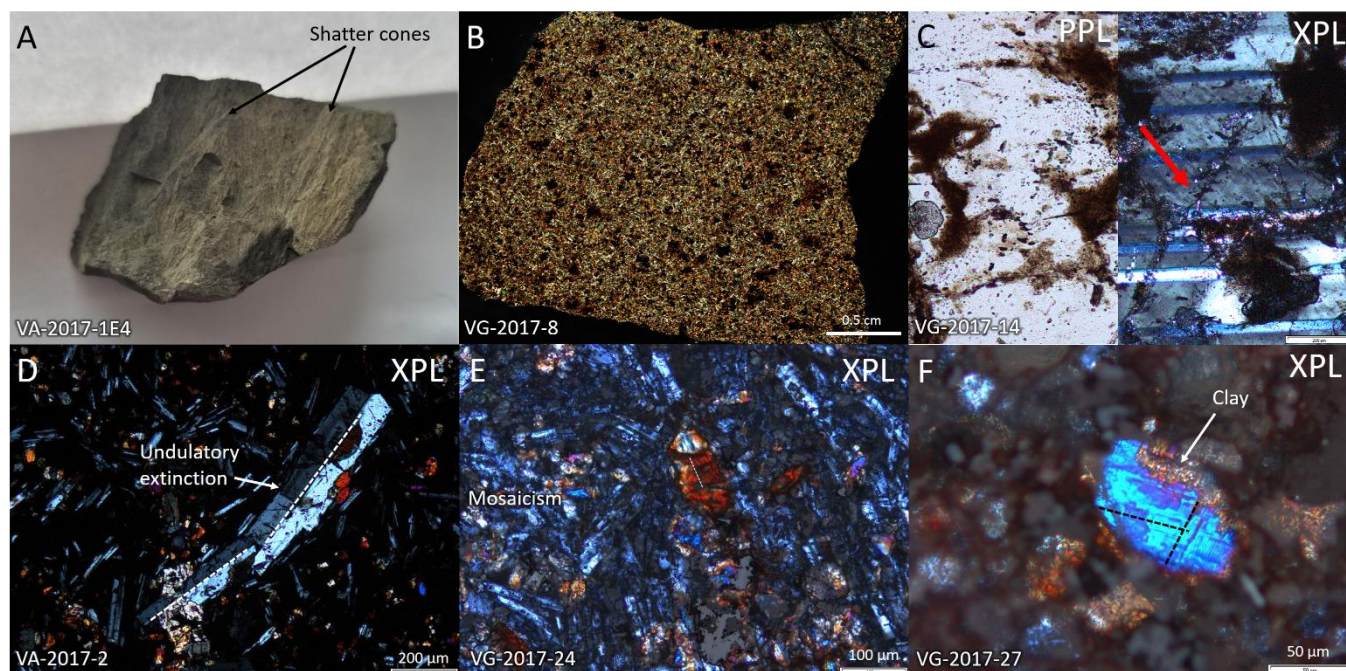
Figure 2-6. Petrography and shock effects in Vargeão Dome and Vista Alegre basaltic target rock. A) Hand sample from the quarry at Vista Alegre, exhibiting shatter cone features. The rock is ~4 x 6 cm in size. B) Typical textures and composition of the basalt target rocks. The aphanitic target basalt is composed of feldspar, pyroxene, ulvöspinel and quartz. C) Plagioclase feldspar grain in PPL and XPL displaying twinning and an irregular fracture (red arrow). D) Kinked and bent plagioclase clast showing undulatory extinction and Carlesbad twinning. E) Intergranular texture where lath-shaped crystals of plagioclase are grouped around crystals of mafic minerals. The plagioclase grains display mosaicism, albite twinning and planar fracturing. Pyroxene grain in the centre displays planar fractures. F) Pyroxene grain displaying cleavage fractures and replacement by clays along the grain boundary.
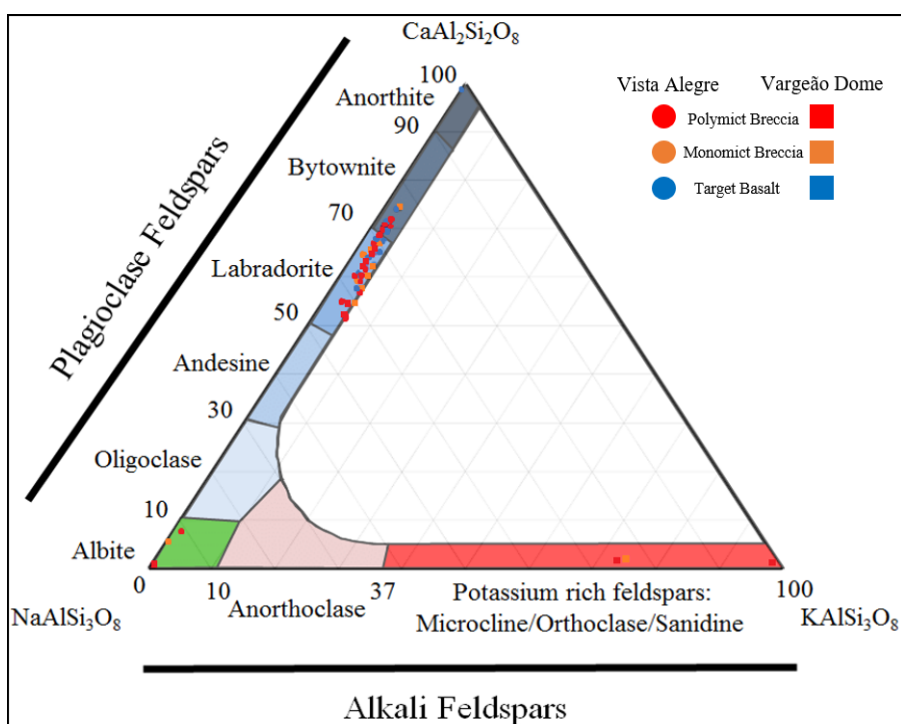
Figure 2-7. Ternary plot of feldspar major elemental composition plotted against the end members. Two major groups can be recognized: Mid-range Ca (labradorite), and Mid-high Ca (bytownite) plagioclase feldspars. Some of the less common groups include Albite, Orthoclase, and Anorthite. The ternary composition diagram is from Harrison et al., 2016, based on similar figures in the literature (Wittke and Sykes, 1990).

Table 2-3. Compositional analysis of plagioclase intermediate compositions in basaltic target rock and breccia samples throughout Vargeão Dome and Vista Alegre impact structures (Labradorite= Lab., Anorthite= Ano., Bytownite= Byt., surrounding= s).

| Plagioclase:	Lab.	Lab.	Lab.	Lab.	Lab.	Lab.	Lab.	Ano.	Ano.	Ano.	Ano.	Ano.	Byt.	Byt.	Byt.	Byt.
Sample:	VG-14	VG-25	VA-1C	VA-3B	VG-24	VG-10	VA-2	VG-12	VG-27	VG-24	VA-1C	VA-1B	VG-25	VA-1E	VA-2	VA-1B
Spot #:	Spot 2	Spot 4	Spot 4	Spot 1-s	Spot 1	Spot 1	Spot 2	Spot 1	Spot 2	Spot 3	Spot 3	Spot 7a	Spot 1	Spot 1-3	Spot 3	Spot 7b
Rock type:	breccia	breccia	breccia	breccia	Target rock	Target rock	Target rock	Target rock	Target rock	Target rock	breccia	breccia	breccia	breccia	Target rock	Breccia
SiO_2	57.614	56.397	55.407	54.702	55.373	54.667	55.471	54.576	53.939	53.338	53.875	53.799	52.928	53.146	52.471	54.216
Al_2O_3	26.161	27.119	27.605	27.631	27.462	27.969	27.561	28.573	28.676	28.773	28.492	28.656	29.407	28.811	29.276	28.368
Na_2O	6.109	5.574	5.080	4.826	5.297	4.761	4.900	4.54	4.493	4.374	4.529	4.711	3.892	4.203	3.952	4.306
MgO	0.058	0.070	0.088	0.107	0.036	0.083	0.121	0.16	0.050	0.050	0.065	0.038	0.176	0.107	0.155	0.180
TiO_2	0.089	0.080	0.075	0.069	0.089	0.075	0.104	0.069	0.079	0.077	0.066	0.060	0.056	0.069	0.118	0.062
FeO	0.612	0.713	0.927	0.820	0.821	0.889	0.714	0.651	0.864	0.897	0.981	0.943	0.449	0.847	0.842	1.212
CaO	8.668	9.863	10.792	11.225	10.576	11.199	10.654	11.866	11.729	12.042	11.805	11.734	12.786	12.231	12.721	12.001
K_2O	0.717	0.656	0.463	0.441	0.372	0.338	0.557	0.323	0.302	0.294	0.340	0.313	0.370	0.354	0.324	0.354
Total	100.028	100.471	100.437	99.821	100.026	99.981	100.082	100.758	100.132	99.845	100.153	100.254	100.064	99.768	99.859	100.699
Cations																
SiO_2	7.773	7.606	7.495	7.451	7.513	7.429	7.516	7.364	7.330	7.281	7.330	7.314	7.206	7.263	7.176	7.342
Al_2O_3	4.160	4.311	4.401	4.436	4.392	4.480	4.402	4.544	4.593	4.630	4.569	4.592	4.719	4.641	4.719	4.528
Na_2O	1.598	1.458	1.332	1.275	1.394	1.255	1.287	1.188	1.184	1.158	1.195	1.242	1.028	1.114	1.048	1.131
MgO	0.012	0.014	0.018	0.022	0.007	0.017	0.025	0.032	0.010	0.010	0.013	0.008	0.036	0.022	0.032	0.036
TiO_2	0.009	0.008	0.008	0.007	0.009	0.008	0.011	0.007	0.008	0.008	0.007	0.006	0.006	0.007	0.012	0.006
FeO	0.069	0.080	0.105	0.093	0.093	0.101	0.081	0.074	0.098	0.102	0.112	0.107	0.051	0.097	0.096	0.137
CaO	1.253	1.425	1.564	1.638	1.538	1.631	1.547	1.715	1.708	1.761	1.721	1.709	1.865	1.791	1.864	1.742
K_2O	0.123	0.113	0.080	0.077	0.064	0.059	0.096	0.556	0.052	0.051	0.059	0.054	0.064	0.062	0.057	0.061
Total	14.998	15.015	15.003	14.999	15.012	14.980	14.964	14.979	14.984	15.001	15.006	15.032	14.975	14.997	15.004	14.984

Vista Alegre:

Vista Alegre basalts have similar petrographic characteristics to Vargeão Dome, such that the basalts are composed of subhedral to euhedral crystals of ~60% plagioclase, ~30% clinopyroxene, and ~5–10% Fe-Ti oxides. Interstitial groundmass is fine-grained and composed of altered plagioclase, pyroxene, oxides, quartz, clays, and zeolites. WDS analysis of Vista Alegre samples reveal that the plagioclase compositions are 83% labradorite (An_{56-70}) and 17% bytownite (An_{71-76}) (Fig. 2-7). Veins infilled and lined by secondary phases overlay and crosscut shocked basalt minerals such as plagioclase and pyroxene, suggesting post-impact hydrothermalism. Additional evidence of hydrothermal alteration (potentially pre-impact) are expressed in the form of hydrothermal phases infilling and lining open spaces and replacement of primary basaltic minerals and altered glass. The main secondary phases in the shocked target basalts of Vista Alegre are heulandite-Ca zeolites, Fe-rich saponite octahedral clays, and chlorite-smectite interlayered clays (see Chapter 3).

2.4.1.3   Shock Metamorphism

Shock levels were assigned based on the presence or absence of well-defined shock effects in feldspar, pyroxene and, if present, quartz. Shock features are more abundant and better preserved in the coarser grained minerals. Plagioclase is commonly seen as mineral clasts in the breccias, individual larger phenocrysts throughout the basalt, and fine-grained crystals within the basaltic matrix. The shock effects observed in plagioclase include kinking and bending (Figs. 2-4 G, 2-5 E, 2-6 D), irregular fracturing (Fig. 2-6 C), a decrease in birefringence (Fig. 2-4 H), loss of grain boundary (Figs. 2-5 C, G), undulatory extinction (Figs. 2-5 G, 2-6 D), mosaicism (Fig. 2-6 E), and PDFs (Fig. 2-4 F). Shocked pyroxene minerals displayed loss of grain boundary (Fig. 2-6 F), irregular and planar fracturing (Figs. 2-5 D, 2-6 F), undulatory and mosaic extinction (Figs. 2-4 G, H) and PDFs (Figs. 2-5 B). Although less common in our sample set, both deformed and unshocked quartz are present. The larger sub-rounded to sub-angular shocked quartz grains display PFs, PDFs accompanied by feather features (Fig. 2-5 E), undulatory

extinction (Fig. 2-4 C), and mosaicism (Fig. 2-4 D). Fractures are random and not preferentially oriented.

Thin sections were characterized into shock levels based on the petrographic shock effects in plagioclase, pyroxene and quartz, in accordance with the mafic rock shock classification scheme (M-S) of Stöffler et al. (2018). The shock effects in the Vargeão Dome and Vista Alegre target basalts indicate mafic shock levels M-S–3 (shock stages 0–2a, Stöffler & Grieve, 2007) which corresponds to shock pressures ranging from 0 to ~22 GPa (Stöffler et al., 2018). The maximum shock level is based on the presence of mosaicism extinction in pyroxene.

Given that plagioclase is the most abundant mineral in basalts, comparative analyses of shock level and μXRD strain mosaicity measurements were performed on plagioclase grains. For this purpose, a separate shock metamorphism classification system was developed for individual feldspar grains of intermediate plagioclase composition (~An_{63}) (Table 2-4). Plagioclase shock effects representative of S-4 and higher were not seen in our sample set. Table 2-5 compiles the six main plagioclase shock classification schemes (Kieffer et al., 1976; Singleton, 2019; Singleton et al., 2011; Stöffler 1971; Stöffler et al., 1991, 2018) to demonstrate the development of feldspar shock classification as well as the variability that has resulted from different target compositions. Seeing as the low to moderate plagioclase shock effects in our study compare most favourably to Singleton's (2019) Table 3-1 summary of shock effects in feldspars hosted in the central uplift of the Mistastin Lake impact structure, our classification scheme is adapted from Singleton (2019), with modifications based on the petrographic shock features observed in the Vargeão Dome and Vista Alegre basaltic plagioclase grains of intermediate plagioclase composition (~An_{63}). Individual plagioclase grains from Vargeão Dome and Vista Alegre were assigned shock levels S1–3b.

Table 2-4. Shock effects in plagioclase feldspar used to indicate shock levels in the host rocks found in the Vargeão Dome and Vista Alegre impact structures.

Posnov (2021) Shocked Vargeão Dome and Vista Alegre Impact Basalt (Modified from Singleton (2019))		
Shock level	**Shock effects**	**Pressure (GPa)**
S1	Sharp optical extinction, irregular fractures, loss of grain boundary, kinking and bending (deformed twins)	1-5
S2	Fractures, planar features and undulatory extinction	~5 to 10
S3a	Undulatory extinction, slight mosaicism	10-12
S3b	Mosaicism	10-20
S3c	Mosaicism and PDFs	18- 24
S4	PDFs, mosaicsim, diaplectic glass	20-35
S5	Diaplectic glass	32-~45
S6	Melting	>45-50

Table 2-5. Summary of the six main plagioclase shock classification schemes (Kieffer et al., 1976; Singleton, 2019; Singleton et al., 2011; Stöffler 1971; Stöffler et al., 1991; Stöffler et al., 2018).

Stöffler (1971) Shocked and Brecciated Impact Rock			Kieffer et al. (1976) Experimentally Shocked Lonar Basalt			Stöffler et al. (1991) Ordinary Chondrites			Singleton et al. (2011) Shocked and Brecciated Haughton Impact Crystalline Rocks			Stöffler et al. (2018) Shock Metamorphism of Mafic Rocks			Singleton (2019) Shocked Plagioclase Feldspar from Mistastin Lake Impact Structure		
Shock stage	Shock effects	Pressure (GPa)	Shock level	Shock effects	Pressure (GPa)	Shock level	Shock effects	Pressure (GPa)	Shock level	Shock effects	Pressure (GPa)	Shock level	Shock effects	Pressure (GPa)	Shock level	Shock effects	Pressure (GPa)
0	Fractured					S1 Unshocked	Sharp optical extinction, irregular fractures		0		0	M-S1	Sharp optical extinction. Irregular fracturing		0	Unshocked	0

Table 2-5 (Cont.)

										1		2-5	**M-S2**	Fracturing	1-5	**1**	Fracturing	1-5
						S2 Very weakly shocked	Undulose extinction, irregular fractures	<4-5								**2**	Fracturing, undulatory extinction	5-10
I	Diaplectic feldspar (shocked, but not yet amorphous)	10				**S3 Weakly shocked**	Undulose extinction	5-10								**3a**	Fracturing, undulatory extinction, mosaicism	10-12
																3b	Mosaicism	12-15
										2	Fracturing checkerboard	10-20				**3c**	Mosaicism	15-20
			class 1	Minor undulatory extinction. Irregular fracturing	20	**S4 Moderately shocked**	Undulose extinction, partially isotropic, PDFs	15-20					**M-S3**	PDFs and partially converted to diaplectic glass, mosaicism.	20-22			
			class 2	Index and birefringence reduced and variable. Partially isotropic. Extreme undulatory extinction	25					**3**	PDFs, reduced refractive index, lower birefringence, checkerboard	20-30				**3d**	PDFs, mosaicism, diaplectic glass	20-30
				Index reduced. Birefringence reduced. Over 90% isotropic	27													
				Index and birefringence reduced even more	28.1								**M-S4**	Diaplectic plagioclase glass	28-34			
II	Diaplectic feldspar glass	35		Index reduced. Most isotropic. Locally traces of melt	33.4	**S5 Strongly shocked**	Maskelynite	30-35		**4**	PDFs	30-35						
																4	PDFs, mosaicism, diaplectic glass	30-35

Table 2-5 (Cont.)

								5	Diaplectic to flowed and vesicular, partial melting normal (melted) glass	35-45			**5a**	Diaplecic glass	35-45
III	Fused feldspar (vesiculated glass)	45				**S6 Very strongly shocked**	Shock melted (normal glass) restricted to local regions in or near melt zones	45-55		Diaplectic to flowed and vesicular, partial melting	45-55	**M-S5**	Melted plagioclase glass with incipient flow structure and vesciles	42-45	**5b**	Melting	45-50
			class 3	Isotropic. Minor flow and vesiculation	42.8-44.2								
				Isotropic. Over 90% highly vesiculated and flowed	44.5								
				Isotropic. Minor flow and vesiculation	51								
IV	Inhomogenous rock glasses	55-60		Isotropic. Flow and vesiculation well developed	59.4			**6**	Flowed to frothy glass, partial melting	55-60	**M-S6**	Melted plagioclase glass with vesicles and flow structure	55-60			
														6	Loss of diaplectice outlines, flowed to frothy glass	55-60
			class 4	Isotropic. Highly vesiculated	64.2			**7**	Complete melting of all minerals, frothy siliceous and minor mafic glasses	60-80				
														7	Complete melting of all minerals, frothy siliceous and minor mafic glasses	60-80
												M-S7	Whole rock melt	>60-65	
V	Slicate vapor	>80				**shock melted**	Whole rock melting	75-90	**8**	Complete rock vaporizaton	<80				**8**	Rock vaporization until complete vaporization at <100 GPa	80-100

2.4.2　Micro-X-ray Diffraction Results

Basaltic target rock (unbrecciated) and breccia samples containing plagioclase grains ~300 microns in diameter or larger (if possible) were selected for µXRD analysis. In both target rock and breccia samples, Miller indices are based on ICDD card labradorite; # 78-0435 (Triclinic, Space Group C1). The plagioclase diffraction peak at ~32° 2θ (3.2 Å) was the most frequently occurring and always yielded the highest intensity (counts) in the intensity versus °χ plots. Multiple Miller indices are known to occur at that location, of which the most consistent in all the collected data are ($\bar{2}$02), (002), (040), ($\bar{2}$20), and ($\bar{2}$04). No systemic variation in $FWHM_\chi$ between Miller indices was noticed, therefore they were not differentiated for this study. For comparative analysis, (1) averaged $FWHM_\chi$ of all the plagioclase diffraction peaks, (2) averaged $FWHM_\chi$ values at ~32° 2θ (3.2 Å) peaks and (3) the maximum $FWHM_\chi$ values for each grain were considered. All three methods used for measuring $FWHM_\chi$ of the grain are directly correlated with known shock levels based on shock features obtained petrographically.

Using method (1), plagioclase samples yielded an average steak length of 0.763° for shock level S1, 0.897° for shock level S2, and 1.273° for shock level S3. The average $FWHM_\chi$ using method (2) is 0.768° for shock level S1, 0.908° for shock level S2, and 1.440° for shock level S3. Lastly, method (3) yielded averages of 0.947° for S1, 1.183° for S2, and 1.730° for S3.

All methods illustrate a positive, nonlinear correlation between shock level and $FWHM_\chi$ values (Table 2-4) where streak length along χ increases with the shock level (Fig. 2-8). Methods 1 and 2 display similar trends among the same samples set. Method 1 is slightly less variable than method 2 meaning the range between maximum and minimum $FWHM_\chi$ is smaller. Method 2 produces a slightly higher average $FWHM_\chi$ value than method 1 for the representative shock level. Method 3 produces the highest variability with the greatest overlap between the shock levels. The average $FWHM_\chi$ values in method 3 are the most centered meaning they are not influenced by outliers as much. In addition, regardless of the method used, the feldspar grains with the highest $FWHM_\chi$ (higher shock level) produce the largest variability in $FWHM_\chi$ values (Table 2-6).
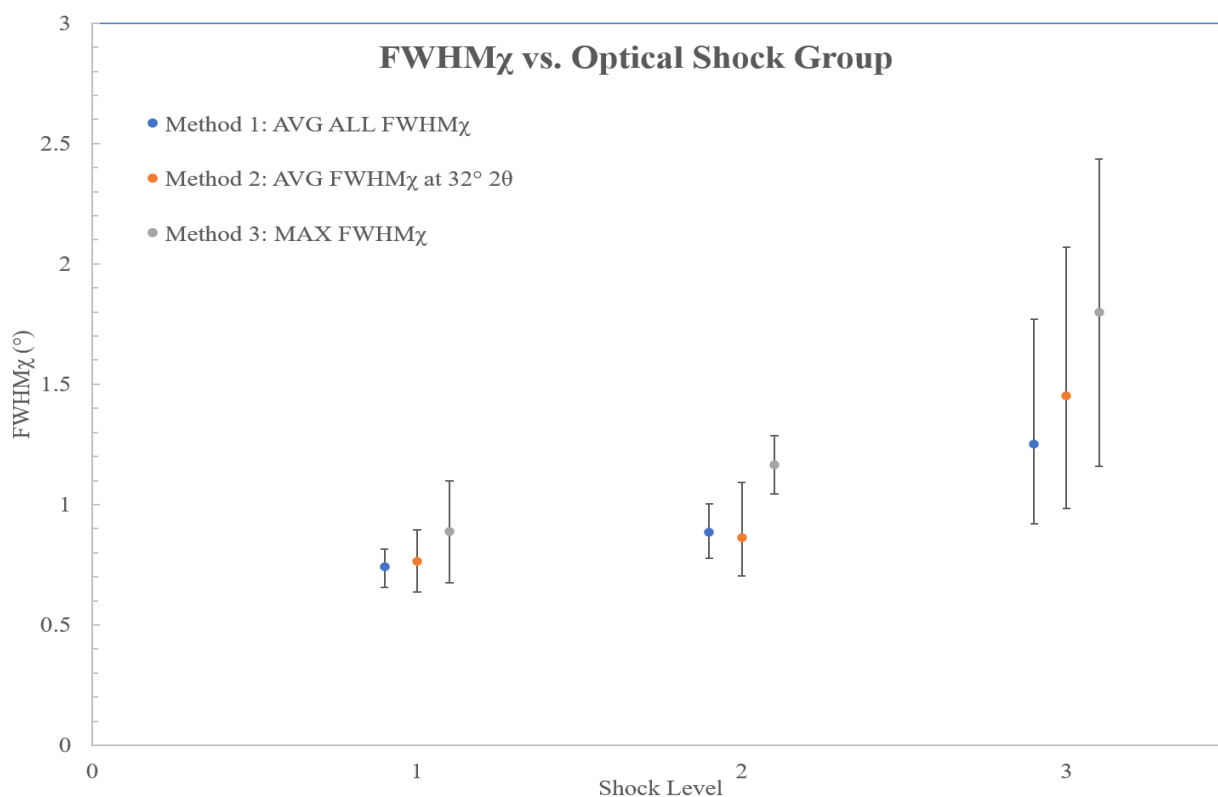
Figure 2-8. Graph of FWHMχ vs. shock groups for the three methods tested. The average FWHMχ value for the shock level using each method is plotted with error bars indicative of the minimum and maximum values.

The complete set of FWHM$_\chi$ values from the analyzed plagioclase grains for each thin section are summarized in Appendix B supplied as supplementary information. Samples that do not have a FWHM$_\chi$ value (represented with N/A in Table 2-6) did not have large enough individual plagioclase feldspar grains to complete accurate FWHM$_\chi$ measurements. In the case of method 2, peaks at 32° 2θ (3.2 Å) sometimes display overlapping peaks due to twinning in the plagioclase grain, which also resulted in the inability to obtain an individual FWHM$_\chi$ value.

Table 2-6. Summary of averaged FWHMχ measurements, FWHMχ at ~32° 2θ and standard deviations (σ) for Vargeão Dome and Vista Alegre target rocks containing plagioclase grains (≥300 microns) in order of increasing FWHMχ at ~32° 2θ measurements. Blue= shock level 1, grey=shock level 2, green= shock level 3a, yellow= shock level 3b.

Sample Name	Spot #	Distance from the centre of the crater column (km)	Grain shock level based on optical observations	Method 1: averaged FWHMχ at 25-49 ° 2θ	SD (σ)	Max for sample	Method 2: averaged FWHMχ 32° 2θ	SD (σ)	Max for sample	Method 3: Max FWHMs	Max for sample	Sample shock level
VG-2017-8	1	2.58 SE (151°)	3a	0.789	0.1256	1.358	0.835	0.0130	1.831	1.015	2.543	3b
VG-2017-8	3		3b	0.894	0.3893		0.575	0.0545		1.543		
VG-2017-8	4		2	0.797	0.1635		0.826	0.0165		1.051		
VG-2017-8	5		3b	1.358	0.6913		1.831	0.7125		2.543		
VG-2019-9	1	1.83 SE (138°)	3a	1.029	0.3778	1.029	1.269	0.3821	1.269	1.8	1.8	3a
VG-2019-9	2		1	0.721	0.0820		0.746	0.1005		0.91		
VG-2019-9	3		1	0.749	0.1039		0.76	0.0379		0.983		
VG-2019-9	4		2	1.003	0.1915		0.912	0		1.271		
VG-2019-9	5		1	0.814	0.1160		0.847	0.1150		0.973		
VG-2017-10	1		2	0.751	0.0760	0.873	N/A	0	0.797	0.827	1.163	

Table 2-6 (Cont.)

VG-2017-10	2	1.83 SE (138°)	2	0.873	0.1565		0.797	0.0150		1.163		2
VG-2017-12	1	3.70 N (346°)	2	0.92	0.1114	0.92	0.984	0.0949	0.984	1.16	1.16	2
VG-2017-12	3		1	0.759	0.1293		0.657	0		0.931		
VG-2017-13b	1	3.46 NE (41°)	1	0.788	0.1097	0.788	0.894	0.0980	0.894	0.992	0.992	1
VG-2017-13b	1.2		1	0.745	0.1731		0.757	0.1090		0.951		
VG-2017-13b	4.2		1	0.725	0.1340		N/A	0		0.859		
VG-2017-13b	3.3		1	0.655	0.0157		0.638	0		0.676		
VG-2017-13b	4.3		1	0.678	0.1107		N/A	0		0.816		
VG-2017-14	1	4.74 NE (41°)	3a	1.252	0.3263	1.537	1.373	0.3405	1.859	1.713	2.092	3a
VG-2017-14	3		2	0.814	0.1890		0.813	0		1.045		
VG-2017-14	ISXRD 1		3a	1.537	0.4926		1.859	0.2335		2.092		
VG-2017-14	ISXRD 2		2	1.407	0.0264		1.449	0.0280		1.38		
VG-2017-22	1	0.85 NE (24°)	2	0.869	0.1415	1.108	0.703	0	1.481	1.053	1.481	3a
VG-2017-22	2		3a	1.108	0.3404		1.481	0		1.481		

Table 2-6 (Cont.)

VG-2017-22	3		2	0.886	0.1830		0.788	0		1.233		
VG-2017-24	3	1.14 E (70°)	3b	1.14	0.4705	1.14	2.07	0.5518	1.106	2.07	2.07	3b
VG-2017-24	4		3a	1.043	0.2450		1.106	0.1605		1.41		
VG-2017-24	5		3a	0.902	0.2160		1.093	0.0510		1.144		
VG-2017-27	1	2.79 NE (37°)	3a	0.877	0.1378	0.877	1.017	0.0285	1.017	1.045	1.3	3a
VG-2017-27	2		3a	0.805	0.2895		0.71	0		1.3		
VA-2017-1E4	1	2.8 NW	2	1.19	0	1.769	N/A	0	1.769	1.19	1.769	3b
VA-2017-1E4	1.2		2	0.958	0.2100		0.958	0.2100		1.168		
VA-2017-1E4	2.2		3b	1.769	0		1.769	0		1.769		
VA-2017-2	1	5.30 N (6°)	2	0.95	0.1829	1.74	1.001	0.2065	1.001	1.207	2.079	3b
VA-2017-2	2		2	0.993	0.1590		N/A	0		1.345		
VA-2017-2	3		1	0.786	0.1220		N/A	0		0.908		
VA-2017-2	4		3b	1.74	0.4434		N/A	0		2.079		

GADDS images and petrographic plane- and cross-polarized light microphotographs for each grain were directly compared to the average FWHMχ measurements (Table 2-4) for each shock level (Fig. 2-9). As the diffraction intensities on the GADDS image progress from individual spots (i) to short streaks (ii), to long streaks (iii), to asterism (row of spots), the FWHMχ value increases accordingly. No amorphous bands indicative of an amorphous XRD pattern are seen in the sample set. In addition, it can be noted that within the μXRD GADDS images there are various instances of doublets (two spots in the same chi ring) that are believed to correspond with albite twinning (Figs. 2-9 A, B, C, D). The two spots making up the doublet are at a constant chi angle apart and repeat within its own and other chi rings. Doublets are best seen in samples with shock levels S1-2, before plagioclase deforms significantly resulting in the loss of twinning features.

A) VG-2017-9 spot 3 — S1 — FWHM$_\chi$ = 0.749°/ 0.760°/ 0.985°

B) VG-2017-13b spot 1 — S1 — FWHM$_\chi$ = 0.788°/ 0.984°/ 0.992° — 500 μm

C) VG-2017-12 spot 1 — S2 — FWHM$_\chi$ = 0.920°/ 0.984° /1.160°
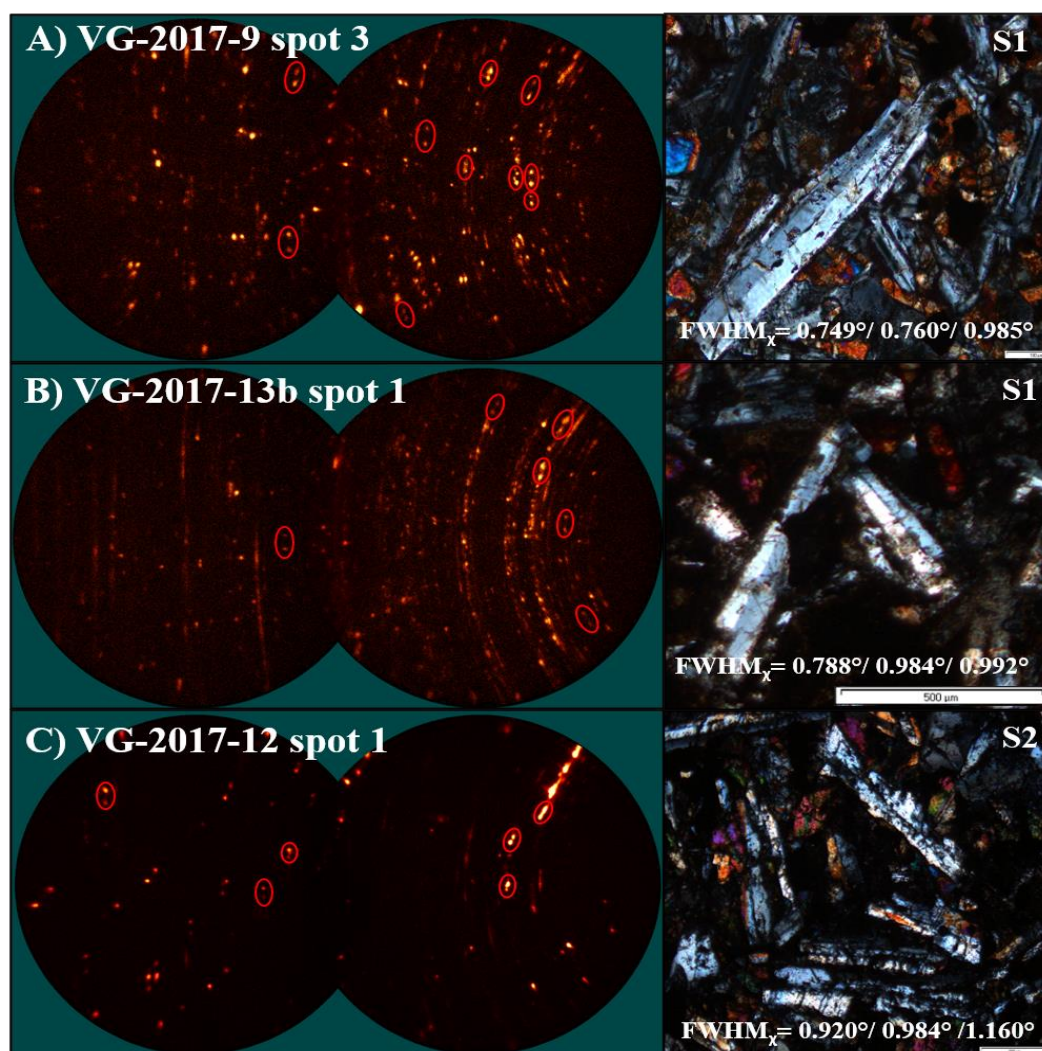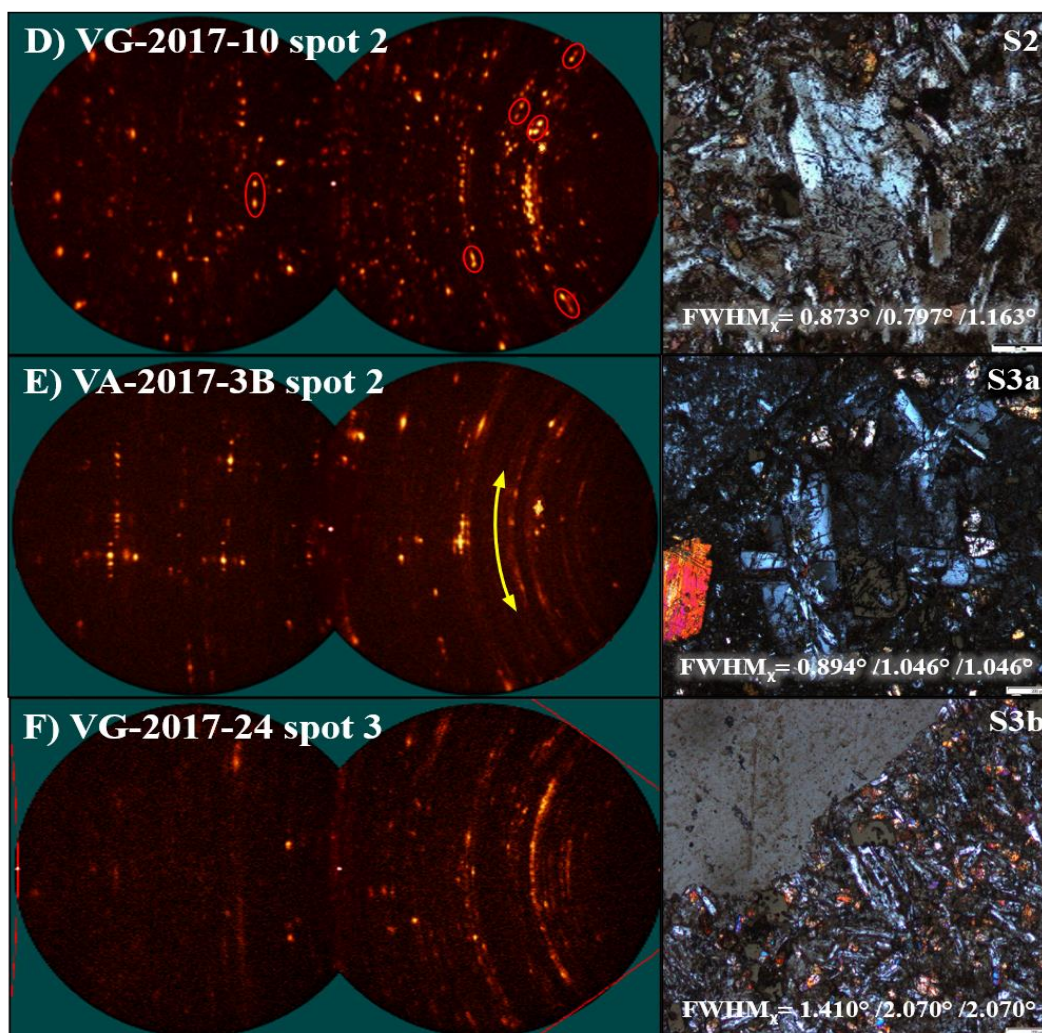
Figure 2-9. Plagioclase grain comparative analyses using GADDS images, petrographic images, shock level (based on the scheme developed for this study, Table 2-4) and corresponding FWHMχ values at 2θ (method 1, 2, 3), in order of increasing strain-related mosaicity. GADDS images (left) display: A-B) Both display clear individual spots, and red circles indicate doublets. C-D) Spots are beginning to streak into 'ellipsoids' that are slightly longer than they are wide. Red circles indicate doublets in both images. E) Short streaks, with asterism (yellow arrow). F) Long streaks resolving into rows of spots due to crystallite size being 15-50 μm. Petrographic images (XPL) on the right show: A-B) Lightly shocked plagioclase crystals displaying albite twinning. C) Kinked and bent twinned plagioclase with loss of grain boundary, fracturing, as well as undulatory extinction. D) Plagioclase grain displaying irregular fractures and undulatory extinction. E) Heavily fractured plagioclase grain with undulatory extinction and slight mosaicism. F) Plagioclase with mosaicism extinction.

It is well established that one specific shock level cannot be assigned to breccia samples. As breccias are allochthonous, their plagioclase grains may have originated from target rock fragments from various locations, so each distinct plagioclase grain receives its own unique average $FWHM_\chi$ value. Additionally, studies have shown that grains within a target rock may also vary in shock level due to the grain's physical characteristics and surroundings (Dence, 2004; Jaret et al., 2018; Robertson & Grieve, 1977). $FWHM\chi$ measurements for target and brecciated rocks can only be averaged for the unique plagioclase 2θ diffraction peaks of each individual plagioclase grain (≥ 300 microns) within a sample. Figure 2-10 shows a cumulative plot sorted by increasing average $FWHM_\chi$ values (method 1). The Y-axis is the cumulative percent of the number of grains contributing to any given sample and the X-axis is $FWHM_\chi$ values for each plagioclase grain within a sample as determined by μXRD measurement. Heterogeneity of shock is seen by the variability of $FWHM\chi$ values, where a larger distribution of $FWHM\chi$ values (along Y-axis) within an individual sample indicates more heterogeneity throughout the sample, and vice versa for homogenous rocks. Polymict breccias contain plagioclase grains that are the most shocked ($FWHM\chi$ values farthest to the right) and also the most heterogenous in $FWHM_\chi$ values within an individual sample. Monomict breccia plagioclase grains are on average less shocked and more homogenous in shock level. Target basalts are relatively homogenous in $FWHM_\chi$ values; however, the more highly shocked samples display a larger variation between $FWHM\chi$ in comparison to the lower shock samples. Cumulative plots using $FWHM_\chi$ values obtained with method 2 show the same trend. Cumulative plots cannot be made for single values such as the maximum $FWHM_\chi$ in method 3.
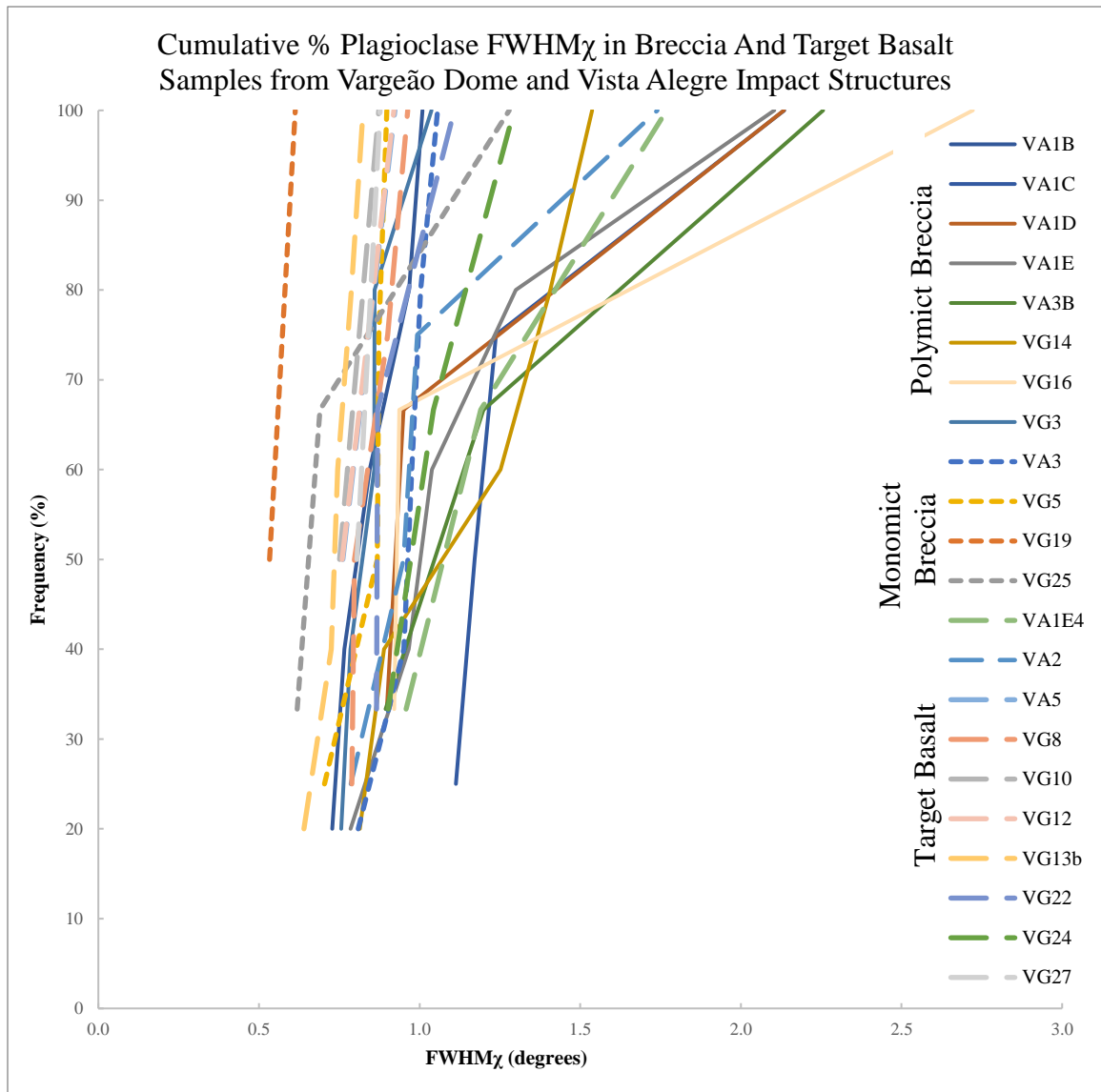
Figure 2-10. Cumulative plot of FWHMχ distribution for individual plagioclase grains from Vargeão Dome and Vista Alegre breccia and basaltic rock samples.

2.4.3   Raman Spectroscopy Results

Raman spectra of unshocked and shocked plagioclase (~An_{50} composition) from Mistastin Lake (Xie et al., 2020) and experimentally shocked plagioclase (An_{50-57} composition) (Fritz et al., 2019) were used as reference for shock level measurements (Fig. 2-11). Although the feldspar grains analyzed with Raman did not provide a large range of shock pressures, band broadening is seen between the unshocked and lightly shocked samples (Fig. 2-12). As expected, the two most characteristic Raman peaks of feldspars are between 477 and 482 cm^{-1} and 508 and 509 cm^{-1}. There is no evidence for diaplectic glass.
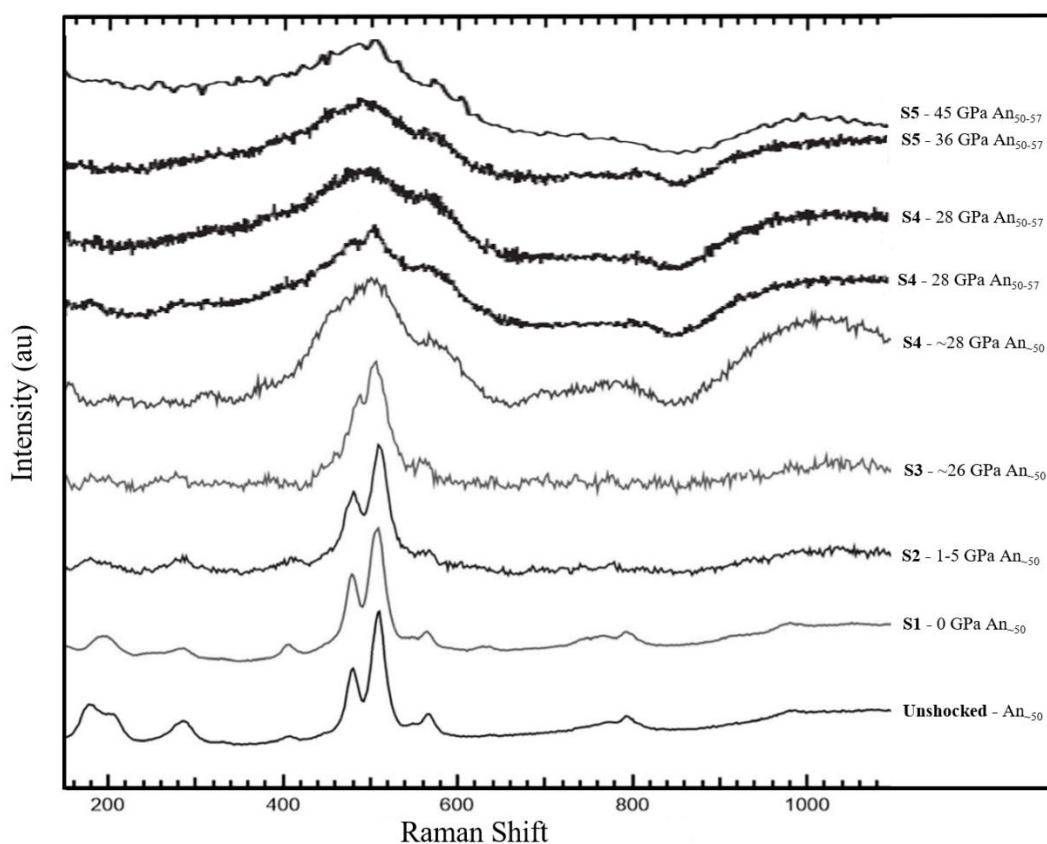
Figure 2-11. Reference Raman spectra of unshocked and shocked plagioclase. Unshocked to shock level 4 (~28 GPa) spectra of plagioclase An$_{50}$ composition is obtained from Mistastin Lake (Xie et al., 2020). Shock level S4 (~28 GPa) and above spectra of plagioclase An$_{50-57}$ composition is experimentally shocked plagioclase (Fritz et al., 2019).
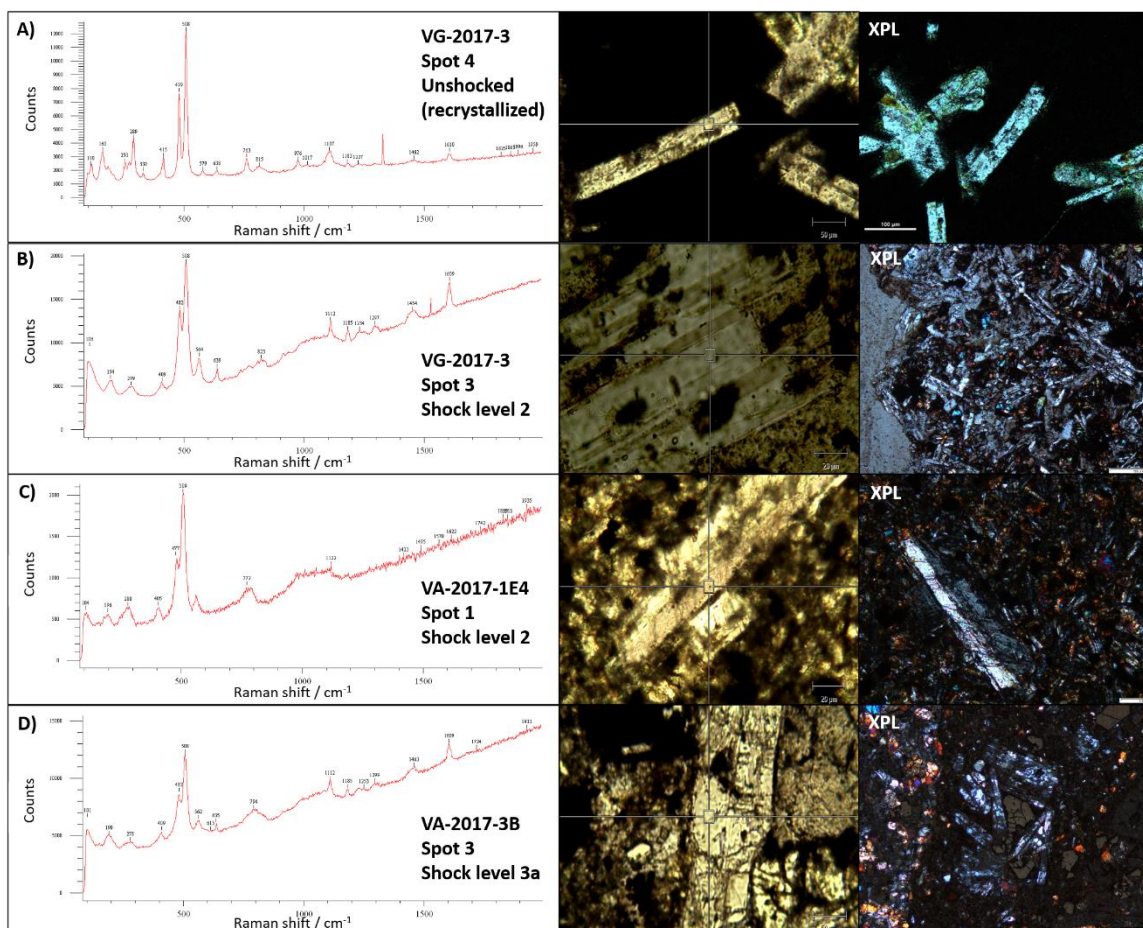
Figure 2-12. Raman spectra of unshocked and shocked plagioclase from Vargeão Dome and Vista Alegre target basalts and breccias and corresponding photomicrographs (taken with the Raman instrument and XPL). A) The main diagnostic peaks are sharp and narrow. Unshocked plagioclase grains recrystallized in a breccia melt clast. B-C) Diagnostic peaks show slight broadening and lattice modes peaks under 350 cm^{-1} slightly weakened. Lightly shocked plagioclase grains displaying fracturing, twinning and undulatory extinction. D) Greater broadening of the main peaks. Shock level 3 plagioclase displaying mosaicism.

2.4.4   Density and Porosity Analysis

Bulk densities of 12 target rock samples were obtained using the specific gravity water displacement method providing values ranging from 1.98 to 2.91 g cm^{-3}. Samples are grouped into four categories: (1) unshocked samples collected from outside the Vista Alegre impact structure, representative of the Paraná Basin basalts that are unaffected, or very minimally affected by the impact event, (2) lightly shocked sample (M-S1-2) from within the Vargeão Dome impact structure with minimal shock effects, (3) moderately shocked samples (M-S3) from within the Vista Alegre and Vargeão Dome craters containing undulatory and mosaicism extinction as the maximum petrographic shock effects, and (4) heavily altered samples that lack obvious petrographic indicators of shock metamorphism, however where there is less alteration, plagioclase and pyroxene display potential PDFs.

The bulk densities of the unshocked samples range from 2.54 cm^{-3} to 2.68 cm^{-3}, lightly shocked (M-S1-2) samples range from 2.90 g cm^{-3} to 2.91 g cm^{-3}, moderately shocked samples (M-S3) have bulk density values from 2.47 g cm^{-3} to 2.91 g cm^{-3}, and samples of shock level higher than M-S3 have bulk densities of 1.98 g cm^{-3} to 2.22 g cm^{-3}. The bulk densities of five samples were additionally measured with µCT analysis. The variability between bulk densities measured by specific gravity water displacement versus those measured with µCT is not systematic. The greatest deviation occurred in the lowest shock sample measured: VG-2017-13b, with a density value 0.34 cm^{-3} higher than that measured with displacement, and the highest shock sample measured: VG-2017-21, with a density value 0.51 cm^{-3} lower than that measured with displacement. The rest of samples in between deviated by 0.04 to 0.18 cm^{-3} from the values obtained with the specific gravity water displacement method (Table 2-7). The grain density, measured with He pycnometry, of unshocked samples (M-S0) ranges from 2.54 cm^{-3} to 2.72 cm^{-3}, samples of low shock levels (M-S1–2) range from 2.90 cm^{-3} to 2.93 cm^{-3}, moderately shocked samples have grain densities ranging from 2.65 cm^{-3} to 2.91 cm^{-3}, and samples of shock level above M-S3 range from 2.15 cm^{-3} to 2.72 cm^{-3} (Table 2-7).

Table 2-7. Results for basaltic target rock bulk and grain density, porosity, plagioclase FWHMχ at 32° 2θ, and shock level based on Stöffler et al. (2018) classification. Samples VA-2017-5, VA-2017-5C, VG-2017-15, VG-2017-28 and VG-2017-30b do not have a usable FWHMχ measurement for plagioclase feldspar.

Sample ID	Sample shock level (M-S) (Stöffler et al., 2018)	Bulk Density (g/cm³) by water displacement method	Bulk Density (g/cm³) by microCT	Grain Density (g/cm³) by Helium Pycnometry	Porosity by density (%)
VA-2017-5	0	2.54		2.54	0.12
VA-2017-5C	0	2.68		2.72	1.31
VG-2017-13b	1	2.90	3.24	2.90	-0.55
VG-2017-10	2	2.90		2.93	1.01
VG-2017-12	2	2.91		2.91	1.52
VA-2017-2	3	2.91		2.91	-0.08
VG-2017-22	3	2.85		2.87	0.77
VG-2017-9	3	2.79		2.81	0.70
VG-2017-8	3	2.80		2.80	5.86
VA-2017-1E4	3	2.67		2.85	6.28
VG-2017-15	3	2.65	2.47	2.65	7.06
VG-2017-24	3	2.47	2.51	2.85	13.09
VG-2017-30b	4	2.22	2.26	2.72	18.57
VG-2017-28	4	1.98		2.59	23.69
VG-2017-21	4	2.21	1.70	2.15	26.50

The porosity of the 12 target rocks was measured using both the Helium Pycnometry and μCT methods. Unshocked samples have 0.12-1.31% porosity, poorly shocked (M-S1-2) target rocks have 0–1.52% porosity, moderately shocked samples have porosities ranging from 0–13.09%, and samples of higher shock levels (>M-S3) have porosities of 18.57–26.50%. Slightly negative porosity values are reasoned to have no porosity (0%). μCT scan photographs of slices within target rocks of varying porosity can be seen in Fig 2-13.
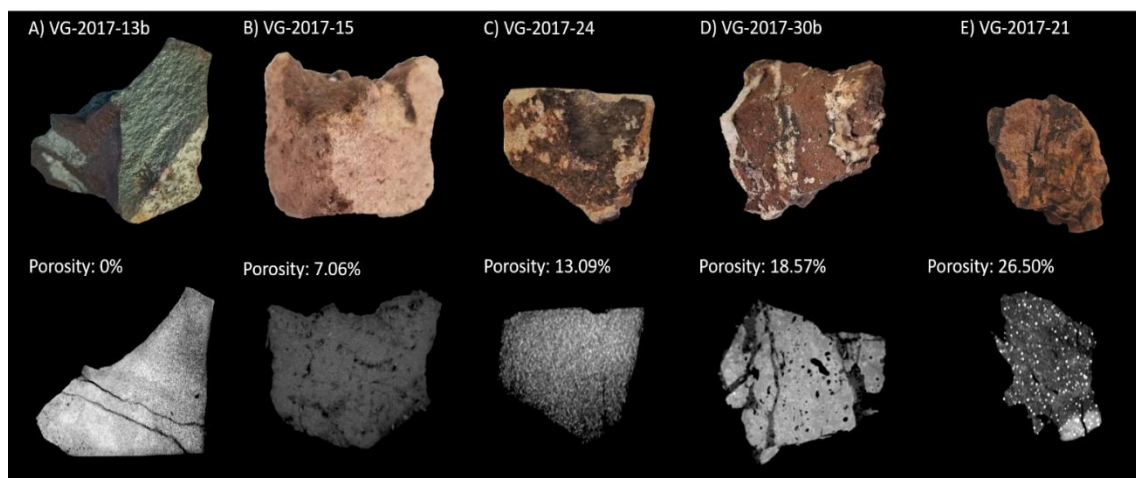
Figure 2-13. Photo vs CT scan of target basalt samples from Vargeão Dome. Samples increasing in porosity (%) from left to right. Top: A photograph of whole rock samples. Bottom: CT slice through the surface of the corresponding rock, collected on the speCZT at 120 kVp and 20 mA. A) snapshot of a CT slice 22.5 mm deep across the y-axis. B) snapshot 19.5mm deep across x-axis. C) snapshot 3.75 mm deep across y-axis. D) snapshot 18 mm deep across y-axis. E) snapshot 9 mm deep across y-axis.

Figure 2-14 plots the variation of bulk density, grain density, and porosity with increasing shock stage, with a grey horizontal bar used as a reference for average density and porosity values of normal basalts (Hamouda et al., 2014). Both bulk density and grain density of our basaltic samples follow a similar trend to each other. The densities display a slight initial increase from unshocked to slightly shocked sample and decrease from the normal starting at shock level M-S3. The unshocked samples (VA-2017-5 and VA-2017-5C) have lower densities and porosities than the average values of normal reference basalts. Additionally, Vista Alegre samples appear denser than Vargeão Dome samples. A clear, non-linear correlation is seen between the shock level of target rocks and porosity, in which increased shock level appears to result in greater porosity. Porosity of Vargeão Dome basalts begins to vary from the normal at shock levels M-S3 and in correlation to the higher Vista Alegre densities at shock level M-S3, Vista Alegre basalts appear to be less porous than Vargeão Dome.
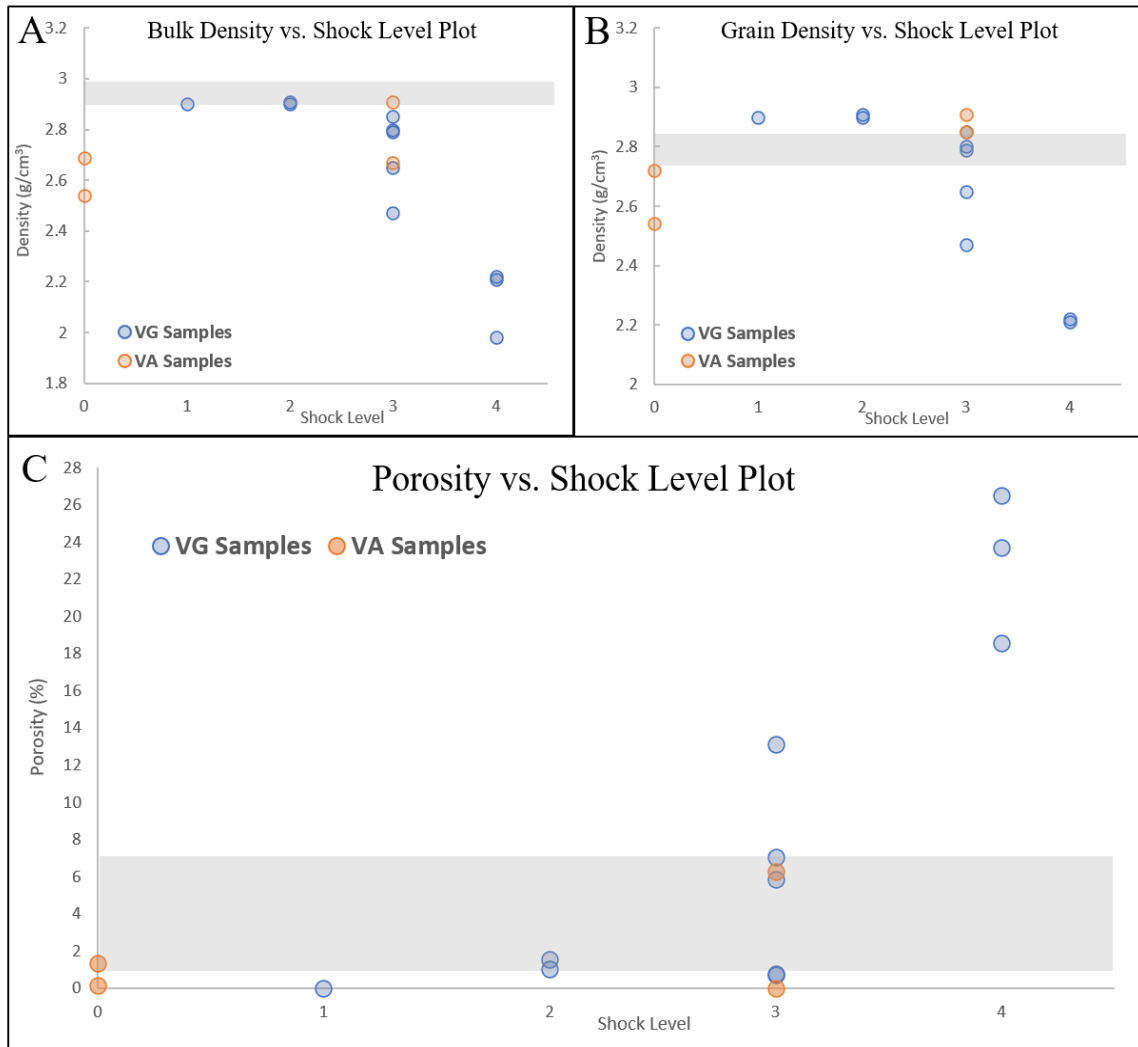
Figure 2-14. Variation of bulk density, grain density and porosity with shock stage level. Grey Horizontal bar indicates the normal bulk and grain density and porosity averages of basalts (Hamouda et al., 2014).

2.5   Discussion and Conclusions

2.5.1   Shock Metamorphism in Basalt

The Vargeão Dome and Vista Alegre impact structures provide an excellent opportunity to further our understanding of shock metamorphism in basaltic target rocks. This also makes these structures excellent analogues for Mars. Indeed, the composition of Vargeão Dome and Vista Alegre target basalts (Crósta et al., 2001) closely matches the composition of Martian basalt (McSween, 1994; McSween, 2002), which also have higher Fe and lower Al abundances than most terrestrial basalts.

The most common mineral in basalt is plagioclase. Plagioclase from the Vargeão Dome and Vista Alegre craters are predominantly comprised of labradorite, bytownite and albite, with an average composition of An_{63} (Fig. 2-7). Plagioclase feldspar grains developed a variety of shock-metamorphic features including kinking and bending (Figs. 2-4 G, 2-5 E, 2-6 D), irregular fracturing (Fig. 2-6 C), a decrease in birefringence (Fig. 2-4 H), loss of grain boundary (Figs. 2-5 C, G), undulatory extinction (Figs. 2-5 G, 2-6 D), mosaicism (Fig. 2-6 E), and PDFs (Fig. 2-4 F).

Crósta et al. (2011) reported the presence of partial and complete diaplectic glass in the central uplift of Vargeão Dome impact crater. Several areas were identified in target rock samples VG-2017-15, VG-2017-24, and VG-2017-21 from the central uplifts of Vargeão Dome that under the optical microscope, appear isotropic suggesting the presence of diaplectic glass. However, Raman spectroscopy analyses of these areas did not show any diagnostic peaks for diaplectic glass (Fig. 2-12); this fits with the XRD data that suggests that these are areas of alteration.

The peak shock pressure of target rocks from the central uplift of smaller (~20 km diameter) complex craters such as Vargeão Dome (12.9 km) is expected to be in the range of ~25–30 GPa, (Grieve & Cintala, 1992; Grieve & Therriault, 2004; Melosh & Ivanov, 1999), and therefore the formation of diaplectic glass (which forms around 35–45 GPa, [e.g., Therriault et al., 2002; Stöffler et al., 2018]) is unexpected for craters of this size. However, further analyses were conducted in Vargeão Dome in light of the recent discovery of higher than predicted peak shock pressure in the central uplift of the

~28 km Mistastin Lake impact structure (Canada) (Singleton, 2019). The peak shock pressure expected in the central uplift of Mistastin Lake impact structure based on its size is around 30 GPa (e.g., French, 1998; Stöffler et al., 1988), but Singleton (2019) provided Raman-based spectroscopic evidence of diaplectic feldspar in the central uplift indicative of a maximum pressure of 45 GPa.

The previous classification scheme of shocked basalts compiled by Kieffer et al. (1976) based on experimentally shocked Lonar samples does not compare favorably with the shock effects in the Vargeão Dome and Vista Alegre basalts. It appears that there are some discrepancies between experimentally shocked feldspars and those naturally shocked. For example, the onset of undulatory extinction in experimentally shocked plagioclase occurs at much higher shock pressures in comparison to our naturally shocked plagioclase grains. In addition, Kieffer et al.'s (1976) classification system does not encompass the lower pressure shock effects seen in our sample set. Instead, the progression of petrographic shock features in Vargeão Dome and Vista Alegre plagioclase feldspars are most similar to those described by Singleton et al. (2011) and Stöffler et al. (2018). Our results enable a more gradational progression in lower shock level grains via the addition of transitional divisions that enable more accurate intermediate characterization (i.e., between shock levels 1–3b).

Entire target rock samples were classified based on Stöffler et al.'s (2018) shock classification system for mafic rocks with assigned shock levels M-S1–3 and formation pressures ranging from 0 to ~20–22 GPa. Only approximate formation pressure and temperature estimates are possible because the energy of impact can be extremely localized and can manifest heterogeneously depending on a wide range of pre-existing physical properties (temperature of target, water content, strain rate, porosity, composition) (Dence, 2004; Robertson & Grieve, 1977).

2.5.2   µXRD for Quantifying Shock

The XRD approach used in this study is based on work by Pickersgill et al. (2015a) with a few key modifications. In their method, Pickersgill et al. (2015a) averaged all the FWHMχ values for all representative plagioclase Miller indices for each feldspar grain.

Using this method for Vargeão Dome and Vista Alegre basalts, FWHMχ values for different 2θ peaks display considerable variability within feldspar grains (Fig. 2-8). For this reason, this study compared the accuracy and efficiency of the methodology by assessing Pickersgill's et al. (2015a) technique (referred to as method 1 in this study), method 2 which averages only FWHM$_\chi$ values at the most intense and frequently occurring diffraction peak within the feldspar grains, and method 3 which measures the maximum FWHM$_\chi$ value among all grains in each sample (Fig. 2-8, Table 2-6). In our intensity vs. 2θ peak plots, the ~32° 2θ (3.2 Å) diffraction peaks are of the highest intensity in almost all of the samples. Averaging FWHM$_\chi$ values at ~32° 2θ for each grain analyzed within the sample (method 2) provides results that are comparatively accurate to those produced when following Pickersgill's et al. (2015a) method, but results are obtained in a much more efficient way by only having to measure the FWHM$_\chi$ of one diffraction peak.

It is important to note that when collecting data using method 2, the ~32° 2θ peaks sometimes overlap or may be indicative of X-ray diffraction from other nearby minerals that produce spots at lattice planes of the same Miller indices as the target plagioclase, such as enstatite (Izawa et al. 2011). This issue can be circumvented by selecting large (>300 micron) plagioclase grains expressing distinctive feldspathic petrographic characteristics, carefully indexing the observed lattice plane to the appropriate ICDD card from the database, and correlating μXRD GADDS images to the mineral and shock features observed petrographically. Recording only the maximum FWHM$_\chi$ value for each grain was also tested (method 3) for quantitively measuring strain-related mosaicity of shocked feldspar grains. Method 3 FWHM$_\chi$ results positively correlate with shock level but exhibits significant variability in FWHM$_\chi$ distribution within a shock group, and overall higher mean values that does not reflect the range of strain experienced as a function of feldspar orientation in the basalt (Table 2-6). In addition, this method is not very time efficient as FWHM$_\chi$ measurements of all diffraction peaks need to be assessed prior to attaining a maximum value. While all three methods can be successfully applied to quantify shock deformation of labradorite from terrestrial basaltic target rocks, method 2 achieves the same results in a shorter amount of time.

Pickersgill et al. (2015a) applied in situ µXRD to shock metamorphosed andesine and labradorite samples from Mistastin Lake and shocked anorthosite from the Moon. In agreement with Pickersgill et al. (2015a), Vargeão Dome and Vista Alegre FWHM$_\chi$ measurements across all Miller indices of labradorite grains fall within the streak length ranges of the Mistastin Lake suite associated with the shock group category (Table 2-8). Results reliably correlate to the patterns on the GADDS images and optically observed shock metamorphism features.

Table 2-8. Comparison of µXRD strain-related mosaicity results from Pickersgill et al. (2015a) to Vargeão Dome and Vista Alegre results in this study. GADDS image pattern and average FWHMχ measurements across all Miller indices for progressing shock levels.

	Pickersgill et al. (2015a) – Shocked lunar anorthite and Mistastin Lake andesine and labradorite					Vargeão Dome and Vista Alegre labradorite			
Shock level	Shock effects	GADDS	Mistastin avg FWHMχ (°)	Apollo avg FWHMχ (°)	Shock level (Table 2-4)	Shock effects	GADDS	VG/VA avg FWHMχ (°)
A	Uniform extinction and low degree of fracturing	Individual spots	0.67	0.79	**1**	**Sharp optical extinction, irregular fractures, loss of grain boundary, kinking and bending (deformed twins)**	**Clear individual spots**	**0.76**
B	Slight undulose extinction, irregular fractures	"Lozenges"	0.89	0.93	**2**	**Fractures, planar features and slight undulatory extinction**	**Elliptical spot**	**0.90**
C	Undulose extinction, signs of mosaicism, irregular fracturing and bent and/or offset twins	Streaks and beginning to show asterism	1.07	2.58	**3a**	**Undulatory extinction, slight mosaicism**	**Short streaks**	**1.27**

Table 2-8 (Cont.)

				3b	Mosaicism	Long streaks beginning to show asterism
				3c	Mosaicism and PDFs	Asterism
D	Partial isotropism, irregular fracturing and undulose extinction	Clear steaks (similar to C)	2.54	3.14	4	PDFs, mosaicsim, diaplectic glass	Clear streaks
E	Diaplectic glass (fully isotropic)	No streaks			5	Diaplectic glass	Amorphous, no streaks
					6	Melting	

µXRD strain-related mosaicity analyses in this study demonstrate that grains within a single target rock are not all exposed to the same shock pressure during impact. Previous studies have shown variability in shock pressure up to 10 GPa between grains within the same sample as a result of grain size, composition, crystallographic orientation, water affects and surrounding matrix composition (Dence, 2004; Jaret et al., 2018; Robertson & Grieve, 1977).

An interesting phenomenon in the µXRD-generated GADDS images are the doublets, which are two spots separated by a particular chi angle within the same chi ring, while also commonly repeating with similar angles in other chi rings directly correlating to albite twinning in plagioclase (Figs. 2-9- A, B, C, D). Doublets are also visible in Figure 2B in Pickersgill et al. (2015a). For future work, it may be of interest to analyze how the angle in chi relates to the optical appearance of the Carlesbad twins in plagioclase feldspar to definitively determine their impact on effective shock experienced in varying environments.

This study strongly supports the effectiveness of µXRD as a tool for future extra-terrestrial research, especially *in situ* analysis for use in discerning shocked material's minerology and resolving crystal plastic deformation in a non-destructive way. The

combination of μXRD data with microscopic petrography is more quantitative than using optical data alone. FWHMχ measurements of strain-related mosaic spread separates shock levels into more definitive subdivisions, which eliminates some (but not all) bias that may arise from the same optical shock effects that often appear indistinguishable over a broad range of shock pressures, particularly where shock features are masked or precluded by alteration. While the promising results from this study bolster the usefulness of feldspar for determining shock level in basaltic impact lithologies, it is important to note that strain-related mosaicity cannot be used to differentiate impact-shock-related strain from endogenic-strain, without further study.

2.5.3 Effect of shock on Density and Porosity of Basalt

The effects of shock on density and porosity in basaltic compositions have not been studied in detail before; however, prior qualitative and quantitative studies of the effects of hypervelocity impacts on the target material's bulk physical properties suggests that shock metamorphism in crystalline rocks will result in an increased porosity and decreased density (Cockell et al., 2002; Pontefract et al., 2012, 2014; Singleton et al., 2011). We hypothesized that shocked basalts from Vargeão Dome and Vista Alegre craters will behave similarly to other crystalline lithologies. Using a variety of methods, the bulk density, grain density, and porosity measurements of these samples were collected and plotted against their assigned shock levels to evaluate the correlation between the degree of shock and the bulk physical properties (Table 2-7 and Fig. 2-14). As hypothesized, a strong nonlinear correlation was found between shock level and porosity in basaltic target rocks, in which increased shock level appears to result in greater porosity. The increase in porosity appears to produce a decrease in bulk and grain density which overall is an effect of the hypervelocity impact shock waves producing impact-induced microfractures. Prior to steadily decreasing with increased shock levels, the densities slightly increased. The initial increase from the unshocked to lightly shocked samples is unexpected and may due to a variety of factors. First, due to the small sample size of Vista Alegre basalts, there may be a lot of variation in the target rocks before the impact that hasn't been captured. Secondly, the unshocked samples collected far outside the crater are extremely vesiculated and hydrothermally altered. Although

these samples may have been more vesiculated than the ones inside the crater were originally, even at moderate shock levels (e.g., M- S3), impact basalts are below or within the normal porosity range of basaltic rocks (Fig. 2-14). This suggests the basalts within the crater may have also been highly vesiculated prior to the impact event, and the shock caused the collapse of vesicles and the decrease in porosity. Lastly, the alteration of impact-damaged rocks (e.g., fractures, faults, brecciation, and replacement of mineral by secondary hydrothermal products) results in the lowered bulk and grain densities, which subsequently reduces the porosity of the samples (e.g., Collins, 2013; Collins et al., 2004, 2005; Furukawa et al., 2011; Pirajno, 2009). Highly shocked samples appear more hydrothermally altered, expressing increased partial and complete transformation of plagioclase and pyroxene minerals into low density clay minerals. The greatest overlap in density and porosity measurements occurs in moderately shocked samples which may be owed to the small sample size. Additional sample collection is required for the full picture.

The collection of the bulk physical properties through measurement of the porosity and density of the target rock not only aids in the geophysical interpretation and modelling of impact structures, but also has strong implications for understanding the astrobiological potential of impact craters and their ability to host life. Previous studies by Cockell et al. (2002) and Pontefract et al. (2014) concluded that an impact into a target rock that increases the porosity of the affected material also increases the translucency via selective vaporization of opaque minerals phases. The research further concluded that these altered lithologies are more suitable for hosting endolithic photosynthetic microorganisms than were the local unshocked rock of the same type (Cockell et al., 2002; Cockell & Osinski, 2007; Fike et al., 2003; Pontefract et al. 2014). Similar trends are expected for Vargeão Dome and Vista Alegre basalts.

2.5.4   Conclusions

In conclusion, this research has verified the effectiveness of classifying the shock level of impact basalts using a combination of optical microscopy and µXRD analysis. Comparative analysis of optical shock effects (Singleton, 2019; Stoffler et al., 2018), FWHMχ measurements and GADDS images of plagioclase feldspar grains (Pickersgill et

al., 2015a) quantitively determine the degree of shock experienced by feldspar in the target basalt. In addition, this study illustrates the effects of shock on the bulk physical characteristics of basaltic rock. With increasing shock level, both bulk and grain density decrease and porosity increases. With increased porosity, the probability for microbial colonization increases. These results support the growing evidence suggesting that basaltic impact craters could serve as viable habitable environments not only here on Earth, but also on other planets such as Mars and beyond.

2.6   References

Bandfield, J. L., Hamilton, V. E., & Christensen, P. (2000). A global view of Martian surface compositions from MGS-TES. *Science*, *287*(5458), 1626–1630.

Battler, M. M., Clarke, J. D. A., & Coniglio, M. (2006). Possible analog sedimentary and diagenetic features for Meridiani Planum sediments near Hanskville, Utah: implications for Martian Field studies. In J. D. A. Clarke (Ed.), *Mars Analog Research* (pp. 55–70). American Astronautical Society Science and Technology Series 111.

Bramble, M. S., Flemming, R. L., & McCausland, P. J. A. (2015). Grain size measurement from two-dimensional micro-X-ray diffraction: Laboratory application of a radial integration technique. *American Mineralogist*, *100*(8-9), 1899–1911.

Cao, F., Jaret, S. J., Flemming, R. L., Izawa, M. R. M., & Johnson, J. R. (2020). *Micro X-ray diffraction characteristics of experimentally shocked andesine anorthosite: implications for quantifying shock effects in meteorites* [abstract #2114]. 51st Lunar and Plantary Space Conference, Woodlands, TX.

Chan, M. A., Beitler, B., Parry, W. T., Ornö, J., & Komatsu, G. (2004). A possible terrestrial analogue for haematite concretions on Mars. *Nature*, *429*, 731–734.

Chao, E. C. T. (1968). Pressure and temperature histories of impact metamorphosed rocks based on petrographic observations. In B. M. French B. & N. M. Short (Eds.), *Shock metamorphism of natural materials* (pp. 135-158). Mono Book Corporation.

Clarke, J. D. A. & Stoker, C. R. (2011). Concretions in exhumed channels near Hanksville Utah: implications for Mars. *International Journal of Astrobiology*, *10*(3), 161–175.

Cockell, C. S., Lee, P., Osinski, G. R., Horneck, G., & Broady, P. (2002). Impact-induced microbial endolithic habitats. *Meteoritics & Planetary Science, 37*(10), 1287–1298.

Cockell, C. S. & Osinski, G.R. (2007). Impact-induced impoverishment and transformation of a sandstone habitat for lithophytic microorganisms. *Meteoritics & Planetary Science, 42*(11), 1985– 1993.

Collins, G. S. (2013, March 18-22). *Numerical simulations of complex crater formation with dilatancy: Implications for gravity anomalies of lunar and terrestrial craters* [abstract # 2917]. 44th Lunar and Planetary Science Conference, Woodlands, TX.

Collins, G. S., Melosh, H. J., & Ivanov, B. A. (2004). Modeling damage and deformation in impact simulations. *Meteoritics & Planetary Science*, *39*(2), 217-231.

Collins, G. S., Melosh, H. J., & Marcus, R. A. (2005). Earth impact effects program: A web-based computer program for calculating the regional environmental consequences of a meteoroid impact on Earth. *Meteoritics & planetary science*, *40*(6), 817-840.

Consolmagno, G. J., & Britt, D. T. (1998). The density and porosity of meteorites from the Vatican Collection. *Meteoritics & Planetary Science*, *33*, 1231–1241.

Consolmagno, G. J., Britt, D. T., & Macke, R. J. (2008). The significance of meteorite density and porosity. *Chemie der Erde, 68*(1), 1–29.

Crósta, A. P. (1987). Impact structures in Brazil. In P. J. Wiesbaden (Ed.), *Research in terrestrial impact structures* (pp. 30-38). Friedrich Vieweg & Sohn.

Crósta, A. P., Kazuo-Vieira, C., Pittarello, L., Koeberl, C., & Kenkmann, T. (2011). Geology and impact features of Vargeão Dome, Southern Brazil. *Meteoritics & Planetary Science*, *48*(3), 1–21.

Crósta, A. P., Koeberl, C., Furuie, R. A., & Kazzuo-Vieira, C. (2010). The first description and confirmation of the Vista Alegre impact structure in the Paraná flood basalts of southern Brazil. *Meteoritics & Planetary Science*, *45*(2), 181–194.

Deer, W. A., Howie, R. A., & Zussman, J. (1992). *An introduction to the rock forming minerals* (2nd ed.). Addison Wesley Longman, Harlow, UK.

Edey, D. R., Pollmann, S.I. Lorusso, D., Drangova, M., Flemming, R. L., & Holdsworth, D. W. (2019). Extending the dynamic range of biomedical micro-computed tomography for application to geomaterials. *Journal of X-Ray Science and Technology*, *27*(5), 919–934.

Feldman, V., Sazonova, L. V., Mironov, Y. V. & Kapustkina, I. G. (1983, March 16-17). *Circular structure Logancha as possible meteorite crater in basalts of the Tunguska Syneclise* [abstract]. 14th Lunar and Plantary Science Conference, Houston, TX.

Ferriere, L., & Osinski, G. R. (2013). Shock metamorphism. In G. R. Osinski & E. Pierazzo (Eds.), *Impact cratering: Processes and products* (pp. 316). Oxford: Wiley-Blackwell.

Fike, D. A., Cockell, C. S., Pearce, D., & Lee, P. (2003). Heterotrophic microbial colonization of the interior of impact-shocked rocks from Haughton impact structure, Devon Island, Nunavut, Canadian High Arctic. *International Journal of Astrobiology*, *1*(4), 311–323.

Flemming, R. L. (2007). Micro X-ray diffraction (µXRD): A versatile technique for characterization of Earth and planetary materials. *Canadian Journal of Earth Sciences, 44*(9), 1333–1346.

French, B. M. (1998). *Traces of catastrophe: A handbook of shock-metamorphic effects in terrestrial meteorite impact structures* [LPI Contribution # 954]. Lunar and Planetary Institute, Houston, TX.

French, B., & Koeberl, C. (2010). The convincing identification of terrestrial meteortie impact structures: What works, what doesn't, and why. *Earth-Science Reviews*, *98*(1-2), 123– 170.

French, B. M., & Short, N. M. (Eds.). (1968). *Shock metamorphism of natural materials.* Mono Book Corporation, Baltimore, Maryland.

Fritz, J., Greshake, A., & Stöffler, D. (2003, March 17-21). *Launch conditios for Martian meteorites: Plagioclase as a shock pressure barometer* [abstract #1335]. 34th Lunar and Planetary Science Conference, League City, TX.

Fritz, J., Greshake, A., & Stöffler, D. (2005). Micro-Raman spectroscopy of plagioclase and maskelynite in Martian meteorites: Evidence of progressive shock metamorphism. *Antarctic Meteorite Research, 18*, 96–116.

Furukawa, Y., Sekine, T., Kakegawa, T., & Nakazawa, H. (2011). Impact-induced phyllosilicate formation from olivine and water. *Geochimica et Cosmochimica Acta*, *75*(21), 6461-6472.

Gibson, R. L., & Reimold, W. U. (2005). Shock pressure distribution in the Vredefort impact structure, South Africa. In T. Kenkmann, F. Hörz, and A. Deutsch (Eds.), *Large Meteorite Impacts III*. Geological Society of America.

Grieve, R. A. F., & Cintala, M. J. (1992). An analysis of differential impact melt-crater scaling and implications for the terrestrial impact record. *Meteoritics, 27*(5), 526–538.

Grieve, R. A. F., & Therriault, A. M. (2004). Observations at terrestrial impact structures: Their utility in constraining crater formation. *Meteoritics, 39*(2), 199–216.

Grieve, R. A., & Therriault, A. M. (2012). Impactites: Their Characteristics and Spatial Distribution. In G. R. Osinski & E. Pierazzo (Eds.), *Impact Cratering* (pp. 90–105). Wiley-Blackwell, Chichester.

Hamouda, S. A., Abdelmalik, M. B., & Al-Talhi, E. A. (2014). Porosity Measurements for Some Basalt Rocks from the Gharyan Volcanic Province NW Libya. *Earth Sciences, 3*(1), 26.

Harrison, A. D., Whale, T. F., Carpenter, M. A., Holden, M. A., Neve, L., O'Sullivan, D., Vergara Temprado, J., & Murray, B. J. (2016). Not all feldspars are equal: a survey of ice nucleating properties across the feldspar group of minerals. *Atmospheric Chemistry and Phys*ics, *16*, 10927–10940.

Heymann, D., & Hörz, F. (1990). Raman-spectroscopy and Xray diffractometer studies of experimentally produced diaplectic feldspar glass. *Physics and Chemistry of Minerals, 17*, 38–44.

Hörz, F., & Quaide, W. L. (1973). Debye-Scherrer investigations of experimentally shocked silicates. *The Moon*, *6*(1-2), 45–82.

Izawa, M. R. M., Banerjee, N. R., Osinski, G. R., Flemming, R. L., Parnell, J. & Cockell, C. S. (2011). Weathering of post-impact hydrothermal deposits from the Haughton Impact Structure: implications for microbial colonization and biosignature preservation. *Astrobiology*, *11*(6), 537–550.

Izawa, M. R. M., Flemming, R. L., Banerjee, N. R., & McCausland, P. J. A. (2011). Micro-X-ray diffraction assessment of shock stage in enstatite chondrites. *Meteoritics & Planetary Science*, *46*(5), 638–651.

Jaret, S. (2017). *Changes in Mineralogy and Geochemistry of Quartz and Feldspars in Response to Impact Cratering* (Publication No. 2) [Doctoral thesis, Stony Brook University]. Geosciences Research Data.

Jaret, S. J., Johnson, J. R., Sims, M., DiFrancesco, N., & Glotch, T. D. (2018). Microspectroscopic and petrographic comparison of experimentally shocked albite, andesine, and bytownite. *Journal of Geophysical Research: Planets*, *123*(7), 1701–1722.

Jaret, S. J., Kah, L. C., & Harris, R. S. (2014). Progressive deformation of feldspar recording low barometry impact processes, Tenoumer impact structure, Mauritania. *Meteoritics & Planetary Science*, *49*(6), 1007–1022.

Jenkins, E. J., Flemming, R. L., & McCausland, P. J. A. (2019). Quantitative in situ XRD measurement of shock metamorphism in Martian meteorites using lattice strain and strain-related mosaicity in olivine. *Meteoritics & Planetary Science*, *54*(4), 290-310.

Johnson, J. R. (2007, January 13-17). *Thermal infrared emissivity spectra of experimentally shocked andesine* [abstract #3258]. 7th International Conference on Mars, Ushuaia, Tierra del Fuego, Argentina.

Johnson, J. R., Hörz, F., Lucey, P. G., & Christensen, P. R. (2002). Thermal infrared spectroscopy of experimentally shocked anorthosite and pyroxenite: Implications for remote sensing of Mars. *Journal of Geophysical Research*, *107*, 50–73.

Johnson, J. R., Hörz, F., & Staid, M. I. (2003). Thermal € infrared spectroscopy and modeling of experimentally shocked plagioclase feldspars. *American Mineralogist*, *88*, 1575–1582.

Kazzuo-Vieira, C. (2009). *Caracterizacão geológica e geofisica da estrutura de impacto Domo de Vargeão, SC* [Master's dissertation, University of Campinas]. Repositório da Produção Cientifica e Intelectual da Unicamp.

Kieffer, S. W., & Schaal, R. B. (1976). *Shocked basalt from Lonar impact crater, India, and experimental analogues*. 7th Lunar and Plantary Science Conference, Houston, TX.

Langenhorst, F., Stöffler, D., & Klein, D. (1991, March). *Shock metamorphism of the Zagami achondrite* [abstract]. 22nd Lunar and Planetary Science Conference, Houston, TX.

Mantovani, M. S. M., Stewart, K., Turner, S., & Hawkesworth, C. J. (1995). Duration of Parana´ magmatism and implications for the evolution and source regions of continental flood basalts. *Anais da Academia Brasileira de Cie ˆncias, 67*, 163–169.

Maxwell, T. A., & El-Baz, F. (1982). *Analogs of Martian eolian features in the western desert of Egypt* [paper presentation, pp. 247-259]. Symposium on Planetary Surfaces and Atmospheres, Innsbruck, Austria.

McCausland, P. J. A., Brown, P. G., & Holdsworth, D. W. (2010b, March). *Rapid, reliable acquisition of meteorite volumes and internal features by laboratory X-ray micro-CT scanning* [abstract #2584]. 41st Lunar and Planetary Science Conference, Woodlands, TX.

McCausland, P. J. A., Flemming, R. L., & Izawa, M. R. M. (2010a, December 13-17). *Quantitative shock stage assessment in olivine and pyroxene bearing meteorites via in situ microXRD* [abstract #P14C-03]. American Geophysical Union Fall Meeting, San Francisco, California.

McCausland, P. J. A., Samson, C., & McLeod, T. (2011). Determination of bulk density for small meteorite fragments via visible light 3-D laser imaging. *Meteoritics & Planetary Science, 46*(8), 1097–1109.

McNally, H. H., & Wilson, I. R. (1995). Silcretes of the Mirackina paleochannel, Arckaringa, South Austraia. *AGSO Journal of Australian Geology and Geophysics*, *16*(3), 295–301.

Mcsween, H. Y. (1994). What we have learned about Mars from SNC meteorites. *Meteoritics*, *29*, 757–779.

Mcsween, H. Y. (2002). The rocks of Mars, from far and near. *Meteoritics & Planetary Science, 37*(1), 7–25.

Melanson, D., Samson, C., Herd, R. K., Fry, C., McCausland, P. J. A., Umoh, J., & Holdsworth, D. W. (2012, March). *X-ray micro computed tomography imaging of the Buzzard Coulee chondrite* [abstract #1506]. 43rd Lunar and Planetary Science Conference, Woodlands, TX.

Melosh, H. J. (1989). *Impact cratering: A geologic process*. New York: Oxford University Press

Melosh, H. J., & Ivanov, B. A. (1999). Impact crater collapse. *Annual Review of Earth and Planetary Sciences, 27*(1), 385–415.

Milani, E. J., Melo, J. H. G., Souza, P. A., Fernandes, L. A., & Franca, A. B. (2007). Bacia do Paraná. *Boletim de Geocieˆncias da Petrobras, 15*(2), 265–287.

Nèdèlec, A., Paquette, J. L., Yokoyama, E., Trindade, R. I. F., Aigouy, T., & Baratoux, D. (2013). In situ U/Pb dating of impact-produced zircons from the Vargeão Dome (Southern Brazil). *Meteoritics & Planetary Science, 48*(3), 420–431.

Osinski, G. R., & Pierazzo, E. (2013). *In Impact Cratering: Processes and Products*. Oxford, Blackwell Publishing.

Peate, D. W. (1997). The Paraná -Etendeka Province. In J. Mahoney, and M. Coffin (Eds.), *Large igneous provinces: Continental, oceanic, and planetary flood volcanism* (pp. 217-245). American Geophysical Union Geophysical Monograph.

Pickersgill, A. E., Flemming, R. L., & Osinski, G. R. (2015a). Toward quantification of strain-related mosaicity in shocked lunar and terrestrial plagioclase by in situ micro-X-ray diffraction. *Meteoritics & Planetary Science*, *50*(11), 1851–1862.

Pickersgill, A. E., Osinski, G. R., & Flemming, R. L. (2015b). Shock effects in plagioclase feldspar from the Mistastin Lake impact structure, Canada. *Meteoritics & Planetary Science, 50*(9), 1546–1561.

Pinto, V., Hartmann, L. A., & Wildner, W. (2011). Epigenetic hydrothermal origin of native copper and supergene enrichment in the Vista Alegre district, Paraná basaltic province, southernmost Brazil. *International Geology Review*, *53*(10), 1163–1179.

Pirajno, F. (2009). *Hydrothermal processes and mineral systems*. Springer.

Pittarello, L., Nestola, F., Viti, C., Crósta, A. P. & Koeberl, C. (2015). Melting and cataclastic features in shatter cones in basalt from the Vista Alegre impact structure, Brazil. *Meteoritics & Planetary Science,* 50(7), 1228–1243.

Pontefract, A., Osinski, G. R., Cockell, C. S., Moore, C. A., Moores, J. E., & Southam, G. (2014). Impact-generated endolithic habitat within crystalline rocks of the Haughton impact structure, Devon Island, Canada. *Astrobiology*, *14*(6), 522–533.

Renne, P., Ernesto, M., Pacca, I. G., Coe, R. S., Glen, J. M., Pre´ vot, M., & Perrin, M. (1992). The age of Parana´ flood volcanism, rifting of Gondwanaland, and the Jurassic Cretaceous boundary. *Science*, *258*(5084), 975–979.

Reynard, B., Okuno, M., Shimada, Y., Syono, Y., & Willaime, C. (1999). A Raman spectroscopic study of shock-wave densification of anorthite (CaAl2Si2O8) glass. *Physics and Chemistry of Minerals, 26*(6), 432–436.

Rochette, P., Alac, R., Beck, P., Brocard, G., Cavosie, A. J., Debaille, V., Devouard, B., Jourdan, F., Mougel, B., Moustard, F., Moynier, F., Nomade, S., Osinski, G. R., Reynard, B., & Cornec, J. (2019). Pantasma: Evidence for a Pleistocene circa 14 km diameter impact crater in Nicaragua. *Meteoritics & Planetary Science, 54*(4).

Schaal, R. B., & Hörz, F. (1977, March 14-18). Shock metamorphism of lunar and terrestrial basalts [abstract]. 8th Lunar Science Conference, Houston, TX.

Sims, M., Jaret, S. J., Carl, E., Rhymer, B., Schrodt, N., Mohrholz, V., Smith, J., Konopkova, Z., Liermann, H.-P., Glotch, T. D., & Ehm, L. (2019). Pressure-induced amorphization in plagioclase feldspars: A time-resolved powder diffraction study during rapid compression. *Earth and Planetary Science Letters, 507*, 166–174.

Singleton, A. (2019). *Characteristics of Impactites in the Central Uplift of the Mistastin Lake Impact Structure, Canada* (Publication no. 6476) [Doctoral dissertation, University of Western Ontario]. Electronic Thesis and Dissertation Repository

Singleton, A. C., Osinski, G. R., McCausland, P. J. A., & Moser, D. E. (2011). Shock-induced changes in density and porosity in shock-metamorphosed crystalline rocks, Haughton impact structure, Canada. *Meteoritics & Planetary Science, 46*(11), 1774–1786.

Stewart, K., Turner, S., Kelly, S., Hawkesworth, C., Kirstein, L., & Mantovani, M. (1996). 3-D, 40Ar—39Ar geochronology of the Parana´ continental flood basalt province. *Earth and Planetary Science Letters*, *143*(1-4), 95–109.

Stöffler, D. (1971). Progressive metamorphism and classification of shocked and brecciated crystalline rocks at impact craters. *Journal of Geophysical Research*, *76*, 5541–5551.

Stöffler, D., Bischoff, L., Oskierski, W., & Wiest, B. (1998). Structural deformation, breccia formation, and shock metamorphism in the basement of complex terrestrial impact craters: Implications for the cratering process. In A. Bodén, & K. G. Eriksson (Eds.), *Deep-drilling in crystalline bedrock* (pp. 277-297). New York: Springer- Verlag.

Stöffler, D. & Grieve, R.A.F. (2007). Impactites. In D. Fettes, & J. Desmons (Eds.), *Metamorphic Rocks* (pp. 82-92). Cambridge University Press.

Stöffler, D., Hamann, C., & Metzler, K. (2018). Shock metamorphism of planetary silicate rocks and sediments: Proposal for an updated classification system. *Meteoritics & Planetary Science*, *53*, 5– 49.

Therriault, A. M., Grieve, R. A. F., & Pilkington, M. (2002). The recognition of terrestrial impact structures. *Czech Geological Survey, 77*(4), 253–263.

Turner, S., Regelous, M., Kelley, S., Hawkesworth, K., & Mantovani, M. S. M. (1994). Magmatism and continental break-up in the South Atlantic: High precision 40Ar-39Ar geochronology. *Earth and Planetary Science Letters*, *121*(3-4), 333–348.

Uchizono, A., Shinno, I., Nakamuta, Y., Nakamura, T., & Sekine, T. (1999). Characterization of Artificially Shocked forsterites: (1) Diffraction Profile Analysis by Gandolfi Camera. *Mineralogical Journal*, *21*(1), 15–23.

Vasconcelos, M. A. R., Crósta, A. P., & Molina., E. C. (2010). Geophysical characteristics of four possible impact structures in the Parnaiba Basin, Brazil: Comparison and implications. *Geological Society of American Special Papers, 465*, 201–217.

Velde, B., & Boyer, H. (1985). Raman microprobe spectra of naturally shocked microcline feldspars. *Journal of Geophysical Research*, *90*(B5), 3675–3682.

Velde, B., Syono, Y., Kikuchi, M., & Boyer, H. (1989). Raman microprobe study of synthetic diaplectic plagioclase feldspars. *Physics and Chemistry of Minerals, 16*, 436–441.

Vinet, N., Flemming, R.L., & Higgins, M.D. (2011). Crystal structure, mosaicity and strain analysis of Hawaiian olivines using *in situ* X-ray diffraction. *American Mineralogist*, *96*(4), 486–497.

Von Engelhardt, W., & Stoffler, D. (1968). Stages of shock € metamorphism in crystalline rocks of the Ries Basin, Germany. In B. M., French, and N. M. Short (Eds.), *Shock metamorphism of natural materials* (pp. 159-168). Baltimore, Maryland: Mono Book Corporation.

Wittke, W., & Sykes, R. (1990). *Rock mechanics*. Springer Berlin.

Xie, T., Osinski, G. R., & Shieh, S. R. (2020). Raman study of shock features in plagioclase feldspar from the Mistastin Lake impact structure, Canada. *Meteoritics & Planetary Science*, *55*(7), 1471-1490.

Xie, T., Shieh, S. R., & Osinski, G. R. (2017). *Raman study of shock effects in lunar anorthite from the Apollo missions* [abstract #1596]. 48th Lunar and Planetary Science Conference, Woodlands, TX.

Yin, F., & Dai, D. (2020). A study of shock-metamorphism features of feldspars from the Xiuyan impact crater. *Minerals, 10*(3), 231.

Yokoyama, E., Nèdèlec, A., Baratoux, D., Trindade, R. I. F., Fabre, S., & Berger, G. (2015). Hydrothermal alteration in basalts from Vargeão impact structure, south Brazil, and implication for recognition of impact-induced hydrothermalism on Mars. *Icarus*, *252*, 347–365.

Chapter 3

3 Post-Impact Hydrothermal Alteration of Shocked Basalts from Vista Alegre Impact, Brazil

3.1 Introduction

The hypervelocity impact of an extraterrestrial projectile (e.g., comet, asteroid) into the surface of a solid planetary body is a common and fundamental geological process in our solar system. Any impact into a water-bearing target may result in an active, transient, hydrothermal system (Kirsimae & Osinski, 2012; Osinski et al., 2013), the extent and intensity of which depends on the size of the crater, the lithology and intrinsic properties of the target rock (porosity, permeability), and composition of volatiles (liquid water or ice) (French & Koeberl, 2010; Naumov, 2002; Naumov, 2005; Osinski et al., 2013; Osinski & Pierazzo, 2012; Utada, 2001b). The interaction between heated rocks and H_2O fluids results in the precipitation of new minerals (e.g., carbonates, Mg-clays, Al-clays, zeolites, quartz and Fe-oxides), chemical alteration of pre-existing ones, and the occurrence of fluid inclusions, all of which are accepted as valid indicators of present or past, post-impact hydrothermal activity (Kieffer & Simonds, 1980; Naumov, 2005; Norton, 1984; Osinski et al., 2001; Osinski and Pierazzo, 2012; Utada, 2001b). Through mineralogical, geochemical, fluid inclusion, and stable isotope data, impact-induced hydrothermal alteration has been found to be associated with over seventy impact structures on Earth (Naumov, 2005; Osinski et al., 2013). There are currently no active hydrothermal systems associated with impacts on Earth, so our understanding of these systems is based on the preserved hydrothermal alteration products and textures.

The Mars Reconnaissance Orbiter (MRO) and the Mars Express spacecraft have revealed evidence of hydrated silicates and sulfates associated with large impact craters on Mars (e.g., Bibring et al., 2005, 2006; Ehlmann & Edwards, 2014; Ehlmann et al., 2009; Murchie et al., 2009; Poulet et al., 2007; Squyres et al., 2014). Silicates and sulfates are primary minerals generated during the hydrothermal phase in terrestrial impact structures, and similar processes have been suggested for impact craters on Mars as well (e.g., Allen

et al., 1982; Ehlmann et al., 2011; Ehlmann et al., 2013; Marzo et al., 2010; Michalski et al., 2015; Newson, 1980; Osinski et al., 2013; Sun & Milliken, 2015; Tornabene et al., 2013).

Over the last years, there has been an increased interest in hydrothermal systems associated with impact craters on both Earth and Mars, as exemplified by the current Mars missions at Gale Crater, explored by the Mars Science Laboratory Curiosity rover (Grotzinger et al., 2012), and Jezero Crater, investigated by NASA's 2020 Perseverance rover (Goudge et al., 2018). Impact-induced hydrothermal systems have been proposed to offer habitable environments for the origin and evolution of life on Earth (e.g., Baross & Hoffman, 1985; Damer & Deamer, 2015, 2020; Deamer et al., 2019; Martin et al., 2008; Russell et al., 2013), as well as provide excellent targets for future, *in situ* life detection missions on Mars (e.g., Farmer, 2000; Osinski et al., 2013, 2020). From a biological perspective, the greatest benefit of impact craters and their associated hydrothermal systems is the extension of habitable conditions beyond that of pre-impact. For example, shock metamorphism significantly increases the porosity and permeability of crystalline target rocks, creating new habitats for endolithic (rock-dwelling) microorganisms in what were previously uninhabitable environments (Cockell et al., 2005; Singleton et al., 2011). The increased surface area of the shocked lithologies and substrates are more susceptible to alteration, and can favorably interact with water providing access to nutrients and energy (e.g., Cockell & Lee, 2002; Cockell & Osinski, 2007; Cockell et al., 2009; Osinski et al., 2020). The effects of impacts on Mars are essentially the same as on Earth (Osinski et al., 2020), implying that shocked substrates can provide suitable conditions for the emergence of life by offering energy, nutrients and refugia, as well as protection against the harsh Martian environment (e.g., temperature shifts, low water availability, UV radiation [Cockell et al., 2002; Omelon, 2008; Walker & Pace, 2007]).

It is important to note that despite their astrobiological potential, until recently, impact-generated hydrothermal systems have been understudied from the biological perspective. The majority of existing studies that have looked at microbial activity in hydrothermally altered impact structures on Earth have focused strictly on isotopic signatures (Parnell et al., 2010; Simpson et al., 2017) and microfossil evidence (Glamoclija, 2007; Glamoclija

et al., 2007; Hode et al., 2008; Ivarsson et al., 2013; Lindgren et al., 2010; Sapers et al., 2015) in crystalline and mixed lithology target rocks.

3.1.1 Hydrothermally Altered Basaltic Impact Structures

Although common on extraterrestrial planets and their satellites, impact craters situated entirely in basaltic target rock are rare on Earth, presenting few opportunities to use them as analogues to study Martian impact craters. The six impact structures on Earth that formed in basaltic lithologies are: Lonar crater in India (1.8 km in diameter, Kieffer et al. 1976), Longancha impact structure in East Siberia, Russia (14 km in diameter, Masaitis 1999), Vargeão Dome and Vista Alegre impact structures in Brazil (12 km and 9.5 km in diameter respectively, Crósta et al. 2009, 2012a), as well as the recently confirmed Cerro do Jarau impact structure in Brazil (13.5 km in diameter, Reimold et al., 2019) and the newly discovered Pantasma impact structure in Nicaragua (14 km in diameter, Rochette et al., 2019). The latter two basaltic impact structures were only recently added to the list, and therefore have not been considered for this study. Longancha impact structure is located in only partially basaltic, mixed lithology target rock, and to-date has been poorly studied due to the structure's difficult accessibility (Feldman et al., 1983; Masaitis, 1999). Lonar crater in India was the first discovered impact crater formed entirely in basaltic rock (Fredriksson, 1973). Evidence for hydrothermal alteration at Lonar has suggested that even the smallest 1–2 km craters can generate a short-lived hydrothermal system (Hagerty & Newsom, 2003). However, the hydrothermal alteration at Lonar crater is largely caused by meteoritic water supplied by abundant rain- or snowfall which does not compare favourably with the current Martian conditions (Hagerty & Newsom, 2003). Additionally, any hydrothermal activity at Lonar, if it did occur, would have been very short lived and therefore not a great analogue for Mars (Hagerty & Newsom, 2003). In comparison to Lonar crater, Vargeão Dome and Vista Alegre impact structures are larger in diameter, and as opposed to Longacha crater, these impacts took place entirely in basaltic lithology (Crósta et al., 2010). Vargeão Dome and Vista Alegre are currently the best candidates for analogue systems of Martian hydrothermally altered impact structures.

Both impacts took place within 100 km of each other in the volcanic-sedimentary Paraná Basin of Brazil (Crósta et al., 2004, 2010; Yokoyama et al., 2015). The Paraná Basin was formed as a result of intense volcanism of the paleocontinent dated to ~134 Ma. Thick basaltic flow of the Serra Geral Formation overlayed the thin eolian deposits of the Jurassic sandstone Formation under an arid climate (Scherer, 2000; Yokoyama et al., 2015). Below the Paraná volcanic pile, in the deeper levels of sandstone lies the Mercosul aquifer system, also called the Guarani aquifer, which acts as a major fluid reservoir for hydrothermal activity (Yokoyama et al., 2015). Despite their similarities in size and lithology, hydrothermal alteration has only been studied at the Vargeão Dome impact structure (Yokoyama et al., 2015), but not at Vista Alegre.

Yokoyama et al. (2015) proposed that a transient hydrothermal system was triggered by the Vargeão impact event but has since ceased, leaving behind the weathered minerals and eroded supergene environment that is present today. During the dry climate conditions (lack of or very minor precipitation) under which the crater formed, the Guarani aquifer is believed to have been the source of fluid for the Vargeão Dome hydrothermal system (Yokoyama et al., 2015). Evidence for post-impact hydrothermal activity within shocked Vargeão Dome breccias appears different than most large impact-induced hydrothermal systems that are fed primarily by meteoritic water, where secondary mineral precipitation is limited to the breccia veins, and largely concentrated in the inner collar surrounding the central depression of the crater (Yokoyama et al., 2015). Additionally, based on evidence of amygdales composed of amorphous silica, zeolite, and calcite in the unshocked basaltic samples outside the impact structure, Yokoyama et al. (2015) suggest that the Paraná Basin basalts experienced alteration before the impact event. Previous investigations of the regional alteration processes also revealed petrographic features associated with secondary clays and zeolites infilling vesicles, which are commonly associated with hydrothermal alteration events or low-grade metamorphism processes in substrate with abundant degassing features, such as amygdales and vesicles (Schenato et al., 2003).

Pinto et al. (2011) touched upon hydrothermal alteration with respect to epigenetic hydrothermal copper mineralization, but alteration features in Vista Alegre target basalts

and breccias have otherwise received little attention. The Vista Alegre impact structure is a well preserved, 9.5 km in diameter, circular structure centered at 52º 41'S and 25º 57'W, southern Brazil. The structure's location within the Serra Geral Formation originally placed its origin after ~125 Ma (Crósta et al., 2010a), and subsequent $^{40}Ar/^{39}Ar$ dating of impact glass provided an age of 115 ± 4 Ma (Crósta et al., 2012). The target lithology is composed of tholeiitic basalts from the lower unit of the Cretaceous Serra Geral Formation and Mesozoic eolian sandstones from the Piramboia/Botucatu Formations. Vista Alegre's basaltic lithology, relatively dry climate conditions during crater formation, as well as the large brackish aquifer acting as a source of hydrothermal fluid, compares favourably to Mars' dry surface conditions and presence of subsurface water. Therefore, the Vista Alegre impact structure serves as an excellent analogue environment for studying impact-related hydrothermal systems on Mars. The aim of this research is to identify the mineralogical and morphological characteristics of major hydrothermal phases in the available Vista Alegre basaltic samples, and to determine if the alteration was the result of impact-induced hydrothermal activity. A better understanding of terrestrial basaltic hydrothermally altered impact craters may aid in the interpretation of impact-associated phyllosilicate regions on Mars. In addition, the astrobiological potential of hydrothermal systems has significant implications for habitability and potential for life on Mars.

3.2   Methods

Ten target basalt and polymict breccia rock samples were selected for this study, eight from inside the Vista Alegre impact structure, and two from outside of it. The two samples from outside of the crater (VA-2017-5, 5C) were collected 46.67 km NE (65°) of the structure and are representative of the unshocked basement basalts of the Paraná Basin volcanic field (Fig. 2-1). Of the eight shocked samples from within the crater (Fig. 3-1), five samples (one target rock basalt and four polymict impact breccias) were collected near the village (labelled as location VA1), at a small abandoned quarry that is known for its abundance of polymict breccias (Crósta et al., 2010). The remaining three shocked samples consist of two polymict impact breccias from the inner rim of the crater (VA-2017-3, 3B) and one target rock basalt from the outer rim of the crater (VA-2017-2).

Chapter 2 presents a detailed petrographic and geochemical description and shock metamorphism classification of the rock samples.

Polished thin sections were analyzed using a combination of optical petrography, Electron Probe Microanalysis (EPMA), and *in situ* Micro-X-ray Diffraction (µXRD) to characterize alteration mineral assemblages and replacement textures. Some offcut slabs were also analyzed by µXRD.
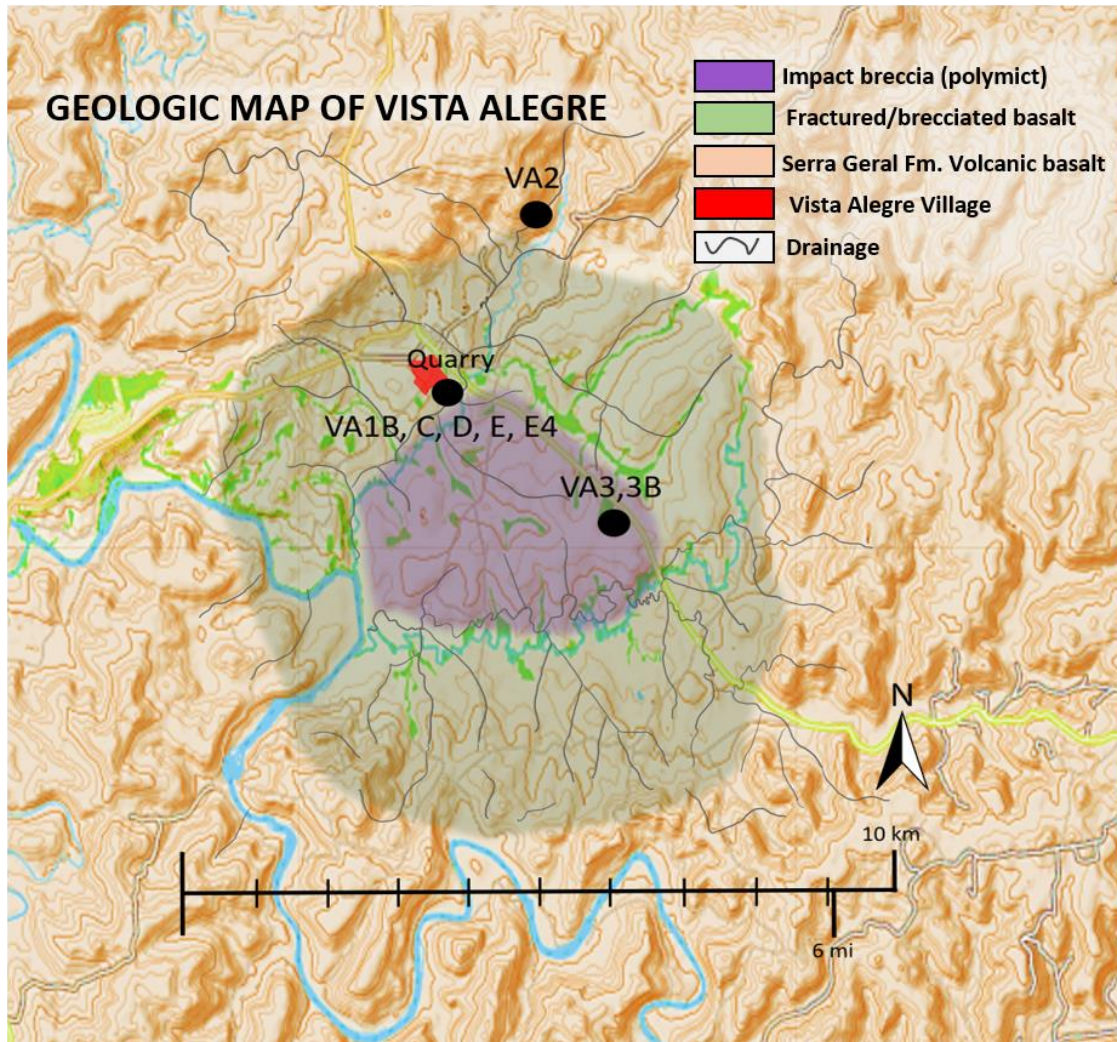
Figure 3-1. Geological map of Vista Alegre impact structure with sample location points, excluding the two unshocked basalt samples (VA-5C, VA-5) from outside the crater. Map is modified from Crósta et al. (2010).

3.2.1   Optical Mineralogy and Petrography

Mineralogical and petrological data was obtained using a Nikon Eclipse LV 100POL Microscope in the High-Resolution Earth and Planetary Materials Imaging and Analysis Laboratory at Western University. Photomicrographs were taken using a Nikon Digital Sight DS-Ri 1 high-resolution digital camera under transmitted light using both plane-polarized and cross-polarized light filters. All thin sections were investigated for hydrothermal alteration features. Features of interest include secondary phases (e.g., carbonates, Fe-Mg clays, Al-clays, zeolites, quartz and Fe-oxides), alteration textures (replacement textures, ubiquitous alteration pockets, alteration of impact glass, and multiple generations of carbonate growth), veining and the occurrences of fluid inclusions (Naumov, 2005).

3.2.2   Wavelength Dispersive X-ray Spectroscopy (WDS) Analysis

Polished thin sections were carbon coated and analyzed using a JEOL-JXA-850F Field Emission Electron Probe Microanalyzer in the Earth and Planetary Materials Analysis Laboratory (EPMA Lab). Primary quantitative measurements were collected using Wavelength Dispersive X-ray Spectroscopy (WDS). The microscope was operated at 15 kV accelerating voltage, 20 nA beam current, with a magnification and spot size of ~5 μm. The following clay and zeolite standards were used to characterize the samples: Si, Mg - Enstatite (Harvard 131709); Al, Na - Albite (Amelia County, VA, USA); Ca - Diopside (Smithsonian USNM 117733 - Natural Bridge, NY, USA); Fe - Hematite (Harvard 92649); K - Orthoclase (C.M. Taylor); Cl - Sodalite (Geller MicroAnalytical); Ti - Rutile (unknown); P - Apatite (Astimex, Wilberforce, ON, Canada); S - Anhydrite (Astimex, Lyon Co., NV, USA); Mn - Rhodonite (Astimex, unknown locality); Cr – Chromite (Smithsonian USNM 117075 - Tiebaghi Mine, New Caledonia); F – Fluorite (Astimex, synthetic Harshaw Chemical Corp, USA); Si, Al, Na - Albite (Amelia County, VA, USA); Ca, Mg - Diopside (Smithsonian USNM 117733 - Natural Bridge, NY, USA); Fe - Hematite (Harvard 92649); and K - Orthoclase (C.M. Taylor). More than 350 quantitative WDS spot analyses were collected, helping to identify minerals previously characterized optically. BSE imagery was used to investigate the geochemical

characteristics, micro-textures of hydrothermal secondary minerals and their petrographic relationship to the surrounding minerals.

3.2.3   Micro-X-Ray Diffraction (µXRD)

Accurate analysis of clays remains a formidable challenge in petrology as a result of their fine particle size and chemical and structural variability (Środoń, 2002). When compared to the more common powder X-ray diffraction method, µXRD is less frequently employed for clay minerals due to the difficulty of analyzing the very low 2θ angles (below 10–15° 2θ) that are characteristic of clay diffraction peaks. To circumvent this limitation, a non-standard procedure (Flemming, unpublished), using the Bruker D8 Discover micro-diffractometer in the Department of Earth Sciences at the University of Western Ontario was performed to achieve clay and zeolite mineral analysis at angles as low as 6° 2θ, which is lower than the traditional µXRD scans ranges. The low angle ($θ_1$) of the detector that is required to obtain the 2θ angular range of clay diffraction peaks necessitates that clay and zeolite sample points be selected within one centimeter of the edges of the thin section when analyzed. The diffractometer was operated with a Cobalt anode source (CoKα radiation, λ=1.7889 Å) and an accelerating voltage of 35 kV with a 45 mA beam current. The instrument was equipped with a Göbel mirror parallel optics system and a 300 µm pinhole collimator, yielding a nominal beam diameter of 300 µm. Diffracted X-rays were detected *in situ* with a Vantec-500 two-dimensional area detector using General Area Diffraction Detection System (GADDS) software. The θ-θ geometry of the diffractometer enabled the source and detector to rotate independently (omega scan mode) while the sample remained horizontal and stationary. Target positions were selected using a microscope and laser system to position the samples via a movable XYZ stage. Images show the nominal 300 µm-diameter spot size analyzed (red circle) (Fig. 3-2 C). The specific parameters used for clays and zeolites in this experiment employed a two-frame coupled scan, where one frame was collected with $θ_1 = 6°$, $θ_2 = 21.5°$ and the second with $θ_1 = 11°$, $θ_2 = 27.5°$ (i.e. width=10°). The data acquisition time for each frame was 60 minutes. The two GADDS frames were combined and integrated to generate a conventional intensity versus 2θ diffraction pattern (Flemming, 2007). The processed diffraction patterns were preliminarily compared to d-spacings and their associated

intensities of well characterized clay (Brindley & Brown, 1980) and zeolite (Treacy & Higgins, 2001) minerals, and further best-matched to International Centre for Diffraction Data (ICDD) cards of different minerals using the Bruker AXS EVA software package and the ICDD PDF-4 Database. In addition to the identification of mineral components in clay and zeolite assemblages, X-ray diffraction patterns and the resulting GADDS images enable the recognition of textural and microstructural information such as interstratification of clay layers (Fig. 3-2 B) (Ali-Ani, 2008; Brindley & Brown, 1980; Sapers et al., 2017). Interstratified clay layers (also referred to as mixed-layering, interlayering or turbostratic layering) such as smectite-illite and smectite-chlorite mixed-layered minerals, are a common characteristic of hydrothermal environments (e.g., Uusinoka, 1975). Disordered structures can also show this lineshape such as disordered kaolinite shown in Figure 3-2 A.
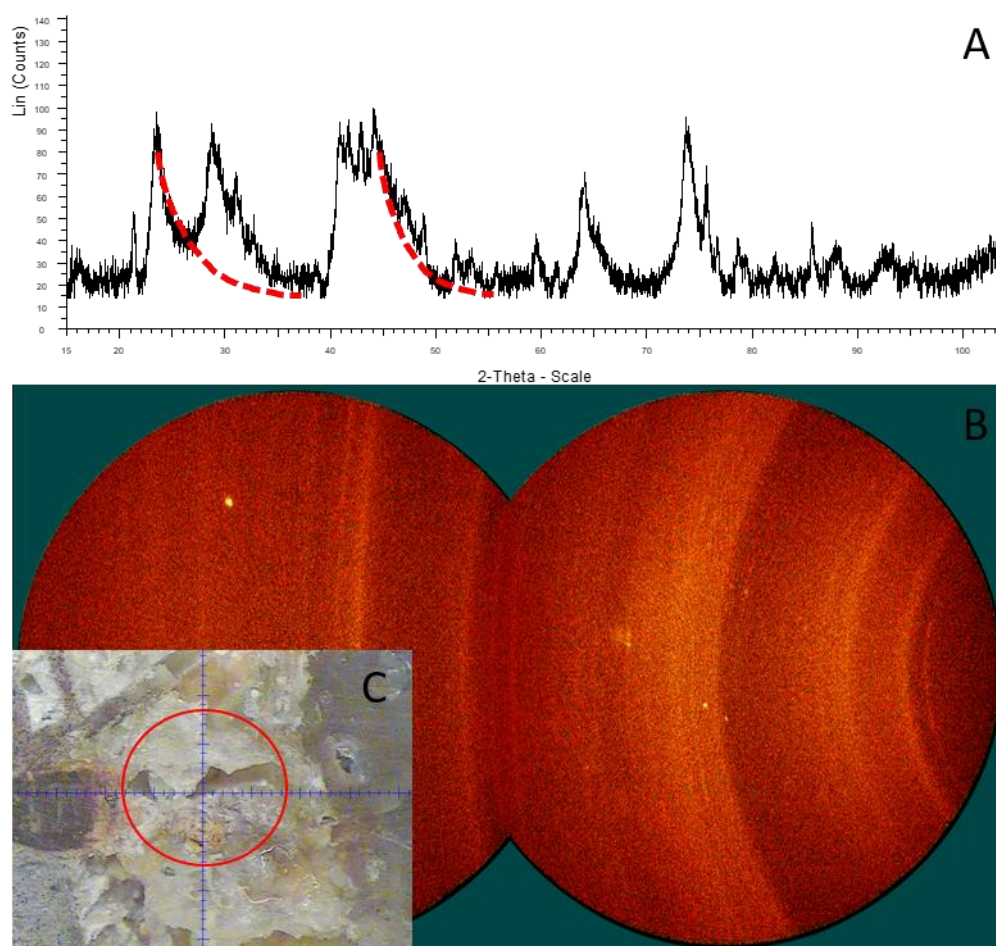
Figure 3-2. Example of turbostratic stacking features in sample VG-2017-16, spot 1. A) X-ray diffraction pattern exhibiting asymmetrical reflection peaks showing a peak with intensity tailing off at higher angle. Note that this analysis was completed following a standard µXRD procedure as opposed to the low angle mineral analysis method. Despite the lack of low angle mineral analysis, turbostratic layering is seen between 22-35° 2θ and between 40-50° 2θ. B) GADDS image displays faint, broad rings that are characteristic of interlayering of fine-grained clay minerals. C) Context image taken with the µXRD instrument of the spot analyzed. 300 µm-diameter spot size analyzed represented with red circle. Field of View= 2 mm.

µXRD analyses were completed on some of the same spots analyzed with WDS, and mineral matches were made independently of WDS to ensure there was no bias during the phase identification process. The two datasets were checked for agreement later.

3.3 Results

Macroscopic evidence of hydrothermal processes in the whole rock samples was limited to calcite/quartz- infilled fractures and cross-cutting veins (Fig. 3-3 A). In thin section analyses, all of the samples displayed some degree of alteration, such as replacement textures, veining, and secondary phases. A list of Vista Alegre samples and rock type, location and coordinates, whole rock description, and thin-section hydrothermal alteration features are presented in Table 3-1.

Table 3-1. **Summary of the Vista Alegre sample set with location information, whole rock descriptions, and hydrothermal alteration features in thin sections.**

Sample Name	Rock Type	Location coordinates (°Lat, °Long)	Whole Rock Description	Hydrothermal Alteration Features in Thin Section
VA-2017-1B	Shocked Polymict Breccia	Quarry (-25.56007, -52.42021)	Poorly sorted breccia with angular to sub-rounded clasts of basalt (light), glassy fragments (dark) and calcite mineral fragments (white) in a strongly altered brownish-grey clastic matrix. Some glassy fragments contain small, irregular feldspar microlites.	Fe/Mg-clay rims around calcite within melt clasts, clays infilling vesicles within glass, radiating zeolite textures, and dissolution texture in pyroxene.

Table 3-1 (Cont.)

VA-2017-1C	Shocked Polymict Breccia	Quarry (-25.56007, -52.42021)	Poorly sorted breccia with rounded lithic rock fragments (light), large glassy fragments (dark) and calcite mineral fragments (white) in a brownish-grey clastic matrix.	Fibrous yellow/brown clays, clays infilling open voids within glass, and dissolution texture in pyroxene and weak plagioclase diaplectic glass (maskelynite).
VA-2017-1D	Shocked Polymict Breccia	Quarry (-25.56007, -52.42021)	Poorly sorted breccia with sub-rounded lithic rock fragments (light) and small glassy fragments (dark) in a brownish clastic matrix.	Multiple generation of calcite and zeolites partially replacing plagioclase crystals.
VA-2017-1E	Shocked Polymict Breccia	Quarry (-25.56007, -52.42021)	Poorly sorted breccia with angular to sub-rounded lithic rock fragments (light) and glassy fragments (dark) in a brownish clastic matrix. Some glassy fragments contain small, irregular feldspar microlites.	Clays infilling open fractures and voids in glass fragments and clays and zeolites replacing minerals.
VA-2017-1E4	Shocked Target Basalt	Quarry (-25.56007, -52.42021)	Fine-grained brownish/grey basalt with evidence of shatter cones.	Red/black veins, fine-grained clays replacing matrix, clays completely replacing pre-existing clasts, and clay lining glass vein.
VA-2017-2	Shocked Target Basalt	Outer crater rim (-25.90248, -52.90248)	Aphanitic black lava basalt with brown weathering on exposed surface.	White spherulitic calcite-filled vein lined with clays and overlaying other minerals and fine-grained, green/brown clays with zeolite rim.
VA-2017-3	Shocked Polymict Breccia	Outer crater rim (-25.95152, -52.6699)	Contact btw poorly sorted brown polymict breccia and target basalt. Breccia composed of sub-angular lithic rock fragments (light) and tiny glassy fragments (black).	Red/black vein networks, yellow/brown fine-grained clays, and plagioclase dissolution.
VA-2017-3B	Shocked Polymict Breccia	Outer crater rim (-25.95152, -52.6699)	Contact btw poorly sorted light brown polymict breccia and target basalt. Breccia composed of rounded to sub-angular lithic rock fragments (light), glassy fragments (black) and calcite mineral fragments (white/clear).	White, zeolite-filled veins, red/black veins within breccia basalt fragments, and dissolution of calcite and partial replacement of plagioclase by zeolite.
VA-2017-5	Unshocked Basalt	Outside crater (-25.77362, -52.26885)	Aphanitic black lava basalt with large white vesicles up to 6 mm in size.	Calcite, quartz and various other minerals-filled vesicles cross-cutting calcite and quartz-filled veins, multiple generations of clay rims, and radiating zeolite spherules.
VA-2017-5C	Unshocked Basalt	Outside crater (-25.77362, -52.26885)	Aphanitic dark brown lava basalt.	White veins filled with calcite, clays lining veins, and complete replacement of minerals by clays and zeolites.

3.3.1 Optical Petrography, EPMA and µXRD Results of Alteration Features in <u>Unshocked Target Basalts</u>

There are two unshocked samples obtained from far outside of the impact structure; VA-2017-5 is a dark cryptocrystalline ("glasslike") target basalt, composed of ~10 vol% plagioclase in a groundmass locally replaced by clays, and VA-2017-5C is an aphanitic to fine-phaneritic, dark brown basalt composed of plagioclase, pyroxene and Fe-Ti oxides locally replaced by phyllosilicates and/or zeolites.
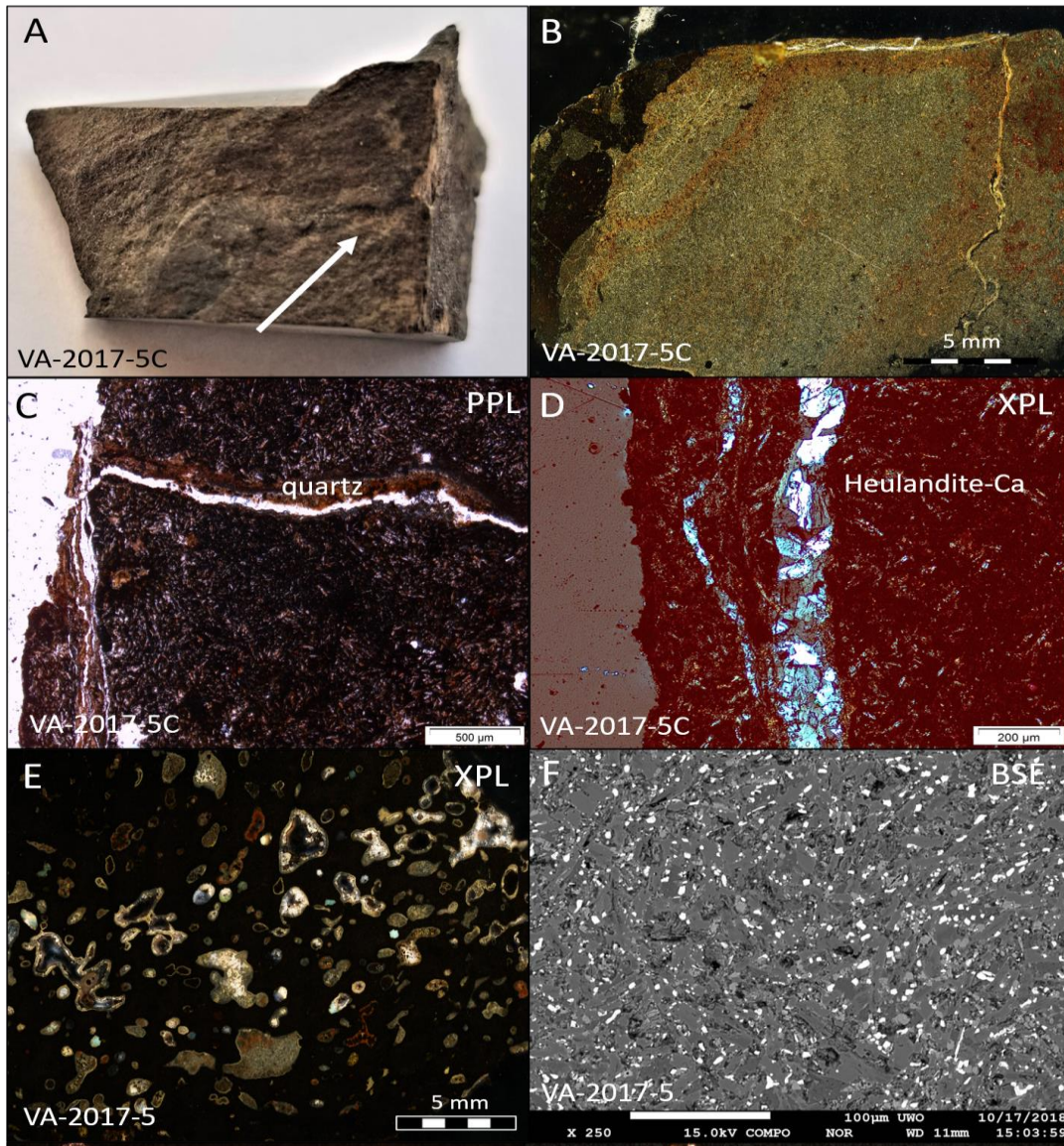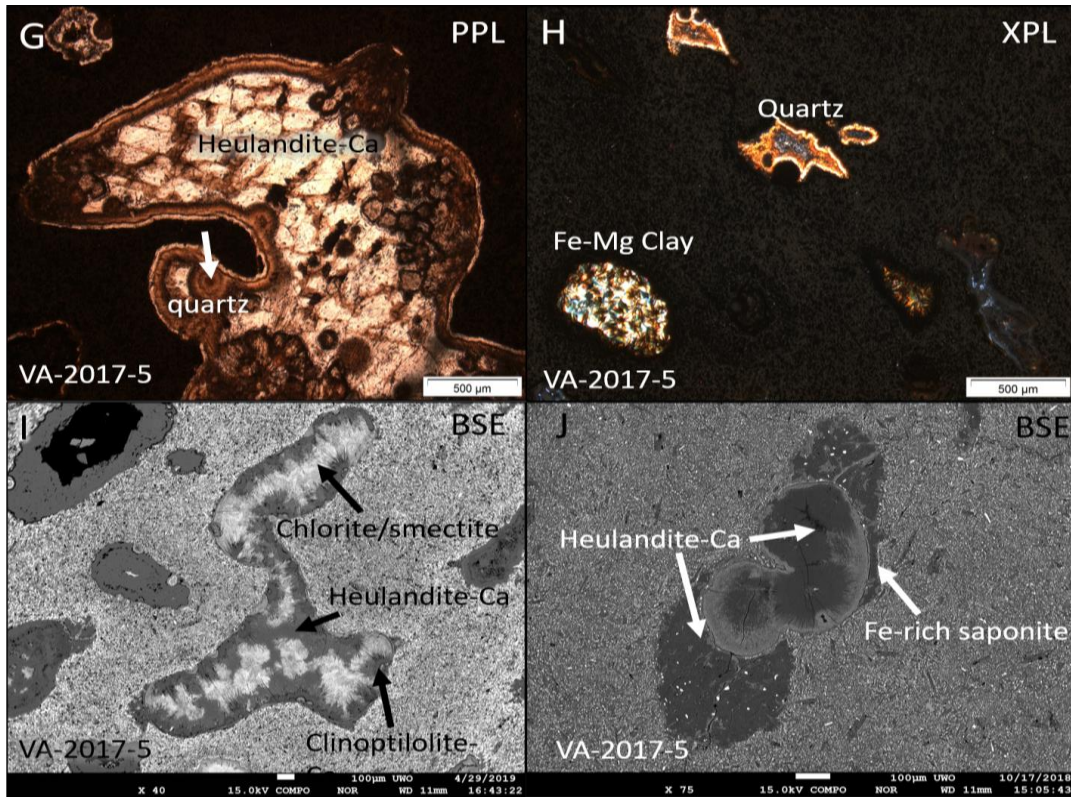
Figure 3-3. Secondary alteration features and textures in unshocked target basalt samples VA-2017-5 and VA-2017-5C, outside of the Vista Alegre impact structure. A) Macroscopic white veins and fractures (white arrow). B) Microscopic white veins. C) Hydrothermal quartz lining a fracture. D) ~200 μm thick zeolite vein and sub-μm veinlet composed of platy heulandite-Ca. E) Distribution and size of vesicles. F) Matrix displaying plagioclase laths, iron-oxides (white), and an overgrowth of clays (smectites). G) Chabazite-Ca filled vesicle with botryoidal habit structures and a quartz followed by Ca-rich zeolite rims. Note the multiple generations of quartz rims indicated by white arrow. H) Fe-Mg clay and quartz pockets within a dark, glassy polycrystalline matrix. Fe-Mg clay pocket exhibit high birefringence and fibrous texture and quartz pocket displays multiple generations of quartz, one filling the pocket and one lining it. I) Irregularly shaped vesicle containing clays and zeolites. The clay (chlorite/smectite mix) is light coloured forming needle-like spherules in the centre of the vesicle and the zeolite is darker and forms fan-shaped, needle-like structures radiating from the inside wall of the vesicle. The zeolite needles are longer than the clay needles and overlap them. J) Vesicle containing radiating heulandite-Ca zeolites in a fan-like spherule surrounded by Fe-rich saponite clay. The vesicle overlays a heulandite-Ca zeolite assemblage.

The unshocked samples display evidence of alteration textures (amygdales, veins, and primary mineral replacement) and secondary phases (C-S mixed clays, Fe-saponite, heulandite-Ca, and clinoptilolite-Ca). Sample VA-2017-5 has an abundance of irregular amygdules ranging from 0.2–3.5 mm in size (Fig. 3-3 E). Based on WDS analyses, the larger sized vesicles are most often infilled by heulandite-Ca zeolite (Fig. 3-3 G). In some cases, acicular crystals composed of clinoptilolite-Ca form as fibrous radiating prisms and display a fan-shape forming inwards of the vesicle, with the roots against the inside wall of the vesicle (Fig. 3-3 I). XRD data further confirmed the infilling material of the large amygdales. The smaller vesicles are infilled by clays and quartz, but exact mineral species were not identified. Additionally, both VA-2017-5 and VA-2017-5C samples contain sub-mm sized white veins. Veining in the samples is displayed in the form of heulandite-Ca filled white veins forming in a platy/blocky texture (Fig. 3-3 D).

Secondary quartz is fairly abundant in both the unshocked samples and is recognized by the lack of shock metamorphism features in comparison to shocked quartz (Fig. 3-3). In sample VA-2017-5, secondary quartz is found infilling smaller vesicles (Fig. 3-3 H) and surrounding larger amygdales and vesicles (Fig. 3-3 G). Single or double rims of quartz, ranging from 50–200 μm in thickness, are uniformly deposited during period of fluid flow, suggesting multiple generations of hydrothermal quartz growth. In sample VA-2017-5C, secondary quartz precipitates along fractures (Fig. 3-3 C).

Clays in the sample set appear brown to brownish-green with compositional and μXRD data compatible with chlorite-smectite mixed clays and Fe-rich saponites. Clays are found either completely infilling vesicles (Fig. 3-3 H) or as fine prismatic crystals radiating inwards of the vesicle wall (Figs. 3-3 I, J). Additionally, in both unshocked samples, components of the mesostatic groundmass in VA-2017-5, and the basaltic groundmass in VA-2017-5C are often replaced with smectite clays and clinoptilolite-Ca zeolites (Fig. 3-3 F). EPMA- WDS data representative of the clays, zeolites and quartz seen in the unshocked basalt samples are provided in Table 3-2.

Table 3-2. Electron microprobe compositional analysis of representative clays and zeolites in unshocked basaltic samples outside Vista Alegre impact structure.

Mineral type	C-S mix clay	C-S mix clay	C-S mix clay	Fe-saponite	Heulandite-Ca	Heulandite-Ca	Heulandite-Ca	Clinoptilolite-Ca	Clinoptilolite-Ca
Sample & spot #	VA-2017-5 spot 5 99	VA-2017-5 spot 7-89	VA-2017-5 spot 5-100	VA-2017-5C spot1-94	VA-2017-5 spot 6- 82	VA-2017-5 Spot 1-75	VA-2017-5C spot 2-50	VA-2017-5 Spot 2-80	VA-2017-5C spot 3- 56
Description	Coarse-grained, fibrous lining a clast	Bladed, infilling vesicle	Coarse-grained, fibrous and vesicle filling	Fine grained, fibrous, fracture lining	Fine-grained, vesicle filling	Vesicle infilling	Platy, vein filling	Needle-like vesicle lining	Fine-grained, matrix filling
SiO_2	35.869	32.742	29.071	33.085	59.188	56.222	58.903	65.884	66.028
Al_2O_3	9.891	12.496	13.147	10.28	17.295	17.071	16.021	13.283	12.657
Na_2O	0.172	0.085	0.047	0.092	0.533	0.434	0.110	0.748	0.559
MgO	13.397	10.617	13.079	15.744	0.005	0	0.447	0.079	0.092
CaO	2.140	0.915	0.402	1.757	8.537	8.213	6.832	4.337	4.661
K_2O	0.147	0.073	0.024	0.069	0.095	0.197	0.852	0.098	0.255
FeO	20.963	26.084	28.456	20.189	nd	0.015	0.551	0.625	0.935
Total	82.579	83.012	84.226	82.394	85.653	82.051	83.716	85.085	85.187
Cations									
SiO_2	6.659	6.220	5.574	6.210	8.952	8.881	9.107	9.797	9.840
Al_2O_3	2.164	2.798	2.971	2.274	3.083	3.179	2.920	2.328	2.223
Na_2O	0.062	0.031	0.018	0.033	0.157	0.133	0.033	0.216	0.161
MgO	3.708	3.007	3.738	4.405	0.001	0	0.103	0.017	0.021
CaO	0.426	0.186	0.083	0.353	1.384	1.390	1.132	0.691	0.744
K_2O	0.035	0.018	0.006	0.016	0.018	0.040	0.168	0.019	0.048
FeO	3.255	4.144	4.563	3.169	0	0.002	0.071	0.078	0.117
Total	16.307	16.405	16.952	16.759	13.594	13.581	13.534	13.145	13.154

3.3.2 Optical Petrography, EPMA and µXRD Results of Alteration Features in Shocked Target Rocks and Breccia Samples

There are two basalt target rocks out of the total eight shocked samples collected within the Vista Alegre impact structure. These include sample VA-2017-1E4 from the quarry and sample VA-2017-2 from the outer rim of the impact structure. VA-2017-1E4 is a brownish-grey basalt exhibiting macroscopic evidence of shatter cones and VA-2017-2 is a heavily altered, black porphyritic basalt, both shocked to level S3 (Chapter 2). The shock-metamorphosed basalts are composed of euhedral to subhedral crystals emplaced in a red to black, to grey, fine-grained matrix of plagioclase, pyroxene, Fe-Ti oxides and

glass derived from basalt (Fig. 3-4 J). Grains are made up of ~55% plagioclase (mainly labradorite), ~30% clinopyroxene (augite and pigeonite) and 10–15% opaque minerals (ulvöspinel, hematite and magnetite), and these phases are often replaced by alteration minerals which will be discussed below.

The six polymict breccias are composed of poorly sorted clasts of variably shocked basaltic lithic rock fragments (plagioclase, pyroxene and quartz), minor amounts of sandstone, impact melt fragments, and calcite crystals. The shock features exhibited in the basaltic plagioclase, pyroxene and quartz minerals include irregular and planar fractures, undulatory extinction, mosaicism, planar deformation features and feather features (Posnov et al., 2019; Chapter 2). The matrix is an altered, fine-grained clastic groundmass composed of plagioclase, pyroxene, calcite, melt droplets, and secondary alteration clays and zeolites.

Textural evidence of hydrothermal alteration identified in the shocked target basalt and polymict impact breccia samples from within the Vista Alegre impact structure include: replacement of primary basaltic minerals (e.g., plagioclase, pyroxene and olivine), ubiquitous infilling of fractures and open-void spaces, lining of vesicles, alteration of impact glasses, and several vein-like structures, all associated with secondary hydrothermal minerals saponite, glauconite, chlorite-smectite mixed clays, heulandite-Ca, calcite, and quartz (Fig. 3-4). The width of the alteration veins is no more than a few millimeters thick and they do not occur in any preferential orientations. Red/black and white veins in target basalts and breccias crosscut the original basaltic matrix (Figs. 3-4 B, D, E) and impact breccia clasts (Fig. 3-4 A). The composition of the red/black veins appear to be varying amounts of sub-angular to sub-rounded altered plagioclase, pyroxene, phyllosilicates, zeolites, quartz, and basaltic lithic fragments in a fine-grained, red to black matrix (Figs. 3-4 B, C). The white veins are filled with secondary zeolites and calcite (Figs. 3-4 D, E).

Panel A: VA-2017-3

Panel B: VA-2017-3

Panel C (XPL): VA-2017-1E4 — scale bar 500 µm

Panel D (BSE): VA-2017-3B — X 110, 15.0kV COMPO, NOR, WD 11mm, 16:29:44, 100µm UWO

Panel E (BSE): VA-2017-1B — Fe-rich saponite, calcite, Zeolite-Ca, Chabazite-Ca — X 140, 15.0kV COMPO, NOR, WD 11mm, 12:18:09, 100µm UWO, 10/24/2018

Panel F (PPL): VA-2017-2 — saponite, glauconite — scale bar 500 µm

Panel G (XPL): VA-2017-1D — Calcite, Calcite — scale bar 500 µm

Panel H (BSE): VA-2017-1B — X 350, 15.0kV COMPO, NOR, WD 11mm, 12:00:58, 10µm UWO, 10/24/2018

Panel I (BSE): VA-2017-3 — X 40, 15.0kV COMPO, NOR, WD 11mm, 09:17:54, 100µm UWO, 10/25/2018

Panel J (BSE): VA-2017-3B — X 40, 15.0kV COMPO, NOR, WD 11mm, 10:11:20, 100µm UWO, 3/28/2019

Panel K (BSE): VA-2017-1B — olv, zeo — X 180, 15.0kV COMPO, NOR, WD 11mm, 11:32:11, 100µm UWO, 10/24/2018

Panel L (BSE): VA-2017-3B — Clinoptilolite-Ca, mordenite, quartz, zeo, plag, Fe-Mg Clay, zeo-Ca — X 220, 15.0kV COMPO, NOR, WD 11mm, 16:37:53, 100µm UWO, 10/24/2018

Figure 3-4. Hydrothermal alteration features and textures in shocked Vista Alegre basalts and polymict breccias. A) Red/black veins within a basaltic breccia clast in whole rock sample (white arrow). B) Network of red/black veins in a clastic basalt matrix. C) Fine-grained clasts within the dark crystalline matrix of the red/black veins. D) A ~100 μm thick grey vein that is bent and kinked and filled with platy zeolites. E) A ~50 μm thick grey calcite vein with Ca-rich zeolite blocks around the edges, all cross-cutting an assemblage of clays and zeolites including Fe-rich saponite ("blotchy", light), chabazite-Ca (rimming, dark) and illite-montmorillonite (outermost dark rim). F) Clay pockets filled with orange saponite clay and lined with brown/green glauconite clay. Clay pockets are in a dark matrix with plagioclase laths appearing white. G) Two generations of calcite, where the first generation calcite is weathered and has pervasive cleavage and two large fractures, whereas the second generation calcite has higher birefringence colours (high order white), and less cleavage and no fractures. H) Dissolution of pyroxene clast (red arrow) and replacement by clays. I) Dissolution (red arrow) where plagioclase was replaced by zeolite. J) Glass with flow features and clay alteration. Note botryoidal clay features. K) Fine-grained zeolite which has almost entirely replaced olivine (light). L) Platy zeolite (chabazite-Ca composition) replacing a plagioclase lath. Irregularly-textured Fe-Mg clay (light), Ca-zeolite (dark), and quartz are also present. Note clays always precede zeolites.

Petrographic analyses reveal that the most commonly observed alteration minerals in breccias (in order of most abundant to least) are Fe-Mg clays, carbonates, zeolites, and quartz. Wavelength Dispersive X-ray Spectroscopy (WDS) data identified that the main secondary phases have a composition compatible with carbonates (calcite), Fe-Mg clays (mixed-layer clay chlorite/smectite, Fe-rich saponite, Fe-rich glauconite and Fe-rich celadonite), Al-clays (montmorillonite and illite-mont mixed clay) and zeolites (heulandite-Ca, chabazite-Ca, mordenite and analcime). WDS analyses of representative hydrothermal clays and zeolites are presented in Tables 3-3 and 3-4. Geochemical trends are differentiated by clay and zeolite group types as shown in the ternary diagram in Figure 3-5.

Table 3-3. Electron microprobe compositional analysis of representative clays of shocked target basalt and breccias from Vista Alegre impact structure. Mineral compositions confirmed using Deer et al. (2013), Kousehlar et al. (2012), and Roberts et al. (1990).

Clay type	C-S mix clay	Fe-rich saponite	Fe-rich glauconite	Fe-saponite	Fe-saponite	Ferrosaponite	Fe-glauconite	Fe-rich celadonite	Fe-rich celadonite	Mnt	Illite-Mnt	Illite	C-S mix clay	C-S mix clay	C-S mix clay	C-S mix clay	C-S mix clay	C-S mix clay	C-S mix clay
Sample	VA-1E4	VA-1E4	VA-2	VA-1B	VA-1C	VA-3B	VA-1E	VA-1D	VA-1B	VA-1E	VA-1E	VA-1D	VA-1C	VA-1C	VA-1D	VA-1D	VA-3B	VA-1D	VA-1B
Spot #	1-49	2-50	1- 23	3-38	1-02	3-65	3-31	3-131	1a-32	3-30	3-32	2 -128	2-111	4-116	5-136	7-139	2-59	3-132	9-123
Rock type	Target basalt	Target basalt	Target basalt	Polymict breccia	Polymict breccia	Polymict breccia	Polymict breccia	Polymict breccia	Polymict breccia	Polymict breccia	Polymict breccia	Polymict breccia	Polymict breccia	Polymict breccia	Polymict breccia	Polymict breccia	Polymict breccia	Polymict breccia	Polymict breccia
Description	Replacing a mineral			Fibrous, associated with calcite	Coarse-grained, fibrous	Blocky, mineral replacing	Fine-grained, void filling			Fine-grained, mineral lining			Fine-grained, void filling	Fine-grained, fibrous	Coarse-grained, fibrous	Glass replacing	Coarse-grained fibrous	Fine-grained lining	Fine-grained fibrous
SiO_2	39.568	35.401	52.714	34.441	32.504	36.484	47.791	47.991	49.441	57.608	55.304	50.360	41.262	31.287	27.332	26.576	36.399	40.800	37.971
Al_2O_3	12.052	10.520	8.758	10.231	12.243	11.054	10.140	3.524	4.093	13.024	16.655	14.590	9.986	12.674	12.797	6.218	10.353	8.182	8.330
Na_2O	1.829	0.089	0.124	0.116	0.041	0.309	0.097	0.046	0.071	0.113	3.600	1.225	0.497	0.220	0.032	0.386	0.237	0.110	0.184
MgO	12.187	15.697	3.966	14.348	17.126	7.883	6.163	8.374	6.392	3.085	3.120	4.021	13.023	13.607	13.147	6.041	9.787	11.185	10.062
CaO	1.709	1.805	0.830	1.781	0.380	2.316	0.252	0.981	0.365	3.433	0.324	1.623	1.693	1.161	0.661	2.242	0.386	2.392	1.816
K_2O	0.078	0.079	5.870	0.034	0.066	0.479	5.976	6.523	8.694	4.354	6.734	7.749	0.500	0.373	0.011	0.028	1.310	0.773	0.673
FeO	16.213	18.963	18.565	20.550	22.890	28.781	11.882	20.284	18.771	5.775	8.172	8.922	19.597	24.302	29.390	15.341	24.448	20.533	22.030
Total	83.735	82.848	91.112	81.973	85.250	87.580	82.301	88.909	88.186	87.392	93.909	89.105	86.936	84.050	83.660	58.002	83.590	84.238	81.066
Cations																			
SiO_2	6.988	6.491	8.589	6.457	5.918	6.637	8.384	6.852	8.613	8.964	8.313	8.133	7.122	5.881	5.357	7.076	6.803	7.343	7.196
Al_2O_3	2.509	2.274	1.682	2.261	2.628	2.370	2.097	1.711	0.804	2.389	2.951	2.778	2.032	2.808	2.957	1.951	2.281	1.736	1.861
Na_2O	0.626	0.032	0.039	0.042	0.015	0.109	0.033	0.045	0.024	0.034	1.049	0.384	0.167	0.080	0.012	0.199	0.086	0.038	0.068
MgO	3.209	4.291	0.963	4.010	4.648	2.137	1.612	2.750	1.660	0.716	0.699	0.968	3.351	3.813	3.841	2.397	2.727	2.001	2.842
CaO	0.323	0.355	0.145	0.358	0.074	0.451	0.048	0.848	0.068	0.572	0.052	0.281	0.313	0.234	0.139	0.640	0.077	0.461	0.369
K_2O	0.018	0.018	1.220	0.008	0.015	0.111	1.337	0.048	1.932	0.864	1.291	1.597	0.110	0.090	0.003	0.010	0.312	0.177	0.163
FeO	2.395	2.908	2.530	3.222	3.485	4.378	1.743	3.973	2.735	0.752	1.027	1.205	2.829	3.821	4.818	3.416	3.821	3.091	3.492
Total	16.076	16.457	15.273	16.446	16.783	16.217	15.253	16.323	15.951	14.291	15.382	15.447	15.980	16.810	17.178	16.002	16.237	15.889	15.989

Table 3-4. Electron microprobe compositional analysis of representative zeolites of shocked target basalt and breccias from Vista Alegre impact structure. Mineral compositions confirmed using Deer et al. (2013), Inoue & Minato (1978), and Roberts et al. (1990).

Zeolite type	Heulandite-Ca	Chabazite-Ca	Stilbite-Ca	Analcime	Mordenite	Heulandite-Ca
Sample	VA-2017-3B	VA-2017-3B	VA-2017-1E	VA-2017-1C	VA-2017-3B	VA-2017-1E4
Spot #	6 -41	4 -44	1-06	3-10	1-55	2-17
Rock type	Polymict breccia	Polymict breccia	Polymict breccia	Polymict breccia	Polymict breccia	Target basalt
Description	Platy, vein filling	Blocky/plated	Platy/blocky rim	Platy texture	"fuzzy" rim	Blocky, infilling vein
SiO_2	58.178	53.779	60.920	67.401	64.756	55.181
Al_2O_3	16.727	20.718	14.873	20.661	12.022	18.091
Na_2O	0.618	0.134	0.176	11.013	0.962	0.226
MgO	0.001	0.008	0.189	0.024	0.857	1.117
CaO	8.250	10.921	7.064	0.162	2.628	7.050
K_2O	0.109	0.688	0.469	0.663	2.059	1.470
FeO	0.128	0.137	0.147	0.455	5.261	0.226
Total	84.011	86.385	83.838	91.835	88.805	83.401
Cations						
SiO_2	8.977	8.243	9.334	8.839	9.597	8.659
Al_2O_3	3.042	3.743	2.686	3.194	2.100	3.346
Na_2O	0.185	0.040	0.052	2.800	0.277	0.069
MgO	0	0.002	0.043	0.005	0.189	0.261
CaO	1.364	1.794	1.160	0.023	0.417	1.185
K_2O	0.021	0.135	0.092	0.111	0.389	0.294
FeO	0.017	0.018	0.019	0.050	0.652	0.035
Total	13.605	13.973	13.364	15.020	13.642	13.850
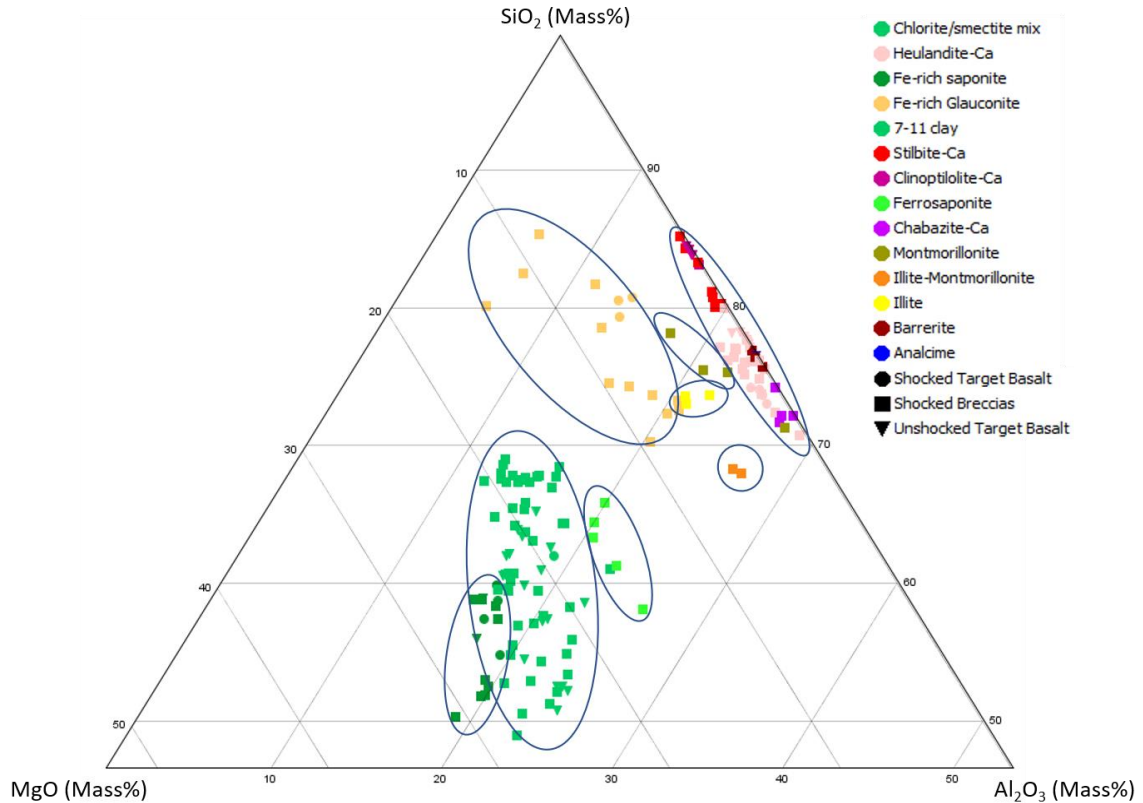
Figure 3-5. **Vista Alegre clays and zeolites ternary diagram. Major clay and zeolite groups are circled and colour-coded (similar to Hagerty et al., 2003).**

Clay and zeolite species were confirmed using µXRD data. Additionally, µXRD detected interstratification of clay layers (e.g., illite-smectite and chlorite-smectite mixed clays), displayed as asymmetrical reflection peaks with a shoulder at a lower angle tail. Representative diffraction patterns of alteration minerals in the samples are presented in Figures 3-6, 3-7 and 3-8. Detailed descriptions of compositions and assemblages of major secondary phases within the shocked target basalts and polymict breccia are provided below.
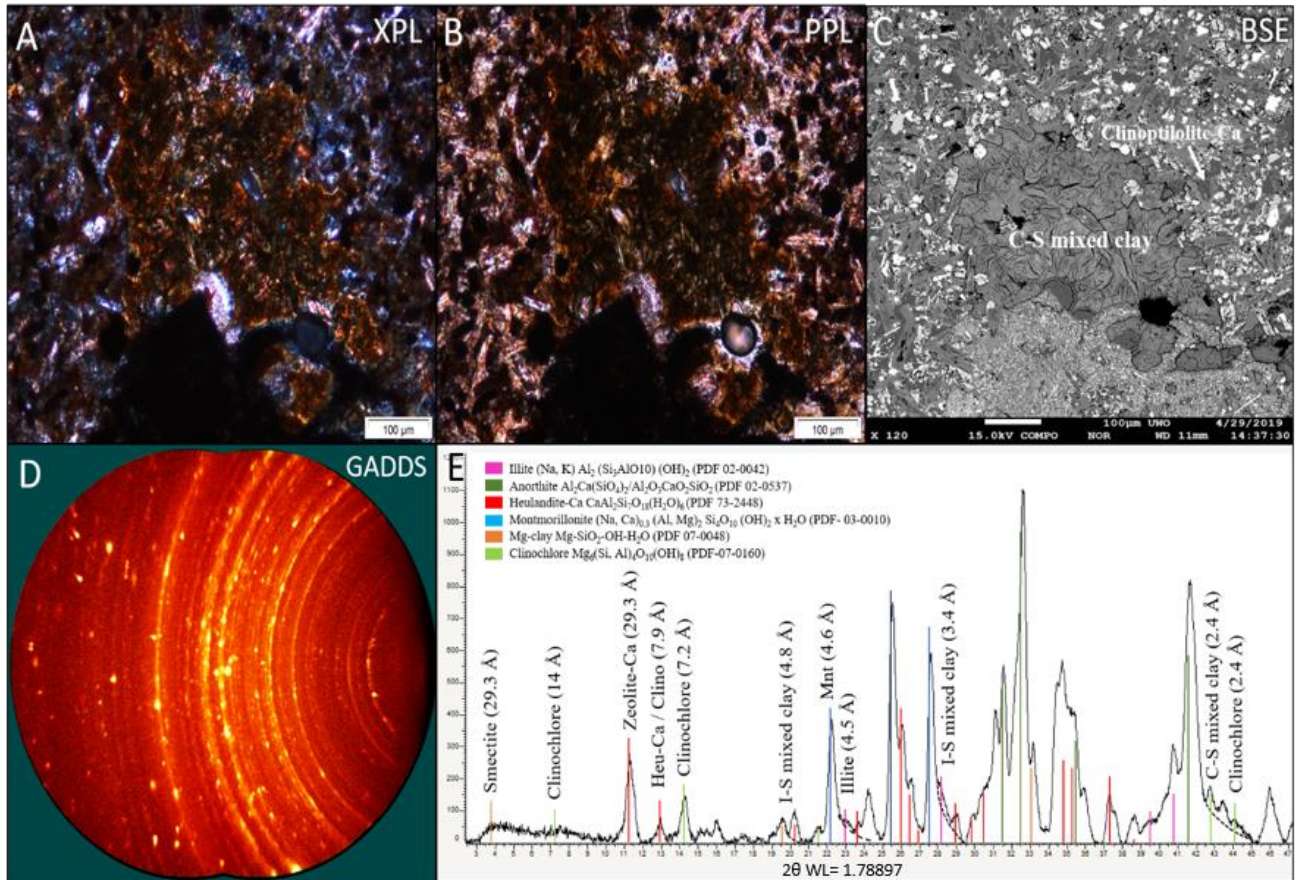
Figure 3-6. µXRD data of clay spot 2 from sample VA-2017-5C supported by EPMA and optical observations. These data were collected using the newly-developed method for clay minerals. A-B) XPL and PPL photomicrographs of a cavity-filling, fibrous clay. C) BSE photomicrograph with spots of interest labelled based on compositional WDS analysis. D) GADDS image of the 300-micron size spot analyzed. E) Intensity vs 2θ plot of corresponding spot with minerals matched to peaks. Minerals selected that best matched to the peaks are anorthite, Mg-clay (smectite), and heualandite. Note the I-S mixed clay turbostratic stacking shapes (dotted lines) formed at 4.5 and 4.8 Å, where montmorillonite is asymmetrical with illite overlapping at the tail. Additionally, turbostratic layering seen by C-S mixed clay at 2.4 Å.
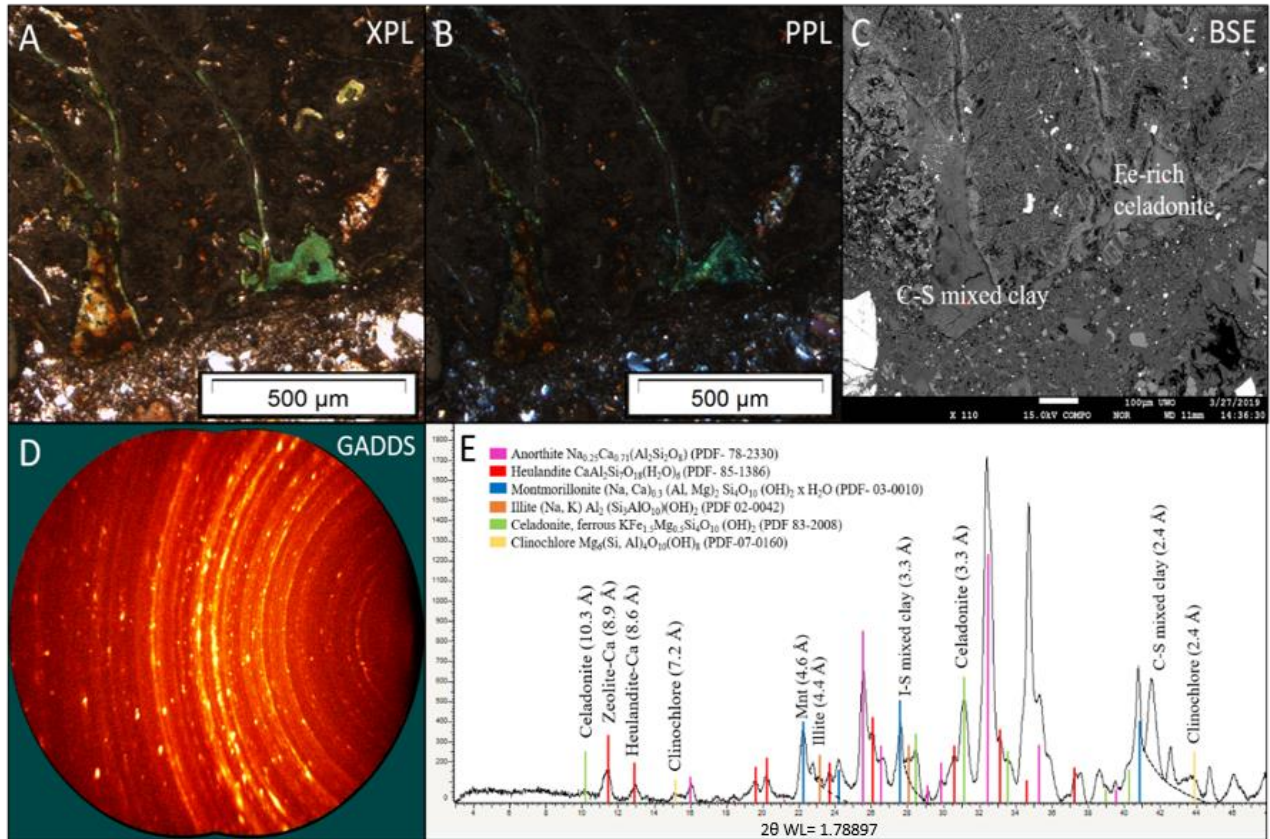
Figure 3-7. µXRD data of clay spot 1a from sample VA-2017-1B supported by EPMA and optical observations. These data were collected using the newly-developed method for clay minerals. A-B) XPL and PPL photomicrographs of fine-grained green and orange-brown clay infilling open spaces and veins in a melt-bearing breccia clast. C) BSE photomicrograph of spot of interest labeled based on compositional analysis by WDS. Celadonite is the fine-grained green clay and C-S mixed clay is the fine-grained orange-brown clay. D) GADDS image of the 300-micron size spot analyzed by µXRD. E) Intensity vs 2θ plot of corresponding spot with minerals matched to X-ray peaks. Minerals selected that best matched the peaks are anorthite, montmorillonite, heulandite, celadonite, illite and clinochlore. Note the turbostratic stacking (dotten lines) shape formed by the I-S mixed clay at 4.5 Å, where montmorillonite is asymmetrical with illite overlapping at the tail. Turbostratic stacking due to C-S mixed clay is visible at ~42° 2θ (~2.4 Å).
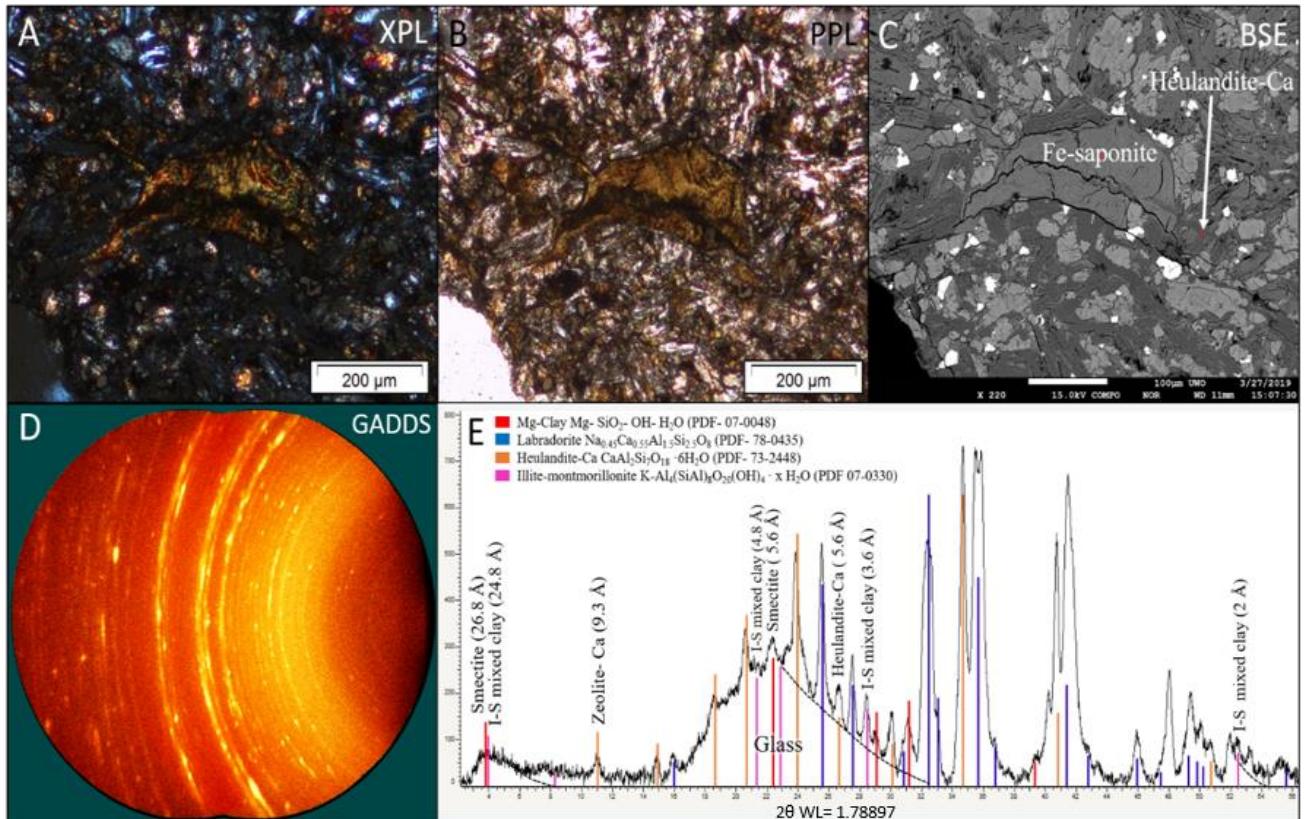
Figure 3-8. µXRD data of clay spot 2 from sample VA-2017-1E4 supported by EPMA and optical observations. These data were collected using the newly-developed method for clay minerals. A-B) XPL and PPL photomicrographs of brown-greenish, fibrous clay with a dark-coloured vein cross-cutting it. C) BSE photomicrograph marked with spots of interest, which were analyzed with WDS. The clay is Fe-rich saponite and it has a heulandite-Ca vein crosscutting it. D) GADDS image of the 300-micron size spot analyzed by µXRD. E) Intensity vs 2θ plot of corresponding spot with minerals matched to peaks. Minerals selected that best matched the peaks are labradorite, heulandite-Ca, illite-montmorillonite and Mg-clay (smectite). Illite-mont that appears in the XRD data is likely infilling the matrix along with labadorite. The large amorphous 'hump' is due to volcanic glass.

3.3.2.1   Clays

Data obtained using petrography, WDS and µXRD reveals that the clays present in the shocked samples, in order of most to least abundant, are: mixed-group chlorite-smectite (C-S) clays, Fe-rich saponite, mixed-layer illite-smectite (I-S) clays, Fe-rich glauconite, celadonite and montmorillonite. In comparison to the shocked and unshocked target basalts, impact breccia samples display the greatest variability in clay types. The majority of clays are rich in Fe and Mg with a Fe/Mg ratio averaging to ~2.125, ranging from 0.949 to 4.332. While Fe-saponite clays are present in all shocked samples, they are more Mg-rich in the impact breccias. Clays are almost always associated with calcite and other zeolite minerals. When associated with zeolites, clays precede the crystallization of zeolites (Figs. 3-4 F, 3-8). When in association with calcite, clays are infilling fractures and lining calcite clasts (Fig. 3-9 B). BSE imaging reveals that even clays of the same mineral group can vary in grain size, but the textures are usually well-defined (e.g., Figs. 3-4 E, 3-6).
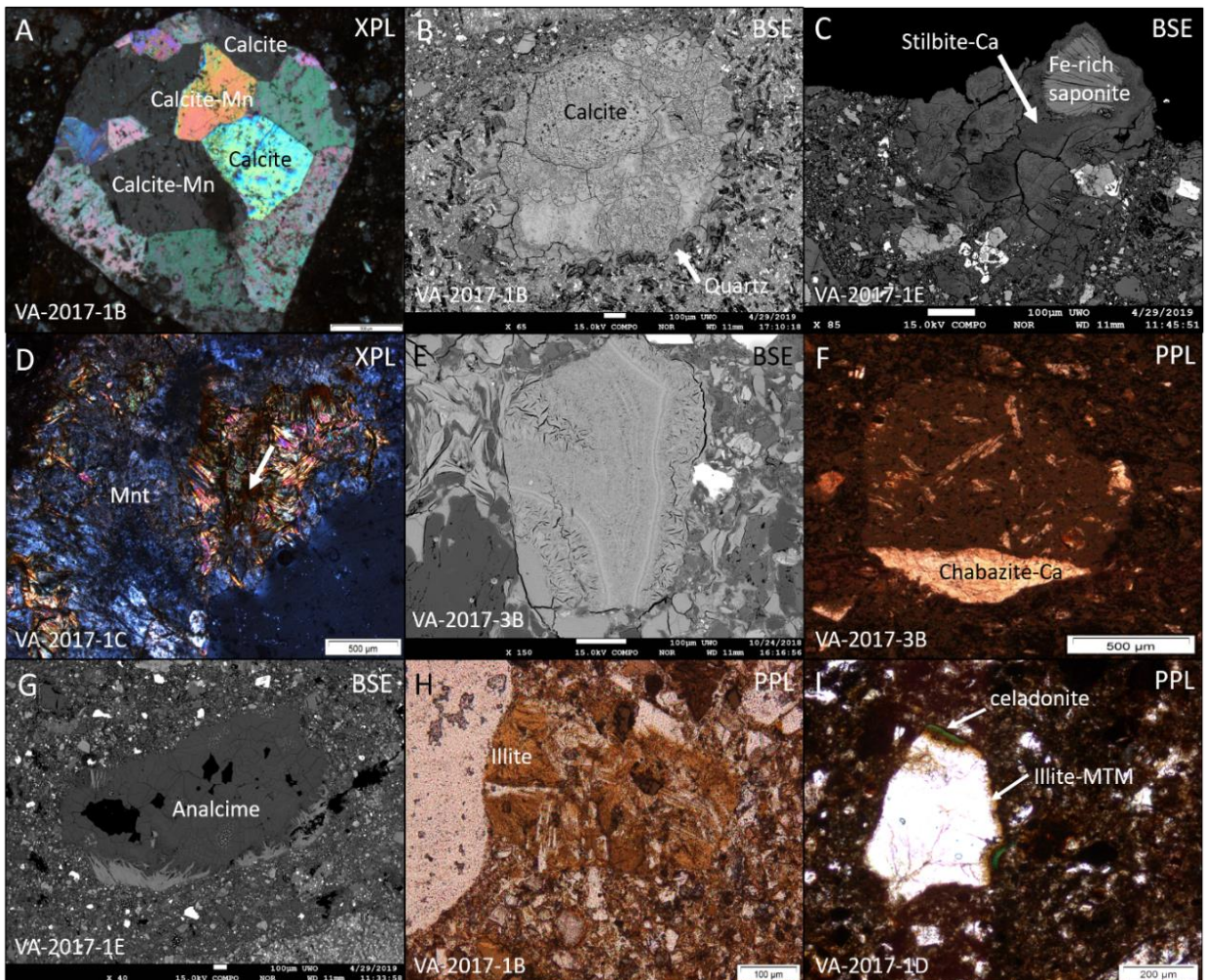
Figure 3-9. Hydrothermal alteration phases in Vista Alegre target basalts and polymict breccia. A) Large 2.3 mm euhedral calcite clast supported by groundmass with some spots containing trace amounts of Mn and others not. There is not a textural difference between these locations. Evidence of clay alteration at the bottom of the clast. B) ~1 mm calcite clast partially replaced by Fe-rich saponite clays within the clast and by quartz around the rim. C) Fibrous Fe-rich saponite crystallites surrounded by fine-grained stilbite-Ca. D) Fibrous clay pocket within a montmorillonite matrix. The light crystallites are Fe-rich saponite and have high birefringence similar to mica. The darker, lower birefringence fibrous crystallites are chlorite/smectite mixture clay, indicated by white arrow. Note the fibrous crystallites radiate out from lenticular void. E) Fe-Mg clays of various sizes (sub-μm to 100 μm) all occurring together. The small and medium sized crystallites occur within the clast, and the largest sized crystallites are forming outside of the clast. F) Blocky/platy analcime zeolite replacing a breccia clast containing elongated plagioclase laths. G) Breccia clast replaced by blocky analcime with fibrous Fe-Mg clay around the edges. H) Fine-grained illite mostly replacing a clast with elongated plagioclase laths. I) Plagioclase clast lined with illite-montmorillonite (orange) and some fine-grained, bright green celadonite clay around the edges. The brightness of the plagioclase is exaggerated to allow to better the see colour of the celadonite.

Smectite and chlorite group clays can be found as fine or coarse-grained crystallites (sub-μm to 300 μm long), and although compositions vary (Table 3-3), variation does not systematically correlate with size (Fig. 3-9 E). Saponite and C-S clays form as elongated crystallites that exhibit a fibrous, bladed, radiating or void-filling textures, all which are characteristic of smectites and chlorites. The interstratified clays in our sample set display turbostratic stacking arrangements (hk planes) as a consequence of highly disordered layers stacked randomly (rotated/translated layers) relatively to each other (Figs. 3-6, 3-7, 3.8) (Biscoe & Warren, 1942; Brindley & Brown, 1980; Warren, 1941). Additionally, chlorite-containing assemblages have a characteristic greenish tint (Fig. 3-7). The coarse fibro-radial clays sometimes have a mica-like appearance due to their high birefringence colours (Fig. 3-9 D), while the finer-grained fibrous assemblages appear orange/brown in colour, and due to the small size of the intertangled fibers, they appear "irregular" in

texture (Fig. 3-4 E). Both course and fine-grained fibrous clays can occur together (Fig. 3-9 E).

The following relationships between diffraction angle and d-spacing are based on Bragg's law ($n\lambda = 2d\sin\theta$, where λ = wave-length of incident radiation (CoKα = 1.78897 Å) and d = interplanar lattic spacing) (Klug and Alexander 1962). The μXRD consistently detected a unique, broad smectite signature peak between ~5–6° 2θ CoKα (~17–20 Å) (Figs. 3-6, 3-8) (Brown & Brindley, 1980). This is the lowest peak the μXRD is able to detect using the novel μXRD technique developed for this study. An additional X-ray reflection peak characteristic of smectites was detected at ~22.5° 2θ CoKα (~5.6 Å) (Fig. 3-8) (Brown & Brindley, 1980). Chlorite peaks are smaller and more narrow occurring at ~6–8.5° 2θ CoKα (~12–16 Å). They are often found in sequence with the smectite group mineral peak when analyzing chlorite-smectite mixed layer clay spots (Brown & Brindley, 1980). C-S mixed clays produces a characteristic peak at 40.4–41° 2θ CoKα (~2.6 Å), which μXRD identifies as chlorite, and a peak at 13.3° 2θ CoKα (~7.7 Å), labeled at smectite (Figs. 3-6, 3-7) (Brown & Brindley, 1980). Chlorite (also represented by clinochlore) displays additional reflection peaks at higher 2θ values such as ~14.3–15° and ~44° 2θ CoKα (~7.2 and ~2.4 Å) (Figs. 3-6, 3-7) (Brown & Brindley, 1980).

Illite, celadonite and glauconite are dioctahedral mica clays that occur as fine-grained, space filling clays. Illite is often found replacing primary phenocrystals and crystallizing in voids (Figs. 3-9 H). Celadonite has a distinct green colour and is found forming along the rims of breccia clasts as well as filling voids and fractures (Figs. 3-9 I, 3-7). Illite clays are often found mixed with smectite clays. Illite-smectite (I-S) clays appear dark brown in colour and are often found replacing minerals (Fig. 3-9 I) and displaying botryoidal habits (Fig. 3-4 J).

Both illite and celadonite have characteristic μXRD peaks at ~10.2° 2θ CoKα (~10 Å) (Brown & Bridley, 1980). Celadonite clay displays another distinguishable peak at ~31° 2θ CoKα (3.3 Å) (Brown & Brindley, 1980; Wainwright et al., 2008), and illite has an additional characteristic peak at ~21.5–24° (~4.5 Å) (Fig. 3-7) (Brown & Brindley, 1980;

Sródón, 1984). Glauconite was detected with WDS analyses but not μXRD. When I-S clays in our sample set are analyzed, illite μXRD diffraction peaks are coupled to a montmorillonite peak, forming an interstratified clay lineshape corresponding to interlayering. Illite-montmorillonite interlayering is the most common type of interstratification of clays in our μXRD dataset. Illite-montmorillonite peaks occur at ~20–21°, 27.5–29°, and ~53° 2θ CoKα (~4.8–5.2, ~3.3–3.5 and ~2 Å) (Sakharov et al., 1999), and the montmorillonite and illite peaks are no more than 1° 2θ apart (Figs. 3-6, 3-7, 3-8). The illite-montmorillonite ICDD card (PDF 07 0330) fits the peaks well, but it only characterizes one of the two peaks involved in illite-montmorillonite interstratification.

3.3.2.2 Zeolites

Based on chemical analyses with WDS and μXRD data, the zeolites in the shocked Vista Alegre samples have compositions compatible with heulandite-Ca, chabazite-Ca, stilbite-Ca, erionite, analcime and mordenite (Table 3-4). Heulandite-Ca is the only zeolite detected in shocked target basalts while impact breccias contain a range of zeolites.

Hydrothermal zeolites are found filling veins (Figs. 3-4 D, 3-8), lining voids (Figs. 3-4 E, 3-6), fractures, and minerals, and partially replacing plagioclase (Fig. 3-4 L) or basaltic groundmass matrix. The crystals form in typical zeolite habits such as prismatic (Figs. 3-4 D, L; 3-9 F, G), or fine-grained void filling (Figs. 3-4 E, K; 3-9 C, H). White veins composed of zeolites are generally mono-zeolitic resembling chabazite-Ca or heulandite-Ca in composition and develop in a tabular-platy habit perpendicular to the walls of the veins (Fig. 3-4 D). Analcime zeolite is easily recognized from its euhedral blocky habit, replacing breccia clasts (Fig. 3-9 G). Zeolites that are lining pore spaces and replacing glass, such as mordenite, are fine-grained with void filling texture. When the zeolites are associated with clays, they always appear overlaying, cross-cutting (Fig. 3-8) or growing from the clays. Heulandite-Ca is the most ubiquitous species of zeolite in this work present in all sample types.

All the zeolites detected with μXRD, other than analcime, display a distinctive peak at ~11° 2θ CoKα (~9–9.4 Å) (Figs. 3-6, 3-7, 3-8) (Treacy & Higgins, 2001). Clinoptilolite

and heulandite may be identified by additional peaks at ~13, 26, and 35° 2θ CoKα (7.9, 3.96, 2.97 Å) (Figs. 3-6, 3-7) (Brown & Brindley, 1980; Treacy & Higgins, 2001). Analcime displays a unique diffraction peak at ~19° 2θ CoKα (~5.5 Å) (Treacy & Higgins, 2001). The peak intensities are dependent on the abundance of zeolite, and in our sample set the intensity ranges from 50–300 counts. μXRD accurately displays the presence of zeolites; however, it is often difficult to determine the exact zeolite species because of similarities in X-ray patterns, in particular the overlap at the ~11° 2θ (~9.2 Å).

3.3.2.3   Calcite

Calcite was only found in the shocked samples. Calcite in melt-bearing polymict breccias usually forms as large euhedral crystals (up to 2.5 mm in size) (Figs. 3-4 G; 3-9 A, B), but otherwise polycrystalline calcite infills veins that are cross-cutting other alteration minerals (Fig. 3-4 E). In most settings, calcite is associated with clays and zeolites (clay rims, zeolites and clays infilling fractures and open spaces within the rock).

BSE imagery reveals that there are no textural differences between calcites from different settings. Quantitative WDS results indicate that secondary calcite is pure $CaCO_3$, except in some cases where calcite grains or twins within a larger clast contain trace amounts of MnO (0.17–2.22 wt %) (Fig. 3-9 A).

μXRD of a cut slab of polymict breccia VA-2017-1E appears to contain pre-impact calcite, as a small clast (or vesicle fill) appears to have experienced shock (Fig. 3-10). This region demonstrates what appears to be strain-related mosaicity as shown by streaking of the diffraction spots in Figure 3-10. Alternatively, this may be a growth-related texture. Optical confirmation of the calcite texture is not possible as this sample is not a thin section but a rock slab.
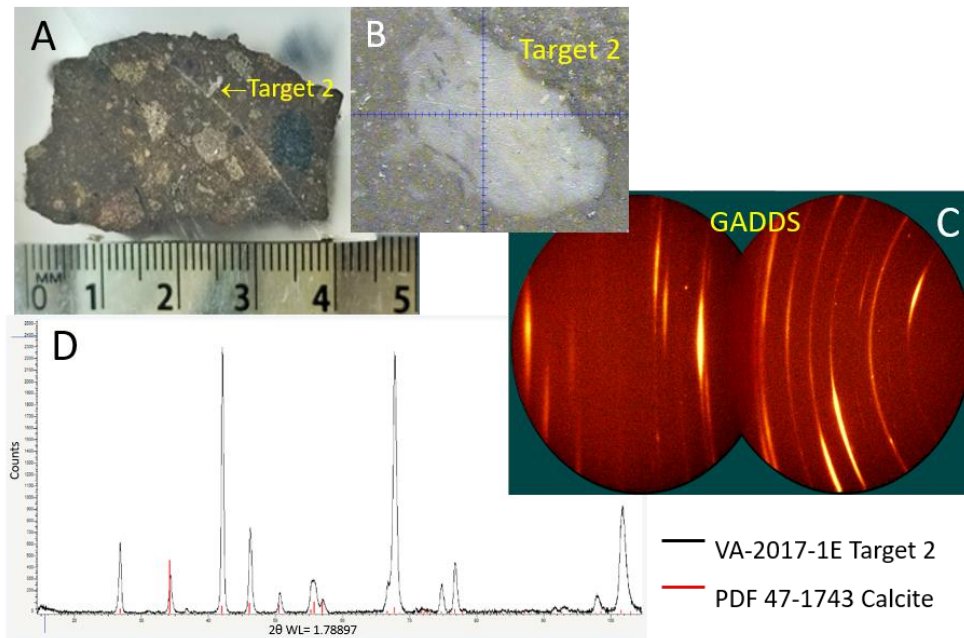
Figure 3-10. µXRD of calcite clast (or vesicle fill) in polymict breccia VA-2017-1E (target 2), indicating shock. In order to have been shocked this calcite must have formed by processes that predated impact. A) Sample VA-2017-1E. B) Context image of target 2 on the µXRD. C) GADDS image showing streaking, likely indicating shock. D) X-ray diffraction pattern identifying the clast as calcite.

3.3.2.4   Quartz

As opposed to the abundance of secondary quartz found in the unshocked sample VA-2017-5, hydrothermal quartz in the shocked Vista Alegre target basalts and breccias is limited. Quartz crystallizes in a non-uniform fashion either infilling open space voids (Fig. 3-4 L) and fractures or replacing clasts and minerals (Fig. 3-9 B). Quartz in the shocked samples also appears different from that in the unshocked sample, it is more altered or "dirty", and brown in colour.

3.4   Discussion

3.4.1   Pre- Versus Impact-Generated Hydrothermal Alteration?

The shocked target basalts and polymict impact breccias from inside Vista Alegre as well as the unshocked basalts from outside the crater exhibit evidence of alteration. This begs the question as to whether the alteration is impact-induced or if it was present in the target rocks before the impact. Therefore, one of the major goals of this study is to shed light on the source of the alteration found in the Vista Alegre impact structure.

Alteration features in the unshocked samples (VA-2017-5 and VA-2017-5C) may be mistaken for evidence of impact-induced hydrothermal alteration. However, these features have previously been reported in other studies of the Paraná Basin basalts, not related to any impact events. Schenato et al.'s (2013) detailed petrographic and mineralogical study of alteration processes in the Paraná Basin reported frequent pervasive albitization of plagioclase yielding zeolites crystallized in vesicles. Additionally, work by Franco (1952) and Murata et al. (1987) classifying zeolites from the Paraná Basin suggested that zeolitization in vesicles may have been promoted by hydrothermal circulation at or near a continental spreading center. A recent study by Yokoyama et al. (2015) compared hydrothermal alteration within and around the Vargeão Dome impact structure, suggesting that although minimal, the shocked samples within the Vargeão impact displayed some additional impact-induced hydrothermal alteration features that are not present in the samples outside the crater. Our results of hydrothermal alteration within and outside the Vista Alegre impact structure, which occurred on the same Paraná basin about 100 km away from Vargeão Dome, have led to similar conclusions. There are several important distinctions between alteration phases and textures in the unshocked versus shocked samples that enabled us to differentiate between pre- and post-impact hydrothermal alteration features.

With the exception of the tabular-platy zeolites infilling veins (Figs. 3-3 D, 3-4 D, 3-8) and the fine-grained zeolites replacing basaltic groundmass, crystallization textures of zeolites are different in the shocked and unshocked samples. In agreement with the literature above, zeolites only infill vesicles in our unshocked basalts (Fig. 3-3 G);

however, in the shocked samples, zeolites are found lining voids, fractures, and minerals (Fig. 3-4 E). The difference in zeolite textures may be related to different durations of fluid flow during different hydrothermal events. Additionally, the veins infilled with secondary minerals in the shocked samples cross-cut shocked basaltic fragments and breccia clasts (Figs. 3-4 A. B, C, D, E, 3-7, 3-8). This cross-cutting relationship indicates that the veining and vein-filling processes occurred after the impact event because of impact-generated hydrothermal activity. Although not often used as a characteristic indicator of hydrothermal alteration, secondary quartz presents differently in shocked Vista Alegre samples in comparison to unshocked Paraná Basin basement basalts, and both appear different from shock metamorphosed quartz. The evenly-deposited quartz rims of the unshocked secondary quartz (Figs. 3-3 G, H) in comparison to the incomplete quartz rims where it preferentially deposits at weak points along the clast's perimeter (Figs. 3-4 L, 3-9 B) suggests that the shocked and unshocked quartz samples formed through distinctly different processes.

The shocked samples, in particular the impact breccias, display a wide range of alteration phases including Fe-Mg clays (smectite, chlorite, saponite, glauconite, and celadonite), Al-clays (montmorillonite and illite), zeolites (heulandite, chabazite, stilbite, analcime, mordenite), carbonates (calcite), and quartz. The clay mineral group may contain a variety of chemical compositions and form in a variety of different assemblages, and this is particularly expressed in the chlorite-smectite (C-S) mixed clays (Table 3-3). Our WDS compositional data of the various C-S mixed clays compares favourably to C-S clays from volcanic rocks of Kahrizak, Iran (Kousehlar et al., 2012).

There is a large number of variables in an impact-induced hydrothermal system that can affect the process (e.g., temperature, fluid composition/amount, pH), therefore a greater variety of alteration minerals can be expected to form under the different hydrothermal environments (Inoue, 1995; Muttik et al., 2008).

In contrast to the wide range of clay and zeolite species in the shocked samples, unshocked samples only contain Fe-saponite and C-S mixed clays, and heulandite-Ca and clinoptilolite-Ca zeolites. Clinoptilolite-Ca, which is a common product of low

geothermal-gradient zeolitization (Utada, 2001a), is only found in the unshocked samples. The presence of clinoptilolite-Ca in the unshocked samples, as well as the petrographic and geochemical data collected on the zeolite-filled vesicles (i.e., amygdales) (Fig. 3-3 G) further support the belief that vesiculation and the associated alteration feature in the Paraná basalts are likely a result of degassing and low-grade metamorphism during the volcanism that formed the basaltic continent (Schenato et al., 2013; Yokoyama et al., 2015). Alternatively, the majority of the alteration features in the shocked Vista Alegre appear to have formed through a different hydrothermal process. While pre-impact hydrothermal effects within the Vista Alegre impact structure are possible, most of the current alteration features are more likely to be a product of post-impact hydrothermal alteration.

3.4.2   Nature of Mineral Assemblages Within the Vista Alegre Hydrothermal System

Hydrothermalism requires a thermal gradient, therefore, it is common for multiple generations of hydrothermal minerals to be present in hydrothermally altered craters (Osinski et al., 2013; Yokoyama et al., 2015). The presence and abundance of different alteration minerals can helps predict the fluid composition, temperatures, and the rate of cooling for hydrothermal systems. Calcite, quartz, and analcime were likely formed early on in the post impact alteration process. Although not distinctly diagnostic of hydrothermal alteration, calcite in the Vista Alegre samples often displays infilling and veining features that are overprinting shocked material, suggesting that most of the calcite formed as a result of post-impact hydrothermal activity. This agrees with a previous study by Pinto et al. (2009) of Vista Alegre native copper, which describes calcite to be common in alteration stages. Fluid inclusion studies of calcite at the Haughton impact structure, Canada, yielded temperatures ranging from 118– 210 ° C (Osinski et al., 2001). Two variations of calcite phases with distinct crystallizations that likely precipitated at different hydrothermal periods were identified. The more abundant of the two are large calcite vugs with highly eroded crystal faces. They appear to be partially replaced by quartz, indicating a temporal relationship between the two phases, where calcite was deposited first, followed by quartz. Hydrothermal quartz is commonly

associated with early high-temperature stages of hydrothermal alteration (e.g., Ames et al., 2006; Osinski et al., 2005; Osinski et al., 2013). Previously studied fluid inclusions within quartz grains of impact-induced hydrothermally altered impact craters suggests that the fluid temperature can vary between 100–350/400 °C (e.g., Boer et al., 1996; Kirsimäe et al., 2002; Komor et al., 1988; Lüders & Rickers, 2004). Analcime zeolite also forms over a large range of temperatures, ~70–300° C, and often represents higher formation temperatures (Coombs, 1989).

No analcime was found associated with calcite or quartz mineralization, so the temporal relationship between these phases is unclear. However, Fe-Mg clays were often seen lining analcime, and their spatial association suggests that clays formed after analcime. Smectites are the most significant alteration clay throughout the Vista Alegre samples. Smectites can be thermally metastable at relatively low temperatures but may also represent high formation temperatures. For example saponite can occur at temperatures <100° C or as high as 300° C (e.g., Beaufort et al., 1995a, b; Schiffman & Fridleifsson, 1991). The presence of chlorite and chlorite-smectite interlayered clays suggests a hydrothermal alteration phase at temperatures as high as 150–300 °C (Schiffman & Fridleifsson, 1991; Shau & Peacor, 1992, and references therein). Illite-Montmorillonite mixed clays are common in Vista Alegre polymict impact breccias as well. The conversion of smectite to illite (and layered illite-smectite byproduct) takes place over a broad temperature interval of 70–150 °C (Pusch, 1993). When found in association with zeolites, clays are always preceding them, meaning the zeolites are crosscutting, overlaying, or surrounding clay minerals. The temporal association of clays with zeolites indicates that clays were the first mineral to precipitate out of the cooling hydrothermal solutions circulating through the polymict impact breccias, followed by the cross-cutting zeolites. Most zeolites have been reported to occur as alteration products at relatively low temperature. For example, the vein-filling zeolites such as chabazite-Ca and heulandite-Ca form at ~25–85° C and ~60–160° C, respectively (Chipera & Apps, 2001). Zeolites crosscut other alteration minerals (Figs. 3-3 D, 3-4 D, E, I, K, L) that form at higher temperature, which would suggest that their precipitation within veins, fractures, voids, as well as replacement of basaltic shocked minerals and groundmass was a late-stage

event. Heulandite-Ca is consistently present in all samples which may indicate that it is a pre-impact zeolite.

Calcite deposition likely continued until the final stages of hydrothermal activity, expressed in the second, less abundant form of the smaller calcite crystals overlaying late-stage zeolite veins. Calcite mineralization is a common feature of distal, low-temperature hydrothermal systems and late stage hydrothermal activity (Bove et al., 2007; Capezzuoli et al., 2018) and is the last precipitated mineral within the Vista Alegre hydrothermal system paragenetic sequence.

3.4.3   Fluid Source of the Vista Alegre Hydrothermal System

Based on assemblages present in the samples, the Vista Alegre hydrothermal system had intermediate to high alkaline aqueous activity (Utada, 2001b; Tables 3-3, 3-4). The fluid sources for the impact-induced hydrothermal system at Vista Alegre are likely the Guarani aquifer and meteoritic water. Geochemical characterization of the fluid composition of the aquifer indicates high Ca^{2+} and HCO_3^- content due to calcite dissolution (Meng & Maynard, 2001). This information agrees well with the observations of calcite in our samples mainly being restricted to high permeability zones, further suggesting that calcite crystallized in pores and fractures during the fluid flow from the underlying Ca-rich aquifer. The aquifer is also rich in sodium, and Na-rich zeolites such as analcime were seen in impact breccias. Based on work by Hay (1966) and Sheppard and Gude (1968, 1969), it was inferred that analcime forms from alkalic and silicic zeolites by increased pH and Na^+ concentrations, indicative of the required external source of Na^+, such as the Guarani aquifer. Hydrothermal zeolites surround probable solution pathways such as filling veins (Figs. 3-4 D, 3-8), lining voids (Figs. 3-4 E, 3-6), pores and glass, and partially replacing clay minerals in altered plagioclase (Fig. 3-4 L) or basaltic groundmass matrix. The precipitation of Na-rich clays at Vista Alegre such as saponite and nontronite is also likely the result of fluid flow from the underlying aqueous system (Sracek & Hirata, 2002).

3.4.4   Comparison to Vargeão Dome Impact Structure

Vista Alegre (9.5 km diameter) and its sister impact structure, Vargeão Dome (12.4 km diameter) are similarly sized impact structures that formed only ~100 km apart on the same basaltic lava field with the same underlying aquifer. Although a double impact is unlikely, there are strong resemblances in mineralogy, shock metamorphism, porosity, density (Chapter 2), and hydrothermal alteration. Similar to Vargeão Dome, the Vista Alegre impact event acted as a source of heat and energy, providing a thermal gradient for the circulating fluids from the Guarani aquifer. The resulting hydrothermal systems formed alteration textures that are alike in both impact craters such as veining, altered glass, infilling of fractures and voids, and replacement of primary basaltic minerals by secondary minerals (Crósta et al., 2011). The two main alteration minerals in both craters are saponite (Mg-Fe octahedral smectite) and zeolite (analcime and Ca-zeolites close to heulandite and stilbite in composition). Additionally, chlorite, chlorite-smectite mixed clays, celadonite, and montmorillonite occur in both Vista Alegre and Vargeão Dome. Natrolite and mesolite zeolites were identified in Vargeão Dome, but not in our sample set. In contrast, illite, illite-smectite mixed clays, and chabazite zeolites were identified in Vista Alegre, but not Vargeão Dome.

3.5   Conclusions

This study is the first to report a detailed description of hydrothermal activity in the Vista Alegre impact structure of Brazil. The novel μXRD method employed in this study can be used to effectively determine alteration phases at low 2θ angles with comparable accuracy to pXRD, but *in situ* and non-destructively, and with little required preparation. Petrographic observations reveal that alteration textures in the polymict impact breccias, in particular zeolite veining, crosscut shocked basaltic minerals and breccia clasts. Using the above methods, we can confidently verify that shocked samples within the Vista Alegre impact structure are altered by impact-induced hydrothermal activity. This alteration is distinct from that occurring outside the impact structure as a result of low-grade metamorphism.

In light of the current NASA-lead Mars Science Laboratory and Mars 2020 sample return missions, as well as in anticipation of future missions to investigate hydrothermal deposits, it is important to understand the development and behavior of hydrothermal minerals in basaltic terrestrial analogues. As seen in impact-induced hydrothermal systems on Earth, pre-impact alteration products can survive an impact event, and post-impact hydrothermal minerals may be persevered long after the cessation of a hydrothermal system. The preservation of such phases has also been predicted to occur on other terrestrial bodies such as Mars. The identification and quantification of hydrothermal alteration minerals may help reconstruct present and past aqueous environments (which there is minimal to no geological context), alteration history of the Martian crust, and the habitability potential for life on Mars (Gainey et al., 2017; Grant et al., 2018; Muttik et al., 2008). Indeed, due to their potential to generate habitats and protect endolithic environments from the inhospitable surface conditions, impact craters have received considerable attention as astrobiological targets (i.e., Jezero Crater lake sediments, Cabrol & Grin, 1999, 2001; Grin & Cabrol, 1997). If life ever did exist on Mars, the uplifted shocked lithologies and substrates formed in impact hydrothermal systems would likely offer the highest probability to find remnants of life and their biosignatures (Onstott et al., 2019; Osinski et al., 2020).

3.6   References

Allen, C. G., Gooding, J. L., & Keil, K. (1982). Hydrothermally altered impact melt rock and breccia: contributions to the soil of Mars. *Journal of Geophysical Research*, *87*(B12), 10083–10101.

Ames D. E., Watkinson D. H., & Parrish, R. R. (1998). Dating of a regional hydrothermal system induced by the 1850 Ma Sudbury impact event. *Geology, 26*(5), 447–450.

Ames, D. E., Watkinson, D. H, & Parrish, R. R. (2006). Impact-generated hydrothermal system- Constraints from the large Paleoproterozoic Sudbury crater, Canada. In: C. S. Cockell, I. Gilmour, C. Koeberl (Eds.), *Biological Processes Associated with Impact Events* (pp. 55-100). Springer, New York.

Baross, J. A., & Hoffman, S. E. (1985). Submarine hydrothermal vents and associated gradient environments as sites for the origin and evolution of life. *Origins of Life and Evolution of Biospheres, 15*, 327–345.

Beaufort, D., Papapanagiotou, P., Fujimoto, K., Patrier, P., & Kasai K. (1995b). High temperature smectites in active geothermal systems. In Y. K. Kharaka, & O. V. Chudaev (Eds.), *Water–Rock Interaction* (pp. 493–496). Balkema, Rotterdam

Beaufort, D., Papapanagiotou, P., Patrier, P., & Traineau, H. (1995a). Les interstratifiés I-S et C-S dans les champs géothermiques actifs: sont-ils comparables à ceux des séries diagénétiques? *Bulletin Centres Recherches Exploration-Production*, *19*(1), 267–291.

Bergaya, F., & Lagaly, G. (2006). General introduction: clays, clay minerals, and clay science. *Development in Clay Science*, *1*, 1–18.

Bettison, L. A., & Schiffman, P. (1988). Compositional and structural variations of phyllosilicates from the Point Sal ophiolite, California: *American Mineralogy*, *73*(1-2), 62–76.

Bettison-Varga, L., Mackinnon, I. D. R., & Schiffman, P. (1991). Integrated TEM, XRD, and electron microprobe investigation of mixed-layer chlorite smectite from the Point Sal ophiolite: *Journal* of *Metamorphic Geolology*, *9*(6), 697–710.

Bibring, J. P., Langevin, Y., Gendrin, A., Gondet, B., Poulet, F., Berthé-Soufflot, A., Arvidson, R., Mangold, N., Mustard, J. F., Drossart, P., & the OMEGA team. (2005). Mars surface diversity as revealed by the OMEGA/Mars Express observations. *Science, 307*(5715), 1576–1581.

Bibring, J.-P., Langevin, Y., Mustard, J. F., Poulet, F., Arvidson, R., Gendrin, A., Gondet, B., Mangold, N., Pinet, P., & Forget, F. (2006). Global mineralogical and aqueous Mars history derived from OMEGA/Mars Express data. *Science*, *312*(5772), 400–404.

Biscoe, J., & Warren, B. E. (2004). An X-ray study of carbon black. *Journal of Applied Physics*, *13*(1942), 364–371.

Boer, R. H., Reimold, W. U., Koeberel, C., & Kesler, S. E. (1996). Fluid inclusion studied on drill core samples from the Manson impact crater: Evidence for post-impact hydrothermal activity. In C. Koeberl, and R. R. Anderson (Eds.), *the Manson Impact Structure, Iowa: Anatomy of an Impact Crater* (pp. 377–282). Geological Society of America, Boulder, Colorado, USA.

Bove, D., Mast, M., Dalton, J. B., Wright, W. G., & Yager, D. (2007). Major Styles of Mineralization and Hydrothermal Alteration and Related Solid- and Aqueous-Phase Geochemical Signatures. In S. E. Church, P. Von Guerard, and S. E. Finger (Eds.), *Integrated Investigations of Environmental Effects of Historical Mining in the Animas River Watershed, San Juan County, Colarado*. Professional paper 1651.

Brindley, G. W. (1980). Order–Disorder in Clay Mineral Structures. In G. W. Brindley, & G. Brown (Eds.), *Crystal Structures of Clay Minerals and Their X-Ray Identification* (pp. 125–195). Mineralogical Society, London, England.

Burke, E. A. J., & Lustenhouwer, W. J. (1987). The application of a multichannel laser Raman microprobe (Microdril-28) to the analysis of fluid inclusions. *Chemical Geology, 61*(1-4), 11–17.

Cabrol, N. A., & Grin, E. A. (1999). Distribution, classification, and ages of Martian impact crater lakes. *Icarus*, *142*(1), 160–172.

Cabrol, N. A., & Grin, E. A. (2001). The evolution of lacustrine environments on Mars: Is Mars only hydrologically dormant?. *Icarus*, *149*(2), 291–328.

Capezzuoli, E., Ruggieri, G., Rimondi, V., Brogi, A., Liotta, D., Alçiçek, M. C., Alçiçek, H., Bülbül, A., Gandin, A., Meccheri, M., Shen, C., & Baykara, M. (2018). Calcite veining and feeding conduits in a hydrothermal system: Insights from a natural section across the Pleistocene Gölemezli travertine depositional system (western Anatolia, Turkey). *Sedimentary Geology, 364*, 180-203.

Chipera, S. J., & Apps, J. A. (2001). Geochemical stability of natural zeolites. *Reviews in Mineralogy Geochemistry*, *45*(1), 117–161.

Chen, Y., Wang, Q., Han, Y., Shen, J., Kong, Y., & Zhang, X. (2019). Crystallization variations in clay minerals with latitude in Jilin province, China: a climate perspective. *Clays and Clay Minerology, 67*, 507–517.

Cockell, C. S., Gronstal, A. L., Voytek, M. A., Kirshtein, J. D., Finster, K., Sanford, W. E., Glamoclija, M., Gohn, G. S., Powars, D. S., & Horton Jr., J. W. (2009). Microbial abundance in the deep subsurface of the Chesapeake Bay impact crater; relationship to lithology and impact processes. In G. S. Gohn, C. Koeberl, K. G. Miller, and W. U. Reimold (Eds.), *The ICDP-USGS Deep Drilling Project in the Chesapeake Bay impact structure: Results from the Eyreville Core Holes* (pp. 941-950). Geological Society of America, Boulder, CO.

Cockell, C. S., Lee, P., Osinski, G. R., Horneck, G., & Broady, P. (2002). Impact-induced microbial endolithic habitats. *MAPS, 37*(10), 1287–1298.

Cockell, C. S., & Osinski, G. R. (2007). Impact-induced impoverishment and transformation of a sandstone habitat for lithophytic microorganisms. *MAPS, 42*(11), 1985–1993.

Coombs, D. S. (1989). *Zeolite Facies.* In Petrology, Encyclopedia of Earth Science. Springer, Boston, MA.

Crósta, A. P., Jourdan, F., & Koeberl, C. (2012b). *$^{40}Ar/^{39}Ar$ dating of the Vista Alegre crater, Brazil* [abstract]. 34th International Geological Congress Conference, Brisbane, Australia.

Crósta, A. P., Kazzuo-Vieira, C., Pitarello, L., Koeberl, C., & Kenkmann, T. (2011). Geology and impact features of Vargeão Dome, southern Brazil. *Meteoritics & Planetary Science, 47*(1), 51–71.

Crósta, A. P., Kazzuo-Vieira, C., Pitarello, L., Koeberl, C., & Kenkmann, T. (2012a). Geology and impact features of Vargeão Dome, southern Brazil. *MAPS, 47*(1), 51–71.

Crósta, A. P., Kazzuo-Vieira, C., & Schrank, A. (2004, August 2-6). *Vista Alegre: A newly discovered impact crater in Southern Brazil* [abstract 50501]. 67th Annual Meteoritics Society Meeting, Rio de Janeiro, Brazil.

Crósta, A. P., Koeberl, C., Furuie, R. A., & Kazzuo-Vieira, C. (2010a). The first description and confirmation of the Vista Alegre impact structure in the Paraná flood basalts of southern Brazil. *Meteoritics & Planetary Science*, *45*(2), 181–194.

Crósta, A. P., Lourenço, F. S., & Priebe, G. H. (2009a). Cerro Jarau, Rio Grande do Sul: A possible new impact structure in southern Brazil. In R. L. Gibson, & W. U. Reimold (Eds.), *Large meteorite impacts and planetary evolution IV* (special paper 465). The Geological Society of America.

Damer, B., & Deamer, D. (2015). Coupled phases and combinatorial selection in fluctuating hydrothermal pools: A scenario to guide experimental approaches to the origin of cellular life. *Life, 5*(1), 872–887.

Damer, B., & Deamer, D. (2020). The hot spring hypothesis for an origin of life. *Astrobiology, 20*(4), 429–452.

De la Fuente, S., Cuadros, J., & Linares, J. (2002). Early stages of volcanic tuff alteration in hydrothermal experiments; formation of mixed-layer illite-smectite. *Clays and Clay Minerals, 50*, 578– 590.

Deamer, D., Damer, B., & Kompanichenko, V. (2019). Hydrothermal chemistry and the origin of cellular life. *Astrobiology*, *19*(12), 1523–1537.

Demant, A., Münch, P., Romeuf, N., & Morata, D. (1998). Distribution and chemistry of secondary minerals (zeolites and clay minerals) from Hole 917A, southeast Greenland Margin. *Proceedings of the Ocean Drilling Program Proceedings of the Ocean Drilling Program, 152 Scientific Results*.

Ehlmann, B. L., Berger, G., Mangold, N., Michalski, J. R., Catling, D. C., Ruff, S. W., Chassefière, E., Niles, P. B., Chevrier, V., & Poulet, F. (2013). Geochemical consequences of widespread clay mineral formation in Mars' ancient crust. *Space Science Reviews*, *174*(1-4), 329–364.

Ehlmann, B. L., & Edwards, C. S. (2014). Mineralogy of the Martian surface, *Annual Review of Earth Planetary Science*, *42*, 291–315.

Ehlmann, B. L., Mustard, J. F., Murchie, S. L., Bibring, J. P., Meunier, A., Fraeman, A. A., & Langevin, Y. (2011b). Subsurface water and clay mineral formation during the early history of Mars. *Nature*, *479*, 53–60.

Ehlmann, B. L., Mustard, J. F., Swayze, G. A., Clark, R. N., Bishop, J. L., Poulet, F., Des Marais, D. J., Roach, L. H., Milliken, R. E., Barnouin-Jha, O., & Murchie, S. L. (2009). Identification of hydrated silicate minerals on Mars using MRO-CRISM: Geologic context near Nili Fossae and implications for aqueous alteration, *Journal of Geophysical Research*, *114*(E2), E00D08

Farmer, J. D. (2000). Hydrothermal systems: doorways to early biosphere evolution. *GSA Today, 10*(7), 1–9.

Feldman, V. I., Sazonova, L. V., Mironov, Y. U., Kapustkina, I. G., & Ivanov, B. A. (1983, March). *Circular structure Longancha as possible meteorite crater in basalts of the Tunguska syneclise* [abstract]. 14th Lunar and Planetary Science Conference, League City, TX.

Flemming, R. L. (2007). Micro X-ray diffraction (μXRD): A versatile technique for characterization of Earth and planetary materials. *Canadian Journal of Earth Sciences*, *44*(9), 1333–1346.

Franco, R. R. (1952). Zeolitas dos Basaltos do Brasil Meridional (Genese e Paragenese) Univ Sao Paul, Fac Filos, 150, *Mineral, 10*, 1–53.

Fredriksson, K., Dube, A., Milton, D. J., & Balasundaram, M.S. (1973). Lonar Lake, India: An impact crater in basalt. *Science, 180*(4088), 862–864.

French, B., & Koeberl, C. (2010). The convincing identification of terrestrial meteorite impact structures: What works, what doesn't, and why. *Earth-Science Reviews, 98*(1-2), 123– 170.

Fritz, J., Greshake, A., & Stöffler, D. (2005). Micro-Raman spectroscopy of plagioclase and maskelynite in Martian meteorites: Evidence of progressive shock metamorphism. *Antarctic Meteorite Research, 18*, 96–116.

Gainey, S. R., Hausrath, E. M., Adcock, C. T., Tschauner, O., Hurowitz, J. A., Ehlmann, B. L., Xaio, Y., & Bartlett, C. L. (2017). Clay mineral formation under oxidized conditions and implications for paleoenvironments and organic preservation on Mars. *Nature Communications, 8*(1), 1230.

Glamoclija, M. (2007). Fossil Microbial Signatures from impact induced hydrothermal settings; Preliminary SEM results from the ICDP-USGS Chesapeake Bay impact

structures drilling project. *Geological Society of America Abstracts with Programs*, 39(6), 316.

Glamoclija, M., Schieber, J., & Reimold, W. U. (2007, March 12-16). *Microbial signatures from impact-induced hydrothermal settings of the Ries Crater, Germany; A preliminary SEM study* [abstract # 1989]. 38th Lunar and Planetary Science Conference, Houston, TX.

Goudge, T. A., Mohrig, D., Cardenas, B. T., Hughes, C. M., & Fassett, C. I. (2018). Stratigraphy and paleohydrology of delta channel deposits, Jezero Crater, Mars. *Icarus, 301,* 58–75.

Grant, J. A., Golombek, M., Wilson, S. A., Farley, K. A., Williford, K., Stack, K. M., & Chen, A. (2018). The Science Process For Selecting The Landing Site For The 2020 Mars Rover. *Planetary and Space Science 164.*

Grin, E. A., & Cabrol, N. A. (1997). Limnologic analysis of Gusev Crater Paleolake, Mars. *Icarus, 130*(2), 461–474.

Grotzinger, J. P., Crisp, J., Vasavada, A. R., Anderson, R. C., Baker, C. J., Barry, R., Blake, D. F., Conrad, P., Edgett, K. S., Ferdowski, B., Geller, R., Giblert, J. B., Golombeck, M., Go´mez-Elvira, J., Hassler, D. M., Jandura, L., Litvak, M., Mahaffy, P., Maki, J., Meyer, M., Malin, M. C., Mitrofanov, I., Simmonds, J. J., Vaniman, D., Welch, R. B., & Wiens, R. C. (2012). Mars Science Laboratory mission and science investigation. *Space Science Review, 170*, 5–56.

Hagerty, J. J., & Newsom, H. E. (2003). Hydrothermal alteration at the Lonar Lake impact structure, India: Implications for impact cratering on Mars. *Meteoritics & Planetary Science, 38*(3), 365–381.

Hay, R. L. (1966). Zeolites and zeolitic reactions in sedimentary rocks. *Geological Society of American Special Papers, 85,* 130.

Hode, T., Cady, S. L., Von Dalwigk, I., & Kristiansson, P. (2008). Evidence of ancient microbial life in an impact structure and its implications for astrobiology- A case study. *From Fossils to Astrobiology*, 249–273.

Hode, T., Dalwigk, I. V., & Broman, C. (2003). A Hydrothermal System Associated with the Siljan Impact Structure, Sweden—Implications for the Search for Fossil Life on Mars. *Astrobiology, 3*(2), 271–289.

Hollister, L. S., Crawford, M. L., Roedder, E., Burruss, R. C., Spooner, E. T. C., & Touret, J. (1981). Practical Aspects of Microthermometry. In L. S. Hollister, & M. L. Crawford (Eds.), *Fluid Inclusions: Applications to Petrology* (6th ed., pp. 278–304). Mineralogical Association of Canada.

Inoue, A., Lanson, B., Marques-Fernandes, M., Sakharov, B. A., Murakami, T., Meunier, A., & Beaufort, D. (2005). Illite-smectite mixed-layer minerals in the hydrothermal alteration of volcanic rocks: I. One-dimensional XRD structure analysis and characterization of component layers. *Clays Clay Minerals, 53*, 423–439.

Ivarsson, M., Broman, C., Sturkell, E., Ormö, J., Siljeström, S., van Zuilen, M., & Bengtson, S. (2013). Fungal colonization of an Ordovician impact-induced hydrothermal system. *Scientific Reports, 3*, 3487.

Izawa, M. R. M., Banerjee, N. R., Osinski, G. R., Flemming, R. L., Parnell, J., & Cockell, C. S. (2011). Weathering of post-impact hydrothermal deposits from the Haughton Impact Structure: implications for microbial colonization and biosignature preservation. *Astrobiology, 11*(6), 537–550.

Jenkins, E. J., Flemming, R. L., & McCausland, P. J. A. (2019). Quantitative in situ XRD measurement of shock metamorphism in Martian meteorites using lattice strain and strain-related mosaicity in olivine. *Meteoritics & Planetary Science, 54*(4), 902-918.

Johnson, J. R. (2007, July 9-13). *Thermal infrared emissivity spectra of experimentally shocked andesine* [abstract #3258]. 7th International Conference on Mars, Pasadena, California.

Kieffer, S. W., & Schaal, R. B. (1976). *Shocked basalt from Lonar impact crater, India, and experimental analogues* [abstract]. 7th Lunar Science Conference, Houston, TX.

Kieffer, S.W. & Simonds, C.H. (1980, March). The role of volatiles and lithology in the impact cratering process. *Reviews of Geophysics and Space Physics, 18*(1), 143–181.

Kirsimäe, K., Jõeleht, A., & Plado, J. (2005). Cooling of the Kärdla impact crater: I. The mineral paragenetic sequence observation. *Meteoritics & Planetary Science*, *40*(1), 3–19.

Kirsimäe, K., Suuroja, S., Kirs, J., Kärki, A., Polikarpus, M., Puura, V., & Suuroja, K. (2002). Hornblende alteration and fluid inclusions in Kärdla impact crater, Estonia: Evidence for impact-induced hydrothermal activity. *Meteoritics & Planetary Science, 37*(3), 449– 457.

Kirsimäe, K., & Osinski, G. R. (2012). Impact-Induced Hydrothermal Activity. In G. R. Osinski, & E. Pierazzo (Eds.), *Impact Cratering: Processes and Products* (pp. 76-89). Wiley-Blackwell.

Klung, H. P. & Alexander, L. E. (1962*). X-ray diffraction procedures for polycrystalline and amorphous materials* (pp. 992). New York: Wiley.

Komor, S. C., Valley, J. W., Brown, P. E., & Collini, B. (1988). Fluid inclusions in granite from the Siljan Ring structure surrounding regions. In A. Boden, & K. S. Eriksson (Eds), *Deep Drilling in Crystalline Bedrock* (Vol 1, pp. 180-208). Springer- Verlag, Berlin, Heidelberg.

Kousehlar, M., Weisenberger, T. B., Tutti, F., & Mirnejad, H. (2012). Fluid control on low-temperature mineral formation in volcanic rocks of Kahrizak, Iran. *Geofluids, 12*(4), 295–311.

Lindgren, P., Ivarsson, M., Neubeck, A., Broman, C., Henkel, H., & Holm, N.G. (2010). Putative fossil life in a hydrothermal system of the Dellen impact structure, Sweden. *International Journal of Astrobiology, 9,* 137–146.

Lüders, V., & Rickers, K. (2004). Fluid inclusion evidence for impact-related hydrothermal fluid and hydrocarbon migration in Creataceous sediments of the ICDP-Chicxulub drill core Yax-1. *Meteoritics & Planetary Science, 39*(7), 1187–1197.

Martin, W., Baross, J., Kelley, D., & Russell, M. J. (2008). Hydrothermal vents and the origin of life. *Nature Reviews Microbiology, 6*, 805–814.

Marzo, G. A., Davila, A. F., Tornabene, L. L., Dohm, J. M., Faire`n, A. G., Gross, C., Kneissl, T., Bishop, J. L., Roush, T. L., & McKay, C. P. (2010). Evidence for Hesperian impact-induced hydrothermalism on Mars. *Icarus, 208*(2), 667–683.

Masaitis, V. L. (1999). Impact structures of northeastern Eurasia: The territories of Russia and adjacent countries. *Meteoritics & Planetary Science, 34*(5), 691–711.

Masaitis, V. L., & Naumov, M. V. (1993). Principal model of hydrothermal circulation in impact craters (in Russian). *Doklady Transactions of Russian Academy of Sciences, 333*(3), 70–72.

McCausland, P. J. A., Flemming, R. L., & Izawa, M. R. M. (2010a, Decemeber). *Quantitative shock stage assessment in olivine and pyroxene bearing meteorites via in situ microXRD* [abstract #P14C-03]. American Geophysical Union Fall Meeting, San Francisco, California.

Meng, S. X., & Maynard, J. B. (2001). Use of statistical analysis to formulate conceptual models of geochemical behavior: water chemical data from the Botucatu aquifer in São Paulo state, Brazil. *Journal of Hydrology, 250*(1-4), 78–97.

Michalski, J. R., Cuadros, J., Bishop, J. L., Darby Dyar, M., Dekov, V., & Fiore, S. (2015). Constraints on the crystal-chemistry of Fe/Mg-rich smectitic clay minerals on Mars and links to global alteration trends. *Earth and Planetary Science Letters, 427*, 215–225.

Murata K. J., Milton, L. L., & Roisenberg, A. (1987). Distribution of zeolites in lavas of southeastern Parana Basin, State of Rio Grande Do Sul. *Brazilian Journal of Geology, 95*, 455–467.

Murchie, S. L., Mustard, J. F., Ehlmann, B. L., Milliken, R. E., Bishop, J. L., McKeown, N. K., Noe Dobrea, E. Z., Seelos, F. P., Buczkowski, D. L., Wiseman, S. M., Arvidson, R. E., Wray, J. J., Swayze, G., Clark, R. N., Des Marais, D. J., McEwen, A. S., & Bilbring, J. P. (2009). A synthesis of Martian aqueous mineralogy after 1 Mars year of observations from the Mars Reconnaissance Orbiter. *Journal of Geophysical Research, 114*(E2), E00D06.

Muttik, N., Kirsimäe, K., Somelar, P., & Osinski, G. R. (2008). Post-impact alteration of surficial suevites in Ries crater, Germany: Hydrothermal modification or weathering processes? *Meteoritics & Planetary Science, 43*(11), 1827–1840.

Naumov, M. V. (2002). Impact-generated hydrothermal systems: data from Popigai, Kara, and Puchezh-Katunki impact structures. In J. Plado, & L. J. Pesonen (Eds.), *Impacts in Precambrian Shields* (pp. 117– 71). Springer-Verlag, Berlin.

Naumov, M. V. (2005). Principal features of impact-generated hydrothermal circulation systems: Mineralogical and geochemical evidence. *Geofluids, 5*(3), 165–184.

Nèdèlec, A., Paquette, J. L., Yokoyama, E., Trindade, R. I. F., Aigouy, T., & Baratoux, D. (2013). In situ U/Pb dating of impact-produced zircons from the Vargeão Dome (Southern Brazil). *Meteoritics & Planetary Science, 48*(3), 420–431.

Newsom, H. E. (1980). Hydrothermal alteration of impact melt sheets with implications for Mars. *Icarus, 44*(1), 207–216.

Norton D. L. (1984). Theory of hydrothermal systems. *Annual Review of Earth and Planetary Science, 12*, 155–177.

Omelon, C. R. (2008). Endolithic microbial communities in polar desert habitats. *Geomicrobiology Journal*, *25*(7-8), 404-414.

Osinski, G. R. (2005). Hydrothermal activity associated with the Ries impact event, Germany. *Geofluids, 5*(3), 202–220.

Osinski, G. R., Cockell, C. S., Pontefract, A., & Sapers, H. M. (2020). The role of meteorite impacts in the origin of life. *Astrobiology, 20*(9), 1121-1149.

Osinski, G. R., Lee, P., Parnell, J., Spray, J. C., & Baron, M. (2005). A case study of impact-induced hydrothermal activity: the Haughton impact structure, Devon Island, Canadian High Arctic. *Meteoritic and Planetary Sci*ence, *40*(12), 1859–1878.

Osinski, G. R., & Pierazzo, E. (2012). *Impact Cratering: Processes and Products.* Oxford, Blackwell Publishing.

Osinski, G. R., Spray, J. G., & Lee, P. (2001). Impact-induced hydrothermal activity within the Haughton impact structure, arctic Canada: Generation of a transient, warm, wet oasis. *Meteoritics & Planetary Science, 36*(5), 731–745.

Osinski, G. R., Tornabene, L. L., Banerjee, N. R., Cockell, C. S., Flemming, R., Izawa, M. R., & Southam, G. (2013). Impact-generated hydrothermal systems on Earth and Mars. *Icarus, 224*(2), 347–363.

Ottens, B., Götze, J., Schuster, R., Krenn, K., Hauzenberger, C., Zsolt, B., & Vennemann, T. (2019). Exceptional Multi Stage Mineralization of Secondary Minerals in Cavities of Flood Basalts from the Deccan Volcanic Province, India. *Minerals, 9*(6), 351.

Parnell, J., Boyce, A., Thackrey, S., Muirhead, D., Lindgren, P., Mason, C., Taylor, C., Still, J., Bowden, S., Osinksi, G. R., & Lee, P. (2010). Sulfur isotope signatures for rapid colonization of an impact crater by thermophilic microbes. *Geology, 38*(3), 271–274.

Petersen, M. T., Newsom, H. E., Nelson, M. J., & Moore, D. M. (2007). Hydrothermal alteration in the Bosumtwi impact structure: Evidence from 2M1-muscovite, alteration veins, and fracture fillings. *Meteoritics & Planetary Science, 42*(4-5), 655–666.

Pickersgill A. E., Flemming R. L., & Osinski G. R. (2015a). Toward quantification of strain-related mosaicity in shocked lunar and terrestrial plagioclase by in situ micro-X-ray diffraction. *Meteoritics & Planetary Science, 50*(11): 1851–1862.

Pinto, V. M., Hartmann, L. A., & Wildner, W. (2010). Epigenetic hydrothermal origin of native copper and supergene enrichment in the Vista Alegre district, Paraná basaltic province, southernmost Brazil. *International Geology Review, 53*(10), 1163–1179.

Posnov, N., Osinski, G. R., Flemming, R. L., McCausland, P. J. A., Pontefract, A., & Crósta, A. (2019, March 18-22). *Classification of shocked basalt from Vargeão Dome and Vista Alegre: Implication for the search for life on Mars* [abstract # 2863]. 50th Lunar and Planetary Science Conference, Houston, TX.

Poty, B., Leroy, J., & Jachimowicz, L. (1976). Fluid inclusions studies in quartz from fissures of western and central Alps. *Schweizer Mineralogische und Petrographische Mitteilungen, 54*, 717–752.

Poulet, F., Gomez, C., Bibring, J. P., Langevin, Y., Gondet, B., Pinet, P., Belluci, G., & Mustard, J. (2007). Martian surface mineralogy from Observatoire pour la Mineralogie, l'Eau, les Glaces et l'Activite on board the Mars Express spacecraft (OMEGA/MEx): Global mineral maps. *Journal of Geophysical Research, 112*, E08S02

Robbins, S. J., & Hynek, B. M. (2012). A new global database of Mars impact craters ≥1 km: 2. Global crater properties and regional variations of the simple-to-complex transition diameter. *Journal of Geophysical Research: Planets, 117*(E6).

Rochette, P., Alac, R., Beck, P., Brocard, G., Cavosie, A. J., Debaille, V., Devouard, B., Jourdan, F., Mougel, B., Moustard, F., Moynier, F., Nomade, S., Osinski, G. R., Reynard, B., & Cornec, J. (2019). Pantasma: Evidence for a Pleistocene circa 14 km diameter impact crater in Nicaragua. *Meteoritics & Planetary Science, 54*(4).

Pusch, R. (1993). *Evolution of models for conversion of smectite to non-expandable minerals* (No. SKB-TR--93-33). Swedish Nuclear Fuel and Waste Management Co., Stockholm, Sweden.

Russell, M. J., Nitschke, W., & Branscomb, E. (2013). The inevitable journey to being. *Philosphical Transaction of the Royal Society B: Biological Sciences, 368*(1622).

Sakharov, B. A., Lindgreen, H., Salyn, A. & Drits, V. A. (1999). Determination of illite-smectite structures using multispecimen X-ray diffraction profile fitting. *Clays and Clay Minerals, 47*, 555-566.

Sapers, H. M., Osinski, G. R., Flemming, R. L., Buitenhuis, E., Banerjee, N. R., Tornabene, L. L., Blain, S., & Hainge, J. (2017). Evidence for a spatially extensive hydrothermal system at the Ries impact structure, Germany. *Meteoritic and Planetary Science, 52*, 351-371.

Schenato, F., Formoso, M., Dudoignon, P., Meunier, A., Proust, D., & Mas, A. (2003). Alteration processes of a thick basaltic lava flow of the Paraná Basin (Brazil): Petrographic and mineralogical studies. *Journal of South American Earth Sciences, 16*(5), 423–444.

Scherer, C. M. (2000). Eolian dunes of the Botucatu Formation (Cretaceous) in southernmost Brazil; morphology and origin. *Sedimentary Geology, 137*(1-2), 63–84.

Schiffman P., & Fridleifsson G.O. (1991). The smectitechlorite transition in drill hole NJ-15, Nesjavellir geothermal field, Iceland: XRD, BSE and electron microprobe investigations. *Journal of Metamorphic Geology*, *9*, 679–696.

Shau Y. H. & Peacor D. R. (1992). Phyllosilicates in hydrothermally altered basalts from DSDP Hole 504B, Leg 83 – a TEM and AEM study. *Contributions to Mineralogy and Petrology*, *112*, 119–133.

Sheppard R. A., & Gude, A. J. 3rd. (1968). Distribution and genesis of authigenic silicate minerals in tuffs of Pleistocene Lake Tecopa, Inyo County, California. *USGS Professional Paper, 597*, 1-38.

Sheppard, R. A., & Gude, A. J. 3rd. (1969). Diagenesis of ruffs in the Barstow Formation, Mud Hills, San Bernardino County, California. *USGS Professional Paper, 634*, 1-35.

Sherriff, B. L., Grundy, H. D., & Hartman, J. S. (1987). Analysis of fluid inclusions using nuclear magnetic resonance. *Geochimica et Cosmochimica Acta*, *51*(8), 2233–2235.

Simpson, S. L., Boyce, A. J., Lambert, P., Lindgren, P., & Lee, M. R. (2017). Evidence for an impact-induced biosphere from the d34S signature of sulphides in the Rochechouart impact structure, France. *Earth and Planet Science Letters, 460*, 192–200.

Squyres, S. W., Grotzinger, J. P., Arvidson, R. E., Bell, J. F., Calvin, W., Christensen, P. R., Clark, B. C., Crisp, J. A., Farrand, W. H., Herkenhoff, K. E., Johnson, J. R., Klingelhöfer, G., Knoll, A. H., McLennan, S. M., McSween Jr., H. Y., Morris, R. V., Rice Jr., J. W., Rieder, R., & Soderblom, L. A. (2004). In situ evidence for an ancient aqueous environment at Meridiani Planum, Mars, *Science, 306*, 1709–1713

Sracek, O., & Hirata, R. (2002). Geochemical and stable isotopic evolution of the Guarani Aquifer System in the state of São Paulo, Brazil. *Hydrogeology Journal, 10,* 643–655.

Środoń, J. (1984). X-Ray Powder Diffraction Identification of Illitic Materials. *Clays and Clay Minerals, 43*(5), 337–349.

Środoń, J. (2001). Quantitative X-Ray Diffraction Analysis of Clay-Bearing Rocks from Random Preparations. *Clays and Clay Minerals, 49*(6), 514–528.

Środoń, J. (2002). Quantitative mineralogy of sedimentary rocks with emphasis on clays and with applications to K-Ar dating. *Mineralogical Magazine, 66*(5), 677–687.

Stöffler, D., Hamann, C., & Metzler, K. (2018). Shock metamorphism of planetary silicate rocks and sediments: Proposal for an updated classification system. *Meteoritics & Planetary Science, 53*(1)*,* 5–49.

Sturkell, E. F. F., Broman, C., Forsberg, P. & Torssander, P. (1998). Impact-related hydrothermal activity in the Lockne impact structure, Jämtland, Sweden. *European Journal of Mineralogy, 10*(3), 589–606.

Sun, V. Z., & Milliken, R. E. (2015). Ancient and recent clay mineral formation on Mars as revealed from a global survey of hydrous minerals in crater central peaks. *Journal of Geophysical Research: Planets*, *120*(12), 2293–2332.

Tomita, K., Yamane, H., & Motaharu, K. (1993). Synthesis of smectite from volcanic glass at low temperature. *Clays and Clay Minerals, 41*, 655–661.

Tornabene, L. L., Osinski, G. R., McEwen, A. S., Wray, J. J., Craig, M. A., Sapers, H. M., & Christensen, P. R. (2013a). An impact origin for hydrated silicates on Mars: A synthesis. *Journal of Geophysical Research: Planets, 118*(5), 994–1012.

Treacy, M. M. J., & Higgins, J. B. (2001). *Collection of Simulated XRD Powder Patterns for Zeolites* (1st Ed,). Elsevier Science.

Treiman, A. H., Morris, R. V., Agresti, D. G., Graff, T. G., Achilles, C. N., Rampe, E. B., Bristow, T.F., Blake, D.F., Vaniman, D.T., Bish, D.L., Chipera, S.J., Morrison, S.M., & Downs, R. T. (2014). Ferrian saponite from the Santa Monica Mountains (California, U.S.A., Earth): Characterization as an analog for clay minerals on Mars with application to Yellowknife Bay in Gale Crater. *American Mineralogist, 99*(11-12), 2234–2250.

Uchizono, A., Shinno, I., Nakamuta, Y., Nakamura, T., & Sekine, T. (1999). Characterization of Artificially Shocked forsterites: (1) Diffraction Profile Analysis by Gandolfi Camera. *Mineralogical Journal*, 21, 15–23.

Utada, M. (2001a). Zeolites in Burial Diagenesis and Low-grade Metamorphic rocks. *Reviews in Mineralogy and Geochemistry, 45*(1), 277–304.

Utada, M. (2001b). Zeolites in hydrothermally altered rocks. In D. L. Bish, & D. W. Ming (Eds.), *Natural zeolites: occurrence, properties, application. Reviews in Mineralogy and Geochem* (pp. 305-322). Mineralogical Society of America.

Vinet, N., Flemming, R. L., & Higgins, M. D. (2011). Crystal structure, mosaicity and strain analysis of Hawaiian olivines using *in situ* X-ray diffraction. *American Mineralogist*, *96*(4): 486–497.

Walker, J. J., & Pace, N. R. (2007). Endolithic microbial ecosystems. *Annual Review of Microbiology, 61*, 331-347.

Warren, B. E. (1941). X-ray diffraction in random layer lattices. *Physical Rev*iew, *59*(9), 693–698.

Xie, T., Shieh, S. R., & Osinski, G. R. (2017). *Raman study of shock effects in lunar anorthite from the Apollo missions* [abstract #1596]. 48th Lunar and Planetary Science Conference, Houston, TX.

Yokoyama, E., Nèdèlec, A., Baratoux, D., Trindade, R. I. F., Fabre, S., & Berger, G. (2015). Hydrothermal alteration in basalts from Vargeão impact structure, south Brazil, and implication for recognition of impact-induced hydrothermalism on Mars. *Icarus 252,* 347–365.

Zaag, P. T., Reimold, W. U., Oliveira, G. J. G, & Crósta, A. P. (2016). *Vargeão Dome impact crater and the Cerro Do Jarau structure (Brazil)- A first report after recent fieldwork* [abstract #6247]. 79th Annual Meeting of the Meteoritical Society, Berlin, Germany.

Zwell, L., & Danko, A. W. (1975). Applications of X-ray diffraction methods to quantitative chemical analysis. *Applied Spectroscopy Reviews, 9*(1), 167–221.

Chapter 4

4 Discussion and Conclusions

This study was primarily designed to help better understand the astrobiological potential of impact craters developed in basaltic target rocks. Based on the results, I recommend a similar approach for missions searching for evidence of life on Mars: first, characterize the mineralogy of the target rock, then identify potential alteration products that can indicate processes that can both increase habitability within the host rock as well as allow for the preservation of biological activity. The Brazilian impact structures Vargeão Dome and Vista Alegre were investigated as planetary analogues for Mars in this study. The structures are excellent analogues for Mars since they are both predominantly composed of basaltic volcanic rock and have a substantial amount of liquid water sourced from the underlying Guarani aquifer.

The objectives of this thesis were to (1) utilize the μXRD method developed by Pickersgill et al. (2015a) for measuring strain-related mosaic spread to quantify shock level in plagioclase, and adjust the technique to support basaltic lithologies; (2) investigate the influence of shock on the physical properties of basaltic rocks, with a particular focus on the effects of shock pressure on the density and porosity of the target rock; (3) investigate impact-induced hydrothermal alteration at the Vista Alegre impact structure; (4) differentiate between pre- and post-impact hydrothermal alteration within and outside of the impact structure; and (5) tie the results together to obtain a better understanding of the habitability of the shocked basalts and breccias from the Vargeão Dome and Vista Alegre impact structures for future investigations of colonization by endolithic microorganisms.

4.1 Shock Effects in Basalt

To achieve the aforementioned goals, I began with a comprehensive optical examination of shock effects in the Vargeão Dome and Vista Alegre impact target basalts and breccias using the Stöffler et al. (2018) updated shock classification system adapted specifically for mafic rocks. Stöffler et al.'s (2018) shock classification system is excellent for quartz

but there is still a wide variation within each shock level ranking when this system is applied to quartz-poor lithologies, which can make shock estimates unreliable. Basaltic systems are dominated by plagioclase feldspar minerals which are known to have complex crystal structures and are particularly susceptible to weathering and degradation. The demand for classification systems to quantitatively assign shock level to plagioclase feldpars has been rapidly growing as research expands beyond the quartz-rich lithology of Earth. I developed a separate shock metamorphism classification system based on optical deformation features in plagioclase feldspar grains from Vargeão Dome and Vista Alegre impact structures (Table 2-4).

Overall, the shock features detected in this study are consistent with previous findings and endorse the impact origin of Vargeão Dome and Vista Alegre (Crósta et al., 2004, 2006, 2010, 2011; Hachiro & Coutinho, 1993; Kazzuo-Vieira et al., 2004). It is important to note that the suspected planar deformation features (PDFs) in plagioclase feldspar grains (which were also claimed to have been detected by Crósta et al., 2006, 2011; Hachiro et al., 1993; Kazzuo-Vieira et al., 2004) require additional study in order to confirm that they are impact-derived shock metamorphism products. At present, it is not conclusive that the planar features believed to be PDFs are not pre-existing planar fractures (PFs), cleavages, or twin planes masked as PDFs. Previous work by Pickersgill et al. (2015a) and Xie et al. (2020) revealed a lack of PDFs in plagioclase feldspar grains from Mistastin Lake impact structure. Their absence is believed to be related to the composition of the plagioclase feldspar (in comparison to alkali feldspars) and the triclinic crystal symmetry of the mineral (higher crystal symmetry required for the development of PDFs) (Pickersgill, 2014). Similar to the feldspar species found in Mistastin, EPMA analysis revealed that Vargeão Dome and Vista Alegre samples are dominated by the intermediate plagioclase species: labradorite and bytownite ($\sim An_{63}$). Based on these results, the suspected PDFs found in the Vargeão Dome and Vista Alegre feldspars should be further analyzed with finer scale instrumentation (e.g., transmission electron microscopy).

Another shock feature of great interest that requires further attention is diaplectic feldspar glass. Diaplectic glass has been recently proposed to form in the central uplift of much

smaller craters than previously expected, although it is fragmented and incorporated into brecciated rocks (Singleton, 2019). This implies that the presence of diaplectic feldspar glass recorded by Crósta et al. (2010) in the central uplift of Vargeão Dome (12.9 km) may, in fact, be reasonable and would confirm that the formation of diaplectic glass is possible in smaller impact structures. Several areas in samples within the Vargeão Dome central uplift were petrographically identified as potential diaplectic glass. However, upon further analysis, µXRD and Raman spectroscopy failed to show diagnostic peaks indicative of diaplectic glass. No isotropic feldspar was found. The lack of diaplectic glass is what I expected, as the presence of isotropic feldspar is indicative of shock pressures of ~45 GPa (Stöffler et al., 2018; Therriault et al., 2002), and even larger impact structures (e.g., Siljan: 75 km, Charlevoix: 54 km, West Clearwater: 35–40 km and Slate Islands: 30 km) do not show evidence of shock pressures exceeding 30 GPa (Dence, 2004; Farley and McKeon, 2015; Grieve and Robertson, 1976; Halls & Grieve, 1976; Rae et al., 2017; Robertson, 1975; Robertson & Grieve, 1977; Stesky & Halls, 1983). There are many factors that can affect the propagation of shock waves through a target material (such as lithology and grain size), however, the extent to which this influences the recorded shock pressure in relation to crater size is still poorly understood and requires further study.

Shock characterization using optical deformation analysis is still very limited when used on its own. Recent studies have been developed combining petrography with thermal infrared spectroscopy (Johnson et al. 2002, 2003), Raman spectroscopy (Fritz et al., 2005; Heymann & Hörtz, 1990; Reynard et al., 1999; Velde & Boyer, 1985; Velde et al., 1989; Xie et al., 2017; Xie et al., 2020; Yin & Dai, 2020), and µXRD methods (Pickersgill et al., 2015a, 2015b; Sims et al., 2019) to determine shock level in feldspars, but none of these methods have been tested on naturally shocked plagioclase-rich basaltic impact rocks.

This study adds to the recognition that µXRD is a promising technique for not only compositional characterization of minerals, but also for measuring strain of the mineral of interest (Flemming, 2007). All µXRD measurements can be completed without special preparation or alteration of the sample, making it ideal for delicate or rare samples.

Pickersgill et al. (2015a) measured the strain-related mosaicity of feldspar grains from the Mistastin impact structure by averaging the FWHMχ values of all diffraction peaks that are characteristic to plagioclase. In this study, I have demonstrated that the previously applied method by Pickersgill et al. (2015a) may not be the most efficient or accurate technique. The method described as method 2 in this study uses the most abundant and intense labradorite diffraction peak, which in our case was at ~32° 2θ (3.2 Å), and averages all of the FWHMχ values for the grain (Chapter 2). This technique produced values that are comparable to Pickersgill's method, but the results are acquired much more efficiently. The Miller indices recommended to be used for this method are ($\bar{2}$02), (002), (040), ($\bar{2}$20), and ($\bar{2}$04) for triclinic plagioclase, ICDD card 78-0435.

Additional methods were investigated using only the maximum FWHMχ value throughout the feldspar grain (method 3) and was tested alongside method 2 and the original technique described by Pickersgill et al. (2015a) (method 1). Method 3 produced the highest variability between FWHMχ values with the greatest overlap between the shock levels, however still illustrated a positive correlation between shock level and FWHMχ values where streak length along χ increases with the shock level. There is still uncertainty regarding which method should be used, but the potential variability between grains within a sample indicates grain FWHMχ values should not be averaged. Grain size, crystallographic orientation, and effects of water and nearby mineralogy all play a role in the amount of shock a grain will experience and therefore the maximum FWHMχ of a peak consistent throughout the samples in theory should represent the peak impact pressure experienced by the target rock (Dence, 2004; Robertson & Grieve, 1977).

Our results indicate that the new methods developed in this study have improved the efficiency of the process in comparison to the original technique, but there is still variation in streak length and overlap between shock levels. Additional work to develop more subdivisions and more precise smaller groups is recommended. μXRD data calibration curves for various shocked plagioclase compositions have been proposed and preliminary results for shocked andesine anorthosite have been promising (Cao et al., 2020). However, prior to standardizing universally applicable calibration curves for naturally shocked samples, it is important to determine the most effective technique for

assessing metamorphic shock and the quantitative relationship between the strain-related mosaicity in the χ dimension and the corresponding shock pressure.

4.2   Changes in Density and Porosity

Impact metamorphism increases the porosity of the target rock (Cockell et al., 2005), and the porosity was found to increase proportionally with shock level while density decreased (Cockell & Osinski, 2007; Singleton et al., 2011). Unlike sedimentary lithologies, crystalline rocks do not experience a collapse of pore space at pressures over 35 GPa, but rather proportionally increase in porosity until reaching the temperature of vaporization (Cockell & Osinski, 2007).

Singleton et al. (2011) investigated the effect of shock (shock level 0–7) on the porosity of gneiss samples from the Haughton impact structure. The results revealed a large range of values for porosity, especially for samples of higher shock levels. Compared to Haughton (which exhibits shock levels up to 7, Singleton et al., 2011), Vargeão Dome and Vista Alegre only reach shock level M-S3 (Stöffler et al., 2018) and display significantly less variability in the porosity of the shocked basaltic samples. The variability in porosity is likely due to the fact that the gneiss samples from Haughton were collected from crater-fill impactites and samples included a much wider range of shock pressures; also, Haughton is younger and very much less eroded in comparison to Vargeão Dome and Vista Alegre basalts.

Despite their many similarities, Vargeão Dome and Vista Alegre appear to differ in porosity. Vista Alegre impact basalt samples of the same shock level generally exhibit lower porosity than what is seen in Vargeão Dome basalts (Chapter 2). The dissimilarity in porosity is unexpected since the compositional differences between impact structures are minute, the craters are similarly sized, and have both experienced hydrothermal alteration. The differences can likely be attributed to the small Vista Alegre sample size, but further study would be required to confirm this hypothesis.

Similar to the Haughton results, lower shock level samples display slight deviation from the normal density and porosity of basalts and only begin to show an increase in porosity

and decrease in density above shock level S-3 (Table 2-7). Density appears to increase slightly initially and then decrease as expected. The initial increase is likely due to: (1) the small sample size of Vista Alegre basalts failing to capture the variation in the target rock, (2) the unshocked samples may have been highly vesiculated prior to the impact event and the shock caused the collapse of vesicles and decrease in porosity, and (3) the alteration of impact-damaged rocks results in the lowered bulk and grain density, subsequently reducing the porosity of the samples.

4.3   Hydrothermal Alteration

Lonar (India) and Vargeão Dome (Brazil) are the only two basaltic impact structures that have previously been studied for hydrothermal alteration, providing insight into expected impact-induced alteration products on Mars (Hagerty & Newsom, 2003; Yokoyama et al., 2015). Lonar crater was the first analogue to Martian crustal lithology revealing that the dominant alteration minerals produced in terrestrial impact basaltic compositions match the alteration minerals found on Mars (Hagerty & Newsom, 2003). The Vargeão Dome impact structure – studied by Yokoyama et al. (2015) – formed similar post-impact hydrothermal deposits but they are restricted to the basaltic breccia veins. Chapter 3 provides a detailed summation of hydrothermal alteration phases (e.g., carbonate, Fe-Mg clays, Al-clays, zeolites and quartz) and textures (including alteration vesicles, altered impact glass, multiple generation of quartz growth, interlayer compositions and veining) observed in Vargeão Dome's sister structure, Vista Alegre.

The overgrowth present shows signs of selective alteration and sometimes exhibit complete replacement of minerals, a phenomenon that is present in all samples. Using optical microscopy, EPMA and μXRD, this study revealed compositional and textural differences between post-impact hydrothermal alteration within the shocked Vista Alegre samples in comparison to the unshocked and pre-impact hydrothermal alteration of the Parana basin basalts that formed during low-grade metamorphism period.

The main indicator of post-impact hydrothermal alteration is the crosscutting relationship between alteration veins and the surrounding shocked material (e.g., groundmass and breccia clasts).

Additional observations of differences between pre- and post-impact hydrothermal deposits can be seen in the crystallization textures of zeolites and secondary quartz present in the samples. Zeolites infill vesicles in our unshocked basalts acquired from outside the impact structure, however, in the shocked samples from within the impact crater, zeolites are found lining voids, fractures, and minerals. In unshocked samples, quartz rims form evenly around vesicles indicating a uniform deposition. In contrast, post-impact quartz forms unevenly and accumulates preferentially in points of weakness such as fractures, cracks, and pores. The difference in zeolite and quartz textures was likely due to different durations of fluid flow associated with different hydrothermal events.

Alteration minerals in the shocked breccias within the impact structure display a larger variation in mineral compositions and textures. Hydrothermal systems have notably more variables affecting the process (temperature, fluid composition, pH) and therefore form a greater variety of alteration minerals (Inoue, 1995; Muttik et al., 2008). While it is possible that the alteration minerals were produced by pre-impact hydrothermal activity, it is more likely that a majority of these species formed as a result of impact-related processes and subsequent alteration.

Quantified analysis of clay minerals remains a challenge due to the complexity of clay structures; making a standardized and routine quantitative analysis method difficult to achieve. When characterizing hydrothermal alteration minerals, several authors have concluded that an approach combined with electron microprobe work is necessary to obtain precise identification (e.g., Bettison & Schiffman, 1988; Bettison-Varga et al., 1991; Chen et al., 2019). Our results support this idea and endorses the practice of joining µXRD and electron microprobe analysis. The novel µXRD technique described in this study can achieve 2θ limits required to measure various types of clays and zeolites to the extent that pXRD techniques can, however it performs the analysis *in situ* and non-destructively. The current limitation of the modified µXRD method is that it is only capable of analyzing spots within one centimeter from the edge of the thin section. In addition, µXRD utilizes a nominal 300-micron size beam such that when analyzing a sample in-situ, it is difficult to isolate and analyze only a specific mineral. Rather, you

obtain a broader understanding of the variety of different minerals within the sample. Such data may be more beneficial for hydrothermal deposit detection of extraterrestrial surfaces such as Mars where there is no geological context available.

Hydrothermal deposits on Mars are concentrated in the heavily cratered Noachian terrains (Ehlmann et al., 2013; Fairén et al., 2010). With the lack of geological activity that has been recognized in that region, it is important to understand the origin of clay minerals with regard to impact cratering. Schwenzer and Kring (2013) used Martian meteorite mineralogy to model impact hydrothermal alteration on Mars. Similar to the dominant lithology of Mars, the prevailing alteration minerals of shocked basalts at Lonar, Vargeão Dome and Vista Alegre are Fe/Mg smectites ± chlorites, with minor amounts of Fe-rich phyllosilicates (e.g. celadonite) and carbonates (Hagerty & Newsom, 2003; Yokayama et al., 2015). Fe/Mg smectites and chlorites are widely distributed in the Noachian terrains and are thought to have been produced in the subsurface through impact induced hydrothermal alteration (e.g., Allen et al., 1982; Ehlmann et al., 2009; Newsom, 1980; Sun & Milliken, 2015; Tornabene et al., 2013). Chlorite is a high temperature variation of clay and is likely to be produced at depth or at the surface by alteration of crater fill melt sheets on Mars (Naumov, 2002, 2005; Osinski et al., 2004; Sapers et al., 2017; Tornabene et al., 2013). In our samples, chlorite-smectite clays are abundant in both pre-impact and post-impact basalts, but in the shocked impact breccias, chlorite-smectite mixed clays contain a variety of chemical compositions and form in a variety of different assemblages. By further advancing our understanding of textural and compositional differences not only on chlorite-smectite clays, but all alteration minerals that are present on Mars, a better understanding of the origin of hydrothermal phases found on Mars may be achieved.

4.4   Biological Perspective

Meteorite impact events into water-bearing targets form localized environment encompassing many of the requirements for life residing in extreme environments, including, (1) a mineralogical source of energy and nutrients, (2) a water reservoir, (3) shielding from UV light and ionizing radiation, (4) temperature moderation, (5) humidity regulations, and (6) accessible and chemically regulated microhabitats (Cockell, 2006;

Cockell et al., 2002; Omelon, 2008; Osinski et al., 2020; Tait et al., 2016; Walker & Pace, 2007). The resulting decrease in density and increase in porosity resulting from the impact event expands available habitat for both endolithic and subsurface colonization, both through the creation of physical space within the substrate, increased available surface area, and increased rock-water interactions (Pontefract et al., 2016). Based on initial observations in this study, Vargeão Dome and Vista Alegre display features indicative of shock level M-S3 (~20-22 GPa) (Chapter 2). By comparison, one might assume that larger impact structures that experienced greater shock pressures, such as the gneiss samples from the Haughton impact crater which reached 60-70 GPa with significantly higher porosity (~60%) (Singleton et al., 2011), would be more successful in hosting colonizing microbial organisms than Vargeão Dome and Vista Alegre. However, crystalline rocks of very high shock levels result in complete melting and flow of the substrate, inhibiting connections between pores and lowering the effective permeability for microbial colonization (Pontefract et al., 2014). Pores are important for the percolation of water, distribution of dissolved nutrients, and movement of microbiota, making the ~27% porosity at Vargeão Dome and Vista Alegre at the highest shock levels (M-S2) attractive for endolithic microorganisms, especially owing to the increased nutrient availability relative to the Haughton gneisses.

The majority of studies on microbial colonization in basaltic lithologies has focused on young sub-seafloor basalts (Ivarsson et al., 2015; Kelly et al., 2010), older oceanic crust ophiolites (Furnes et al., 2008; Orcutt et al., 2020; Staudigel et al., 2006), volcanic glass (Cockell et al., 2009a, 2009b; Izawa et al., 2011), and meteorites (Tait et al., 2016, 2017). Although deep ocean basaltic glass is often similar in composition, their environments are markedly different. Terrestrial basalts are exposed to freshwater/snowmelt, acidic rainwater, large temperature fluctuations, sunlight (photosynthetically active radiation and UV radiation) and periodic desiccation. A study by Antony et al. (2014) of Lonar crater lake compared colonization between submerged basalts on the soda lakebed and exposed basalts on the crater wall. The results revealed a significant difference in the microbial populations between the submerged/exposed basaltic glass of the crater and studies of deep-ocean and terrestrial basaltic glasses. In actuality, the phylotypes observed were found to be more closely associated with soil and sediment assemblages

(Antony et al., 2014; Mason et al., 2007). This suggests that the Lonar crater environment harbors unique prokaryotic populations and it would be interesting to see if other basaltic impact structures affected by hydrothermal alteration compare favourably, or not, to the microbial diversity at Lonar crater.

No microbiological studies have been completed on the Vargeão Dome and Vista Alegre basalts or the Parana Basin flood basalts. A study by Ramos et al. (2014) on the availability of mineral nutrients such as a fertilizer for soil from the Serra Geral Formation volcanic rocks on which Vargeão Dome and Vista Alegre formed, revealed the presence of calcium, magnesium (as carbonates), and the presence of micronutrients such as zinc, boron, copper, iron and manganese in a high alkalinity environment. Although this study is directed at identifying nutrients in soil, these elements may also be utilized as nutrients by microorganisms. Basalts are among the greatest nutrient supplying rock types, and when associated with impact events and hydrothermal systems, they may form the perfect environment for life on other planets or even facilitate the genesis of novel life. After all, thermophilic roots in the 16S RNA phylogenetic tree of life may suggest that early development of life on Earth formed in hydrothermal environments (Nisbet & Sleep, 2001; Weiss et al., 2016).

4.5　References

Allen, C. G., Gooding, J. L., & Keil, K. (1982). Hydrothermally altered impact melt rock and breccia: contributions to the soil of Mars. *Journal of Geophysical Research*, *87*(B12), 10083–10101.

Antony, C. P., Shimpi, G. G., Cockell, C. S., Patole, M. S., & Shouche, Y. S. (2014). Molecular Characterization of Prokaryotic Communities Associated with Lonar Crater Basalts. *Geomicrobiology Journal, 31*(6), 519–528.

Bettison, L. A., & Schiffman, P. (1988). Compositional and structural variations of phyllosilicates from the Point Sal ophiolite, California. *American Mineralogist, 73*(1-2), 62–76.

Bettison-Varga, L., Mackinnon, I. D. R., & Schiffman, P. (1991). Integrated TEM, XRD, and electron microprobe investigation of mixed-layer chlorite smectite from the Point Sal ophiolite. *Journal of Metamorphic Geology, 9*(6), 697–710.

Cao, F., Jaret, S. J., Flemming, R. L., Izawa, M. R. M., & Johnson, J. R. (2020). *Micro X-ray diffraction characteristics of experimentally shocked andesine anorthosite: implications for quantifying shock effects in meteorites* [abstract # 2114]. 51st Lunar and Planetary Science Conference, Houston, TX.

Chen, Y., Wang, Q., Han, Y., Shen, J., Kong, Y., & Zhang, X. (2019). Crystallization variations in clay minerals with latitude in Jilin province, China: a climate perspective. *Clays and Clay Mineralogy, 67*, 507–517.

Cockell, C. S. (2006). The original and emergence of life under impact bombardment. *Philosophical Transactions of the Royal Society B: Biological Sciences, 361*(1474), 1845-1856.

Cockell, C. S., Lee, P., Broady, P., Lim, D. S. S., Osinski, G. R., Parnell, J., Koeberl, C., Pesonen, L., & Salminen, J. (2005). Effects of asteroid and comet impacts on habitats for

lithophytic organisms —A synthesis. *Meteoritics & Planetary Science, 40*(12), 1901–1914.

Cockell, C. S., Lee, P., Osinski, G. R., Horneck, G., & Broady, P. (2002). Impact-induced microbial endolithic habitats. *Meteoritics & Planetary Science,* 37(10), 1287–1298.

Cockell, C. S., Olsson-Francis, K., Herrera, A., & Meunier, A. (2009b). Alteration textures in terrestrial volcanic glass and the associated bacterial community. *Geobiology, 7*(1), 50–65.

Cockell, C. S., Olsson, K., Knowles, F., Kelly, L., Herrera, A., Thorsteinsson, T., & Marteinsson, V. (2009a). Bacteria in Weathered Basaltic Glass, Iceland. *Geomicrobiology Journal, 26*(7), 491–507.

Cockell, C. S., & Osinski, G. R. (2007). Impact-induced impoverishment and transformation of a sandstone habitat for lithophytic microorganisms. *MAPS, 42*(11), 1985–1993.

Crósta, A. P., Kazzuo-Vieira, C., Choudhuri, A., & Schrank, A. (2006). Vargeão Dome Astrobleme, State of Santa Catarina: A meteoritic impact record on volcanic rocks of the Paraná Basin. In M. Winge, C. Schobbenhaus, M. Berbert-Born, E. T. Queiroz, & D. A. Campos (Eds.), *Sı́tios Geológicos e Paleontológicos do Brasil* (vol. 2, pp. 1-12). Brası́lia, DF: SIGEP ⁄ DNPM.

Crósta, A. P., Kazzuo-Vieira, C., Pitarello, L., Koeberl, C., & Kenkmann, T. (2011). Geology and impact features of Vargeão Dome, southern Brazil. *Meteoritics & Planetary Science, 47*(1), 51-71.

Crósta, A. P., Kazzuo-Vieira, C., & Schrank, A. (2004, August 2-6). *Vista Alegre: A newly discovered impact crater in southern Brazil* [abstract #5051]. 67th Annual Meteoritical Society Meeting, Glasgow, UK.

Crósta, A. P., Koeberl, C., Furuie, R. A., & Kazzuo-Vieira, C. (2010). The first description and confirmation of the Vista Alegre impact structure in the Paraná flood basalts of southern Brazil. *Meteoritics & Planetary Science, 45*(2), 181–194.

Dence, M. R. (2004). Structural evidence from shock metamorphism in simple and complex impact craters: Linking observations to theory. *Meteoritics & Planetary Science, 39*(2), 267–286.

Ehlmann, B. L., Berger, G., Mangold, N., Michalski, J. R., Catling, D. C., Ruff, S. W., Chassefière, E., Niles, P. B., Chevrier, V., & Poulet, F. (2013). Geochemical consequences of widespread clay mineral formation in Mars' ancient crust. *Space Science Reviews*, *174*(1-4), 329–364.

Ehlmann, B. L., Mustard, J. F., Swayze, G. A., Clark, R. N., Bishop, J. L., Poulet, F., Des Marais, D. J., Roach, L. H., Milliken, R. E., Barnouin-Jha, O., & Murchie, S. L. (2009). Identification of hydrated silicate minerals on Mars using MRO-CRISM: Geologic context near Nili Fossae and implications for aqueous alteration, *Journal of Geophysical Research*, *114*(E2), E00D08.

Fairén, A. G., Chevrier, V., Abramov, O., Marzo, G. A., Gavinc, P., Davila, A. F., Tornabene, L. L., Bishop, J. L., Roush, T. L., Gross, C., Kneissl, T., Uceda, E. R., Dohm, J. M., Schulze-Makuch, D., Rodriguez, J. A. P., Amils, R., & McKay, C. P. (2010). Noachian and more recent phyllosilicates in impact craters on Mars. *Proceedings of the National Academy of Sciences of the United States of America*, *107*(27), 12095-12100.

Farley, K. A., & McKeon, R. (2015). Radiometric dating and temperature history of banded iron formation–associated hematite, Gogebic iron range, Michigan, USA. *Geology, 43*(12), 1083–1086.

Fritz, J., Greshake, A., & Stöffler, D. (2005). Micro-Raman spectroscopy of plagioclase and maskelynite in Martian meteorites: Evidence of progressive shock metamorphism. *Antarctic Meteorite Research, 18*, 96–116.

Grieve R. A. F., Dence M. R., & Robertson P. B. (1977). Cratering processes: As interpreted from the occurrences of impact melts. In D. J. Roddy, R. O. Pepin, & R. B. Merrill (Eds.), *Impact and explosion cratering* (pp. 791–814). New York: Pergamon Press.

Grieve, R. A. F., & Robertson, P. B. (1976). Variations in shock deformation at the Slate Islands impact structure, Lake Superior, Canada. *Contributions to Mineralogy and Petrology, 58*, 37–49.

Hachiro J., Coutinho J. M. V., Frasca´ M. H. B., de O., & Menezes, C. M. (1993). *O astroblema de Vargea˜o (SC): Evideˆncias petrogra´ficas de um crateramento criptoexplosivo por petardo extraterrestre.* 3° Simpo´sio de Geologia do Sudeste Rio de Janeiro, Brazil: Sociedade Brasileira de Geologia. pp. 276–281.

Hagerty, J. J., & Newsom, H. E. (2003). Hydrothermal alteration at the Lonar Lake impact structure, India: Implications for impact cratering on Mars. *Meteoritics & Planetary Science, 38*(3), 365–381.

Halls, H. C., & Grieve, R. A. F. (1976). The Slate Islands, a probable complex impact structure in Lake Superior. *Canadian Journal of Earth Science*, *13*(9), 1301-1309.

Heymann, D., & Hörz, F. (1990). Raman-spectroscopy and Xray diffractometer studies of experimentally produced diaplectic feldspar glass. *Physics and Chemistry of Minerals, 17*, 38–44.

Inoue, A., Lanson, B., Marques-Fernandes, M., Sakharov, B. A., Murakami, T., Meunier, A., & Beaufort, D. (2005). Illite-smectite mixed-layer minerals in the hydrothermal alteration of volcanic rocks: I. One-dimensional XRD structure analysis and characterization of component layers. *Clays and Clay Mineralogy, 53*(5), 423–439.

Izawa, M. R. M., Banerjee, N. R., Osinski, G. R., Flemming, R. L., Parnell, J. & Cockell, C. S. (2011). Weathering of post-impact hydrothermal deposits from the Haughton Impact Structure: implications for microbial colonization and biosignature preservation. *Astrobiology, 11*(6), 537–550.

Johnson J. R., Hörz F., Lucey P. G., & Christensen P. R. (2002). Thermal infrared spectroscopy of experimentally shocked anorthosite and pyroxenite: Implications for remote sensing of Mars. *Journal of Geophysical Research, 107*(10), 50–73.

Johnson, J. R., Hörz, F., & Staid, M. I. (2003). Thermal infrared spectroscopy and modeling of experimentally shocked plagioclase feldspars. *American Mineralogist, 88*(10), 1575–1582.

Kazzuo-Vieira, C., Crósta, A. P., & Choudhuri, A. (2004, August 2-6). *Impact features from Vargeã˜o Dome, Southern Brazil* [abstract #5050]. 67th Annual Meteoritical Society Meeting, Glasgow, UK.

Muttik, N., Kirsimäe, K., Somelar, P., & Osinski, G. R. (2008). Post-impact alteration of surficial suevites in Ries crater, Germany: Hydrothermal modification or weathering processes? *Meteoritics & Planetary Science, 43*(11), 1827–1840.

Nayak, V. K. (1972). Glassy objects (impactite glasses?): A possible new evidence for meteoritic origin of the Lonar Crater, Maharashtra State, India. *Earth and Planetary Science Letters*, *14*(1), 1–6.

Newsom, H. E. (1980). Hydrothermal alteration of impact melt sheets with implications for Mars. *Icarus, 44*(1), 207–216.

Nisbet, E. G., and Sleep, N. H., (2001). The habitat and nature of early life. *Nature, 409,* 1083-1091.

Omelon, C. R. (2008). Endolithic microbial communities in polar desert habitats. *Geomicrobiology Journal*, *25*(7-8), 404-414.

Osinski, G. R., Cockell, C. S., Pontefract, A., & Sapers, H. M. (2020). The Role of Meteorite Impacts in the Origin of Life. *Astrobiology*, *20*(9), 1121-1149.

Pickersgill, A. E. (2014). *Shock Metamorphic Effects in Lunar and Terrestrial Plagioclase Feldspar Investigated by Optical Petrography and Micro-X-Ray Diffraction*

[Doctoral dissertation, University of Western Ontario] . Electronic Thesis and Dissertation Repository.

Pickersgill, A. E., Flemming, R. L., & Osinski, G. R. (2015a). Toward quantification of strain-related mosaicity in shocked lunar and terrestrial plagioclase by in situ micro-X-ray diffraction. *Meteoritics & Planetary Science, 50*(11), 1851–1862.

Rae, A. S. P., Collins, G. S., Grieve, R. A. F. Osinski, G. R., & Morgan J. V. (2017). Complex crater formation: Insights from combining observations of shock pressure distribution with numerical models at the West Clearwater Lake impact structure. *Meteoritics & Planetary Science, 52*(7), 1330–1350.

Ramos, C. G., Mello, A. G., & Kautzmann, R. M. (2014). A preliminary study of acid volcanic rocks for stonemeal application. *Environmental Nanotechnology, Monitoring & Management, 1-2*, 30–35.

Reynard, B., Okuno, M., Shimada, Y., Syono, Y., & Willaime, C. (1999). A Raman spectroscopic study of shock-wave densification of anorthite (CaAl2Si2O8) glass. *Physics and Chemistry of Minerals, 26*, 432–436.

Robertson, P. B. (1975). Zones of shock metamorphism at the Charlevoix impact structure, 76 Quebec. *Geological Society of America Bulletin, 86*, 1630–1638.

Robertson, P. B. & Grieve, R. A. F. (1977). Shock attenuation at terrestrial impact structures. In D. J. Roddy, R. O. Pepin, & R. B. Merrill (Eds.), *Impact and explosion cratering: Planetary and terrestrial implications* (pp. 687-702). Pergamon Press (New York).

Sapers, H. M., Osinski, G. R., Flemming, R. L., Buitenhuis, E., Banerjee, N. R., Tornabene, L. L., Blain, S., & Hainge, J. (2017). Evidence for a spatially extensive hydrothermal system at 211 the Ries impact structure, Germany. *Meteoritics & Planetary Science*, *52*(2), 351–371.

Schwenzer, S. P., & Kring, D. A. (2013). Alteration minerals in impact-generated hydrothermal systems - Exploring host rock variability. *Icarus, 226*(1), 487-496.

Sims, M., Jaret, S. J., Carl, E., Rhymer, B., Schrodt, N., Mohrholz, V., Smith J., Konopkova, Z., Liermann, H. P., Glotch, T. D., & Ehm, L. (2019). Pressure-induced amorphization in plagioclase feldspars: A time-resolved powder diffraction study during rapid compression. *Earth and Planetary Science Letters, 507*, 166–174.

Singleton, A. (2019) *Characteristics of Impactites in the Central Uplift of the Mistastin Lake Impact Structure, Canada* [Doctoral dissertation, University of Western Ontario]. Electronic Thesis and Dissertation Repository.

Singleton, A. C., Osinski, G. R., McCausland, P. J. A., & Moser, D. E. (2011). Shock-induced changes in density and porosity in shock-metamorphosed crystalline rocks, Haughton impact structure, Canada. *Meteoritics & Planetary Science, 46*(11), 1774–1786.

Stesky, R. M., & Halls, H. C. (1983). Structural analysis of shatter cones from Slate Islands, northern Lake Superior. *Canadian Journal of Earth Sciences, 20*(1), 1-18.

Stöffler, D., Hamann, C., & Metzler, K. (2018). Shock metamorphism of planetary silicate rocks and sediments: Proposal for an updated classification system. *Meteoritics & Planetary Science, 53*(1), 5– 49.

Sun, V. Z., & Milliken, R. E. (2015). Ancient and recent clay mineral formation on Mars as revealed from a global survey of hydrous minerals in crater central peaks. *Journal of Geophysical Research: Planets*, *120*(12), 2293–2332.

Tait, A. W., Wilson, S. A., Tomkins, A. G., Gagen, E. J., Fallon, S. J., & Southam, G. (2017). Evaluation of meteorites as habitats for terrestrial microorganisms: Results from the Nullarbor Plain, Australia, a Mars analogue site. *Geochimica et Cosmochimica Acta, 215,* 1-16.

Therriault, A. M., Grieve, R. A. F., & Pilkington, M. (2002). The recognition of terrestrial impact structures. *Czech Geological Survey, 77*(4), 253–263.

Tornabene, L. L., Osinski, G. R., McEwen, A. S., Wray, J. J., Craig, M. A., Sapers, H. M., & Christensen, P. R. (2013). An impact origin for hydrated silicates on Mars: A synthesis. *Journal of Geophysical Research: Planets*, *118*(5), 994–1012.

Velde, B., & Boyer, H. (1985). Raman microprobe spectra of naturally shocked microcline feldspars. *Journal of Geophysical Research: Solid Earth, 90*(B5)*,* 3675–3682.

Velde, B., Syono, Y., Kikuchi, M., & Boyer, H. (1989). Raman microprobe study of synthetic diaplectic plagioclase feldspars. *Physics and Chemistry of Minerals, 16*, 436–441.

Walker, J. J., & Pace, N. R. (2007). Endolithic microbial ecosystems. *Annual Review of Microbiology, 61*, 331-347.

Weiss, M. C., Sousa, F. L., Mrnjavac, N., Neukirchen, S., Roettger, M., Nelson-Sathi, S., & Martin, W. F. (2016). The physiology and habitat of the last universal common ancestor. *Nature Microbiology*, *1*, 16116.

Wright, P. S., Christensen, P. R., & Sharp, T. G. (2011). Laboratory thermal emission spectroscopy of shocked basalt from Lonar Crater, India, and implication for Mars orbital and sample data. *Journal of Geophysical Research: Planets 116*(E9).

Xie, T., Osinski, G. R., & Shieh, S. R. (2020). Raman study of shock features in plagioclase feldspar from the Mistastin Lake impact structure, Canada. *Meteoritics & Planetary Science*, *55*(7), 1471-1490.

Xie, T., Shieh, S. R., & Osinski, G. R. (2017). *Raman study of shock effects in lunar anorthite from the Apollo missions* [abstract #1596]. 48th Lunar and Planetary Science Conference, Woodlands, TX.

Yin, F., & Dai, D. (2020). A study of shock-metamorphism features of feldspars from the Xiuyan impact crater. *Minerals, 10*(3), 231.

Yokoyama, E., Nèdèlec, A., Baratoux, D., Trindade, R. I. F., Fabre, S., & Berger, G. (2015). Hydrothermal alteration in basalts from Vargeão impact structure, south Brazil,

and implication for recognition of impact-induced hydrothermalism on Mars. *Icarus, 252*, 347–365.

Appendices

Appendix A: Impact Craters as Habitats for Life: Endolithic Colonization of Shocked Basalts from the Vargeão Dome and Vista Alegre impact structures, Brazil

The ability of microorganisms to tolerate, and even thrive, in extreme environments on Earth has driven the current research on habitats of potential ancient microbial life on Mars. "*Endolithism*" by microorganisms (i.e., seeking refuge in the subsurface where conditions are suitable, and in some cases improved, Coleine et al., 2020) is a survival strategy that is of particular interest to the astrobiology community as it can provide protection from numerous hazardous conditions that make Mars inhospitable on the surface (Nienow & Friedmann, 1998). Rock environments protect microorganisms by: shielding them from (1) ultraviolet light, ionizing radiation, (2) variations in temperature, humidity, and (3) abrasive winds (Osinski et al., 2020; Tait et al., 2016). Furthermore, microorganisms capable of growing as endoliths can make use of detrital/wind blow debris, as well as the *in situ* mineralogy, as a source of energy and nutrients (Barker et al., 1997; Bennet et al., 2001; Ehrlich 1998; de los Ríos et al., 2002; Kornheiser et al., 2008; Welch et al., 1999).

One geological process capable of generating suitable endolithic environments, and common to all rocky planets in the solar system, are meteorite impact events (e.g., Cockell & Lee, 2002; Osinski & Pierazzo, 2012). In otherwise low porosity substrates, the immense kinetic energy released locally during an impact event results in both macro- and micro-scale changes in the lithology, where the increase in porosity of the target rocks creates cryptoendolithic (pore spaces or voids) and chasmoendolithic (fissure and cracks) microhabitats, which facilitate microbial growth by increasing the surface area available for colonization, as well as chemical reactions supporting microbial metabolism (Cockell, 2006; Pontefract et al., 2016).

Furthermore, an impact event into a target rock with pre-existing hydrological activity, such as subsurface ground ice (e.g., Mars), may also generate a transient hydrothermal

system (Naumov, 2002; Naumov, 2005; Osinski et al., 2005; Osinski et al., 2013). Geochemical reactions resulting from the interaction of heated rock and water produce a variety of secondary alteration products (e.g., sulfates, halides, carbonates, Fe-oxyhydroxides, and smectites) which can serve as nutrients for microorganisms, and moreover, have important implications for pre-biotic synthesis and the origin of life (Ferris et al., 1988; Saladio et al., 2001; Smith, 1998; Zamaraev et al., 1997).

To better understand these environments, research is being conducted into evaluating the habitability of impact craters on Earth. To date, the majority of the research on endolithic communities has focused on crystalline rock substrates, in particular, gneisses from Haughton impact structure, Canada (Cockell, 2004; Cockell et al., 2002, 2005; Pontefract et al., 2012, 2014, 2016) and impact glasses from the Ries impact structure, in Germany (Sapers et al., 2014). Geomicrobiological studies on Haughton impact structure reveal a clear relationship between the increase in biomass level and community complexity with increasing shock level (Pontefract et al. 2014). However, the microorganisms living within the shocked gneisses do not strongly utilize the substrate (Cockell & Osinski 2007; Fike et al., 2003; Pontefract et al., 2012). In contrast to this, surficial suevite from the Ries impact structure shows biologically formed tubules within the impact glass (Sapers et al., 2014), which contains higher amounts of biologically relevant nutrients. Other rock types such as basalts are known to have an increased presence of metabolically relevant elements that are readily accessible (Cockell et al., 2009a). Additional factors that may influence the habitability potential of a material are the variation in availability of fractures and pore spaces for growth, differences in permeability and thus fluid flow and albedo, proportion of glass, chemical weathering, and biological factors (Banerjee & Muehlenbachs, 2003; Cockell et al., 2002, 2009a,b, 2011, 2012; Cockell & Osinski, 2007; Freidmann, 1982; Izawa et al., 2010; Lee et al., 2013; Osinski, 2007; Pontefract et al., 2014, 2016; Sapers et al., 2014, 2015; Singleton et al., 2011, etc..).

Unlike the Earth, which is dominated by sedimentary rocks, on Mars the primary lithology is basalt (McSween et al., 2009), a target-rock that is known to have an increased presence of metabolically relevant elements that are readily accessible (Cockell

et al., 2009a), but has been poorly studied to-date in terms of impact-generated habitability, as it relates to planetary exploration. Currently, only one study has been conducted into microbial colonization of impacted basalts, at the Lonar impact structure in India. Though prokaryotic diversity was investigated, the effects of shock level and porosity of the host rocks were not explored (Antony et al., 2014). Our knowledge of microbial habitability within basalts comes mainly from young sub-seafloor basalts (Ivarsson et al., 2015; Kelly et al., 2010), older oceanic crust ophiolites (Furnes et al., 2008; Orcutt et al., 2020; Staudigel et al., 2006), volcanic glass (Cockell et al., 2009a, 2009b; Izawa et al., 2011), and meteorites (Steele et al., 2016; Tait et al., 2016, 2017a,b). The results from these studies highlight the heterogeneity of biomass throughout the samples, and a lack of organismal diversity, where the most common microorganism found is from the Actinobacteria (Antony et al., 2014; Gentry et al., 2017; Kelly et al., 2014). Some volcanic rocks, however, have been found to harbour a significant number of novel organisms that cannot be assigned to a known bacterial phylum (Kelly et al., 2010).

With our current level of understanding, it is clear that additional work on the habitability of impact-shocked basalts is required to yield new insight into microbial ecosystems in extreme endolithic conditions, specifically; does the increased opacity of basaltic samples hinder phototrophic communities at high shock levels, relative to impact-shocked gneisses? Does the shocked-basaltic substrate provide enhanced nutrient availability to endolithic communities?

In this study, we collected impact-shocked basalt and breccia samples from the Vãrgeao Dome and Vista Alegre basaltic impact structures in Brazil to determine the extent to which these substrates can provide viable endolithic habitats. The ultimate objective of this study is to explore the relationship between shock metamorphism in basaltic material and microbial colonization. Specifically, we will determine (1) the efficacy of this substrate as a habitat for microorganisms, and (2) the relationship between biomass and shock level in basalts. Although this work is currently in progress, it will be accomplished by (i) performing cell counts on selected samples to quantify microbial biomass levels, (ii) conducting DNA sequencing to assess microbial diversity, (iii)

analyzing our basaltic samples for the microbial community composition using 16S rRNA sequencing.

Correlating this data with shock level and alteration products found in Vargeão Dome and Vista Alegre samples allows us to characterize the habitability of these environments and determine the optimal conditions for colonization. In particular, what physical, chemical and mineralogical factors within shocked basaltic material are most conducive to hosting life, how they affect the distribution of biomass and diversity in this target lithology, and if it is possible to predict the colonization potential of material given the shock level and its mineralogy. Based on our results, we aim to better understand where in an impact crater microbial life, if present, is likely be found to overall help guide the search for life on Mars.

Methods

Sample Selection

Samples of shocked rock within Vargeão Dome (26°50'S 52°07'W) and Vista Alegre (25°57'S 52°41'W) impact structures were sterilely collected in 2017 by Dr. Alexandra Pontefract and stored in sample collection bags at room temperature. These samples were characterized to assess both shock metamorphism (Chapter 2) and the extent of hydrothermal alteration (Chapter 3). Ten basaltic target rock samples were selected for this study comprising of a range of shock levels and porosities (Appendix Table 1). In addition, two polymict breccia samples were included from each of the two craters. Impact polymict breccias are allochthonous and composed of target rock fragments that originate from various locations. To date, colonization of breccias has not been examined due to their heterogeneity – however, this heterogeneity may lend this target rock to colonization, as the glassy nature and chemical complexity could provide sufficient nutrients to support an endolithic community. However, while the breccia is glassy and highly friable in nature, the porosity is quite low, which will present a constraint to colonization.

The polymict breccias selected for this study are heterogenous in shock metamorphism, displaying a large variation of petrographic deformation features and strain-related mosaicity values (obtained through micro-X-ray diffraction) between plagioclase feldspar

grains within an individual sample, such that each distinct plagioclase grain receives its own unique shock level. Additionally, some polymict breccias minerals are more shocked than the target basalts. Impact breccias also display a variety of hydrothermal textures and contain a greater variation of clay and zeolite mineral compositions than the target basalts.

Table 1. Sample location, rock type, shock level (Stöffler et al., 2018) and porosity by density.

Sample Name	Crater and location	Rock Type	Shock Level (Stöffler et al., 2018)	Porosity (% by density)
VG-2017-10	Vargeão Dome	Target Basalt	2	1.01
VA-2017-2	Vista Alegre	Target Basalt	3	0
VG-2017-12	Vargeão Dome	Target Basalt	3	1.52
VG-2017-8	Vargeão Dome	Target Basalt	3	5.86
VA-2017-1E4	Vista Alegre	Target Basalt	3	6.28
VG-2017-15	Vargeão Dome	Target Basalt	3	7.06
VG-2017-24	Vargeão Dome	Target Basalt	3	13.09
VG-2017-30b	Vargeão Dome	Target Basalt	4	18.57
VG-2017-28	Vargeão Dome	Target Basalt	4	23.69
VG-2017-21	Vargeão Dome	Target Basalt	4	26.50
VG-2017-14	Vargeão Dome	Polymict Breccia	3–5	
VA-2017-1E	Vista Alegre	Polymict Breccia	2–5	

DNA Extraction, Sequencing and Statistical Analysis:

Rock samples were subsampled and homogenized into a coarse powder using a sterile alumina mortar and pestle, disinfected with sterile sand, ethanol and a flame, in a laminar flow hood. DNA extraction was then performed on 0.25 g of powdered sample using DNeasy® PowerSoil® Pro Kit (Qiagen), a DNA extraction kit designed for the isolation of microbial genomic DNA from all soil types, including difficult samples such as compost, sediment, and manure. DNA extraction from rock samples frequently proves challenging due to generally low biomass, and the inhibiting effects of clays and metal cations, therefore the extraction procedure for this kit was modified to maximize extraction yield.

Extractions for each sample were completed in duplicate to ensure sufficient DNA yield. Prior to extraction, 250 mg of sample was mixed with 500 µL of 30 mM sodium pyrophosphate (NaPP), 0.1% Tween 80 solution and incubated at room temperature for 30 minutes. NaPP is used as a competitive binder, preventing negatively charged DNA from binding to mineral surfaces, and at low concentrations, Tween 80 (a surfactant), inhibits cellular attachment. The mixture was then vortexed, gently spun down, and the supernatant was then carried forward to the Qiagen PowerBead Pro Tube. From here, the extraction was conducted as per the manufacturers instructions, with the exception that 1 µL of lysozyme (ReadyLyse^{TM} Lysozyme Solution, Lucigen) and 100 µL of QuickExtract^{TM} DNA Extraction Solution (Lucigen) were added to the C1 extraction solution. The lysozyme extraction solution are particularly important for clay-rich samples as it helps break up the clay structures and enable more efficient penetration of lysis reagent for releasing the DNA. Additional modification steps included adjusting the vortexing time in Step 2 from 10 to 20 minutes, replacing the provided 1.5 ml Elution Tubes with Cryovials or LowBind Tubes in step 15, and heating the elution buffer to 70°C. The elusion buffer is heated in attempt to more efficiently deprotonate the silica beads, thus releasing the DNA. After several experiments, it was determined that the best DNA yields came from combining 2, 250 mg extractions onto one DNA column, and eluting into a volume of 50 µL. If extraction yielded at least 5 ng/µL of DNA, the sample was stored in -80° C until ready for sequencing.

Sequencing:

Nine of the twelve samples yielded sufficient DNA for 16S rRNA sequencing. 16S rRNA gene sequences are the most common genetic markers used today to study bacterial taxonomy, owing to the highly conserved region of the ribosome. This method is efficient, cost effective, is widely used for assessing microbial biodiversity, and has been used to assess endolithic communities previously. Nanodrop and Qubit3 were used to assess DNA concentration and quality. Following extraction, polymerase chain reaction (PCR) for DNA amplification of the 16S rRNA gene will be performed using the Swift Biosciences kit, which will amplify the entire 16S region as 5 amplicons, and the ITS 1 and 2 regions. DNA will be sent for sequencing on an Illumina MiSeq platform, with 150 paired-end (PE) sequencing (16S), and 250 PE (ITS). Lastly, the returned sequences data will be processed using dada2 in R, which includes chimera checking and quality trimming.

Culturing:

Four grams of varying shock level samples were weighed and crushed into a fine gravel using a sterile alumina mortar and pestle in a laminar flow hood. Two grams were placed in BG-11 media and two grams into R2A media for enrichments of phototrophic and heterotrophic communities, respectively, at 24 °C on a shaker table, following a 16-8 hr light-dark cycle. Additionally, two grams of each sample were placed in distilled water to see if growth would occur in un-enriched conditions.

Bulk cell counts:

All twelve samples were hand crushed to a fine sand grain size using an alumina mortar and pestle. 1g of each sample will then incubated in 1000 μL of 60mM Na-pyrophosphate for 30 min. 200 μL of supernatant will be stained with LIVE/DEAD BacLight (ThermoFisher), following the manufacturer's protocols, and then 100 μL of stained supernatant will be mounted on a Petroff-Hauser counting stage for conducting cell counts on a ZI Zeiss Flourescent microscope.

Results

Sample culturing, DNA extraction, and bulk cell count preparation was completed before the COVID-19 pandemic began, however 16S rRNA sequencing, and bulk cell count results could not obtained due to the ensuing pandemic. The DNA has been stored at -80°C and will be sequenced as soon as possible. Samples crushed for bulk cell counts remain to be stained and counted to achieve a value in cells per gram of sample. Work is ongoing.

Based on previous research by Pontefract et al. (2016), we would expect to see a difference in microbial diversity between unshocked and shocked samples, with some phyla (e.g., Actinobacteria) present throughout. Based on previous studies (Pontefract et al., 2014) on gneiss samples from Haughton impact structure, we expect phototrophic organisms to react the most to the shock, meaning the level of porosity will have the greatest effect on phototrophs because greater porosity allows for greater light penetration, as well as space for larger cyanobacteria. When completed, this study will be the first comprehensive assessment of naturally occurring microbial colonies within basaltic impact rocks. This data will add to growing but limited knowledge of culture independent endolithic communities.

Culturing

After one-month, various R2A cultures had shown considerable growth, enough to be plated on R2A agar plates for identification of isolates. Due to COVID-19, samples were mixed 50:50 with glycerol to be frozen at -80°C for further work involved in isolating specific hetero- and phototrophic bacteria.

References

Antony, C. P., Shimpi, G. G., Cockell, C. S., Patole, M. S., & Shouche, Y. S. (2014). Molecular Characterization of Prokaryotic Communities Associated with Lonar Crater Basalts. *Geomicrobiology Journal, 31*(6), 519–528.

Banerjee, N. R., & Muehlenbachs, K. (2003). Tuff life: bioalteration in volcaniclastic rocks from the Ontong Java Plateau. *Geochemistey, Geophysics, Geosystems*, *4*(4), 1037.

Barker, W. W., Welch, S. A., & Banfield, J. (1997). Biogeochemical weathering of silicate minerals. In J. Banfield, & K. H. Nealson (Eds.), *Geomicrobiology: Interactions Between Microbes and Minerals* (Volume 35, pp. 391-428). Reviews in Mineralogy: Atlanta, Mineralogical Society of America.

Bennett, P. C., Rogers, J. R., Hiebert, F. K., & Choi, W. J. (2001). Silicates, silicate weathering, and microbial ecology. *Geomicrobiology Journal*, *18*(1), 3 – 19.

Cockell, C. S. (2004). Impact-shocked rocks – insights into archaean and extraterrestrial microbial habitats (and sites for prebiotic chemistry?). *Advances in Space Research, 33*(8), 1231–1235.

Cockell, C. S. (2006). The origin and emergence of life under impact bombardment. *Philosophical Transactions of the Royal Society B: Biological Science, 361*(1374), 1845–1856.

Cockell, C. S., Balme, M., Bridges, J. C., Davila, A., & Schwenzer, S. P. (2012). Uninhabited habitats on Mars. *Icarus, 217*, 184–193.

Cockell, C. S., Kelly, L. C., Summers, S., Marteinsson, V. (2011). Following the kinetics: Iron-oxidising microbial mats in cold Icelandic volcanic habitats and their rock-associated carbonaceous signature. *Astrobiology*, *11*(7), 679–694.

Cockell, C. S., & Lee, P. (2002). The biology of impact craters—a review. *Biological Reviews*, *77*(3), 279-310.

Cockell, C. S., Lee, P., Broady, P., Lim, D. S. S., Osinski, G. R. R., Parnell, J., Koeberl, C., Pesonen, L., & Salminen, J. (2005). Effects of asteroid and comet impacts on habitats for lithophytic organisms – A synthesis. *Meteoritics & Planetary Science,* 40, 1901–1914.

Cockell, C. S., Lee, P., Osinski, G. R., Horneck, G., & Broady, P. (2002). Impact-induced microbial endolithic habitats. *Meteoritics & Planetary Science, 37*(10), 1287–1298.

Cockell, C. S., Olsson, K., Knowles, F., Kelly, L., Herrera, A., Thorsteinsson, T., & Marteinsson, V. (2009a). Bacteria in Weathered Basaltic Glass, Iceland. *Geomicrobiology Journal, 26*(7), 491–507.

Cockell, C. S., Olsson-Francis, K., Herrera, A., & Meunier, A. (2009b). Alteration textures in terrestrial volcanic glass and the associated bacterial community. *Geobiology, 7*(1), 50–65.

Cockell, C. S., & Osinski, G. R. (2007). Impact-induced impoverishment and transformation of a sandstone habitat for lithophytic microorganisms. *Meteoritics & Planetary Science, 42*(11), 1985–1993.

Coleine, C., Stajich, J., Zucconi, L., Onofri, S., Selbmann, L. (2020). Sun exposure drives Antarctic cryptoendolithic community structure and composition. *Polar Biology, 43,* 607-615.

De los Ríos, A., Wierzchos, J., Sancho, L. G., & Ascaso, C. (2002). Microhabitats and chemical microenvironments under saxicolous lichens growing on granite. *Microbial Ecology*, *43*, 181–188.

De los Ríos, A., Wierzchos, J., Sancho, L. G., & Ascaso, C. (2003). Acid microenvironments in microbial biofilms of Antarctic endolithic microecosystems. *Environmental Microbiology, 5*(4), 231–237.

Ferris, J. P., Huang, V. H., & Hagan, W. J. (1988). Montmorillonite: a multifunctional mineral catalyst for the prebiological formation of phosphate esters. *Origins of Life and Evolution of Biospheres, 18*(1-2), 121–133.

Fike, D. A., Cockell, C. S., Pearce, D., & Lee, P. (2003). Heterotrophic microbial colonization of the interior of impact-shocked rocks from Haughton impact structure, Devon Island, Nunavut, Canadian High Arctic. *International Journal of Astrobiology, 1*(4), 311–323.

Friedmann, E. I. (1982). Endolithic microorganisms in the Antarctic cold desert. *Science 215*(4536), 1045–1053.

Furnes, H., McLoughlin, N., Muehlenbachs, K., Banerjee, N., Staudigel, H., Dilek, Y., de Wit, M. J., Van Kranendonk, M. J., & Schiffman, P. (2008). Oceanic pillow lavas and hyaloclastites as habitats for microbial life through time-A review. In Y. Dilek, H. Furnes, & K. Muehlenbachs (Eds.), *Links Between Geological Processes, Microbial Activities and Evolution of Life* (pp. 1-68). Berlin: Springer.

Gentry, D. M., Amador, E. S., Cable, M. L., Chaudry, N., Cullen, T., Jacobsen, M. B., Murukesan, G., Schwieterman, E. W., Stevens, A. H., Stockton, A., Tan, G., Yin, C., Cullen, D. C., & Geppert, W. (2017). Correlations between life-detection techniques and implications for sampling site selection in planetary analog missions. *Astrobiology,* 17, 1009–1021.

Ivarsson, M., Bengtson, S., Drake, H., & Francis, W. (2018). Fungi in deep subsurface environments. *Advances in Applied Microbioogy, 102*, 83–116.

Ivarsson, M., Bengtson, S., Skogby, H., Lazor, P., Broman, C., Belivanova, V., & Marone, F. (2015). A Fungal-Prokaryotic Consortium at the Basalt-Zeolite Interface in Subseafloor Igneous Crust. *Plos One, 10*(10).

Izawa, M. R. M., Banerjee, N. R., Flemming, R. L., Bridge, N. J., & Schultz, C. (2010). Basaltic glass as a habitat for microbial life: implications for astrobiology and planetary exploration. *Planetary and Space Science, 58*(4), 583–591.

Izawa, M. R. M., Bannerjee, N. R., Osinski, G. R., Flemming, R. L., Parnell, J., & Cockell, C. S. (2011). Weathering of post-impact hydrothermal deposits from the Haughton Impact Structure: implications for microbial colonization and biosignature preservation. *Astrobiology*, *11*(6), 537–550.

Kelly, L. C., Cockell, C. S., Piceno, Y. M., Andersen, G. L., Thorsteinsson, T., & Marteinsson, V. (2010). Bacterial Diversity of Weathered Terrestrial Icelandic Volcanic Glasses. *Microbial Ecology, 60*(4), 740–752.

Kelly, L. C., Cockell, C. S., Thorsteinsson, T., Marteinsson, V., & Stevenson, J. (2014). Pioneer microbial communities of the Fimmvörðuháls Lava Flow, Eyjafjallajökull, Iceland. *Microbial Ecology*, *68*(3), 504–518.

Konhauser, K. O., Lalonde, S. V., & Phoenix, V. R. (2008). Bactieral biomineralization: Where to from here? *Geobiology,* 6, 298–302.

Lee, J. E., Buckley, H. L., Rampal, R. S., & Lear, G. (2013). Both species sorting and neutral processes drive assembly of bacterial communities in aquatic microcosms. FEMS *Microbiolial Ecology, 86*(2), 288–302.

McSween, H. Y., Taylor, G. J., & Wyatt, M. B. (2009). Elemental composition of the Martian crust. *Science, 324*(5928), 736–739.

Naumov, M. V. (2002). Impact-generated hydrothermal systems: data from Popigai, Kara, and Puchezh-Katunki impact structures. In J. Plado, & L. J. Pesonen (Eds.), *Impacts in Precambrian Shields* (pp. 117– 71). Springer-Verlag, Berlin.

Naumov, M. V. (2005). Principal features of impact-generated hydrothermal circulation systems: Mineralogical and geochemical evidence. *Geofluids, 5*(3), 165–184.

Nienow, J. A., McKay, C. P., & Friedmann, E. I. (1988). The cryptoendolithic microbial environment in the Ross desert of Antarctica: mathematical models of the thermal regime. *Microbial Ecology, 16*, 253–270.

Orcutt, B., D'Angelo, T., Jungbluth, S. P., Huber, J. A., & Sylvan, J. B. (2020). Microbial life in oceanic crust. https://doi.org/10.31219/osf.io/2wxe6

Osinski, G. R. (2007). Impact metamorphism of CaCO3-bearing sandstones at the Haughton structure, Canada. *Meteoritics and Planetary Science, 42*(11), 1945–1960.

Osinski, G. R., Cockell, C. S., Pontefract, A., & Sapers, H. M. (2020). The role of meteorite impacts in the origin of life. *Astrobiology, 20*(9), 1121-1149.

Osinski, G. R., Lee, P., Parnell, J., Spray, J. C., & Baron, M., (2005). A case study of impact-induced hydrothermal activity: the Haughton impact structure, Devon Island, Canadian High Arctic. *Meteoritic and Planetary Sci*ence, *40*(12), 1859–1878.

Osinski, G. R., Spray, J. G., & Lee, P. (2001). Impact-induced hydrothermal activity within the Haughton impact structure, arctic Canada: Generation of a transient, warm, wet oasis. *Meteoritics & Planetary Science, 36*(12), 731–745.

Osinski, G. R., Tornabene, L. L., Banerjee, N. R., Cockell, C. S., Flemming, R., Izawa, M. R., & Southam, G. (2013). Impact-generated hydrothermal systems on Earth and Mars. *Icarus, 224*(2), 347–363.

Pontefract, A., Osinski, G. R., Cockell, C. S., Moore, C. A., Moores, J. E., & Southam, G. (2014). Impact-Generated Endolithic Habitat Within Crystalline Rocks of the Haughton Impact Structure, Devon Island, Canada. *Astrobiology, 14*(6), 522–533.

Pontefract, A., Osinski, G. R., Cockell, C. S., Southam, G., Mccausland, P. J., Umoh, J., & Holdsworth, D. W. (2016). Microbial Diversity of Impact-Generated Habitats. *Astrobiology, 16*(10), 775–786.

Pontefract, A., Osinski, G. R., Lindgren, P., Parnell, J., Cockell, C. S., & Southam, G. (2012). The effects of meteorite impacts on the availability of bioessential elements for endolithic organisms. *Meteoritics & Planetary Science*, *47*(10), 1681-1691.

Saladino, R., Crestini, C., Costanzo, G., Negri, R., & Di Mauro, E. A. (2001). Possible prebiotic synthesis of purine, adenine, cytosine, and 4(3H)-pyrimidinone from

formamide: implications for the origin of life. *Bioorganic & Medicinal Chemistry, 9*(5), 1249–1253.

Sapers, H. M., Banerjee, N. R., & Osinski, G. R. (2015). Potential for impact glass to preserve microbial metabolism. *Earth and Planetary Science Letter, 430*, 95–104.

Sapers, H. M., Osinski, G. R., Banerjee, N. R., & Preston, L. J. (2014). Enigmatic tubular features in impact glass. *Geology, 42*(6), 471–474.

Singleton, A. C., Osinski, G. R., McCausland, P. J. A., & Moser, D. E. (2011). Shock-induced changes in density and porosity in shock-metamorphosed crystalline rocks, Haughton impact structure, Canada. *Meteoritics & Planetary Science, 46*(11), 1774–1786.

Smith, J. V. (1998). Biochemical evolution. I. Polymerisation on internal, organophilic silica surfaces of dealuminated zeolites and feldspars. *Proceedings of the National Academy of Sciences of the United States of America, 95*(7), 3370–3375.

Staudigel, H., Furnes, H., Banerjee, N. R., Dilek, Y., & Muehlenbach, K. (2006). Microbes and volcanoes: A tale from the oceans, ophiolites, and greenstone belts. *GSA Today Journal, 16*, 4–102.

Steele, A., McCubbin, F. M., & Fries, M. D. (2016). The provenance, formation, and implications of reduced carbon phases in Martian meteorites. *Meteoritics & Planetary Science, 51*(11), 2203-2225.

Tait, A. W., Fisher, K. R., Srinivasan, P., & Simon, J. I. (2016). Evidence for impact induced pressure gradient on the Allende CV3 parent body: Consequences for fluid and volatile transport. *Earth and Planetary Science Letters, 454*, 213-224.

Tait, A. W., Gagen, E. J., Wilson, S. A., Tomkins, A. G., & Southam, G. (2017b). Microbial Populations of Stony Meteorites: Substrate Controls on First Colonizers. *Frontiers in Microbiology, 8*, 1227.

Tait, A. W., Wilson, S. A., Tomkins, A. G., Gagen, E. J., Fallon, S. J., & Southam, G. (2017a). Evaluation of meteorites as habitats for terrestrial microorganisms: Results from the Nullarbor Plain, Australia, a Mars analogue site. *Geochimica et Cosmochimica Acta*, 2015, 1-16.

Welch, S. A., Barker, W. W., & Banfield, J. F. (1999). Microbial extracellular polysaccharides and plagioclase dissolution. *Geochim. Cosmochim. Acta*, *63*(9), 1405 – 1419.

Zamaraev, K. I., Romannikov, V. N., Salganik, R. I., Wlassoff, W. A., & Khramtsov, V.V. (1997). Modelling of the prebiotic synthesis of oligopeptides: silicate catalysts help to overcome the critical stage. *Origins of Life and Evolution of Biosphere, 27*(4), 325– 337.

Appendix B: Plagioclase µXRD data Supplementary Material

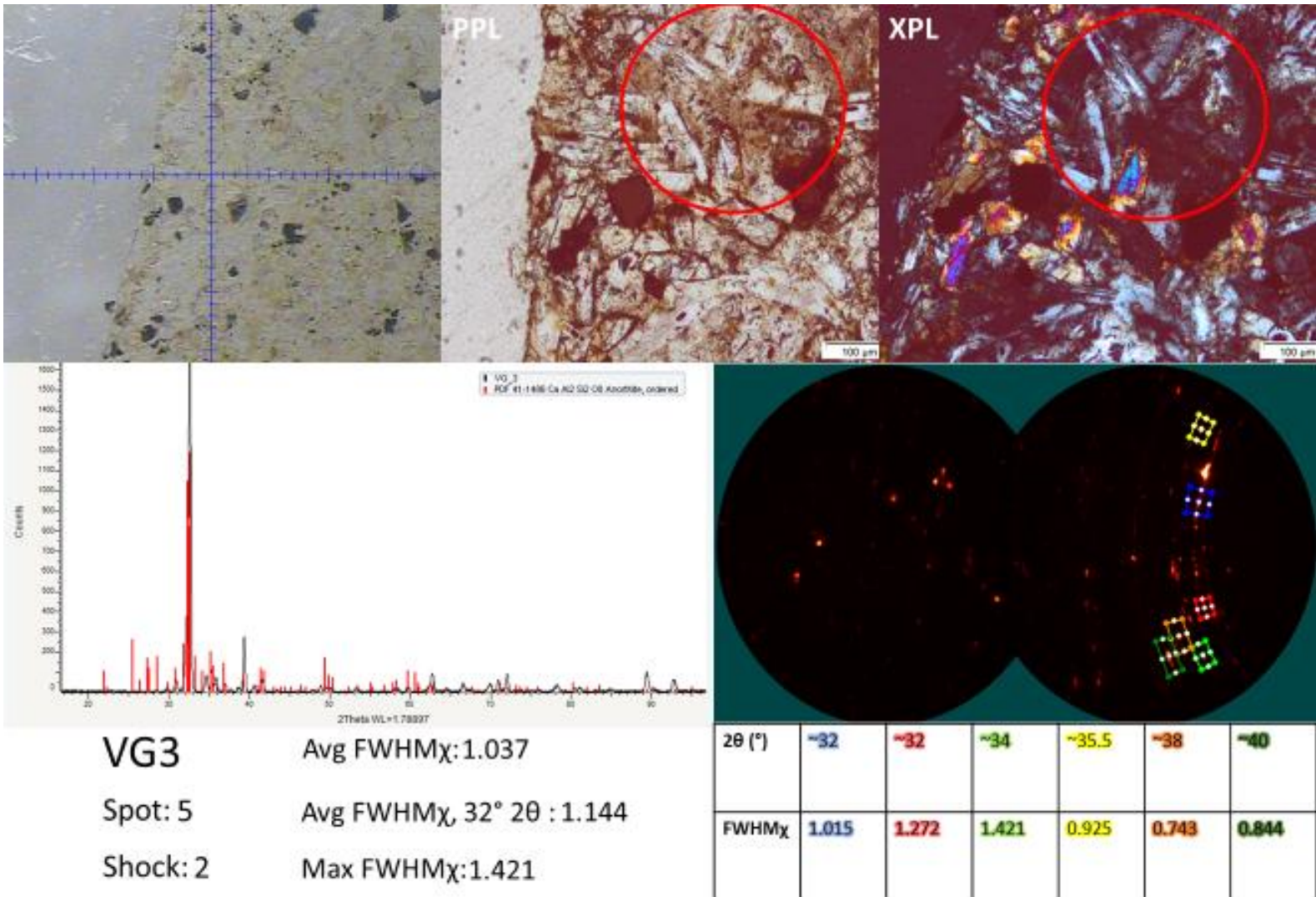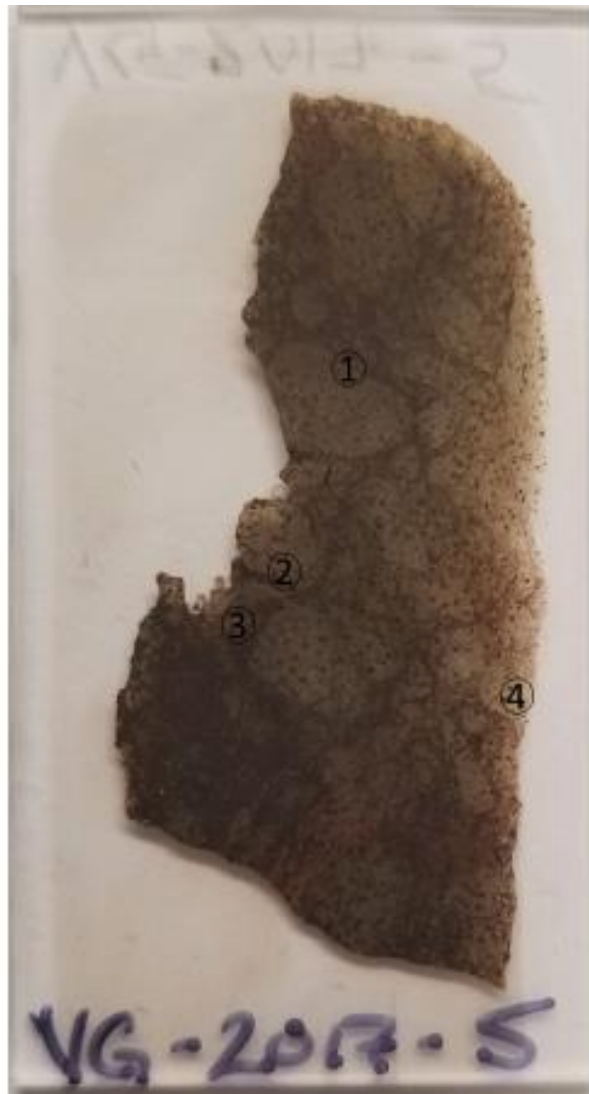**Figure B-1. VA-2017-1B thin section showing spots analyzed**
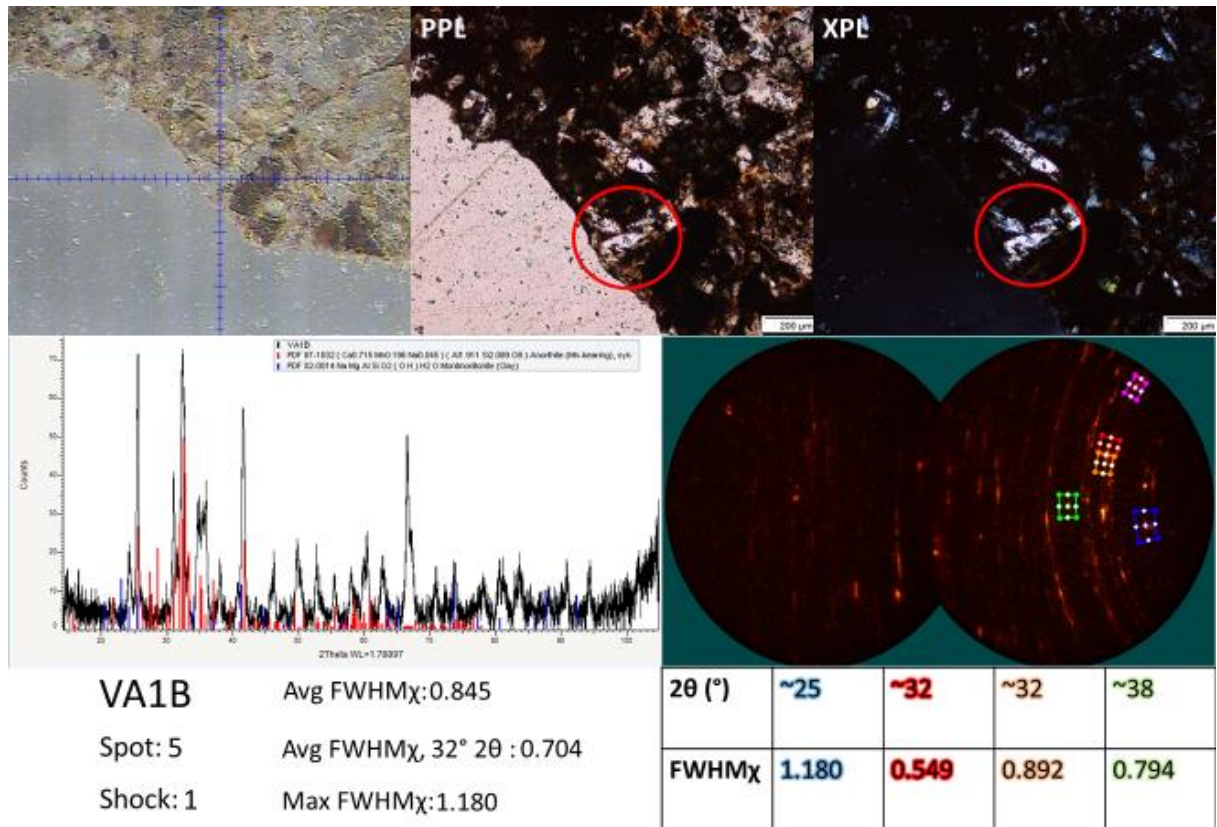
Optical petrography, μXRD analysis, and FWHMχ measurements of plagioclase feldspar grain (spot 5 in Fig. B-1) immersed in the matrix of sample VA1B.

Red: Anorthite, Mn-bearing (Ca0.715 Mn0.196 Na0.045) (Al1.991 Si2.089 O8) (PDF 87-1832)

Blue: Montmorillonite (Na Mg Al Si O2) (OH) H2O (PDF 02-0014)
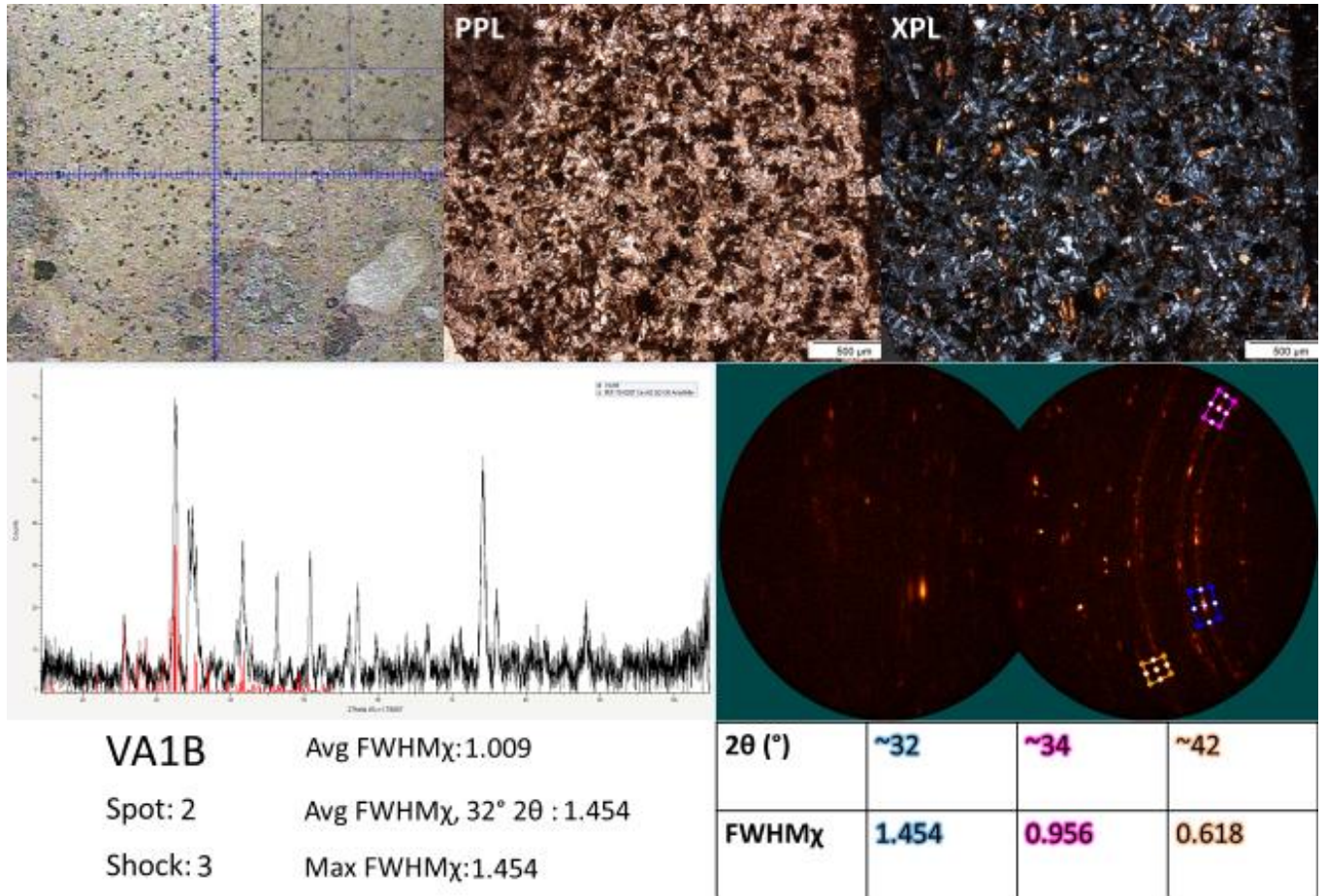
Optical petrography, µXRD analysis, and FWHMχ measurements of plagioclase feldspar grains (spot 2 in Fig. B-1) within the matrix of sample VA1B.

Red: Anorthite (Ca Al2 Si2 O8) (PDF 70-0287)
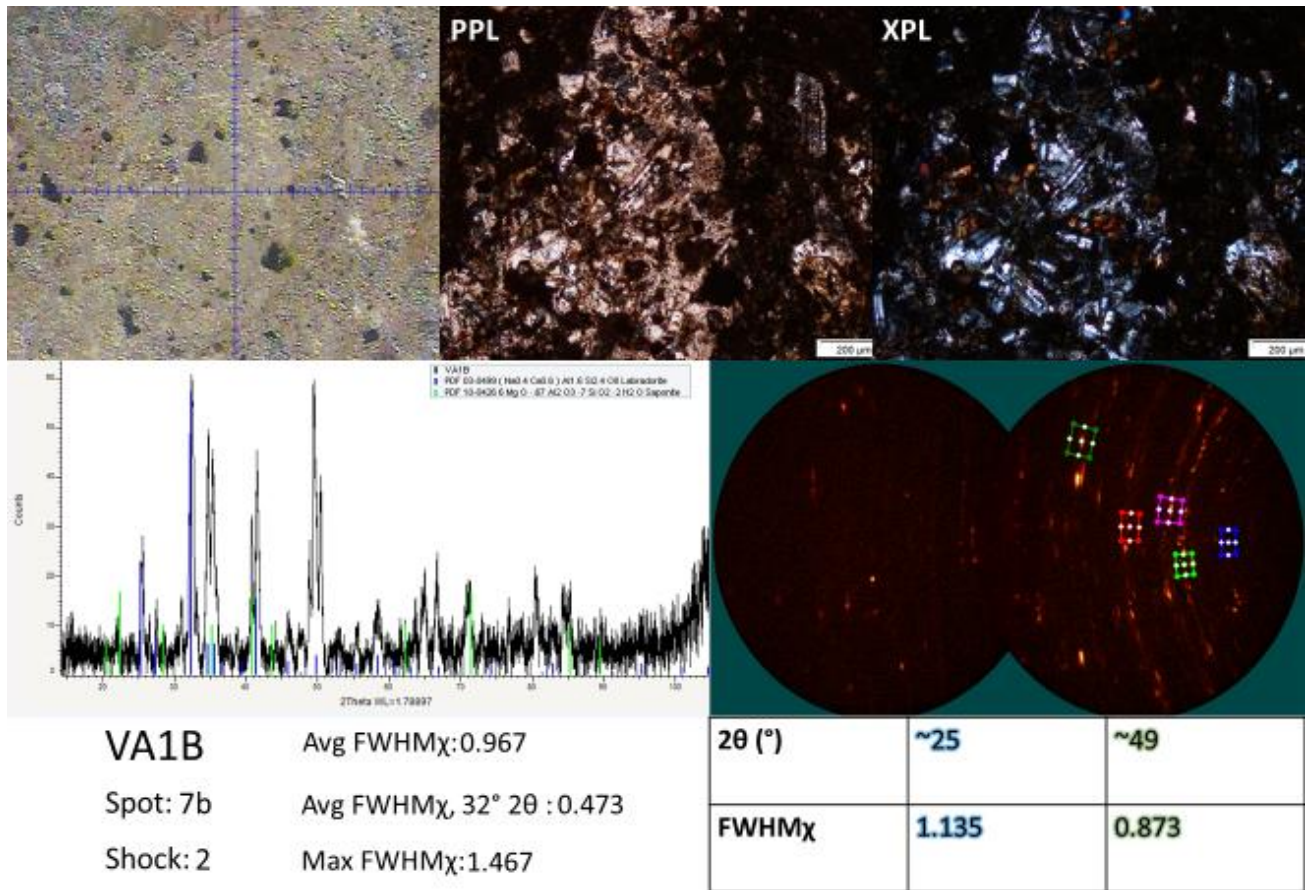
Optical petrography, µXRD analysis, and FWHMχ measurements of plagioclase feldspar grain (spot 7b in Fig. B-1) in a breccia clast from sample VA1B.

Blue: Labradorite (Na0.4 Ca0.6) Al1.6 Si2.4 O8 (PDF 03-0499)

Green: Saponite (MgO · 0.67 Al2 O3 · 7 Si O2 · 2 H2O) (PDF 10-0426)
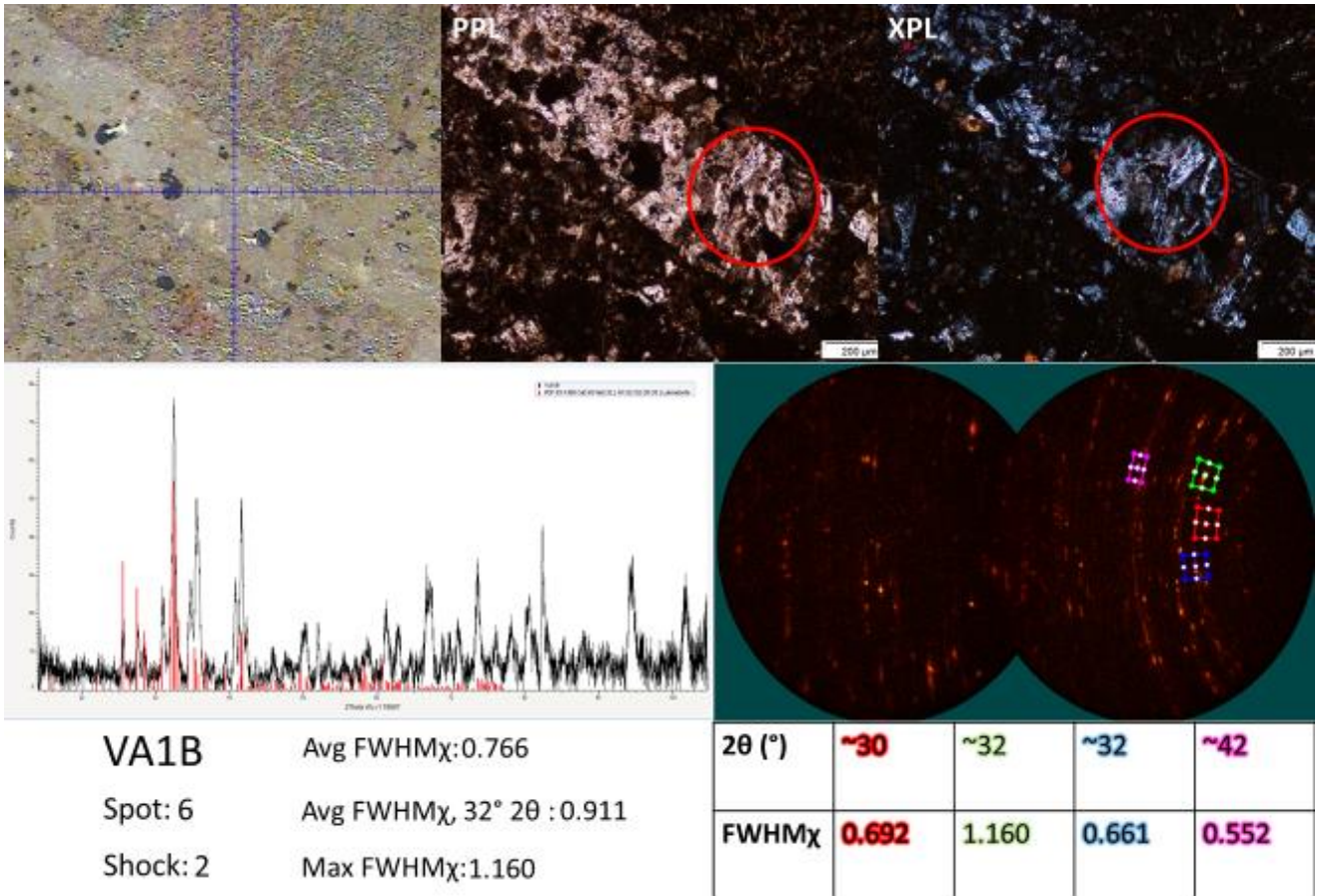
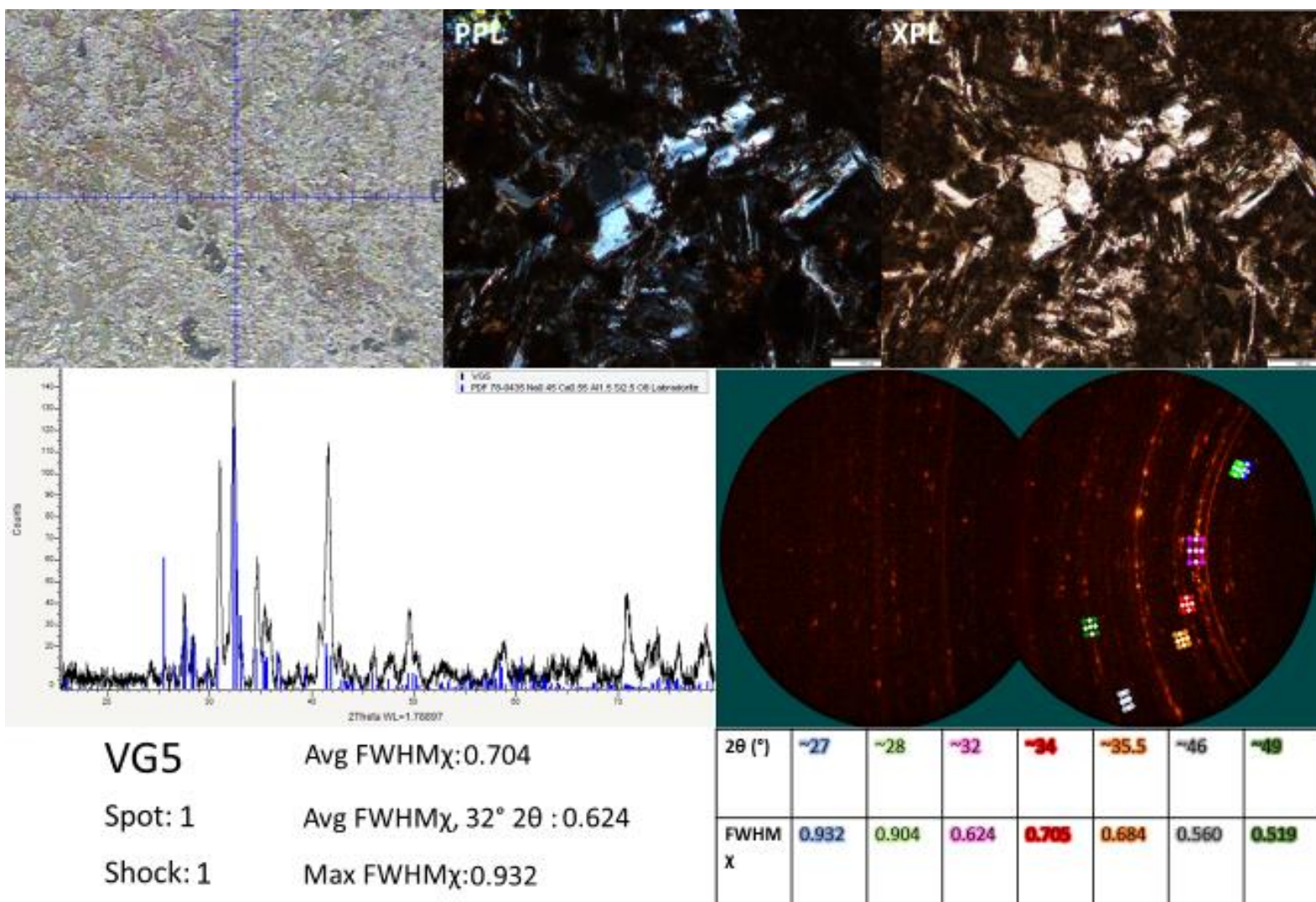**Optical petrography, μXRD analysis, and FWHMχ measurements of plagioclase feldspar grain (spot 6 in Fig. B-1) in a breccia clast of sample VA1B.**

Red: Labradorite (Ca0.65 Na0.32) Al1.62 Si2.38 O8 (PDF 83-1368)
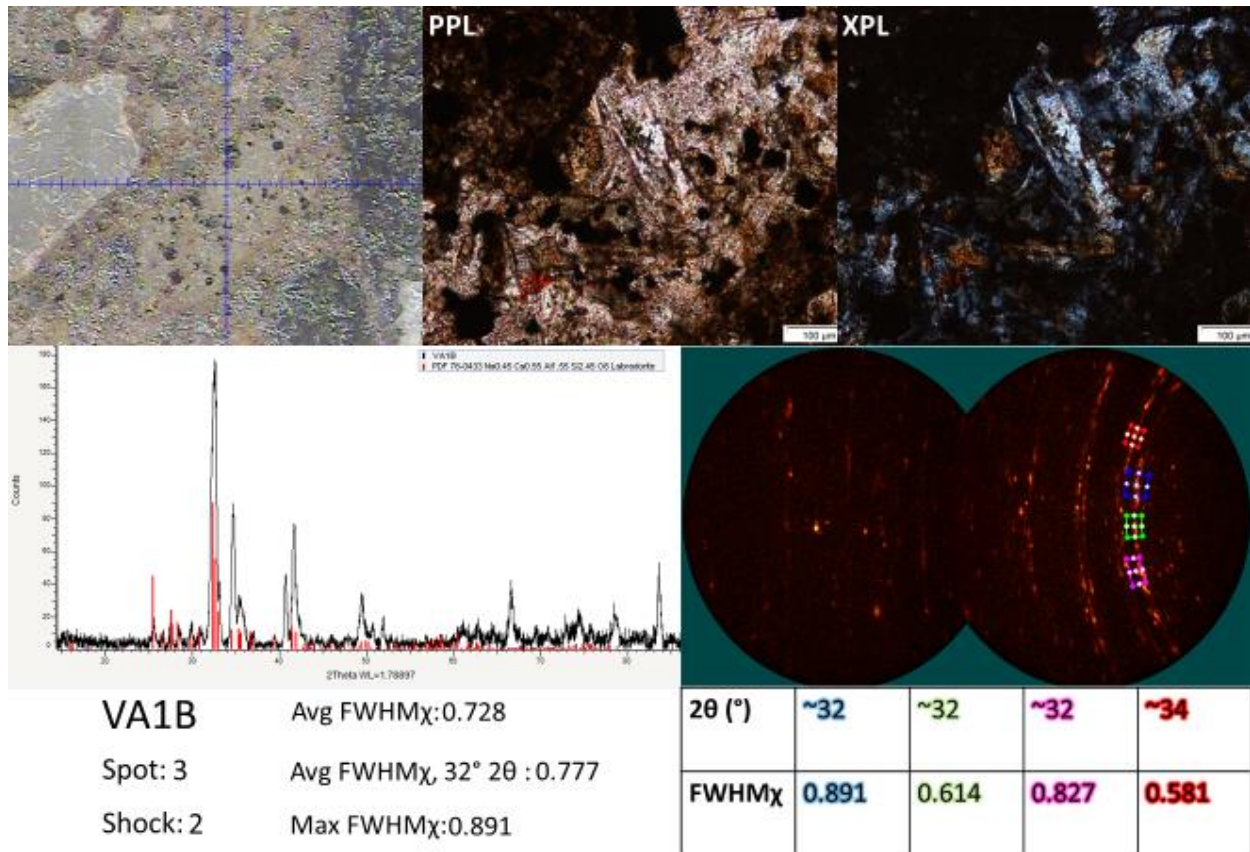
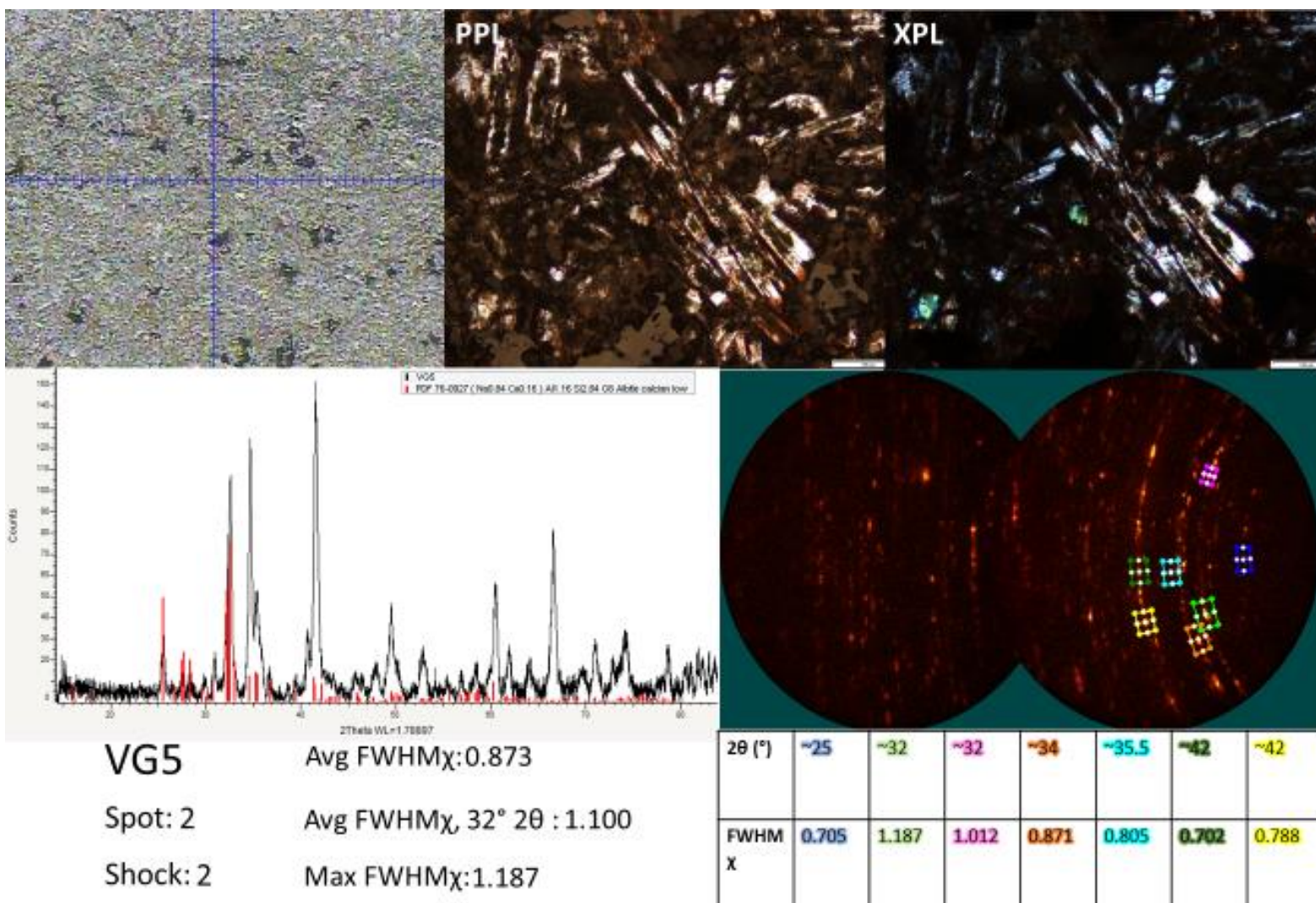**Optical petrography, μXRD analysis, and FWHMχ measurements of plagioclase feldspar grain (spot 3 in Fig. B-1) in a breccia clast of sample VA1B.**

Red: Labradorite (Na0.45 Ca0.55) Al1.55 Si2.45 O8 (PDF 78-0433)

VA1C

Figure B-2. VA-2017-1C thin section showing spots analyzed
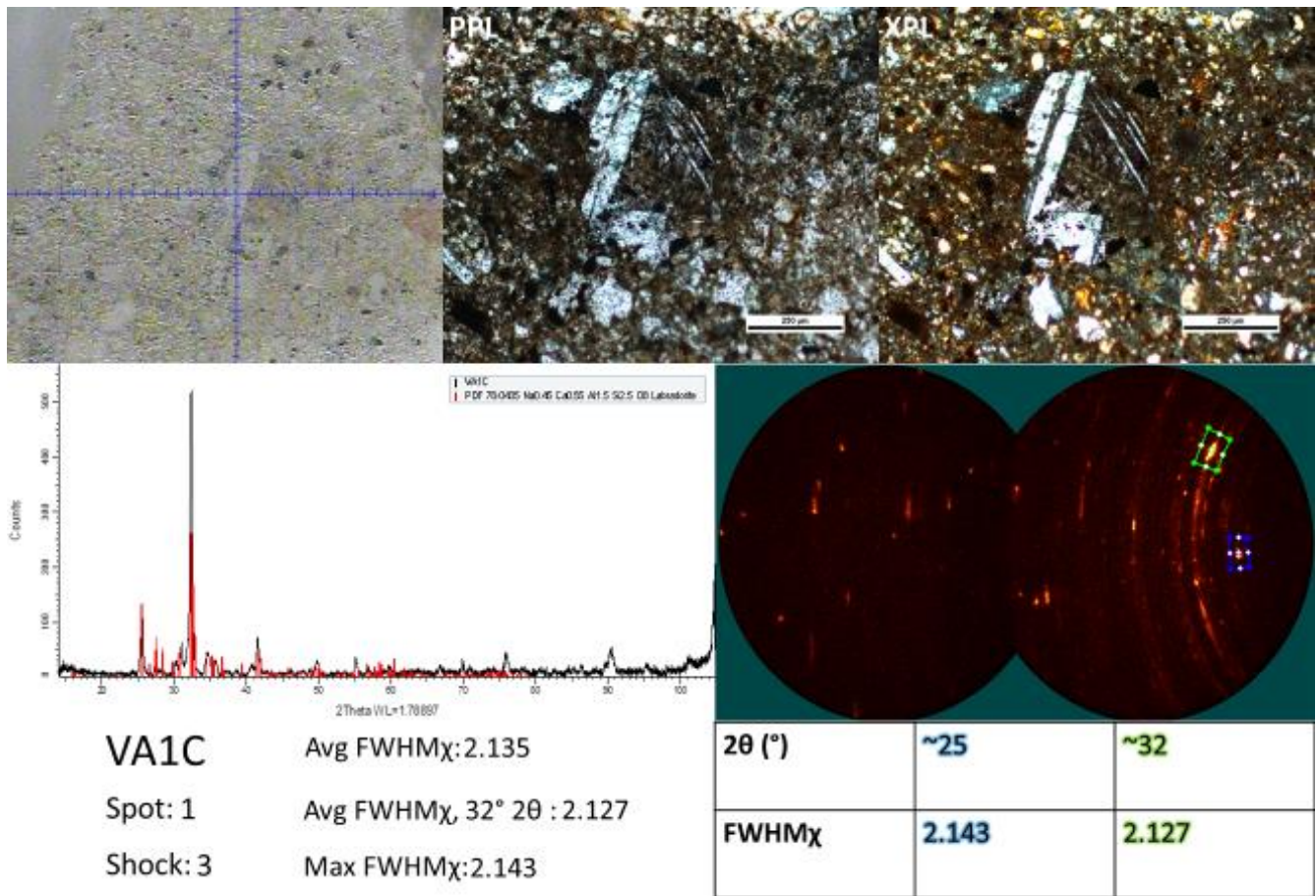
Optical petrography, µXRD analysis, and FWHMχ measurements of plagioclase feldspar grain (spot 1 in Fig. B-2) in sample VA1C.

Red: Labradorite (Na0.45 Ca0.55) Al1.5 Si2.5 O8 (PDF 78-0435)
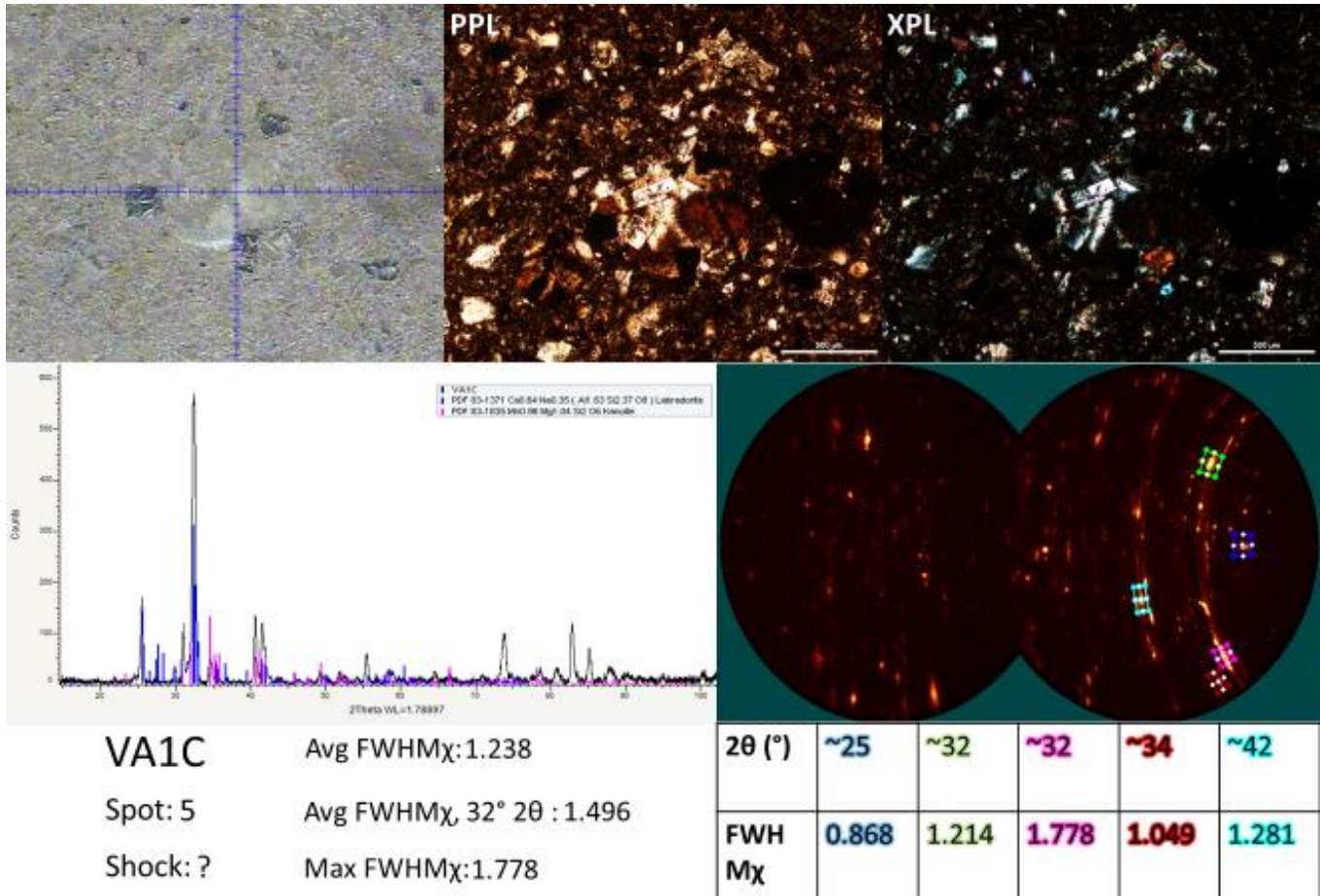
Optical petrography, µXRD analysis, and FWHMχ measurements of plagioclase feldspar grain (spot 5 in Fig. B-2) in sample VA1C.

Blue: Labradorite (Na0.64 Ca0.35) Al1.63 Si2.37 O8 (PDF 83-1371)

Magenta: Kanoite (Mn0.96 Mg1.04 Si2 O6) (PDF 83-1835)
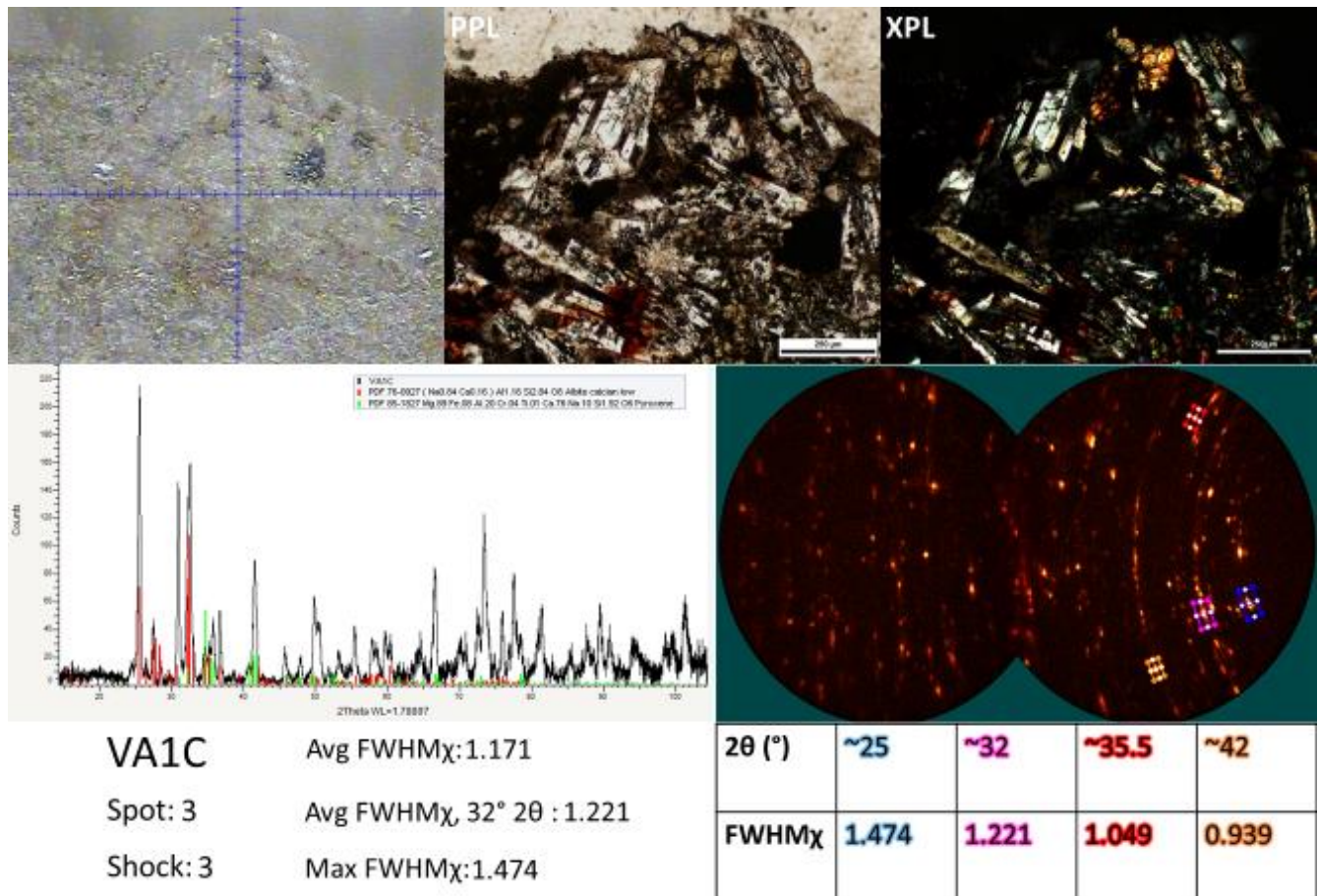
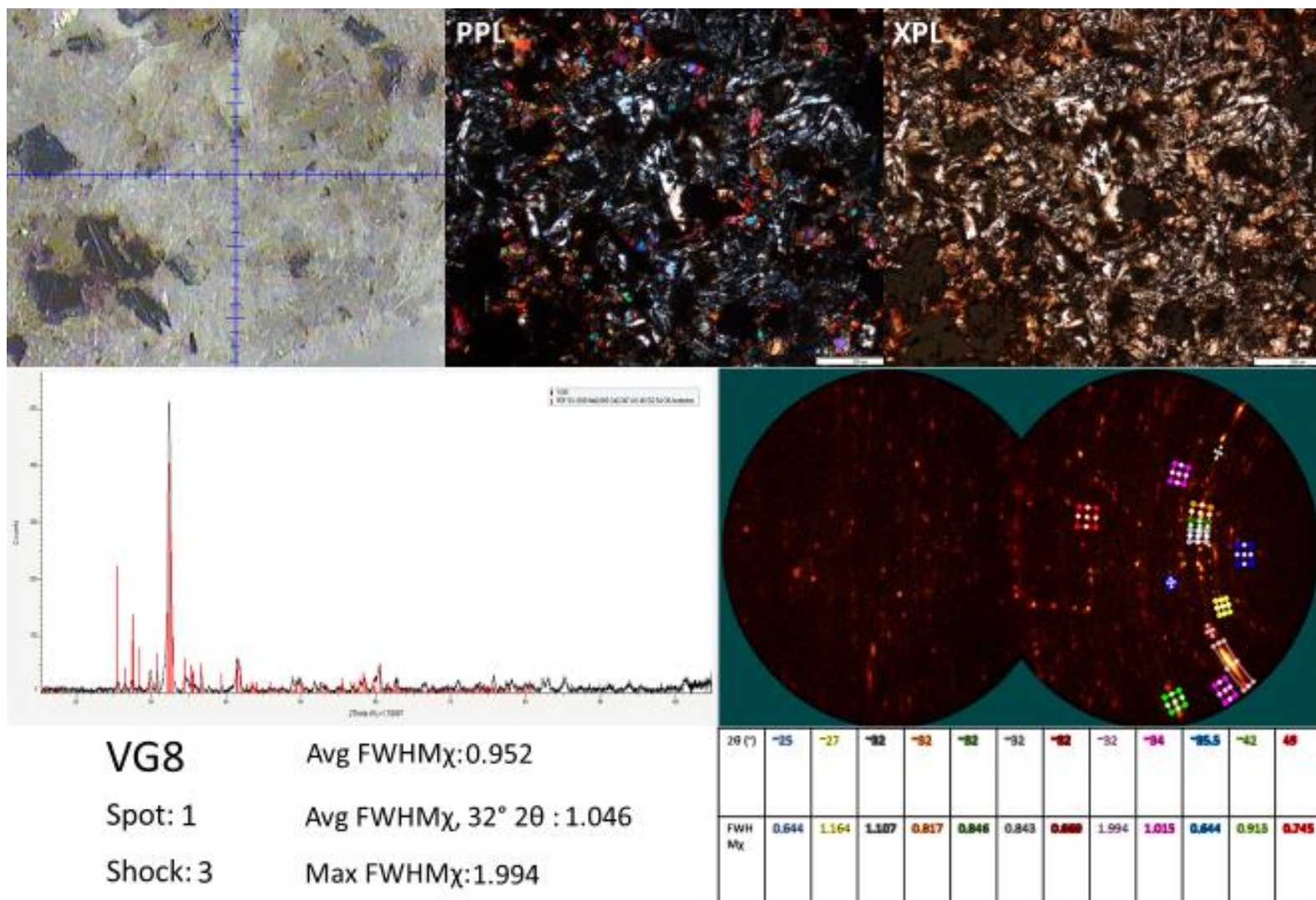**Optical petrography, µXRD analysis, and FWHMχ measurements of plagioclase feldspar grain (spot 3 in Fig. B-2) in sample VA1C.**

Red: Albite calcian low (Na0.84 Ca0.16) Al1.16 Si2.84 O8 (PDF 76-0927)

Green: Pyroxene (Mg0.89 Fe0.08 Al0.20 Cr0.04 Ti0.01 Ca0.76 Na0.10 Si0.92 O6) (PDF 85-1827)
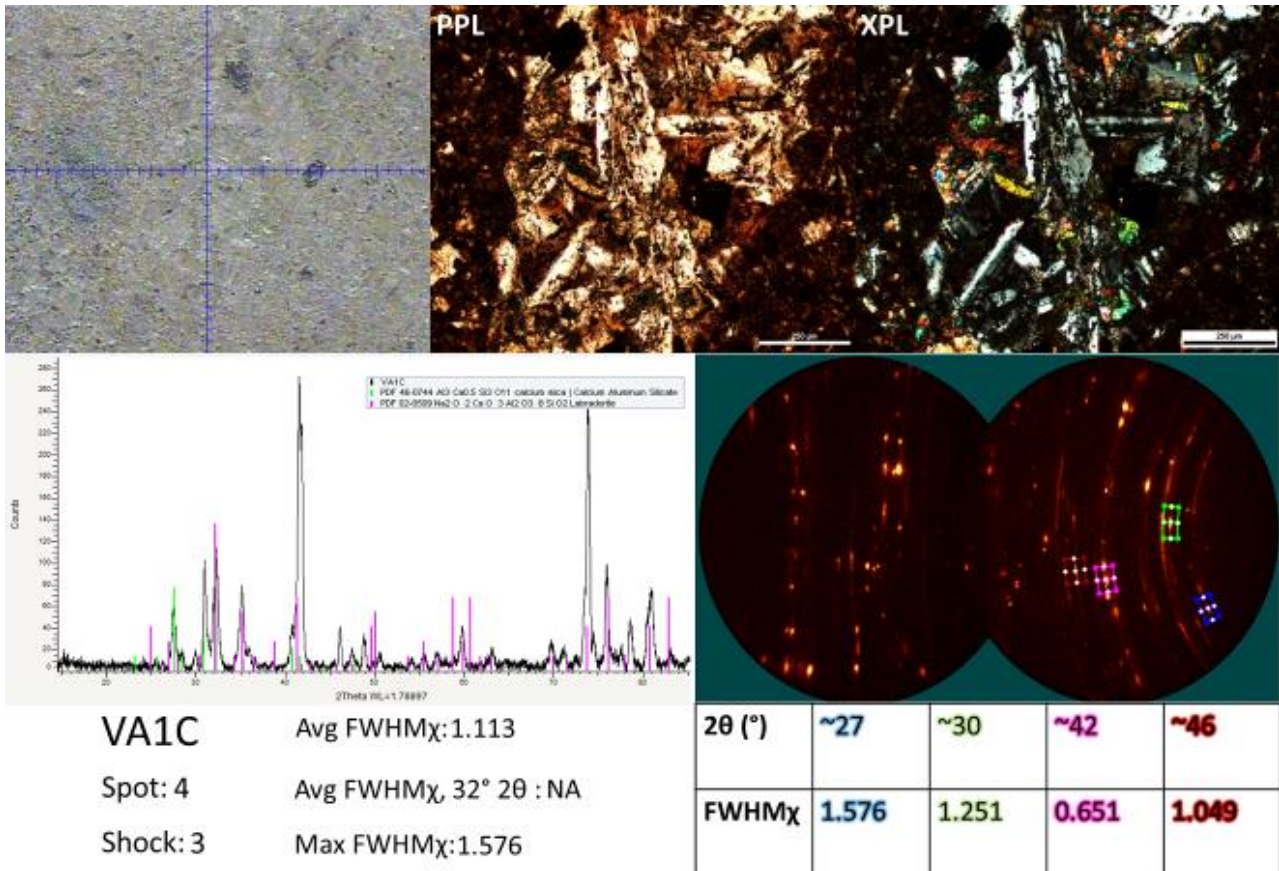
Optical petrography, μXRD analysis, and FWHMχ measurements of plagioclase feldspar grain (spot 4 in Fig. B-2) in a breccia clast of sample VA1C.
Green: Calcium mica (Al3 Ca0.5 Si3 O11) (PDF 46-0744)
**Pink: Labradorite (Na2 O · 2 Ca O · 3 Al2 O3 · 8 Si O2) (PDF 02-0509)**

VA1D

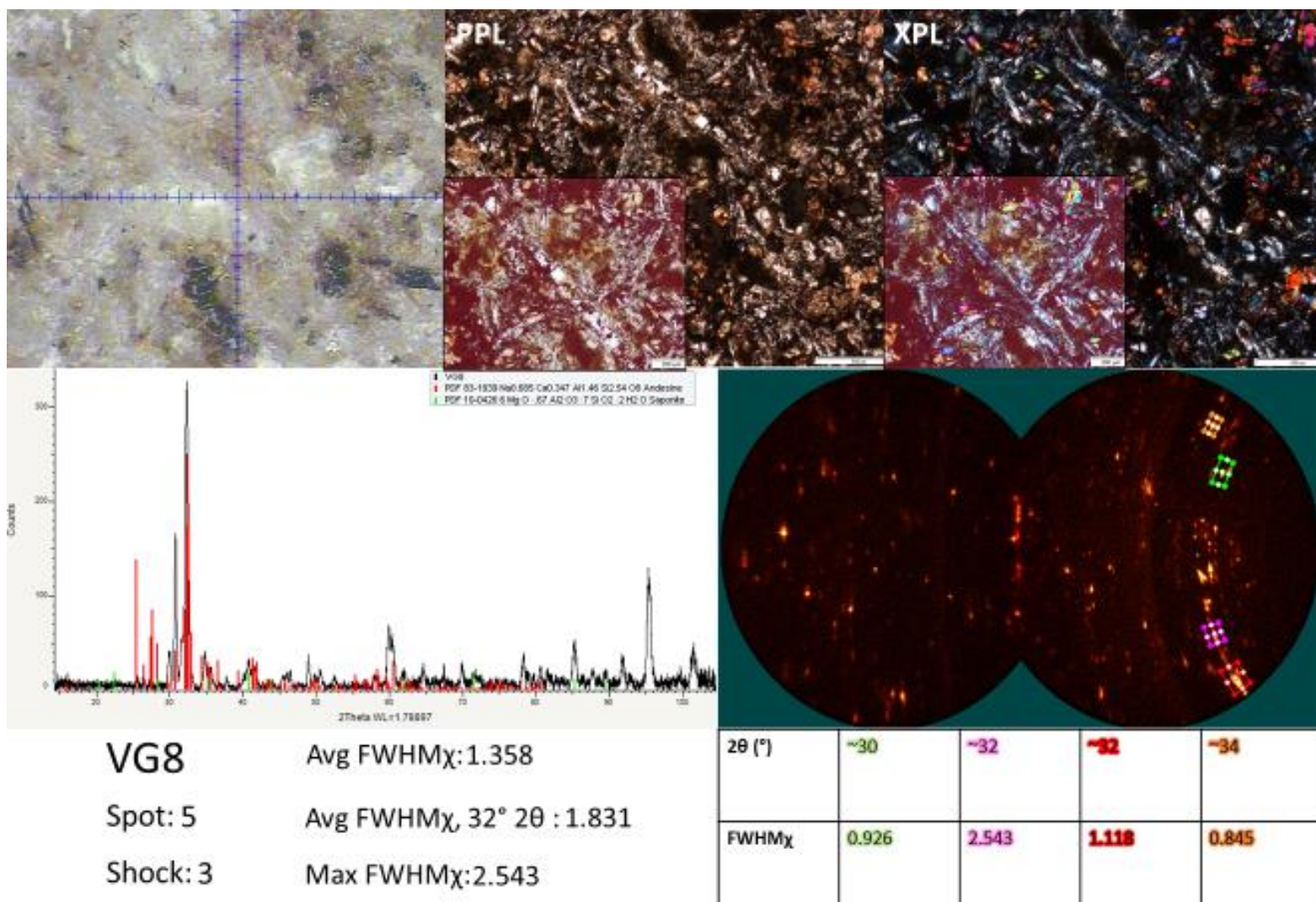**Figure B-3. VA-2017-1D thin section showing spots analyzed**
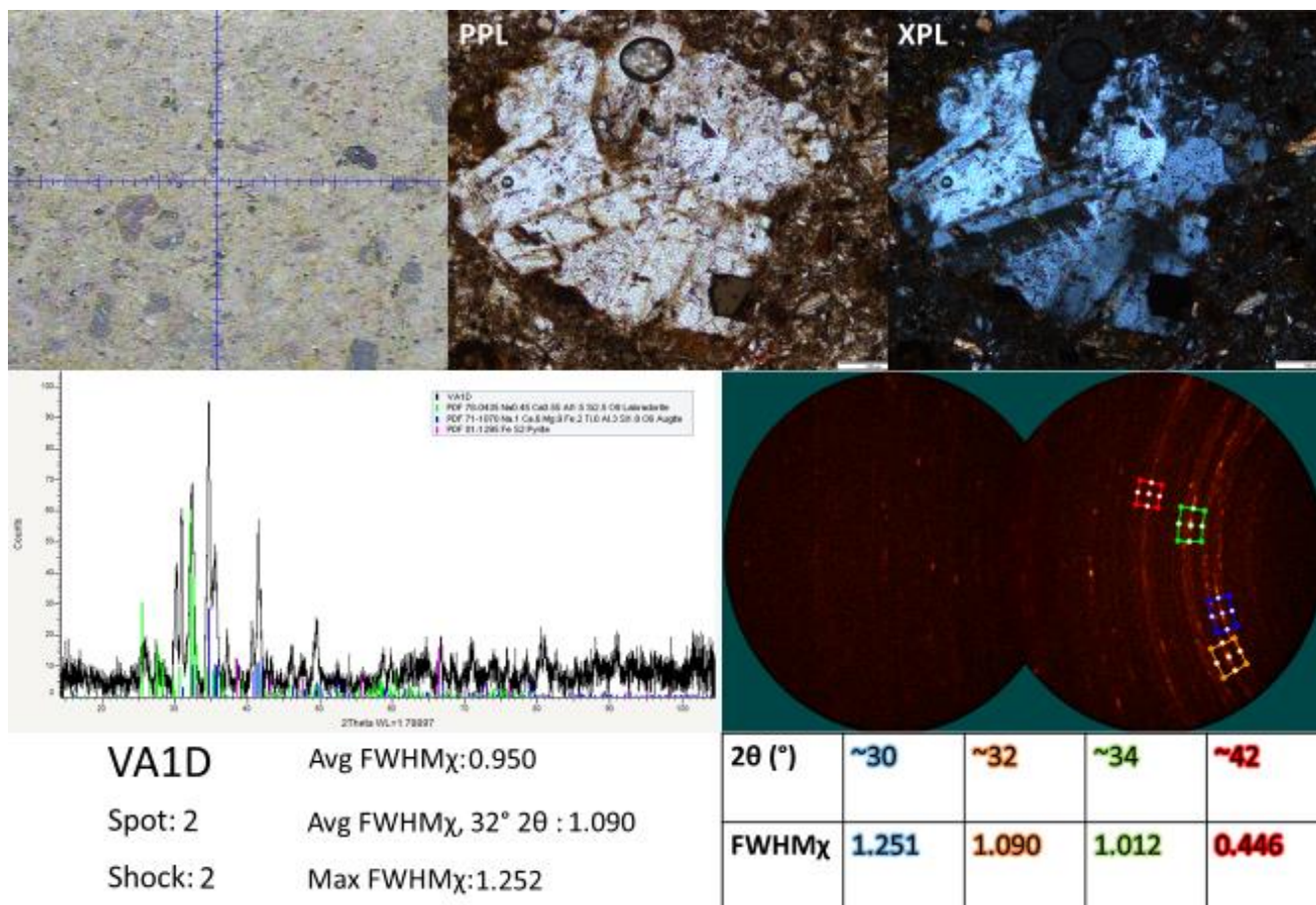
Optical petrography, μXRD analysis, and FWHMχ measurements of plagioclase feldspar grain (spot 2 in Fig. B-3) in sample VA1D.

Green: Labradorite (Na0.45 Ca0.55 Al1.5 Si2.5 O8) (PDF 78-0435)

Blue: Augite (Na0.1 Ca0.6 Mg0.9 Fe0.2 Al0.3 Si1.8 O6) (PDF 71-1070)

Pink: Pyrite (Fe S2) (PDF 01-1295)

VA1E

Figure B-4. VA-2017-1E thin section showing spots analyzed
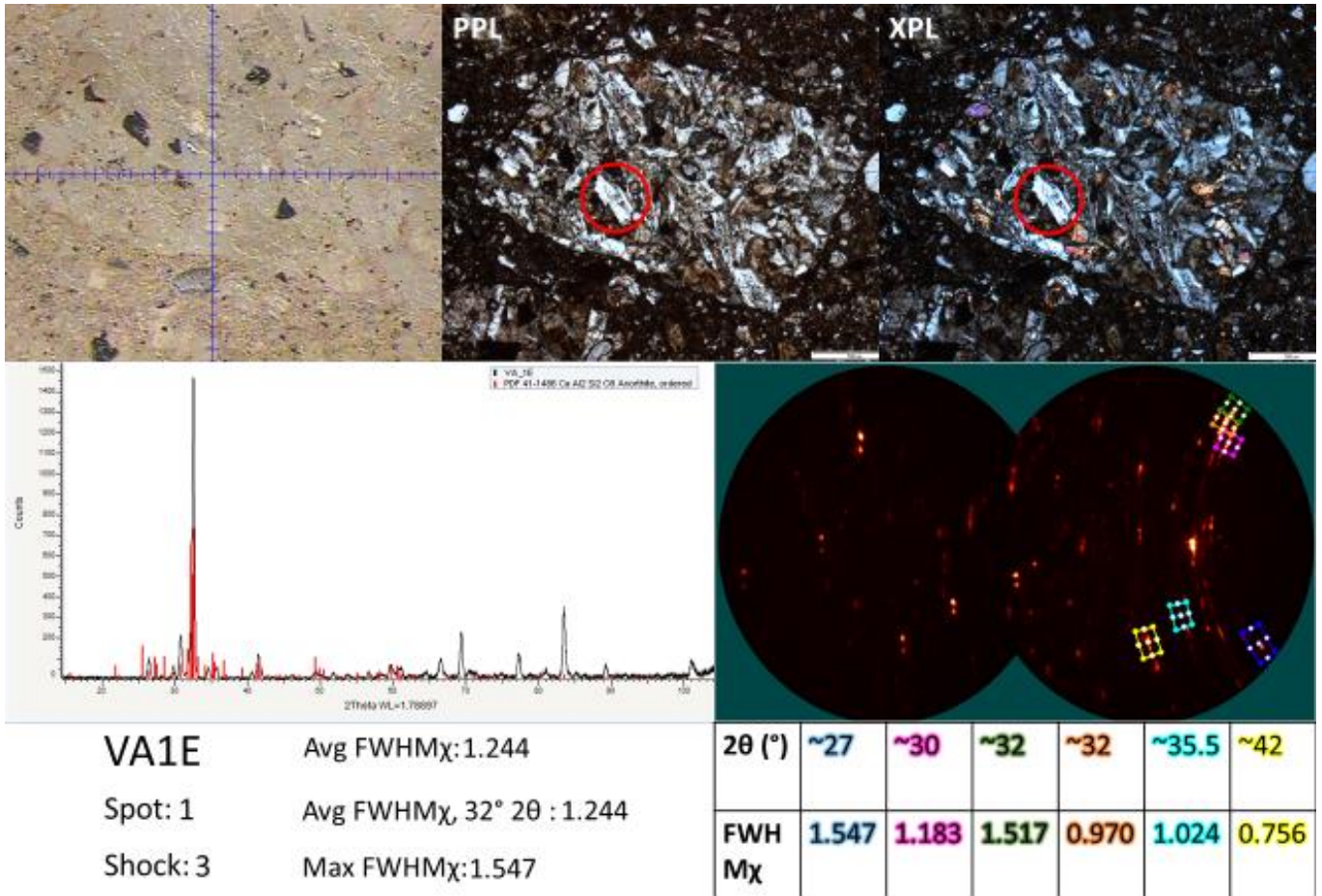
Optical petrography, μXRD analysis, and FWHMχ measurements of plagioclase feldspar grain (spot 1 in Fig. B-4) in a breccia clast of sample VA1E.
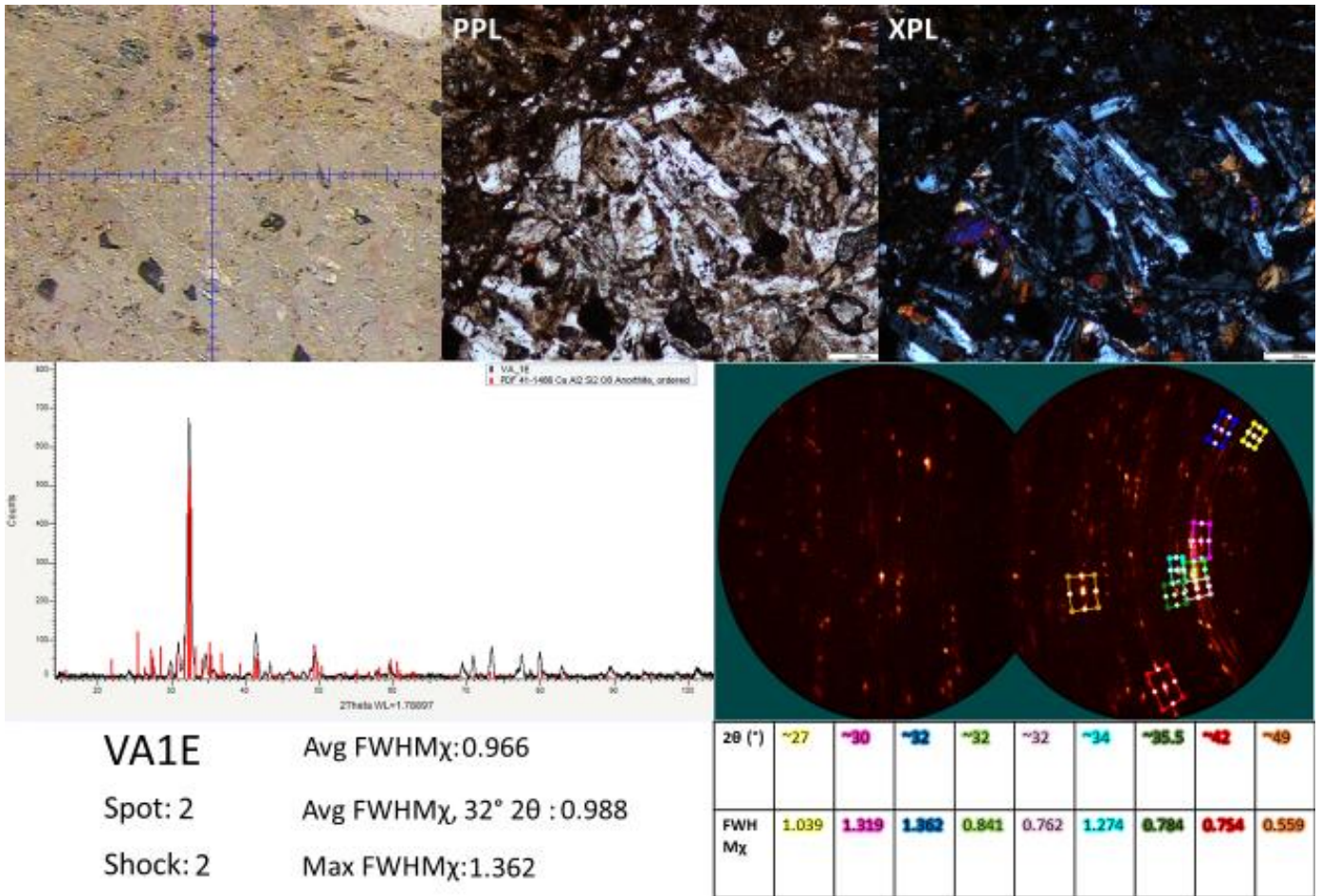
Red: Anorthite (Ca Al 2 Si2 O8) (PDF 41-1486)

2θ (°)	~27	~30	~32	~32	~32	~34	~35.5	~42	~49
FWH Mχ	1.039	1.319	1.362	0.841	0.762	1.274	0.784	0.754	0.559

VA1E

Spot: 2

Shock: 2

Avg FWHMχ:0.966

Avg FWHMχ, 32° 2θ : 0.988

Max FWHMχ:1.362

Optical petrography, µXRD analysis, and FWHMχ measurements of plagioclase feldspar grain (spot 2 in Fig. B-4) in a breccia clast of sample VA1E.
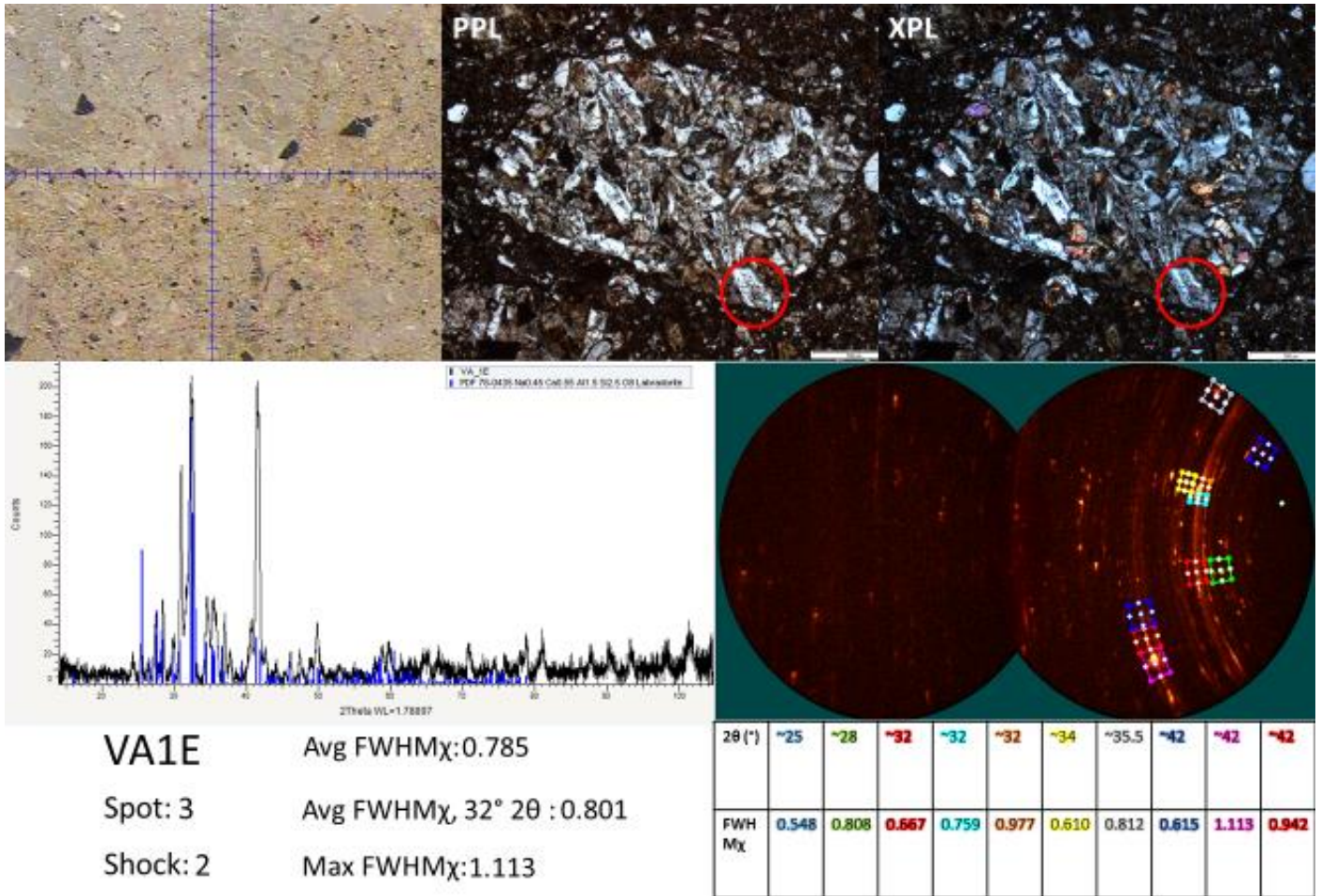
Red: Anorthite (Ca Al 2 Si2 O8) (PDF 41-1486)

VA1E

Spot: 3

Shock: 2

Avg FWHMχ:0.785

Avg FWHMχ, 32° 2θ :0.801

Max FWHMχ:1.113

| 2θ (°)	~25	~28	~32	~32	~32	~34	~35.5	~42	~42	~42
FWHMχ	0.548	0.808	0.667	0.759	0.977	0.610	0.812	0.615	1.113	0.942

Optical petrography, µXRD analysis, and FWHMχ measurements of plagioclase feldspar grain (spot 3 in Fig. B-4) in a breccia clast of sample VA1E.

Blue: Labradorite (Na0.45 Ca0.55 Al1.5 Si2.5 O8) (PDF 78-0435)

VA1E4

Figure B-5. VA-2017-1E4 thin section showing spots analyzed
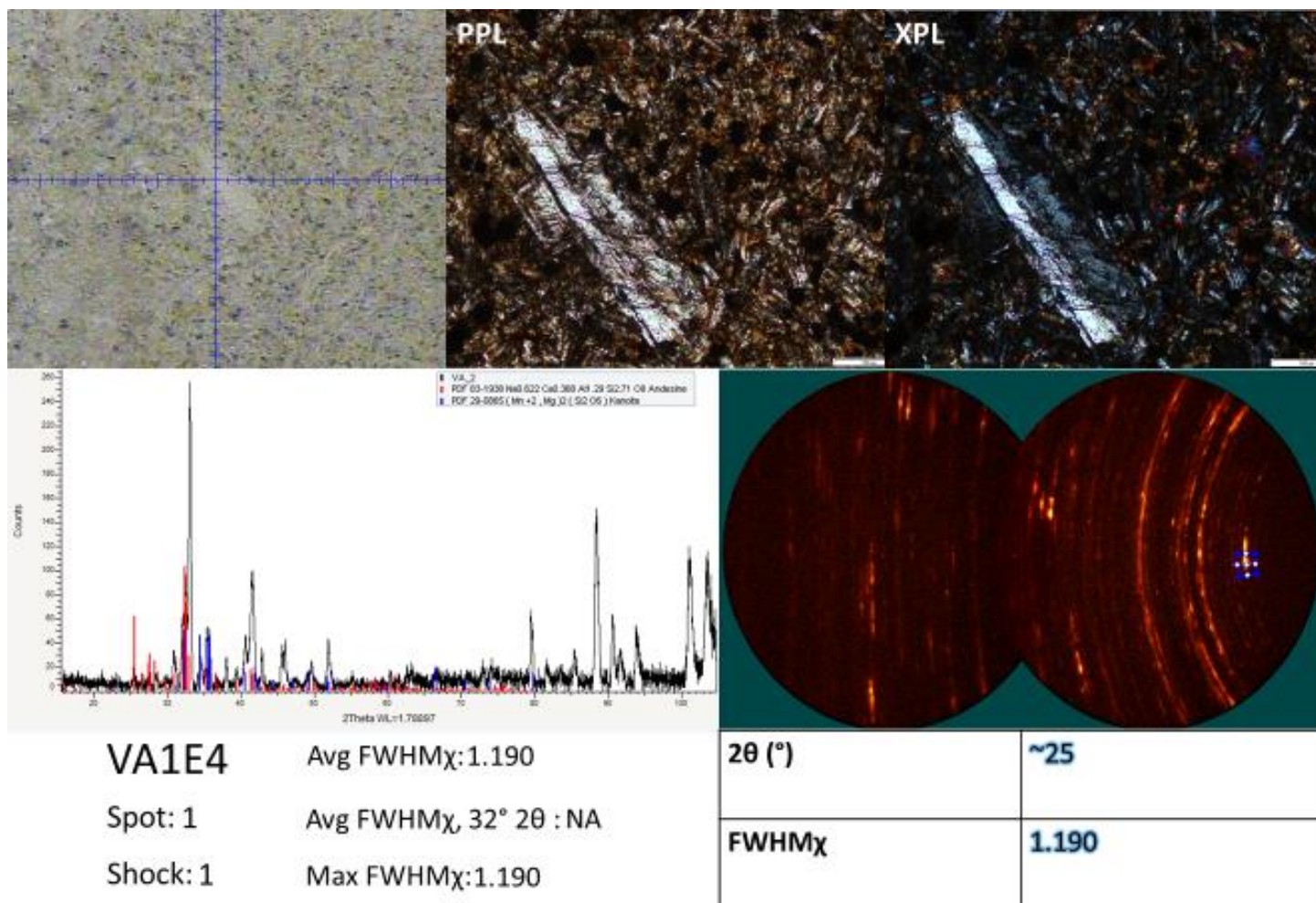
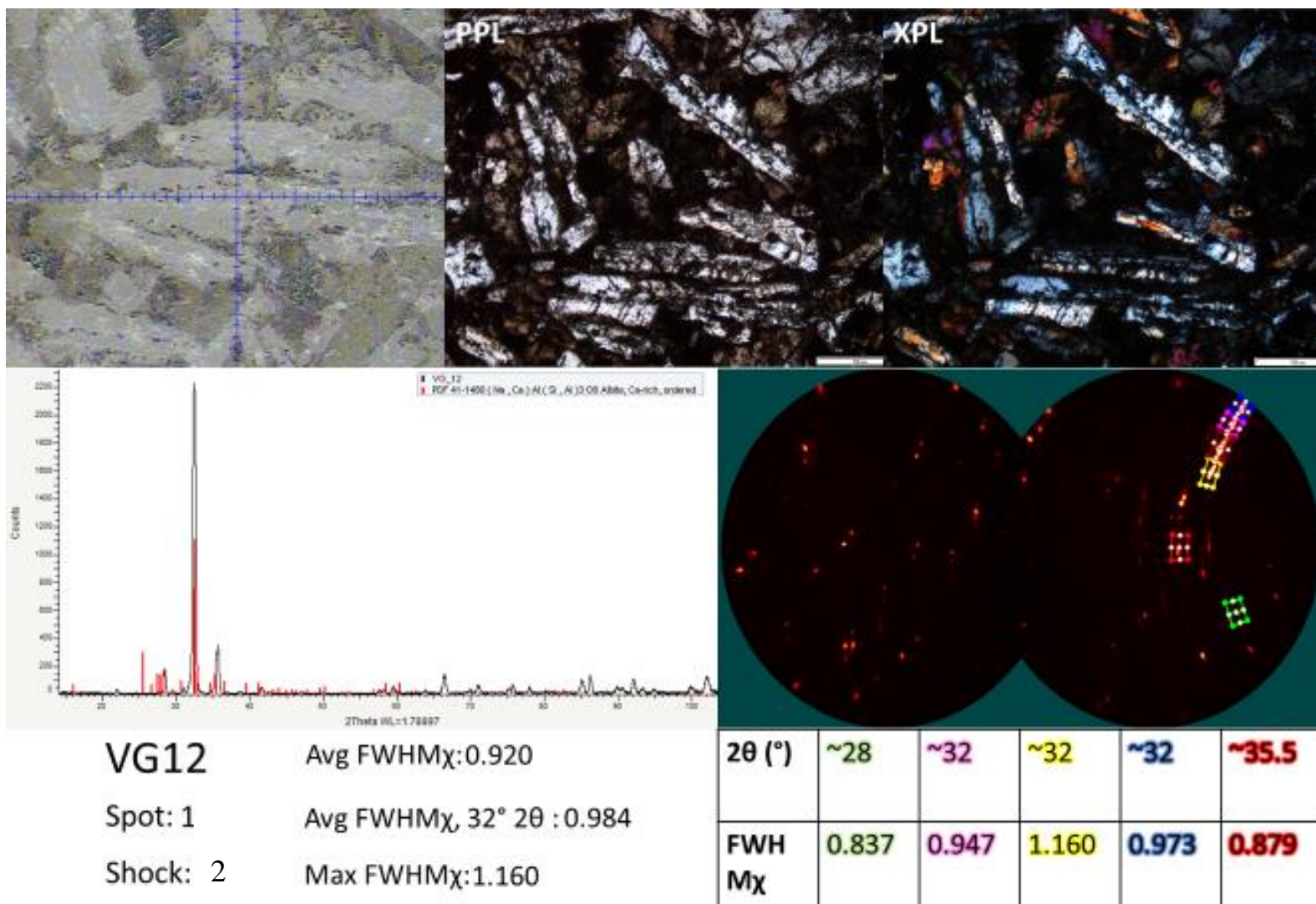**Optical petrography, µXRD analysis, and FWHMχ measurements of plagioclase feldspar grain (spot 1 in Fig. B-5) immersed in the matrix of sample VA1E4.**

Red: Andesine (Na0.622 Ca0.368 Al1.29 Si2.71 O8) (PDF 83-1938)

Blue: Kanoite (Mn +2, Mg)2 (Si2 O6) (PDF 29-0865)

VA2

Figure B-6. VA-2017-2 thin section showing spots analyzed
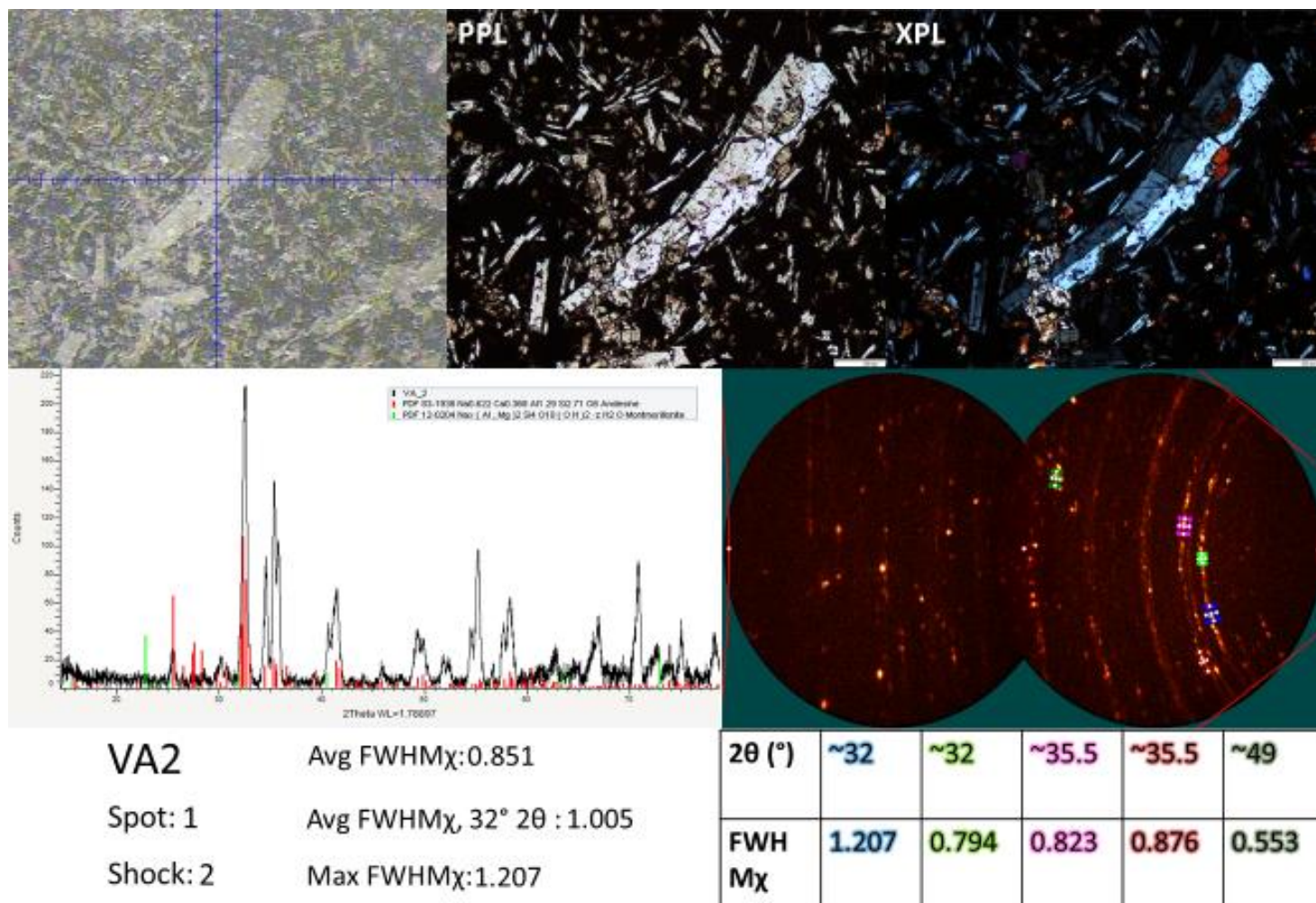
2θ (°)	~32	~32	~35.5	~35.5	~49
FWHMχ	1.207	0.794	0.823	0.876	0.553

VA2   Avg FWHMχ: 0.851

Spot: 1   Avg FWHMχ, 32° 2θ : 1.005

Shock: 2   Max FWHMχ: 1.207

Optical petrography, µXRD analysis, and FWHMχ measurements of plagioclase feldspar grain (spot 1 in Fig. B-6) immersed in the matrix of sample VA2.

Red: Andesine (Na0.622 Ca0.368 Al1.29 Si2.71 O8) (PDF 83-1938)

Green: Montmorillonite (Al, Mg)2 Si4 O10 (OH)2 · z H2O) (PDF 12-0204)
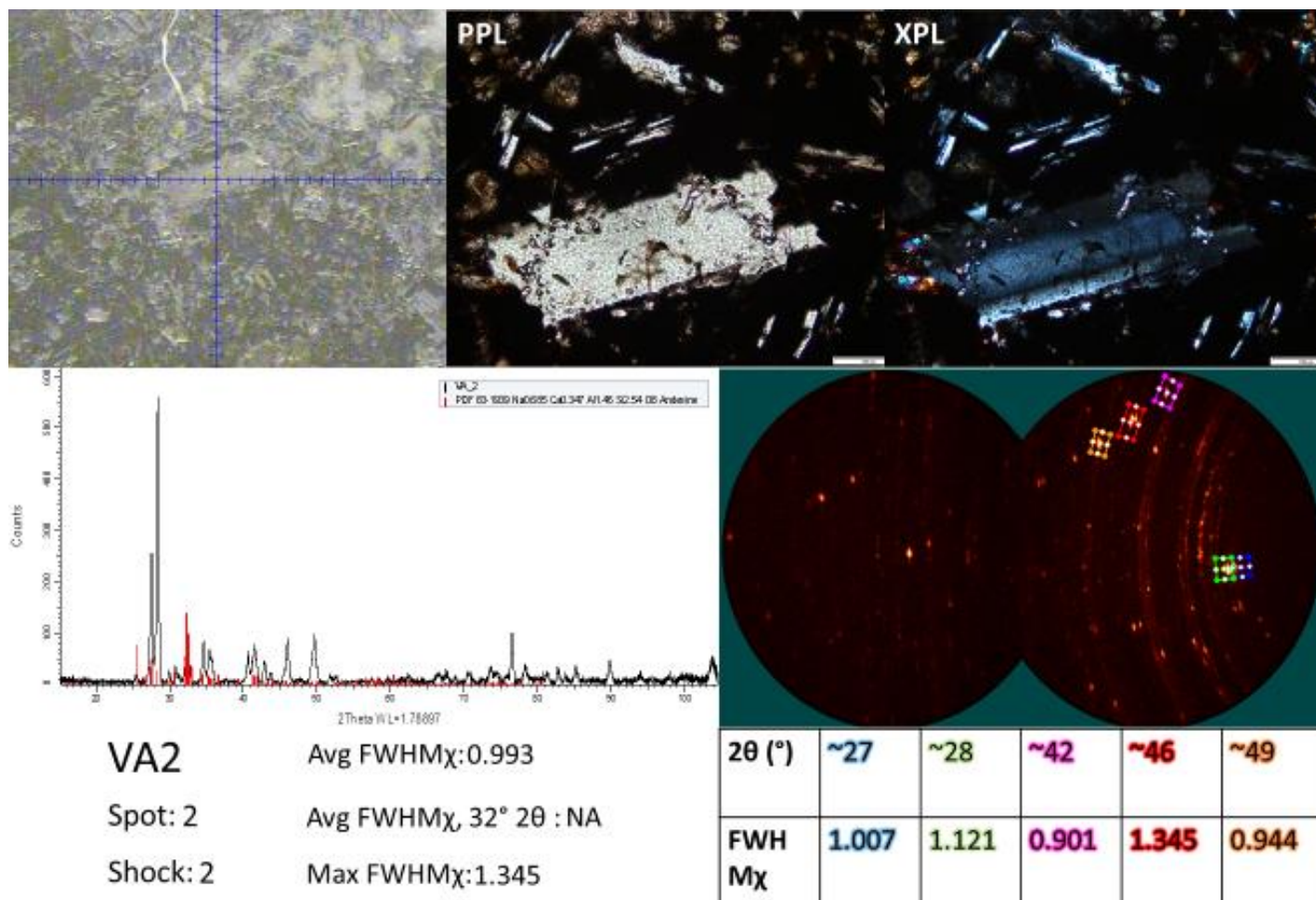
Optical petrography, µXRD analysis, and FWHMχ measurements of plagioclase feldspar grain (spot 2 in Fig. B-6) immersed in the matrix of sample VA2.

Red: Andesine (Na0.685 Ca0.347 Al1.46 Si2.54 O8) (PDF 83-1939)
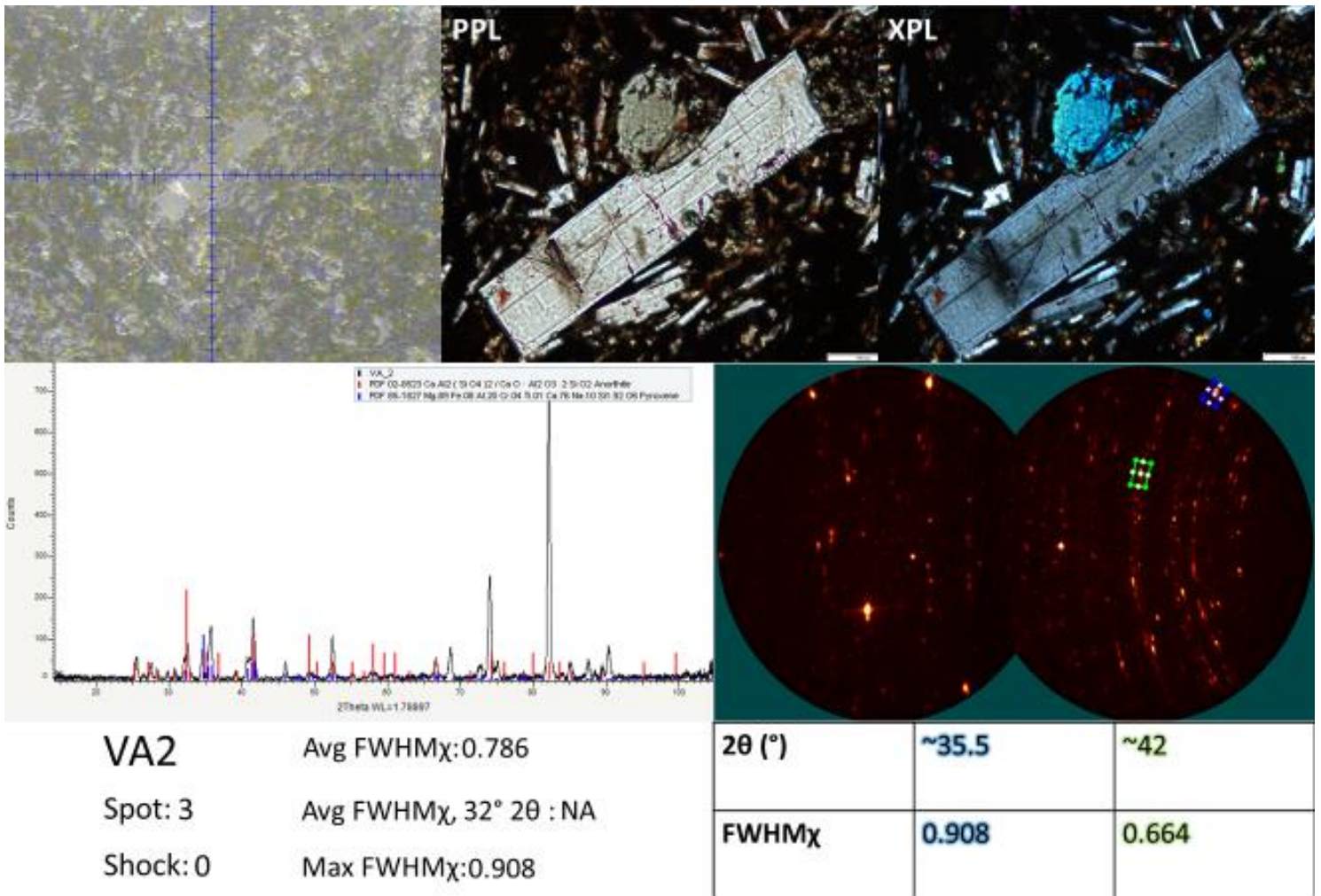
Optical petrography, µXRD analysis, and FWHMχ measurements of plagioclase feldspar grain (spot 1 in Fig. B-6) immersed in the matrix of sample VA2.

Red: Anorthite Ca Al2 (Si O4)2 / Ca O · Al2 O3 · 2 Si O2 (PDF 02-0523)

Blue: Pyroxene (Mg0.89 Fe0.08 Al0.20 Cr0.04 Ti0.01 Ca0.76 Na0.10 Si1.92 O6 (PDF 85-1827)
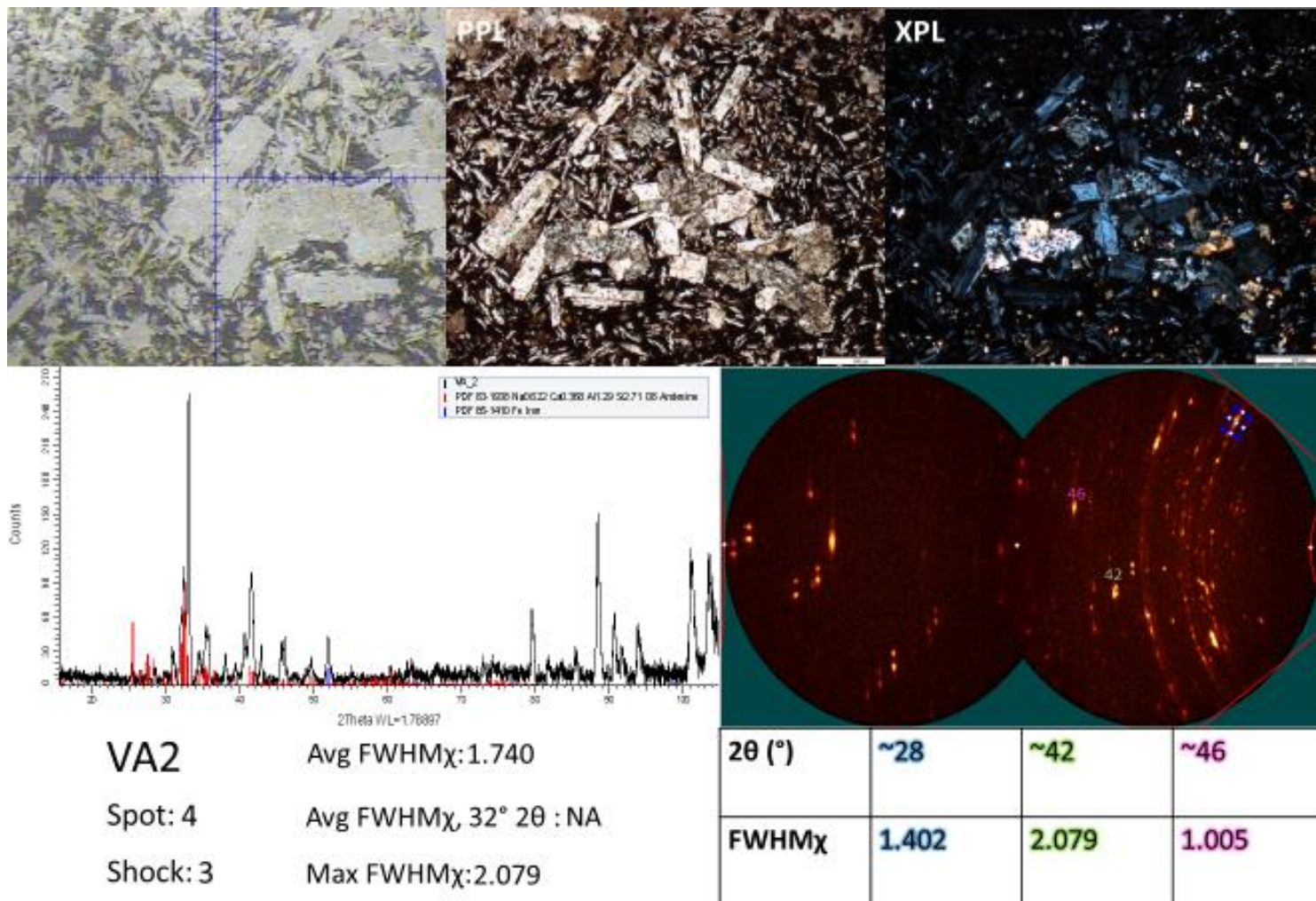
Optical petrography, µXRD analysis, and FWHMχ measurements of plagioclase feldspar grain (spot 4 in Fig. B-6) immersed in the matrix of sample VA2.

Red: Andesine (Na0.622 Ca0.368 Al1.29 Si2.71 O8) (PDF 83-1938)

Blue: Fe Iron (PDF 85-1410)

VA3

Figure B-7. VA-2017-3 thin section showing spots analyzed
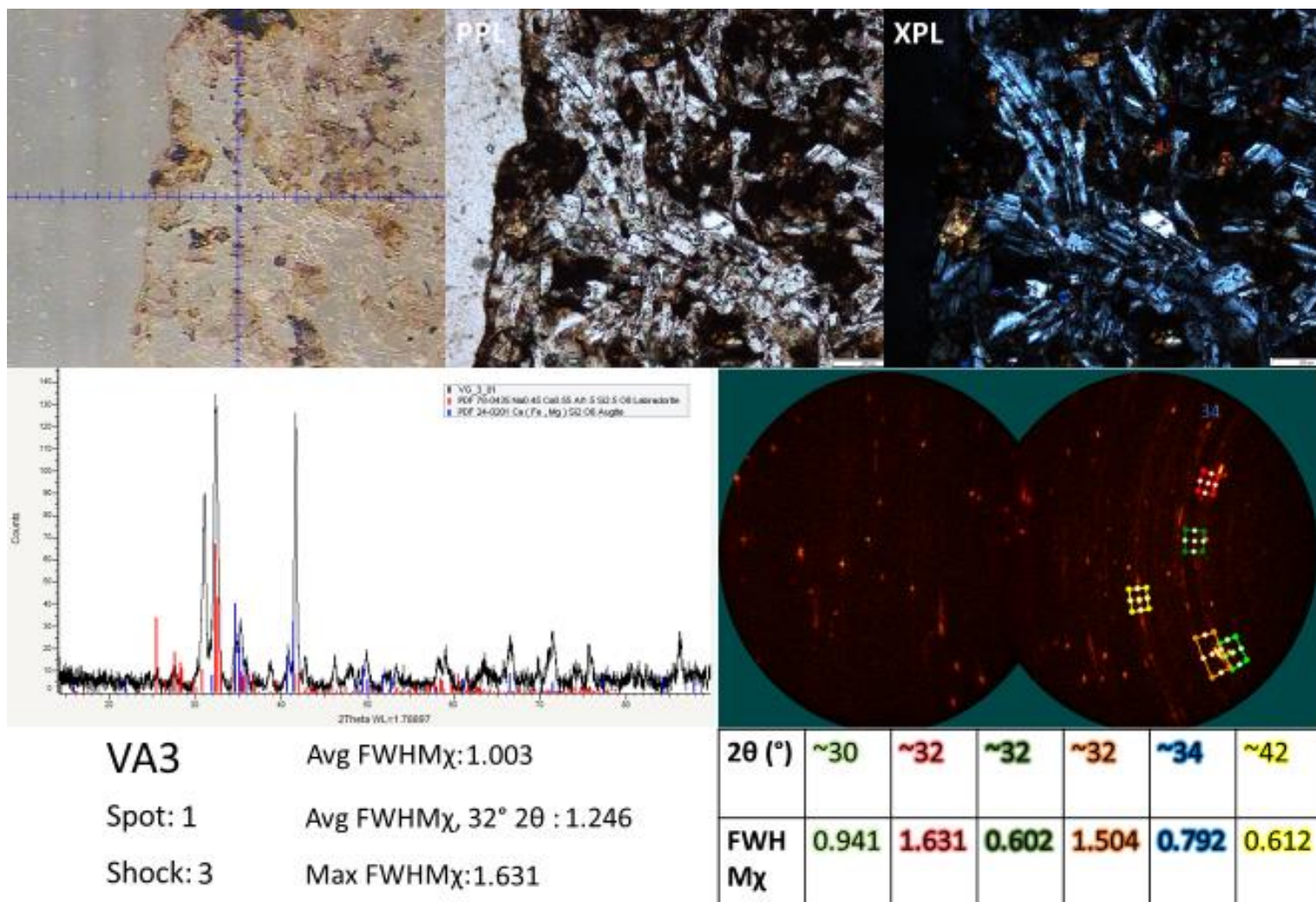
Optical petrography, µXRD analysis, and FWHMχ measurements of plagioclase feldspar grain (spot 1 in Fig. B-7) in sample VA3.
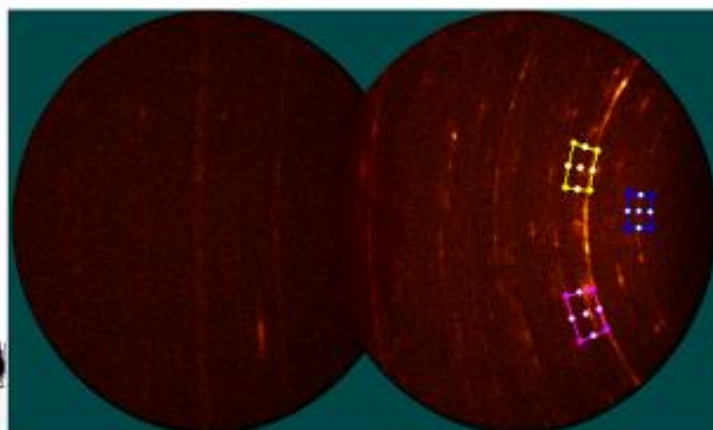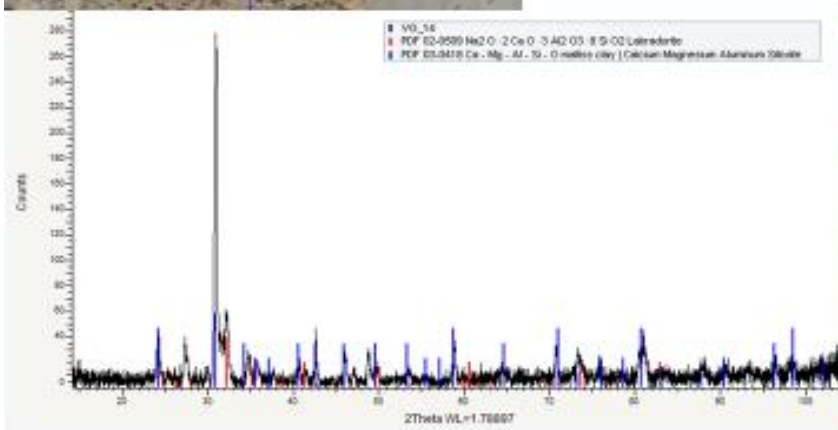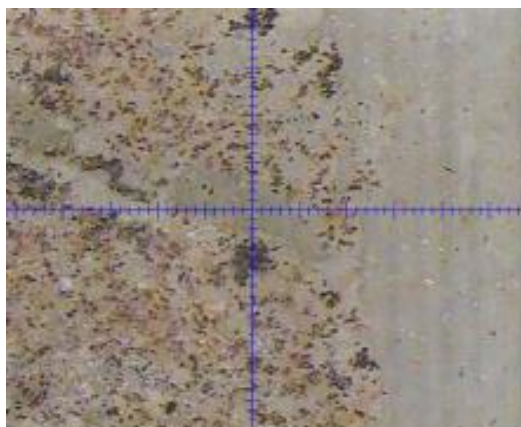
Red: Labradorite (Na0.45 Ca0.55 Al1.5 Si2.5 O8) (PDF 78-0435)

Blue: Augite Ca (Fe, Mg) Si2 O6 (PDF 24-0201)
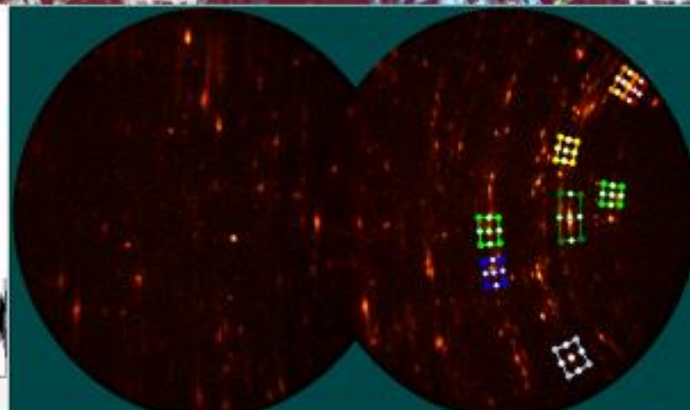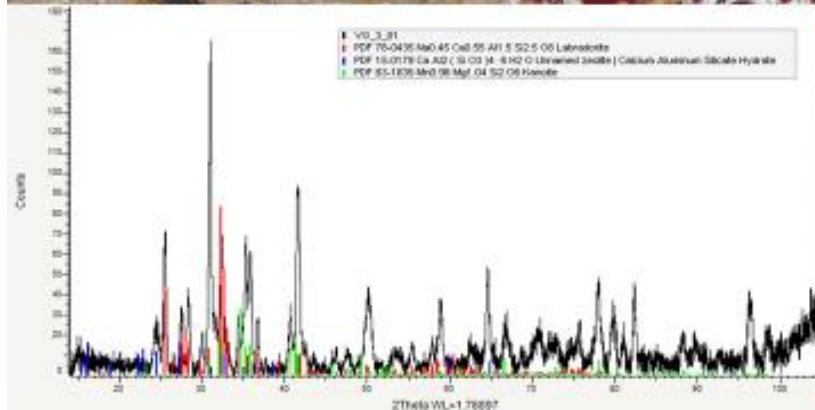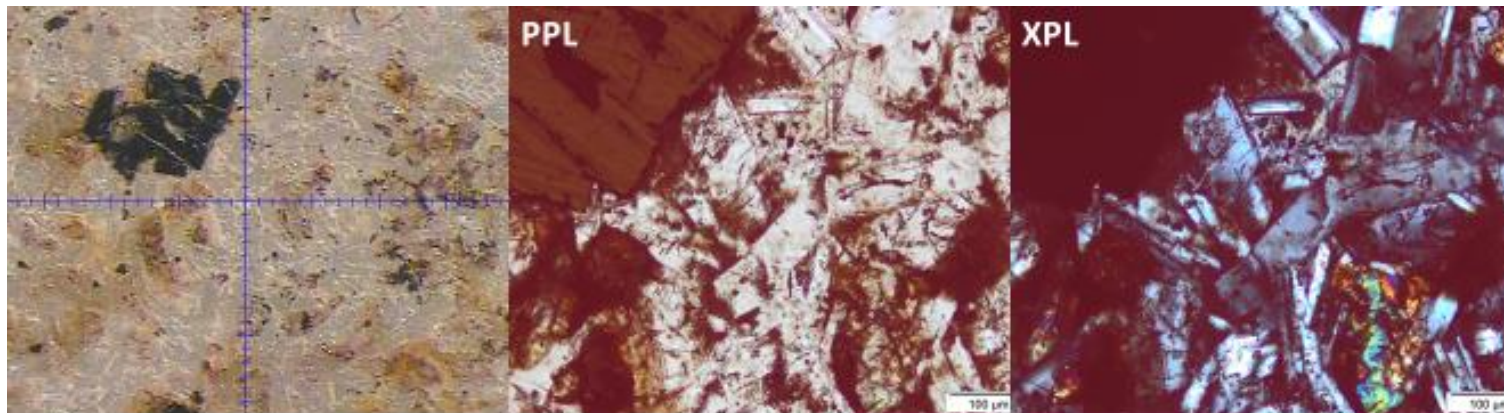
Optical petrography, μXRD analysis, and FWHMχ measurements of plagioclase feldspar grain (spot 2 in Fig. B-7) in sample VA3.

Red: Labradorite (Na0.45 Ca0.55 Al1.5 Si2.5 O8) (PDF 78-0435)

Blue: Calcium Aluminum Silicate/ Zeolite Ca Al2 (Si O3)4 · 6 H2O (PDF 15-0179)

Green: Kanoite (Mn0.96 Mg1.04 Si2 O6) (PDF 83-1835)
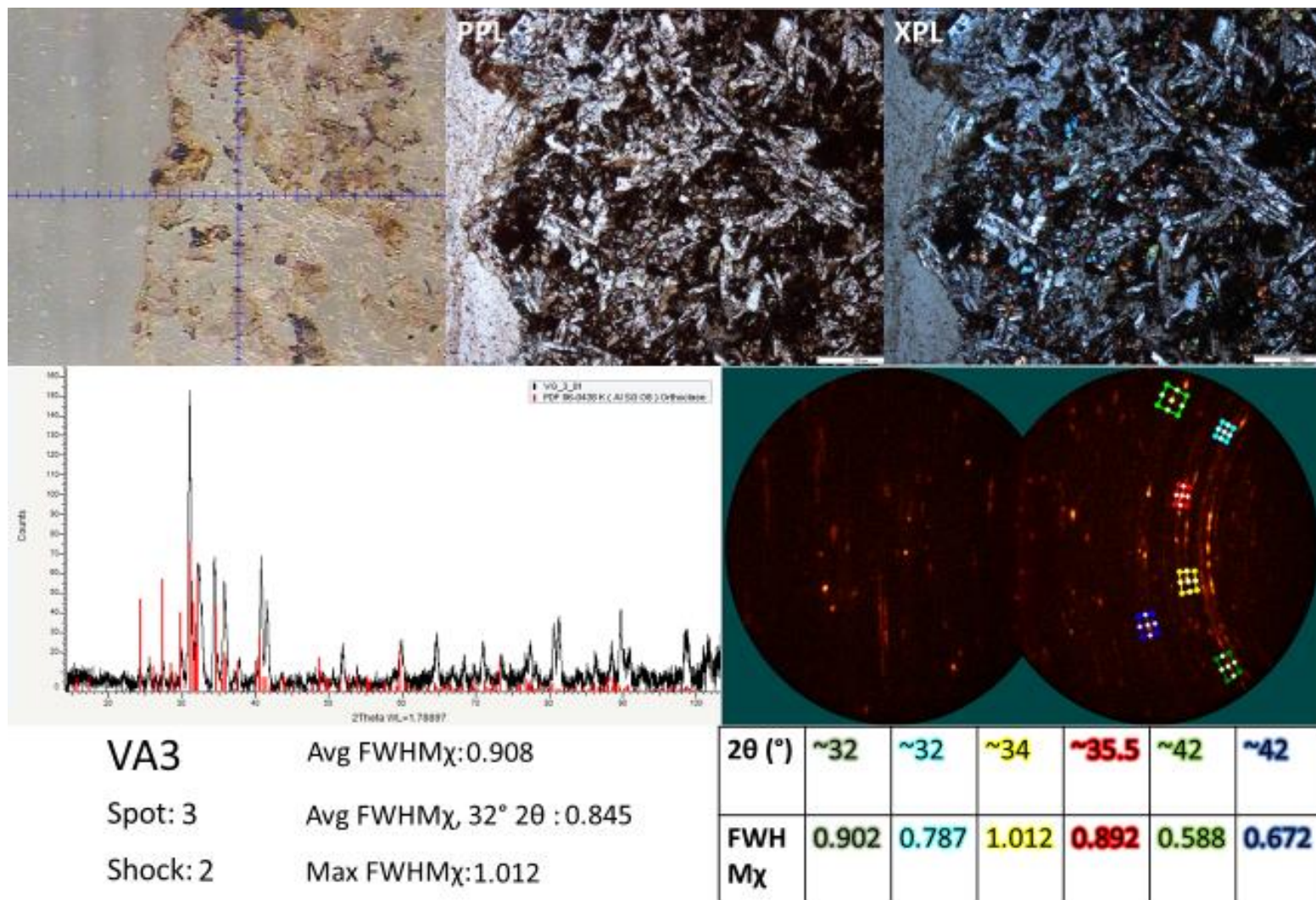
Optical petrography, μXRD analysis, and FWHMχ measurements of plagioclase feldspar grain (spot 3 in Fig. B-7) in sample VA3.

Red: Orthoclase K (Al Si3 O8) (PDF 86-0438)
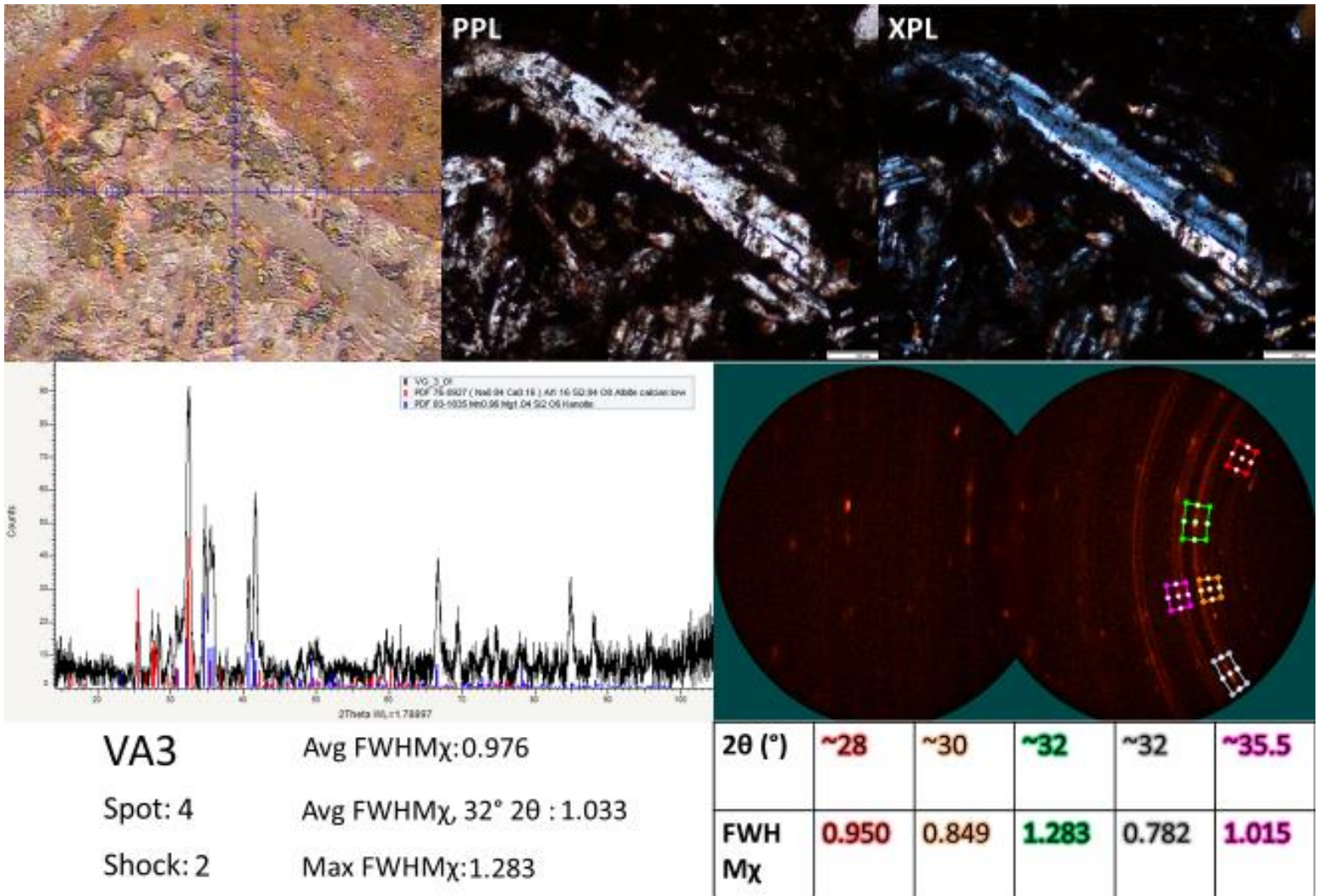
Optical petrography, µXRD analysis, and FWHMχ measurements of plagioclase feldspar grain (spot 4 in Fig. B-7) immersed in matrix of sample VA3.

Red: Albite calcian low (Na0.84 Ca0.16) Al1.16 Si2.84 O8 (PDF 76-0927)

Blue: Kanoite (Mn0.96 Mg1.04 Si2 O6) (PDF 83-1835)
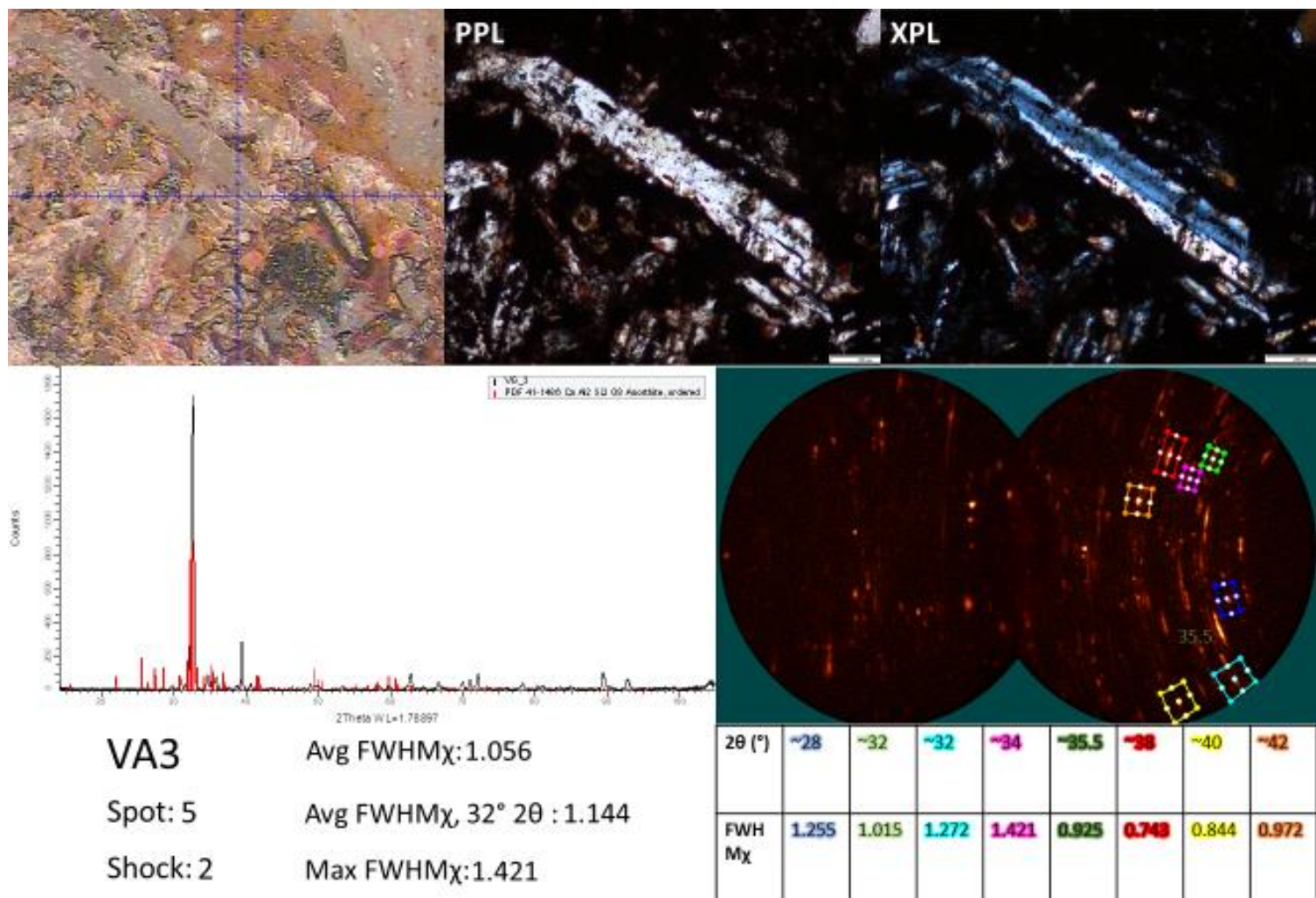
Optical petrography, μXRD analysis, and FWHMχ measurements of plagioclase feldspar grain (spot 5 in Fig. B-7) immersed in matrix of sample VA3.

Red: Anorthite (Ca Al2 Si2 O8) (PDF 41-1486)

VA3B

Figure B-8. VA-2017-3B thin section showing spots analyzed
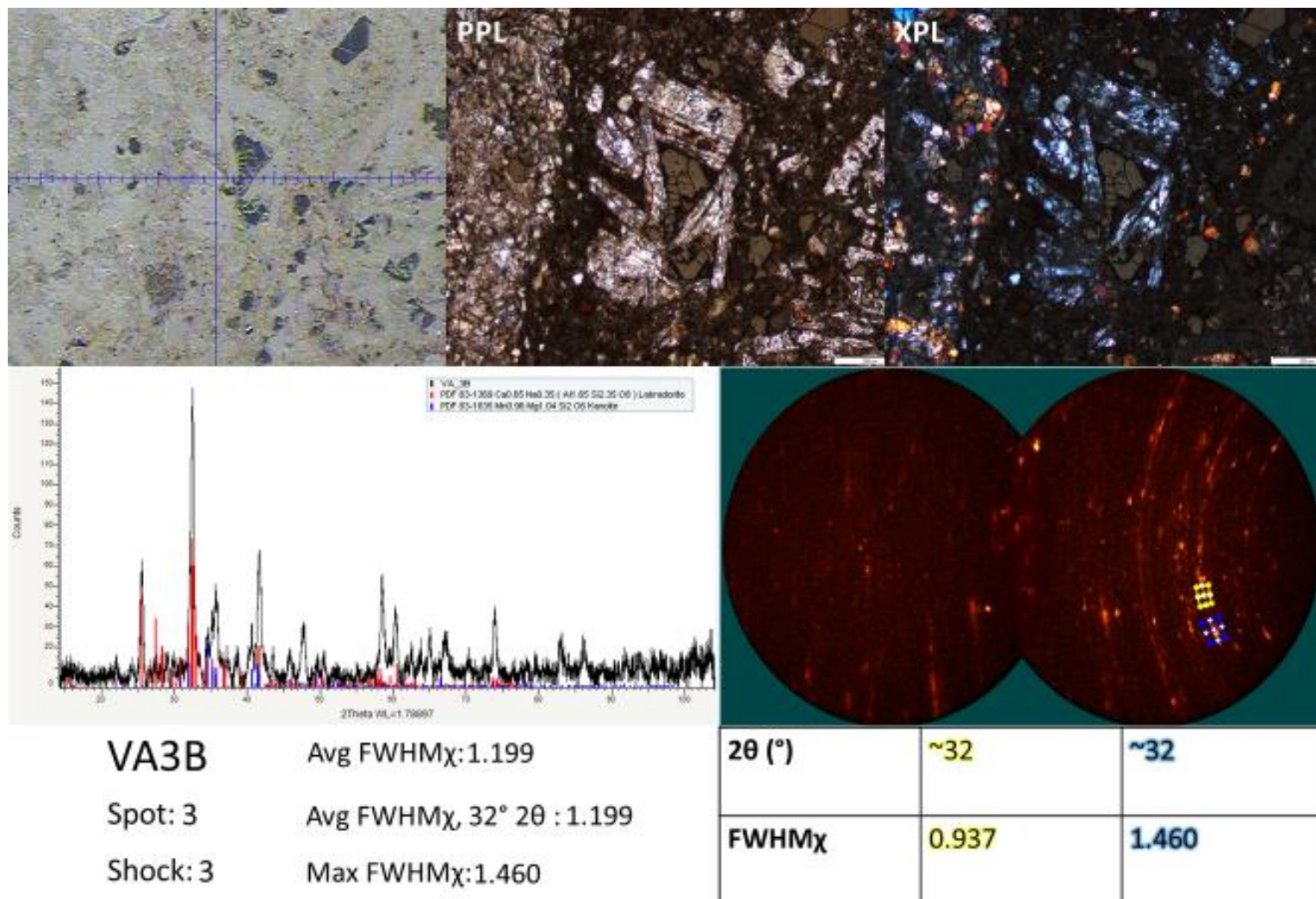
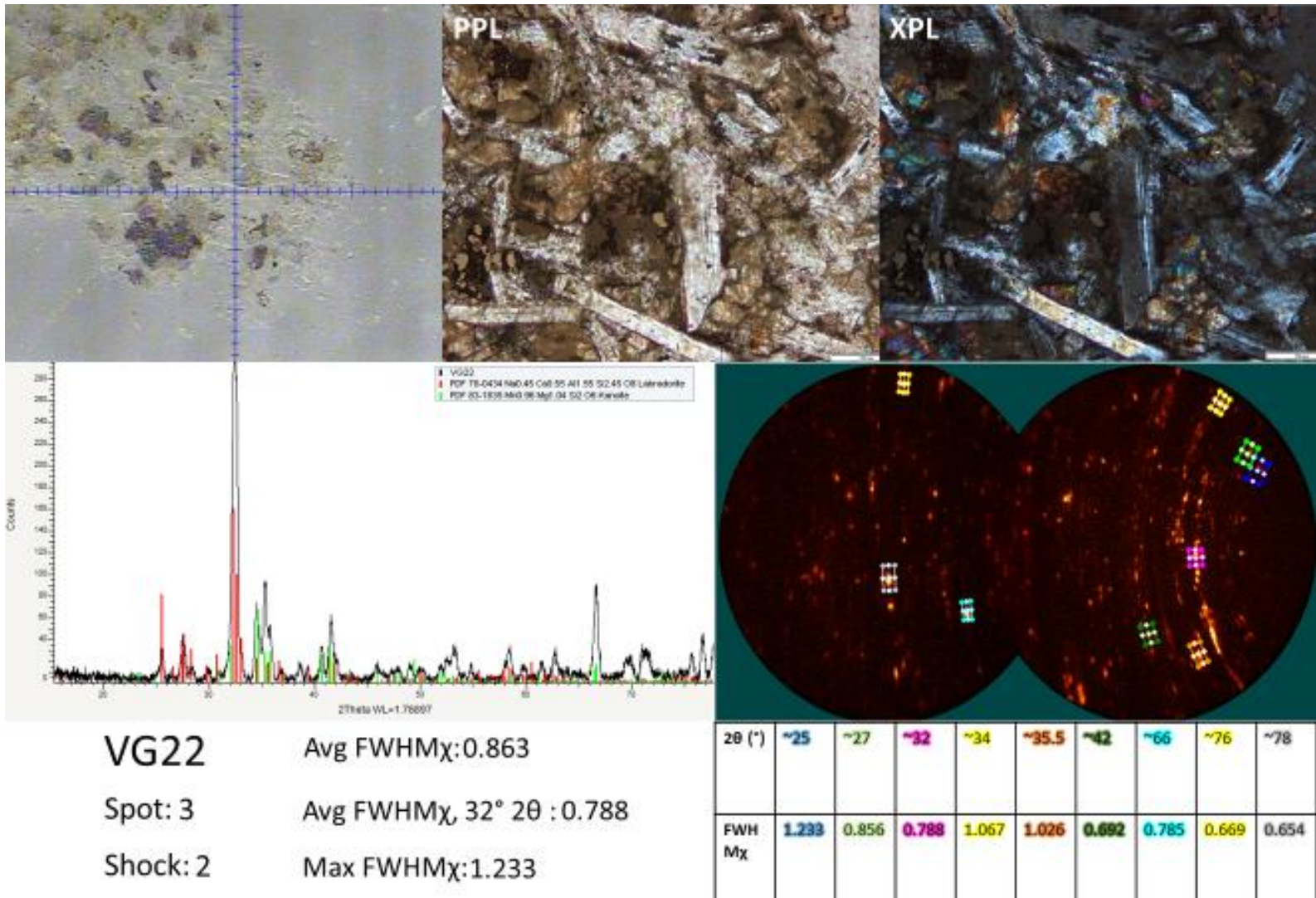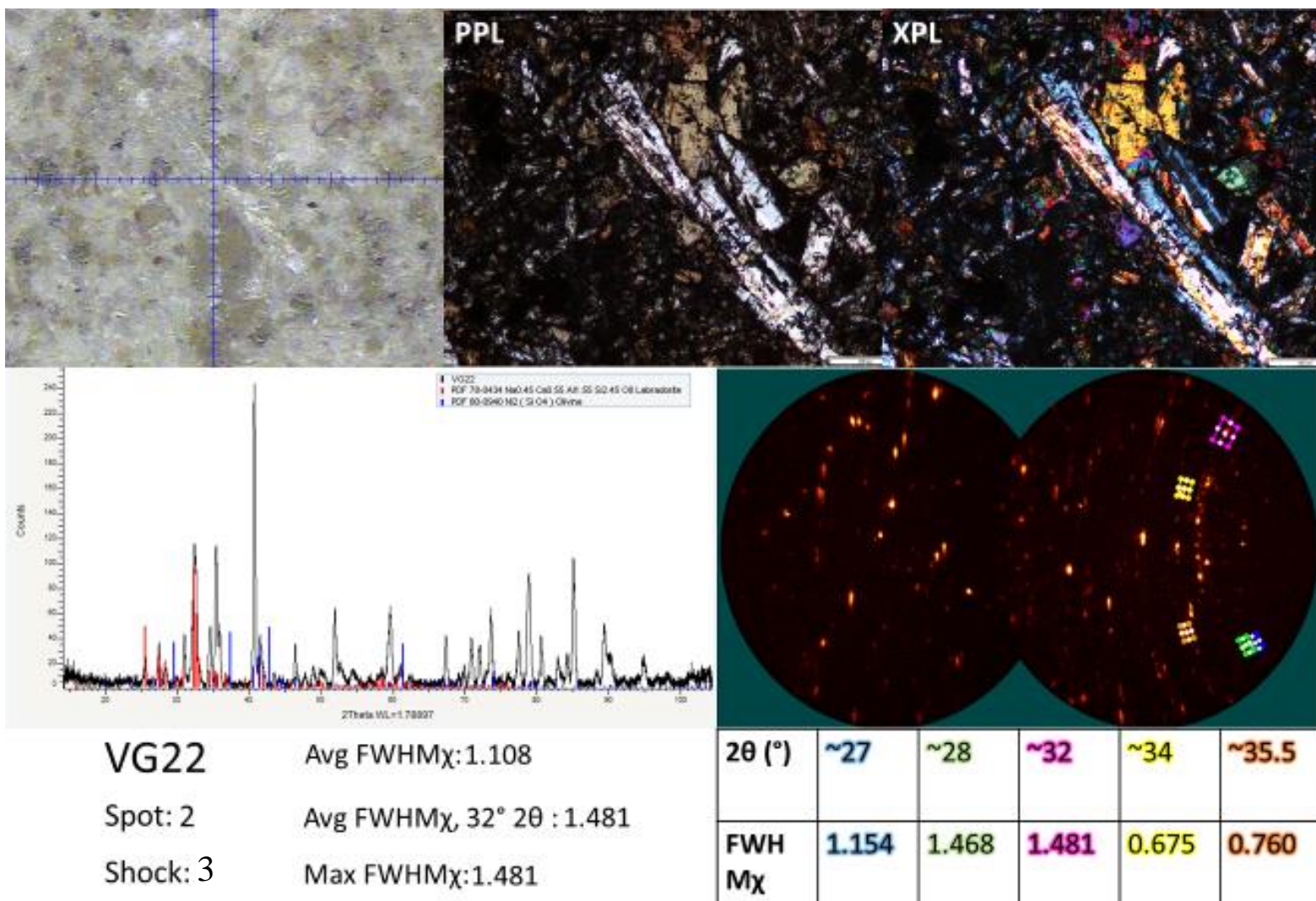Optical petrography, μXRD analysis, and FWHMχ measurements of plagioclase feldspar grain (spot 3 in Fig. B-8) in sample VA3B.

Red: Labradorite Ca0.65 Na0.35 (Al1.65 Si2.35 O8) (PDF 83-1369)

Blue: Kanoite (Mn0.96 Mg1.04 Si2 O6) (PDF 83-1835)
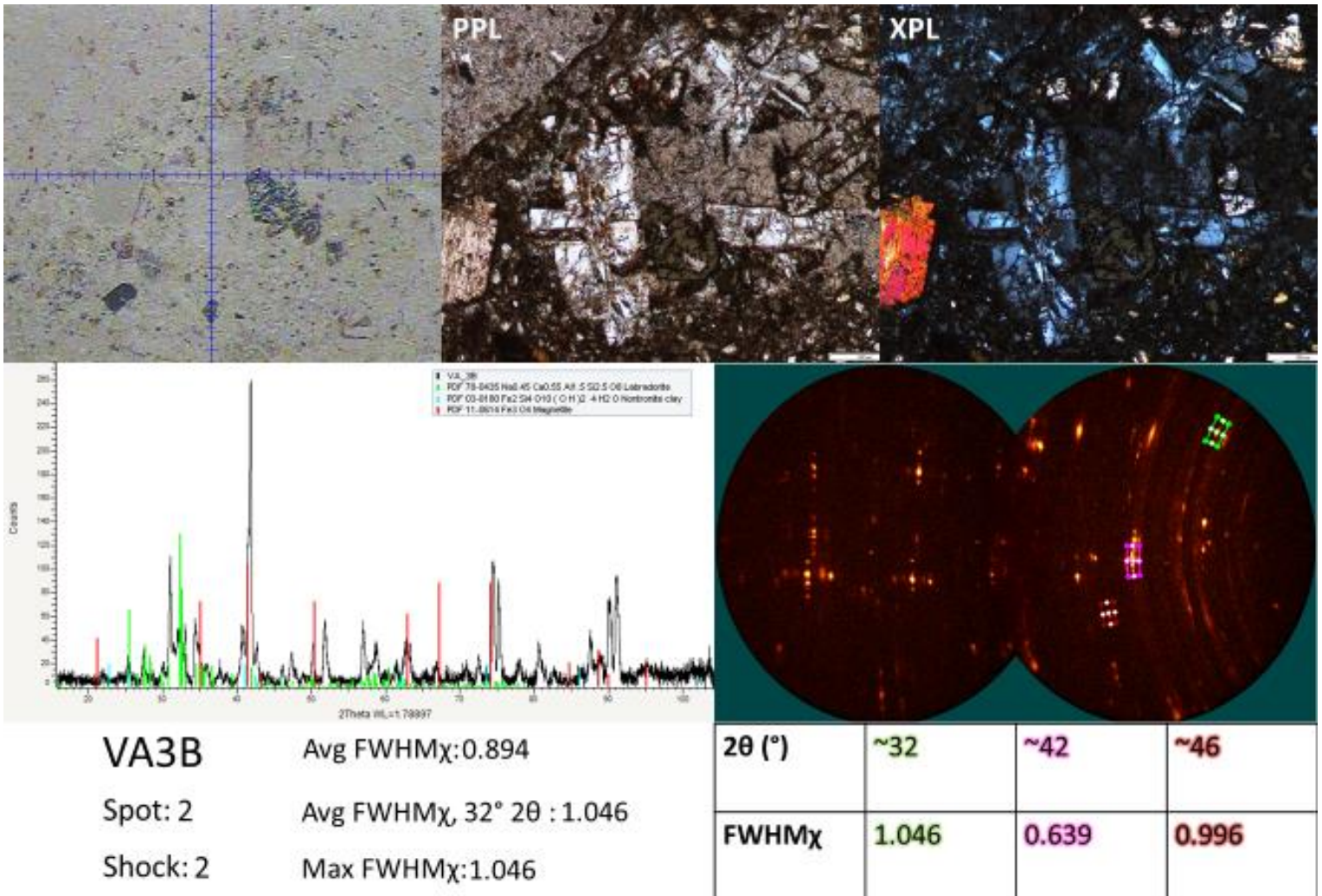
Optical petrography, µXRD analysis, and FWHMχ measurements of plagioclase feldspar grain (spot 2 in Fig. B-8) in sample VA3B.

Green: Labradorite (Na0.45 Ca0.55 Al1.5 Si2.5 O8) (PDF 78-0435)

Light blue: Nontronite clay Fe2 Si4 O10 (OH)2 · 4 H2O (PDF 03-0180)

Red: Magnetite (Fe3 O4) (PDF 11-0614)
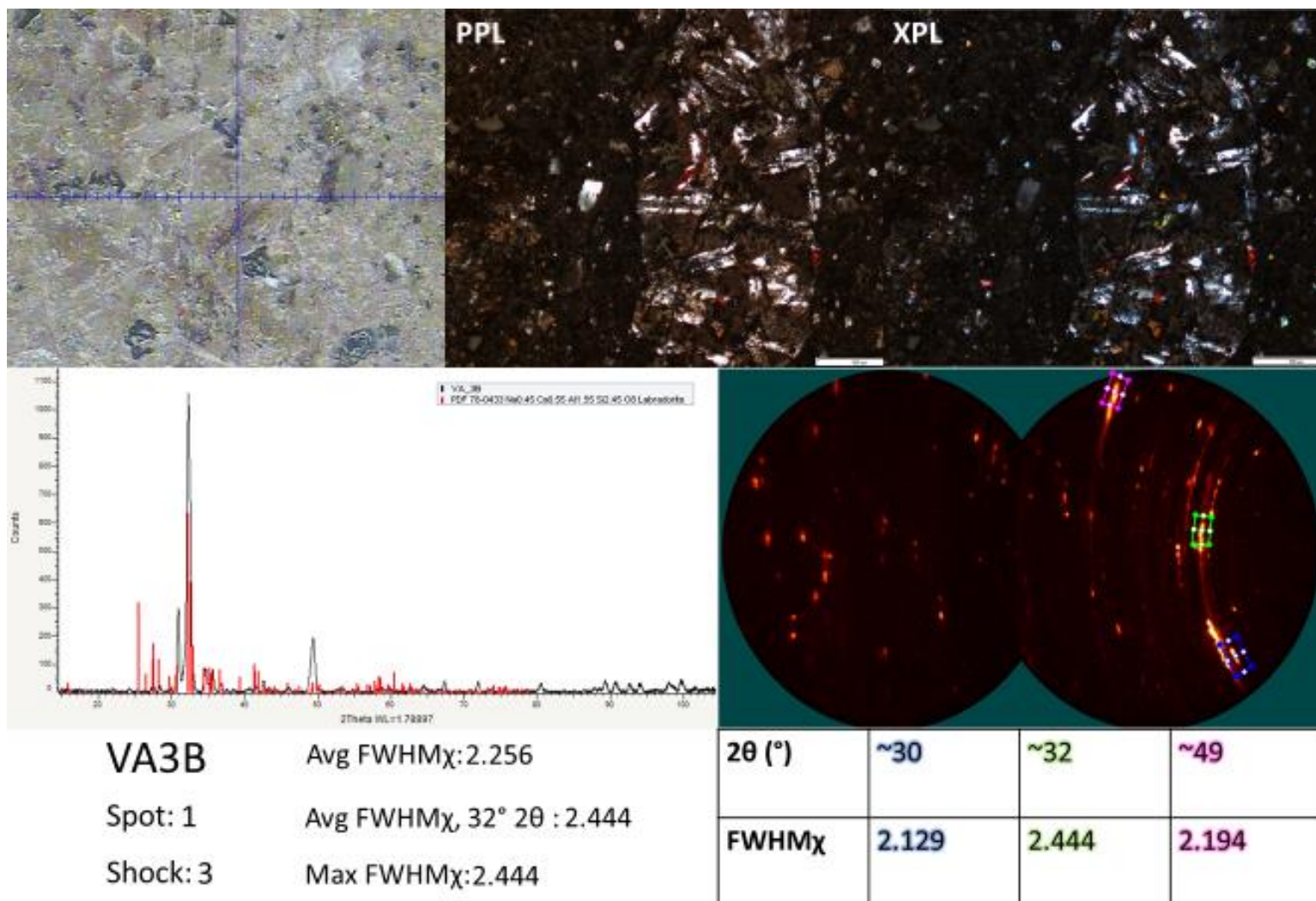
Optical petrography, μXRD analysis, and FWHMχ measurements of plagioclase feldspar grain (spot 1 in Fig. B-8) in breccia clast of sample VA3B.

**Red: Labradorite (Na0.45 Ca0.55 Al1.55 Si2.45 O8) (PDF 78-0433)**

VA5C

Figure B-9. VA-2017-5C thin section showing spots analyzed
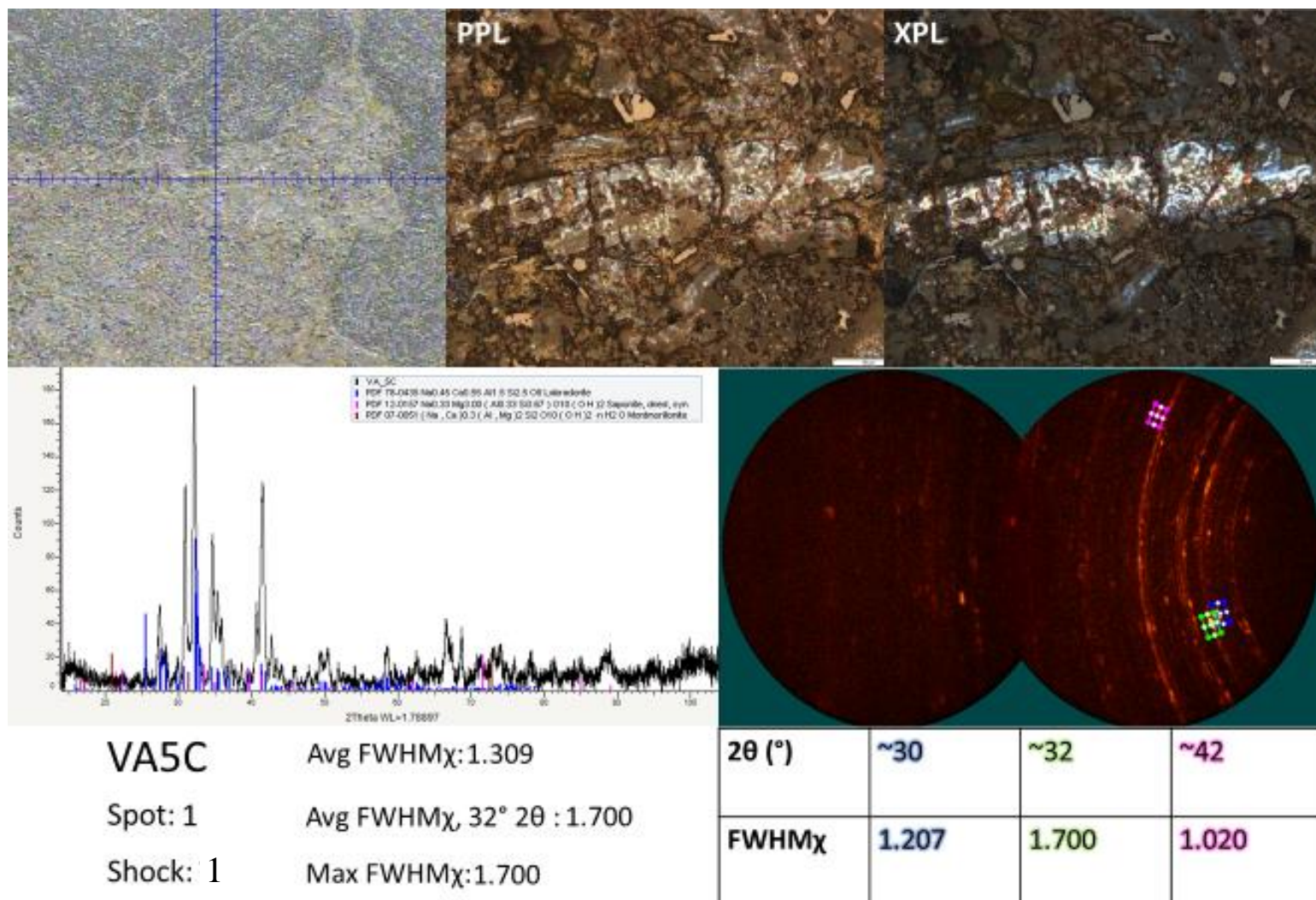
Optical petrography, μXRD analysis, and FWHMχ measurements of plagioclase feldspar grain (spot 1 in Fig. B-9) in sample VA5C.

Blue: Labradorite (Na0.45 Ca0.55 Al1.5 Si2.5 O8) (PDF 78-0435)

Pink: Saponite Na0.33 Mg3.00 (Al0.33 Si3.67) O10 (OH)2 (PDF 12-0157)

Maroon: Montmorillonite (Na, Ca)0.3 (Al, Mg)2 Si2 O10 (OH)2 · n H2O (PDF 07-0051)

VG3

Figure B-10. VG-2017-3 thin section showing spots analyzed
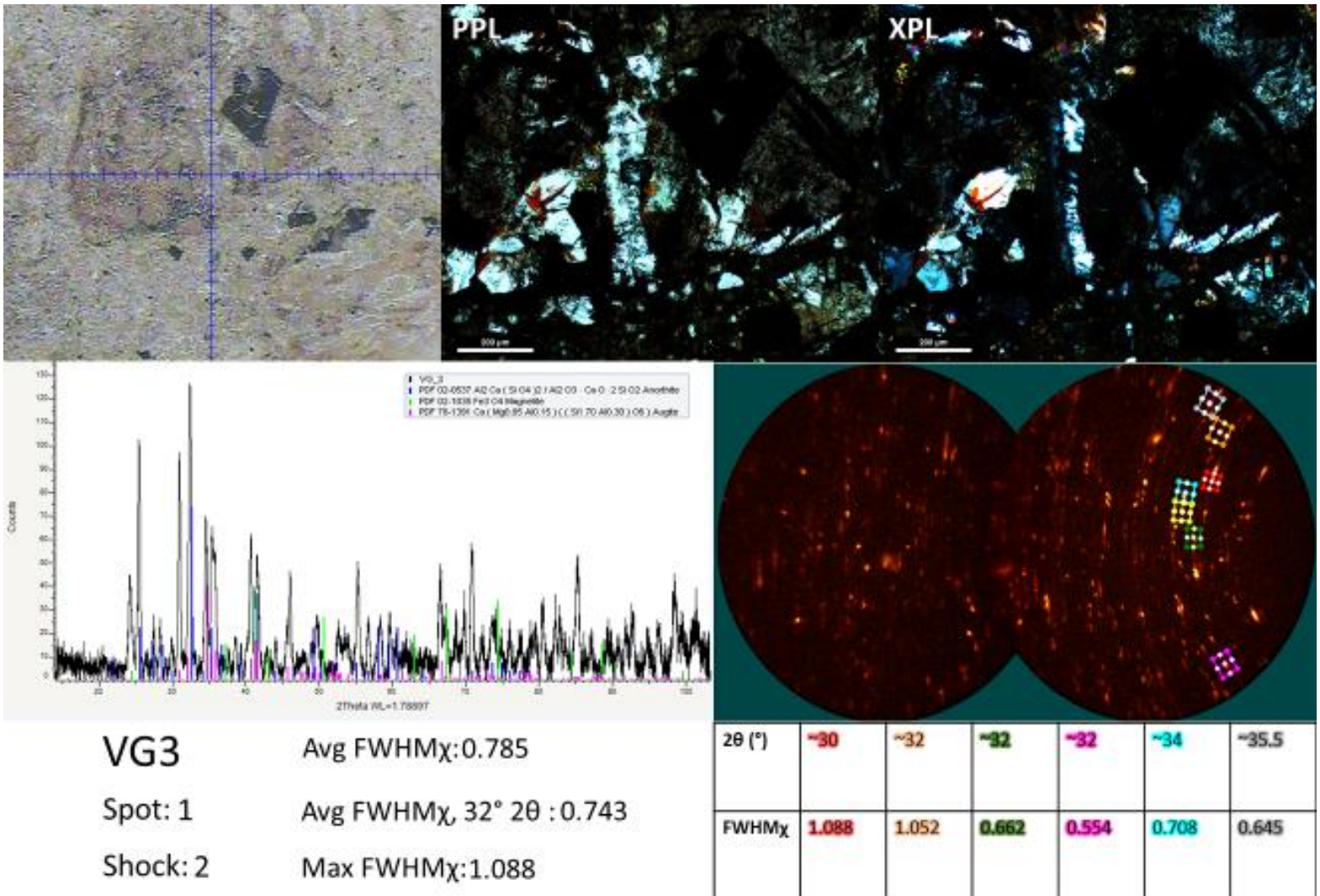
Optical petrography, μXRD analysis, and FWHMχ measurements of plagioclase feldspar grain (spot 1 in Fig. B-10) in a breccia clast of sample VG3.

Blue: Anorthite Al2 Ca(Si O4)2 / Al2 O3 · 2 Si O2 (PDF 02-0537)

Green: Magnetite (Fe3 O4) (PDF 02-1035)
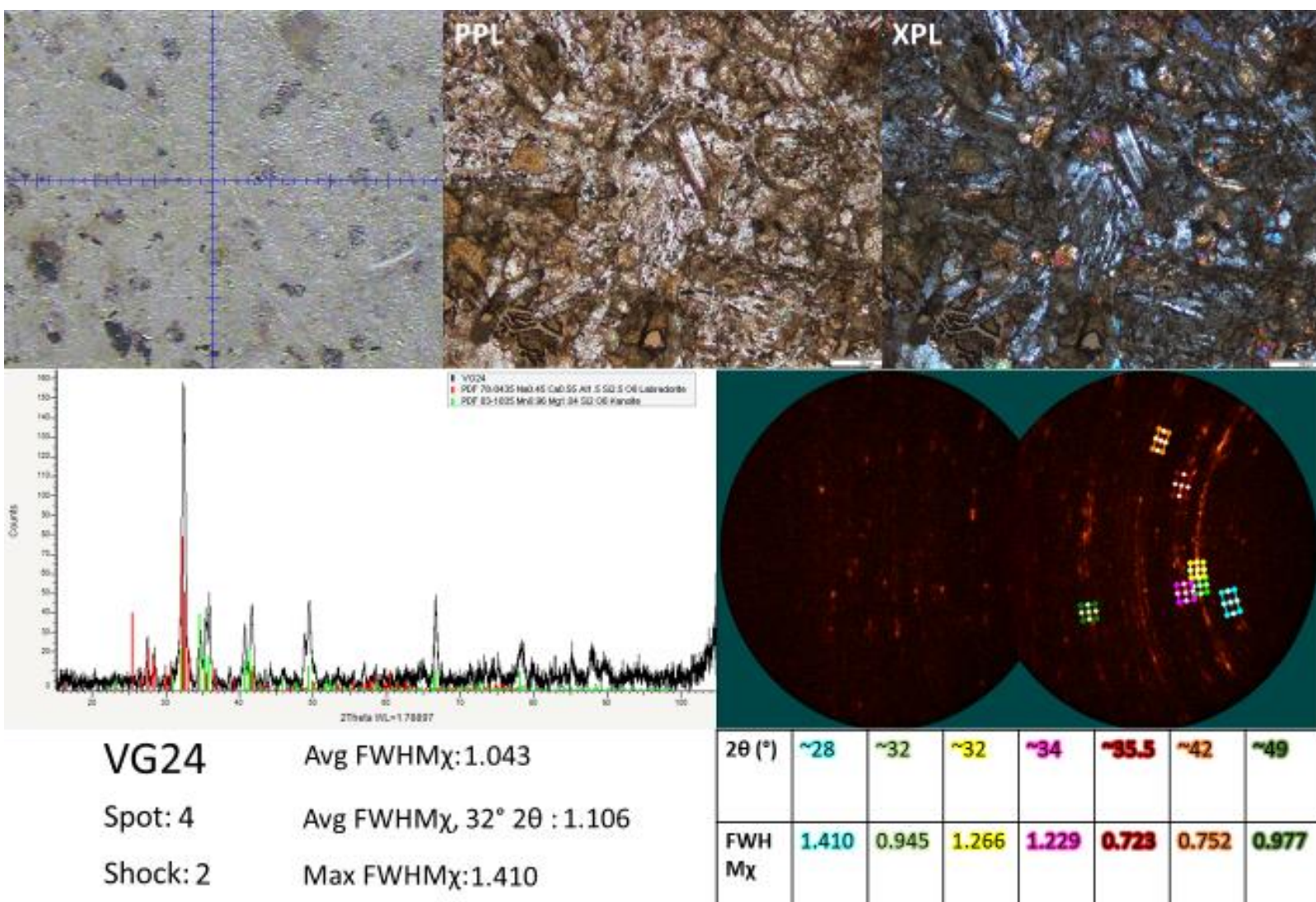
Pink: Augite Ca(Mg0.85 Al0.15) (Si1.70 Al0.30) O6 (PDF 78-1391)
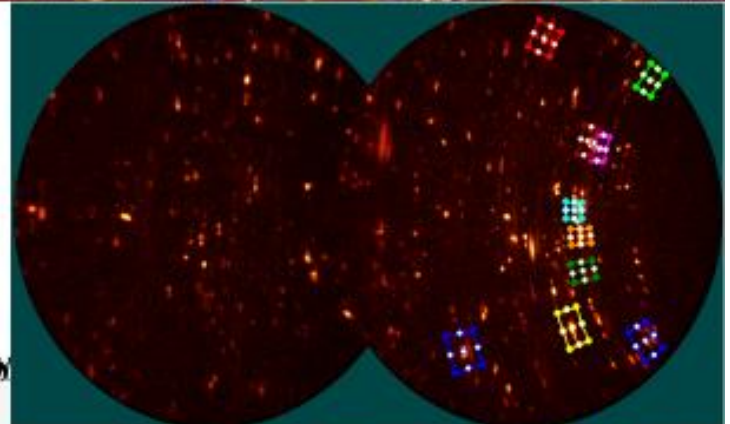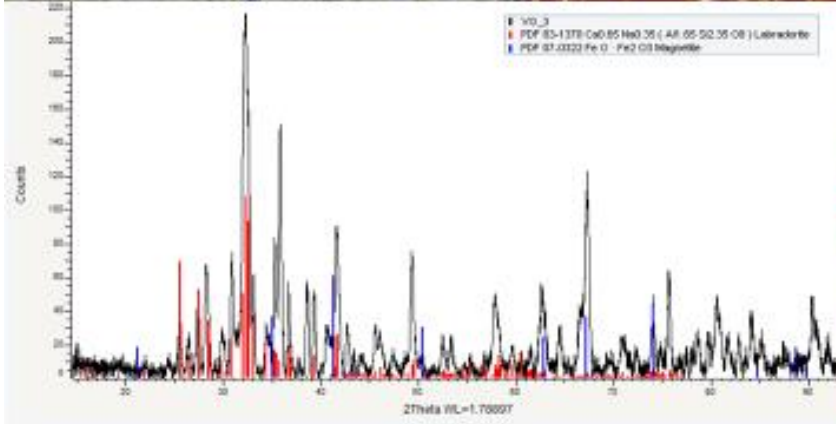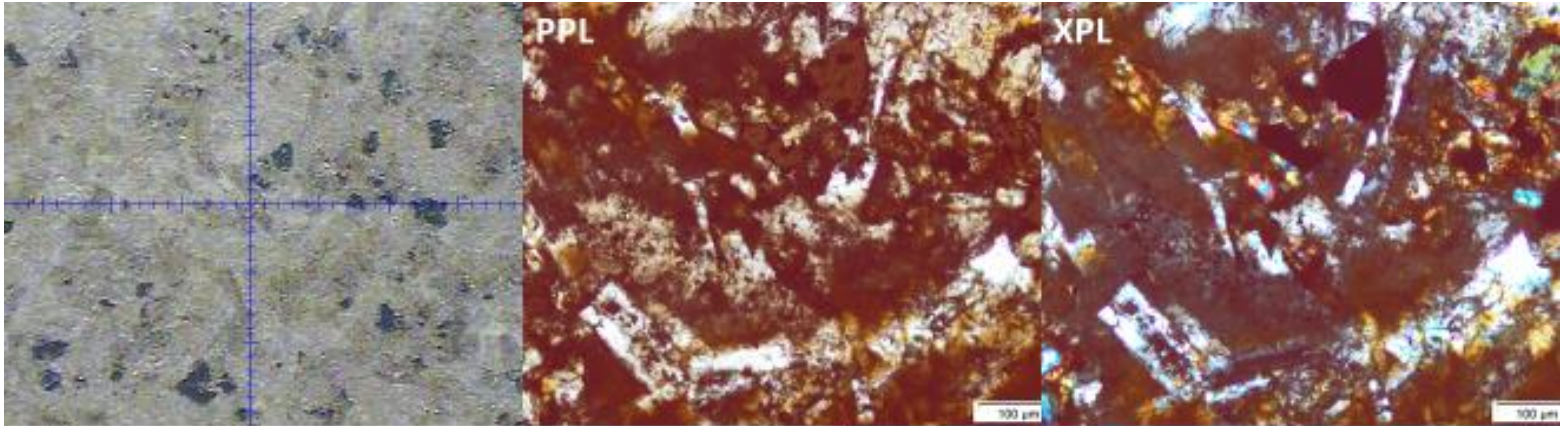
Optical petrography, µXRD analysis, and FWHMχ measurements of plagioclase feldspar grain (spot 2 in Fig. B-10) in a breccia clast of sample VG3.

Red: Labradorite Ca0.65 Na0.35 (Al1.65 Si2.35 O8) (PDF 83-1370)

Blue: Magnetite (Fe2 O3) (PDF 07-0322)
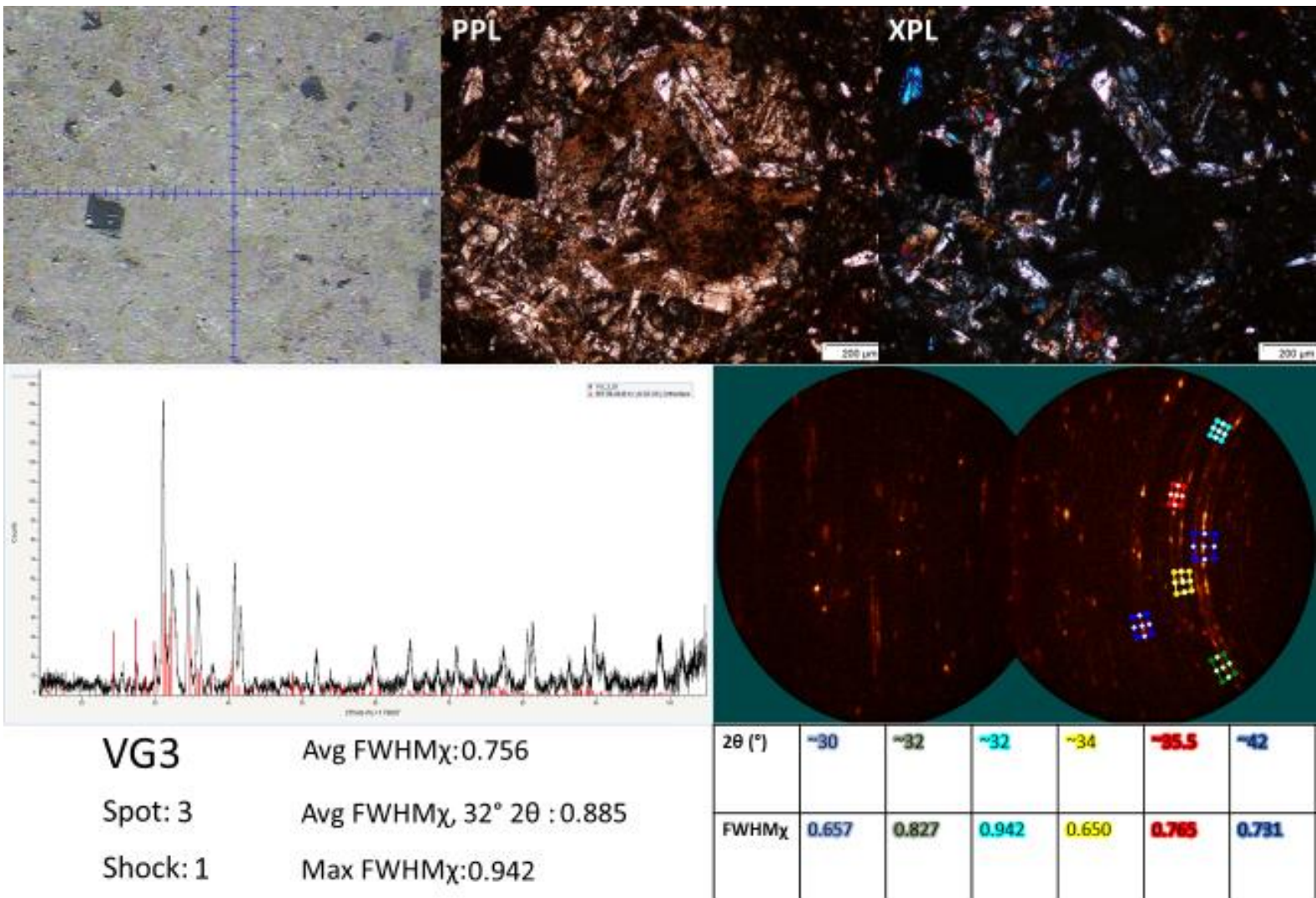
Optical petrography, µXRD analysis, and FWHMχ measurements of plagioclase feldspar grain (spot 3 in Fig. B-10) in a breccia clast of sample VG3.

Red: Orthoclase K(Al Si3 O6) (PDF 86-0438)
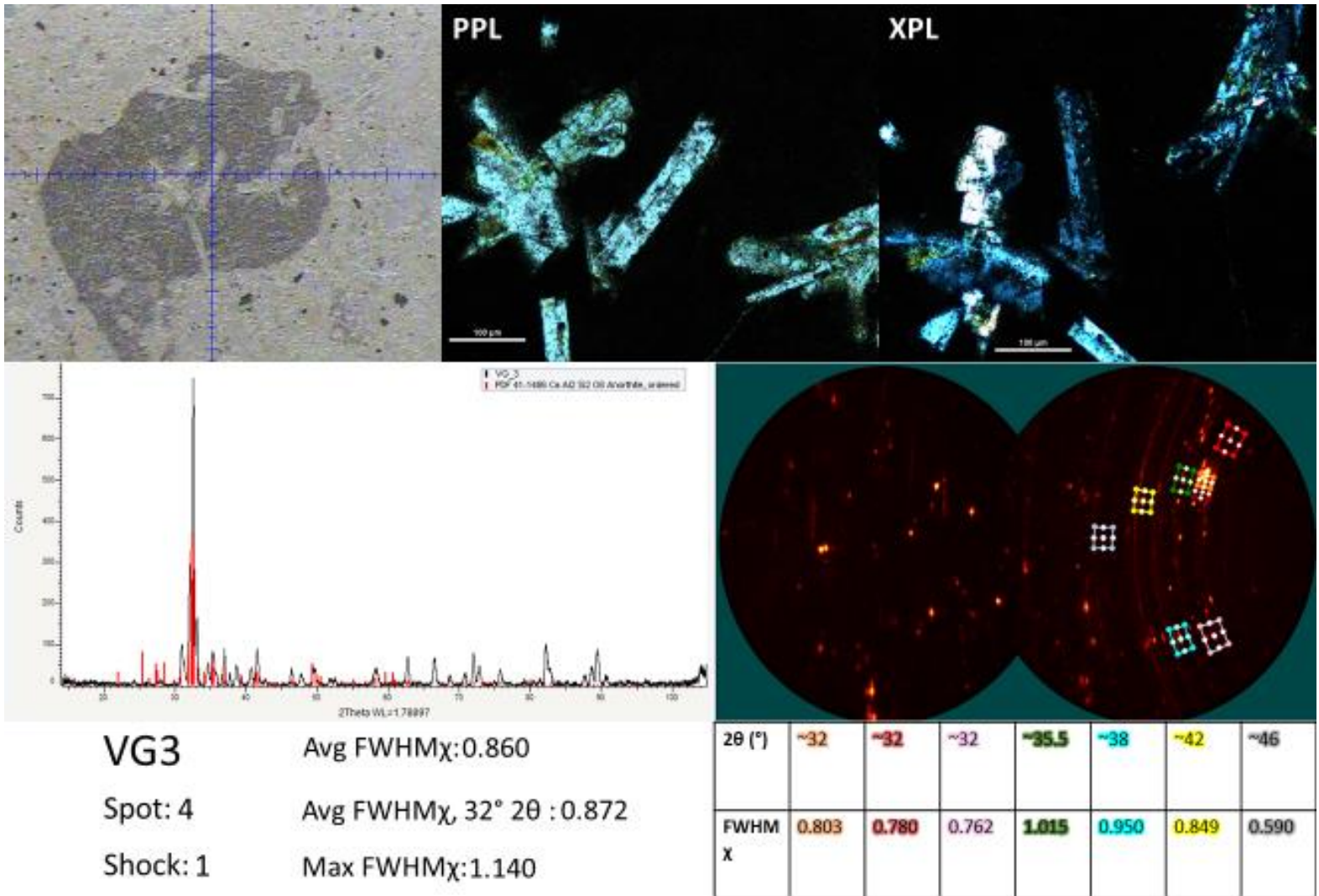
Optical petrography, µXRD analysis, and FWHMχ measurements of plagioclase feldspar grain (spot 4 in Fig. B-10) in a melt clast in sample VG3.

Red: Anorthite (Ca Al2 Si2 O8) (PDF 41-1486)

Optical petrography, μXRD analysis, and FWHMχ measurements of plagioclase feldspar grain (spot 5 in Fig. B-10) in sample VG3.
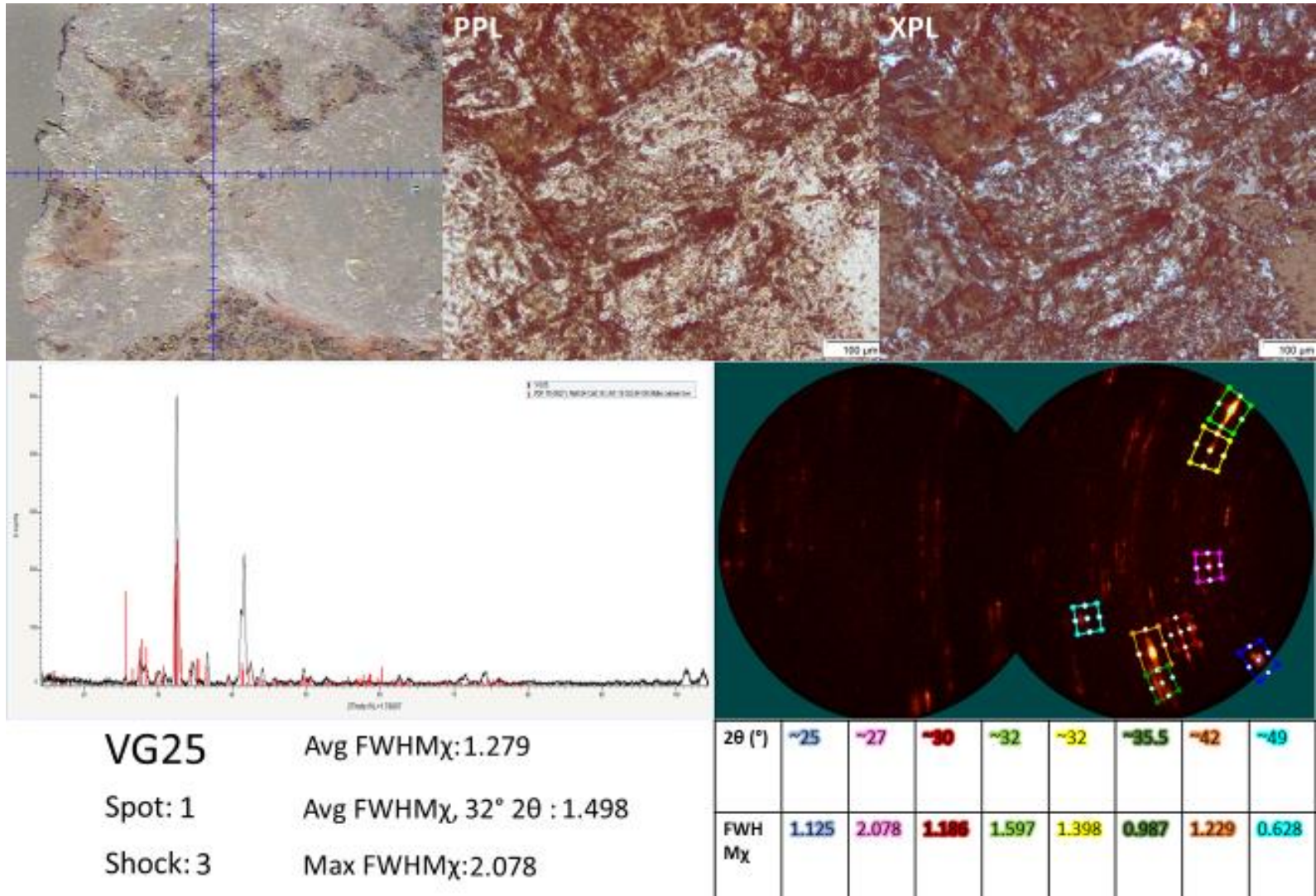
Red: Anorthite (Ca Al2 Si2 O8) (PDF 41-1486)

VG5


Figure B-11. VG-2017-5 thin section showing spots analyzed
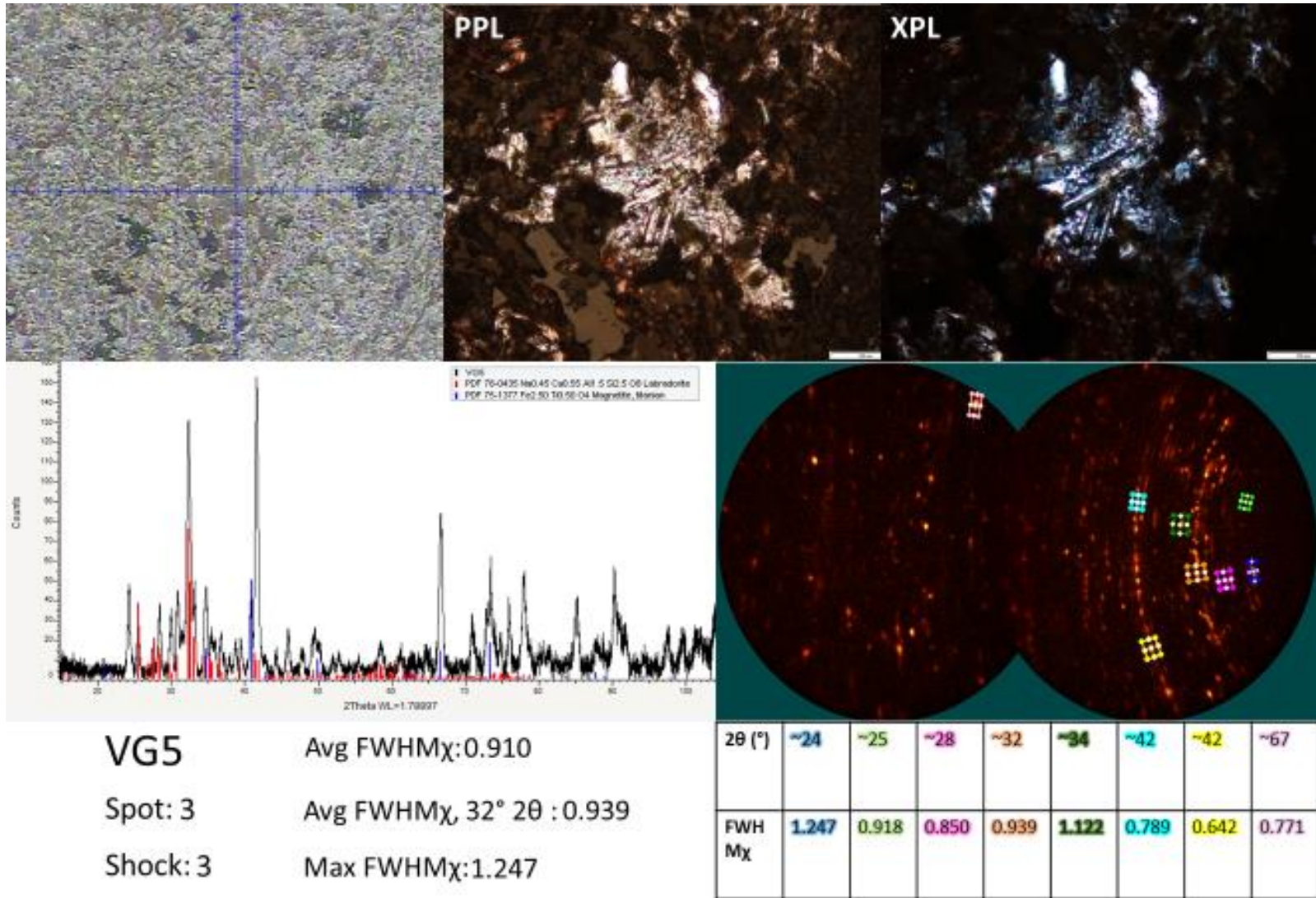
Optical petrography, µXRD analysis, and FWHMχ measurements of plagioclase feldspar grain (spot 3 in Fig. B-11) in sample VG5.

Red: Labradorite (Na0.45 Ca0.55 Al1.5 Si2.5 O8) (PDF 78-0435)

Blue: Magnetite, Titanian (Fe2.50 Ti0.50 O4) (PDF 75-1377)
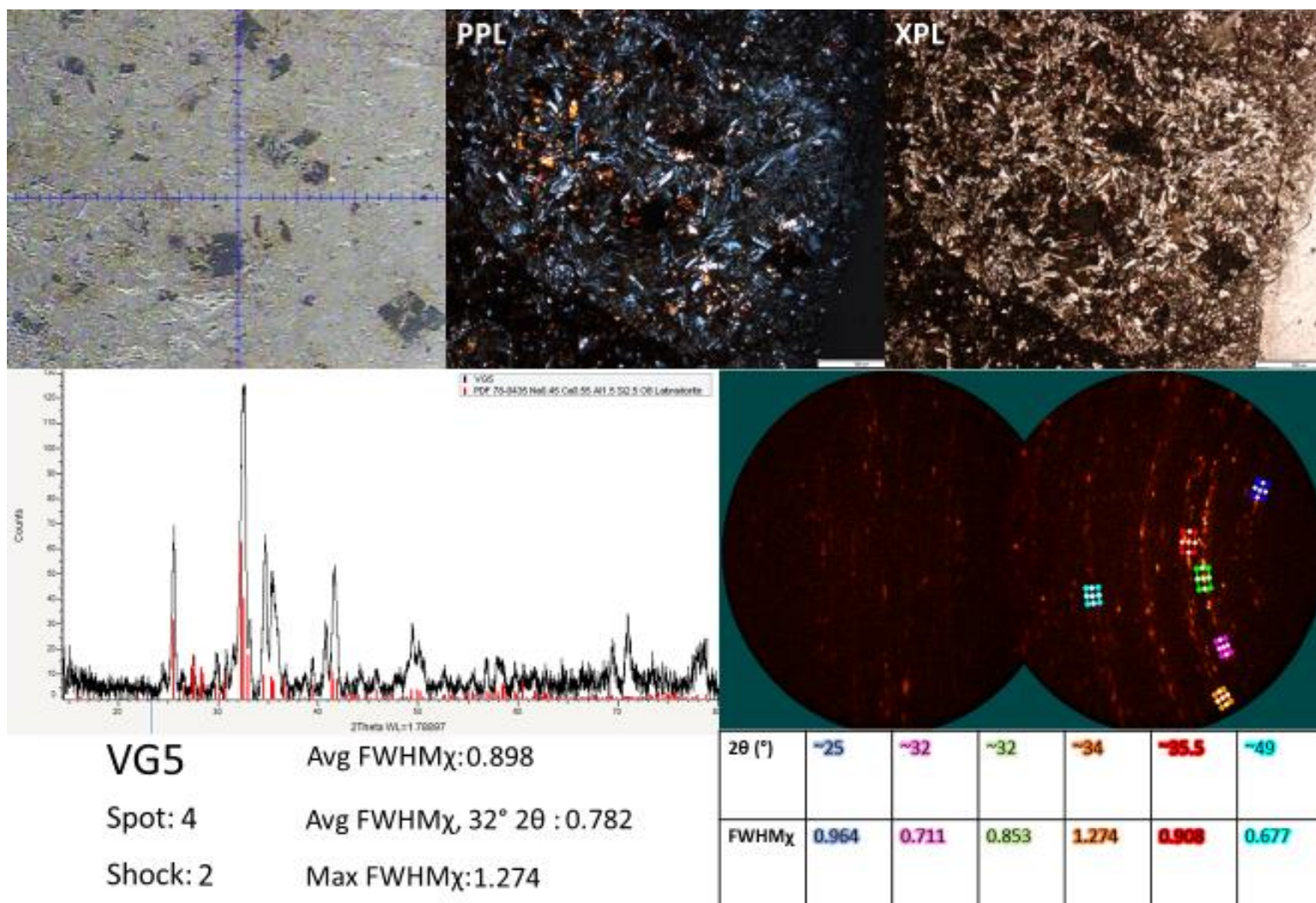
Optical petrography, μXRD analysis, and FWHMχ measurements of plagioclase feldspar grain (spot 4 in Fig. B-11) in a breccias clast of sample VG5.
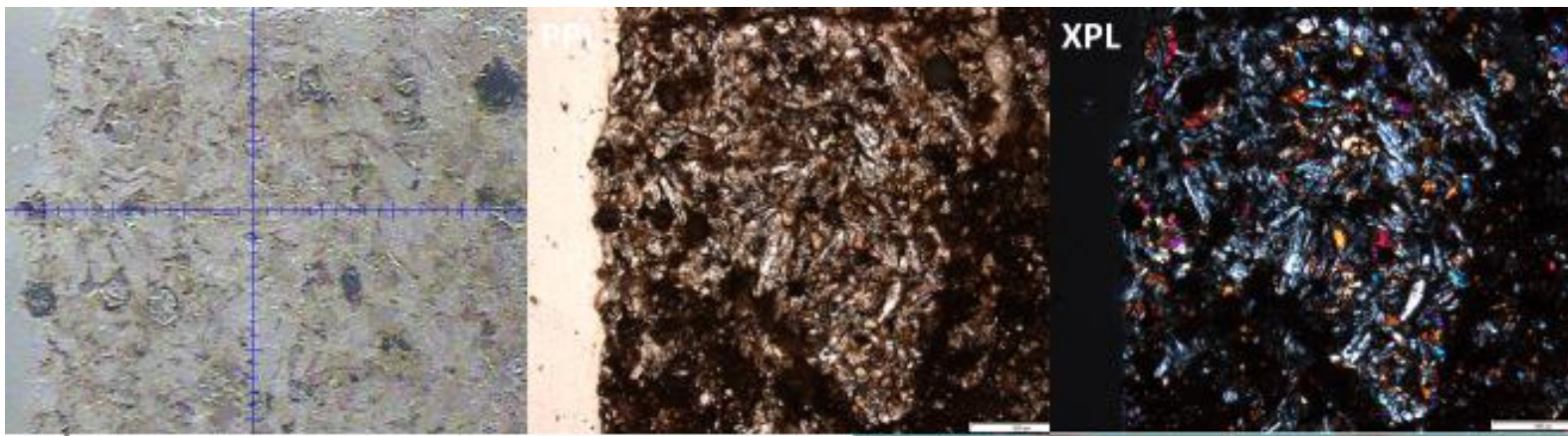
Red: Labradorite (Na0.45 Ca0.55 Al1.5 Si2.5 O8) (PDF 78-0435)

Optical petrography, µXRD analysis, and FWHMχ measurements of plagioclase feldspar grain (spot 1 in Fig. B-11) in sample VG5.

Blue: Labradorite (Na0.45 Ca0.55 Al1.5 Si2.5 O8) (PDF 78-0435)

Optical petrography, μXRD analysis, and FWHMχ measurements of plagioclase feldspar grain (spot 2 in Fig. B-11) in sample VG5.

Red: Albite (Na0.84 Ca0.16) Al1.16 Si2.84 O8 (PDF 76-0927)

VG8

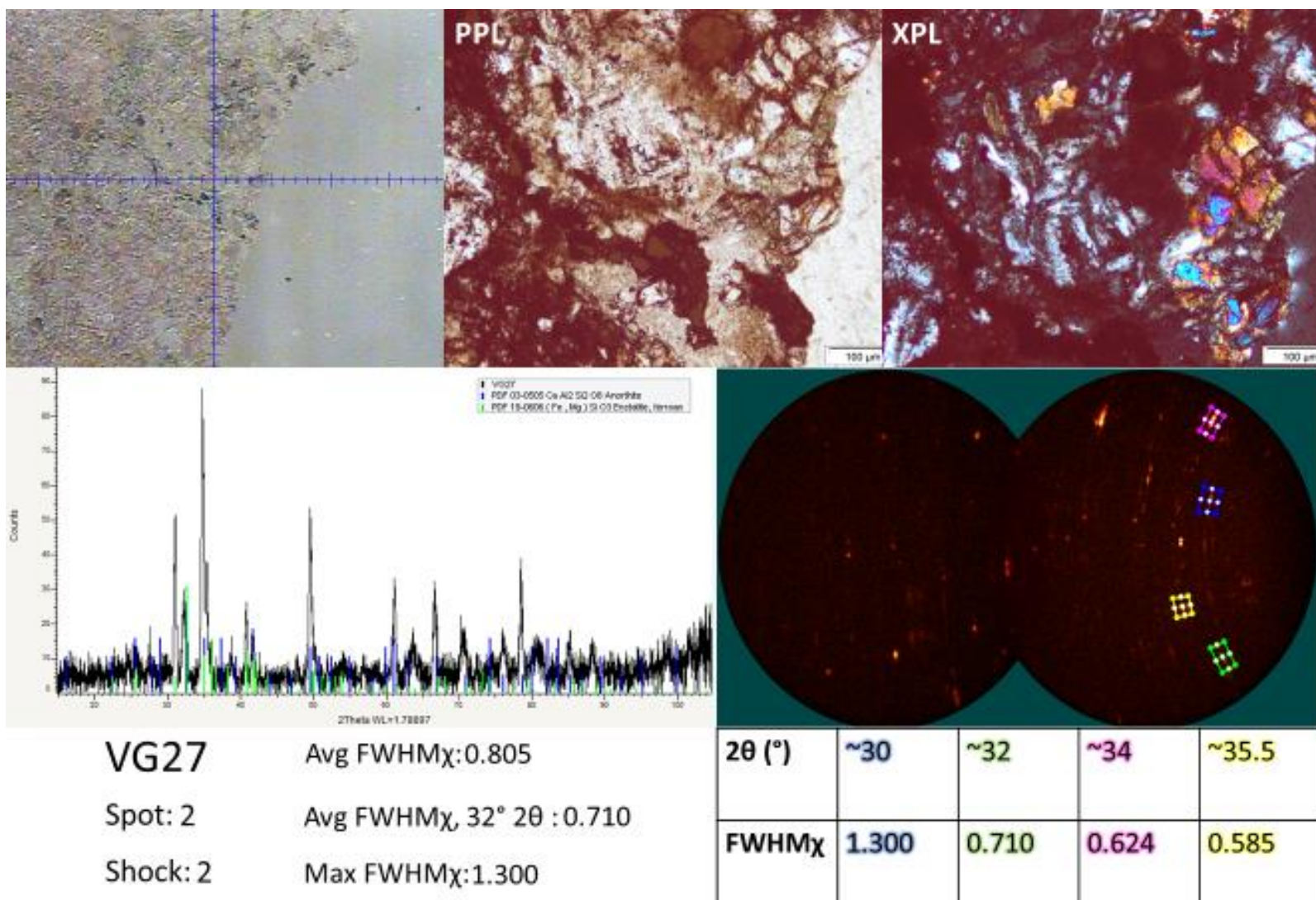**Figure B-12. VG-2017-8 thin section showing spots analyzed**

Optical petrography, μXRD analysis, and FWHMχ measurements of plagioclase feldspar grain (spot 1 in Fig. B-12) in sample VG8.
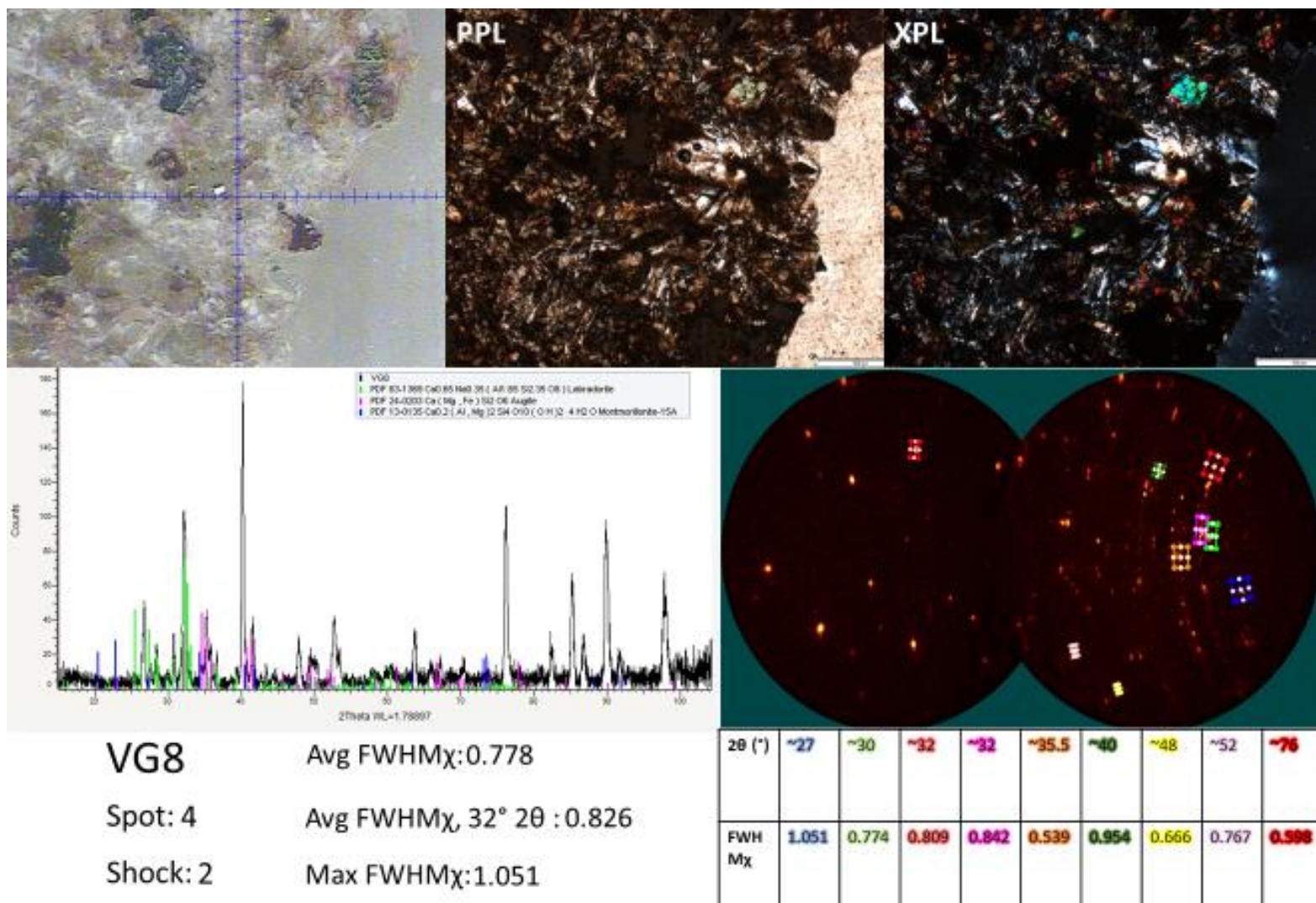
Red: Andesine (Na0.685 Ca0.347 Al1.46 Si2.54 O8) (PDF 83-1939)

Optical petrography, µXRD analysis, and FWHMχ measurements of plagioclase feldspar grain (spot 4 in Fig. B-12) in sample VG8.

Green: Labradorite Ca0.65 Na0.35 (Al1.65 Si2.35 O8) (PDF 83-1369)

Pink: Augite Ca (Mg, Fe) Si2 O6 (PDF 24-0203)

Blue: Montmorillonite Ca0.2 (Al, Mg)2 Si4 O10 (OH)2 · 4 H2O (PDF 13-0135)

Optical petrography, μXRD analysis, and FWHMχ measurements of plagioclase feldspar grain (spot 5 in Fig. B-12) in sample VG8.

Red: Andesine (Na0.685 Ca0.347 Al1.46 Si2.54 O8) (PDF 83-1939)

Green: Saponite (Mg O · 0.67 Al2 O3 · 7 Si O2 · 2 H2O) (PDF 10-0426)

VG9

Figure B-13. VG-2017-9 thin section showing spots analyzed
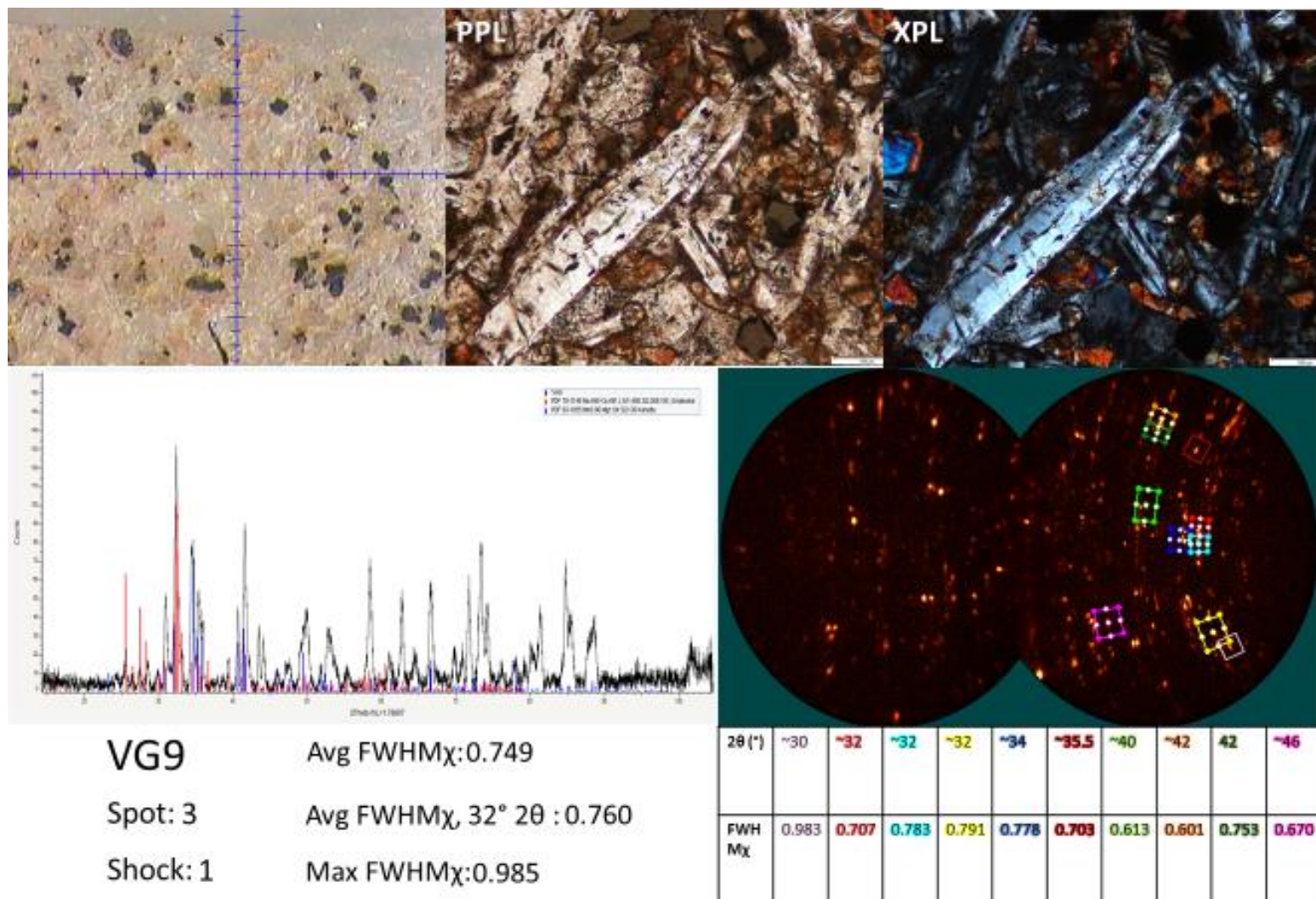
Optical petrography, µXRD analysis, and FWHMχ measurements of plagioclase feldspar grain (spot 3 in Fig. B-13) in sample VG9.

Red: Andesine Na0.499 Ca0.491 (Al1.488 Si2.506 O8) (PDF 79-1148)

Blue: Kanoite (Mn0.96 Mg1.04 Si2 O6) (PDF 83-1835)
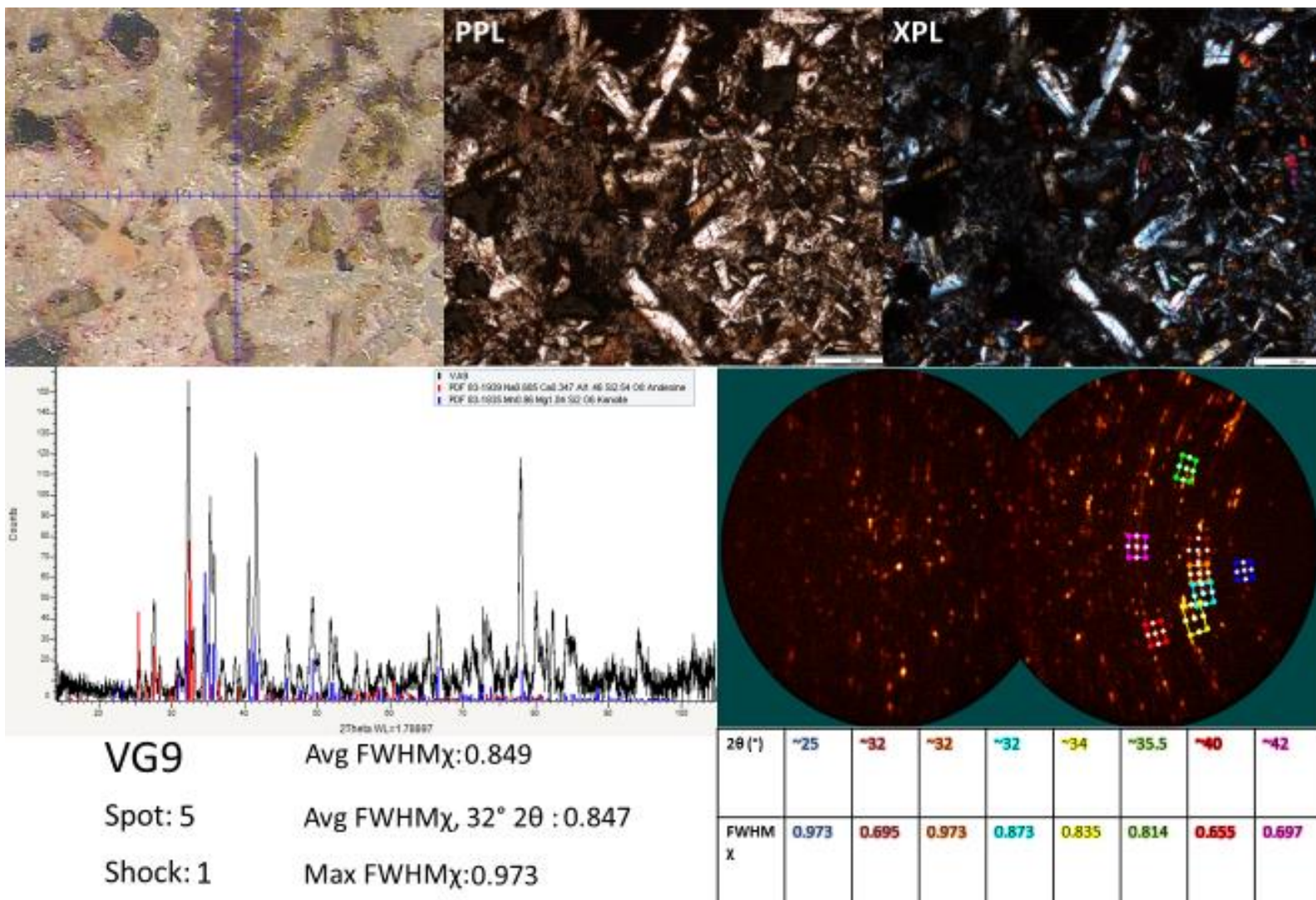
Optical petrography, μXRD analysis, and FWHMχ measurements of plagioclase feldspar grain (spot 5 in Fig. B-13) in sample VG9.

Red: Andesine (Na0.685 Ca0.347 Al1.46 Si2.54 O8) (PDF 83-1939)

Blue: Kanoite (Mn0.96 Mg1.04 Si2 O6) (PDF 83-1835)

Figure B-14. VG-2017-10 thin section showing spots analyzed
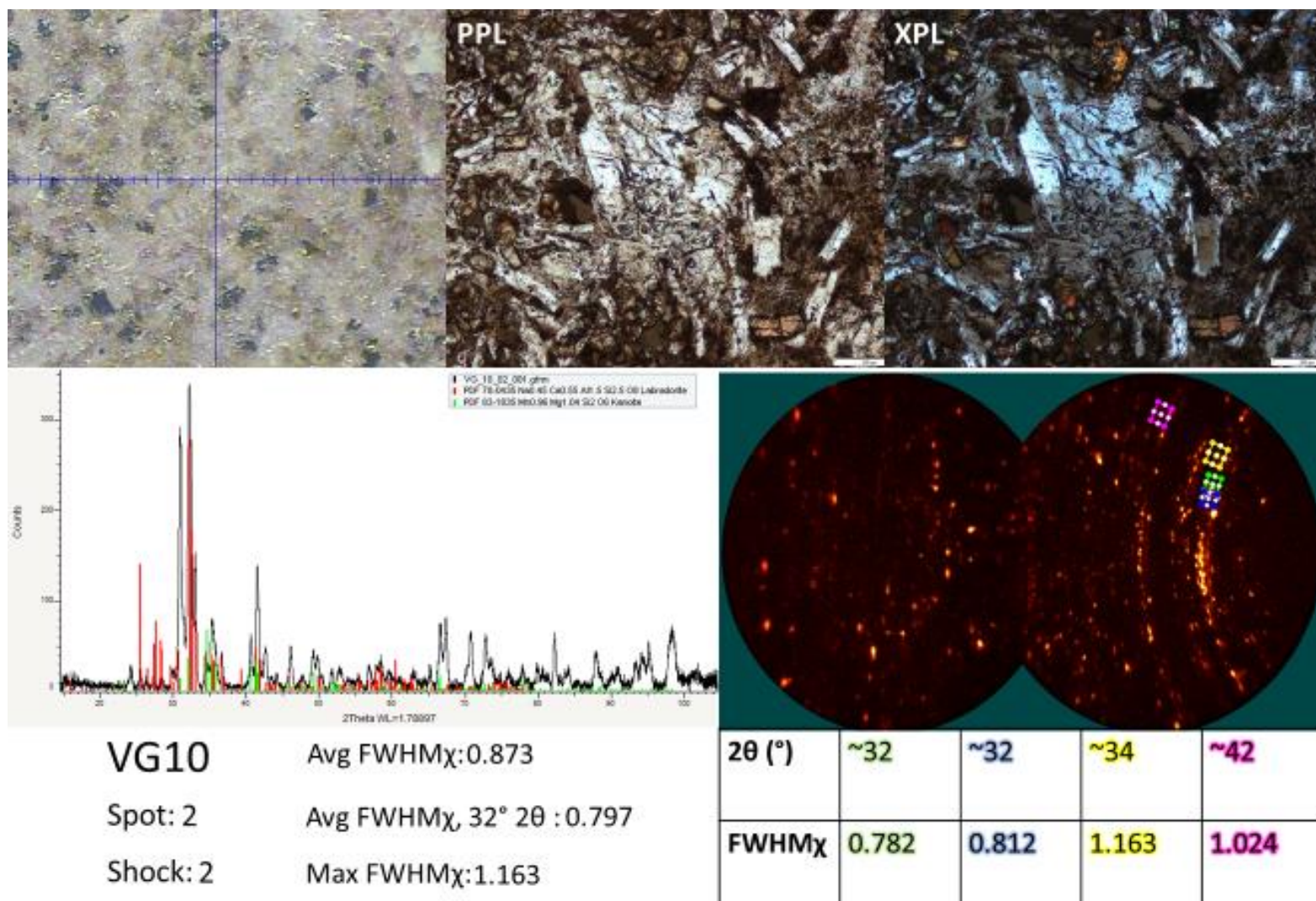
Optical petrography, µXRD analysis, and FWHMχ measurements of plagioclase feldspar grain (spot 2 in Fig. B-14) in sample VG10.

Red: Labradorite (Na0.45 Ca0.55 Al1.5 Si2.5 O8) (PDF 78-0435)

Green: Kanoite (Mn0.96 Mg1.04 Si2 O6) (PDF 83-1835)

VG12

Figure B-15. VG-2017-12 thin section showing spots analyzed

Optical petrography, μXRD analysis, and FWHMχ measurements of plagioclase feldspar grain (spot 1 in Fig. B-15) in sample VG12.

Red: Albite (Na, Ca) Al (Si, Al)3 O8 (PDF 41-1480)

VG13b

Figure B-16. VG-2017-13B thin section showing spots analyzed
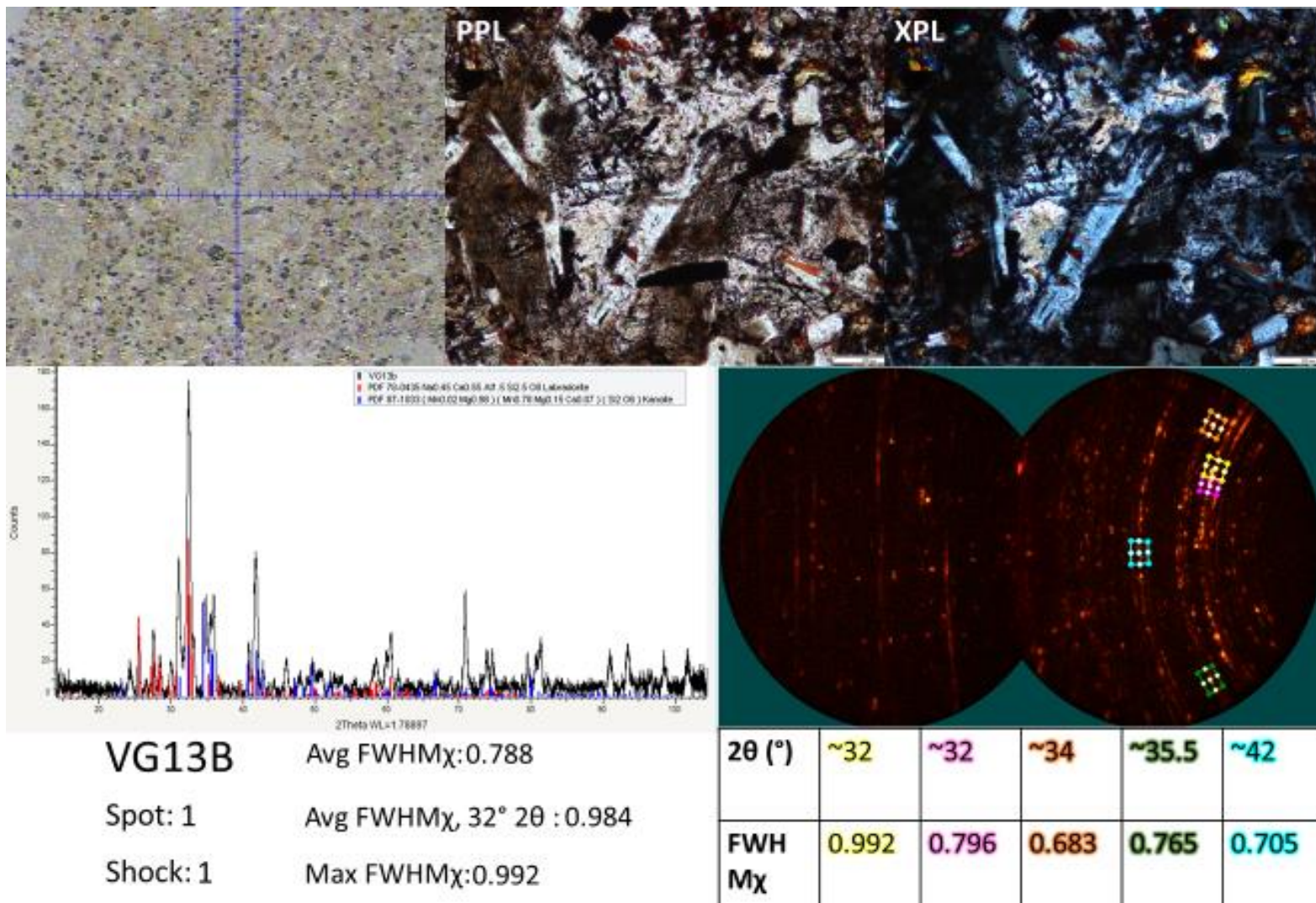
Optical petrography, μXRD analysis, and FWHMχ measurements of plagioclase feldspar grain (spot 1 in Fig. B-16) in sample VG13B.

Red: Labradorite (Na0.45 Ca0.55 Al1.5 Si2.5 O8) (PDF 78-0435)

Blue: Kanoite (Mn0.02 Mg0.98) (Mn0.78 Mg0.15 Ca0.07) (Si2 O6) (PDF 87-1033)

VG14

Figure B-17. VG-2017-14 thin section showing spots analyzed

Optical petrography, µXRD analysis, and FWHMχ measurements of plagioclase feldspar grain (spot 1.1 in Fig. B-17) in sample VG14. XPL and PPL photographs were not obtained for this spot.

Red: Labradorite (Na0.45 Ca0.55 Al1.5 Si2.5 O8) (PDF 78-0435)

Blue: Kanoite (Mn0.02 Mg0.98) (Mn0.78 Mg0.15 Ca0.07) (Si2 O6) (PDF 87-1033)

VG16

Figure B-18. VG-2017-16 thin section showing spots analyzed
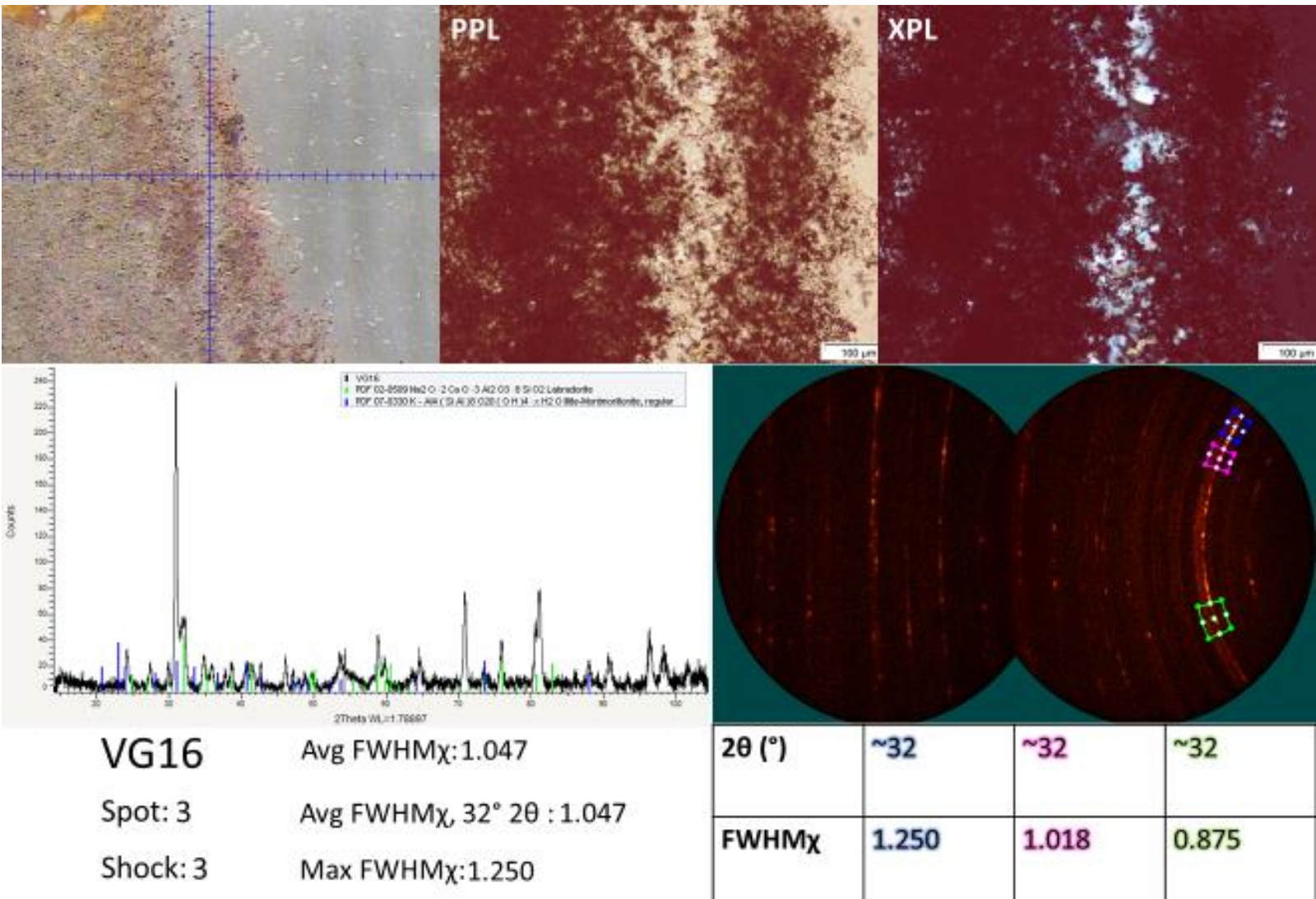
Optical petrography, µXRD analysis, and FWHMχ measurements of plagioclase feldspar grain (spot 3 in Fig. B-18) in sample VG16.

Green: Labradorite (Na2 O · 2 Ca O · 3 Al2 O3 ·8 Si O2) (PDF 02-0509)

Blue: Illite-Montmorillonite Al4 (Si Al)8 O20 (OH)4 · H2O (PDF 07-0330)

VG22

Figure B-19. VG-2017-22 thin section showing spots analyzed

Optical petrography, µXRD analysis, and FWHMχ measurements of plagioclase feldspar grain (spot 3 in Fig. B-19) in sample VG22.

Red: Labradorite (Na0.45 Ca0.55 Al1.55 Si2.45 O8) (PDF 78-0434)

Green: Kanoite (Mn0.96 Mg1.04 Si2 O6) (PDF 83-1835)

Optical petrography, μXRD analysis, and FWHMχ measurements of plagioclase feldspar grain (spot 2 in Fig. B-19) in sample VG22.

Red: Labradorite (Na0.45 Ca0.55 Al1.55 Si2.45 O8) (PDF 78-0434)

Blue: Olivine Ni2 (Si O4) (PDF 80-0940)

VG24
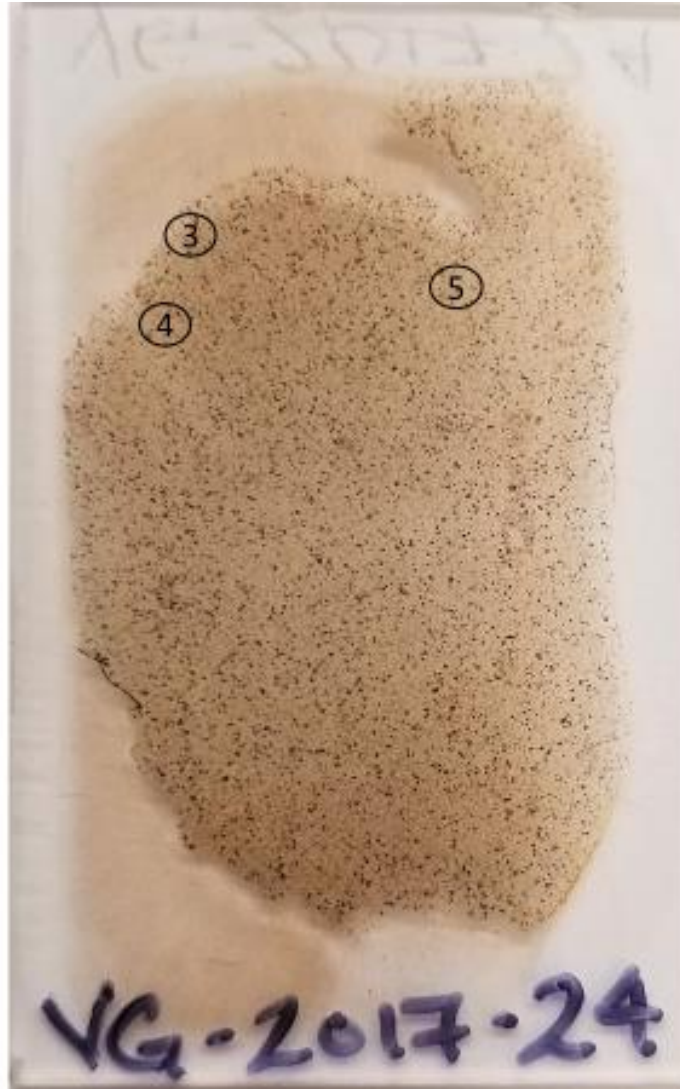
Figure B-20. VG-2017-24 thin section showing spots analyzed
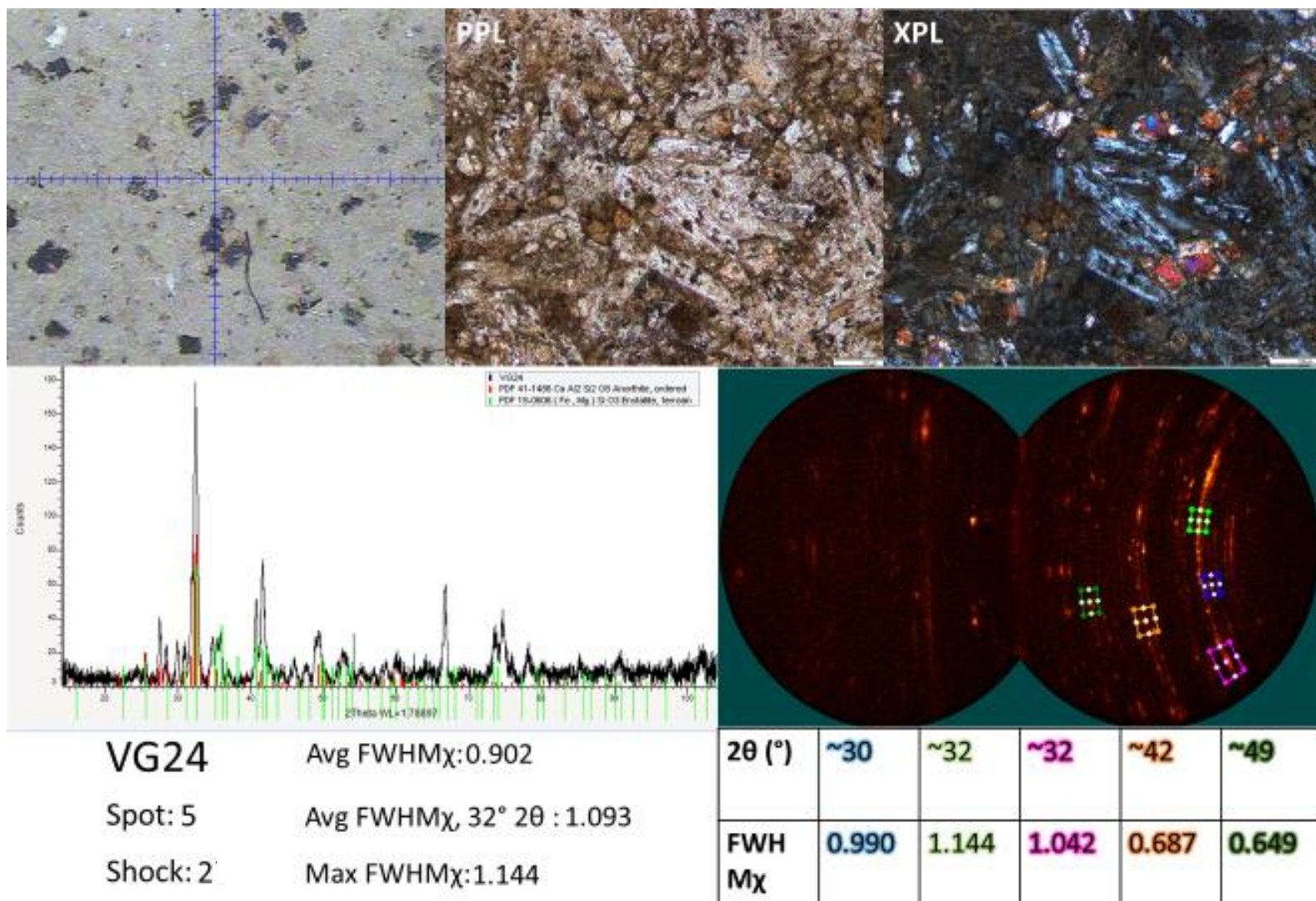
Optical petrography, µXRD analysis, and FWHMχ measurements of plagioclase feldspar grain (spot 5 in Fig. B-20) in sample VG24.

Red: Anorthite (Ca Al2 Si2 O8) (PDF 41-1486)

Green: Enstatite (Fe, Mg) Si O3 (PDF 19-0606)
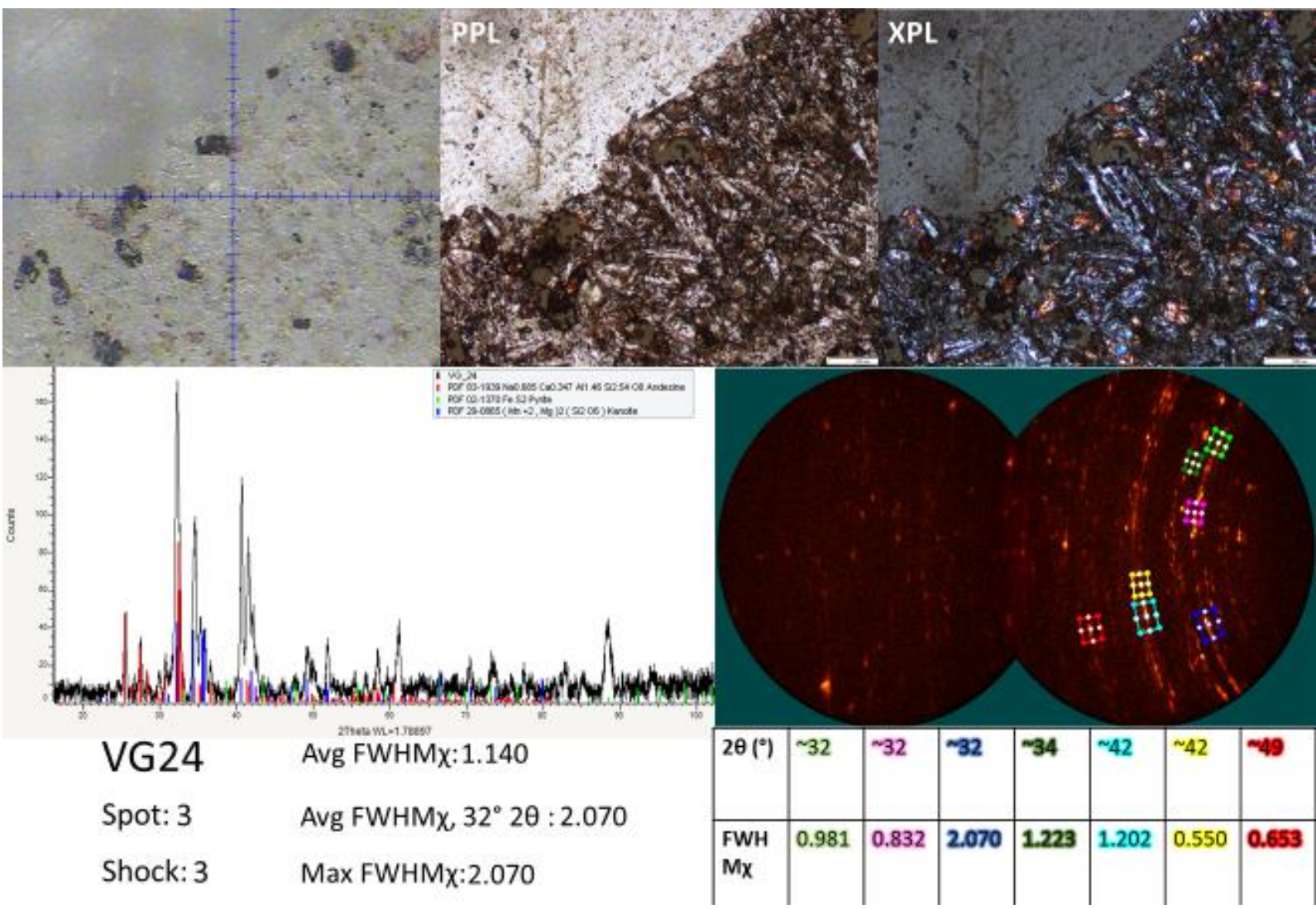
Optical petrography, μXRD analysis, and FWHMχ measurements of plagioclase feldspar grain (spot 3 in Fig. B-20) in sample VG24.

Red: Andesine (Na0.685 Ca0.347 Al1.46 Si2.54 O8) (PDF 83-1939)

Green: Pyrite (Fe S2) (PDF 02-1370)

Blue: Kanoite (Mn +2, Mg)2 (Si2 O6) (PDF 29-0865)

F Optical petrography, µXRD analysis, and FWHMχ measurements of plagioclase feldspar grain (spot 4 in Fig. B-20) in sample VG24.

Red: Labradorite (Na0.45 Ca0.55 Al1.5 Si2.5 O8) (PDF 78-0435)

Green: Kanoite (Mn0.96 Mg1.4 Si2 O6) (PDF 83-1835)

VG25

Figure B-21. VG-2017-25 thin section showing spots analyzed

Optical petrography, µXRD analysis, and FWHMχ measurements of plagioclase feldspar grain (spot 1 in Fig. B-21) in sample VG25.

Red: Albite calcian low (Na0.84 Ca0.16) Al1.16 Si2.84 O8) (PDF 76-0927)

VG27

Figure B-22. VG-2017-27 thin section showing spots analyzed
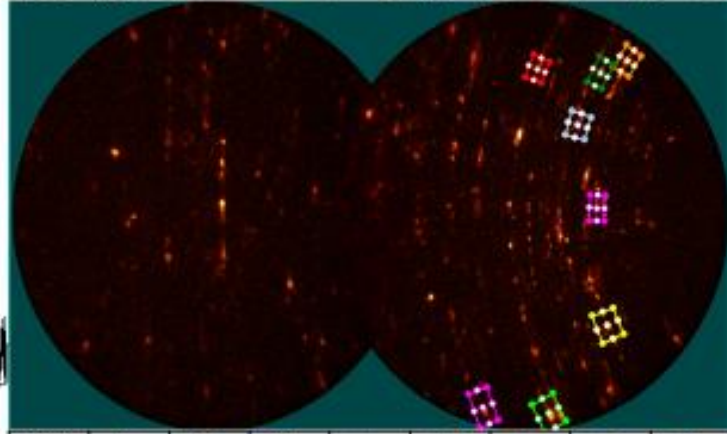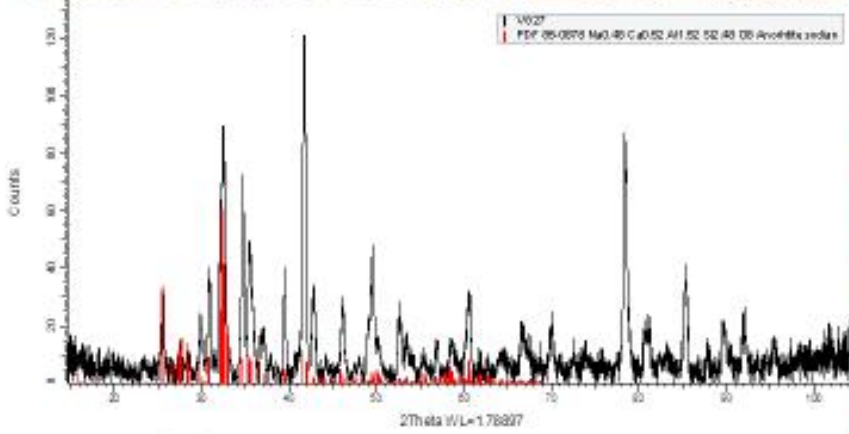
Optical petrography, µXRD analysis, and FWHMχ measurements of plagioclase feldspar grain (spot 1 in Fig. B-22) in breccia from sample VG27.

Red: Anorthite sodian Na0.48 Ca0.52 Al1.52 Si2.48 O8 (PDF 85-0878)

Optical petrography, µXRD analysis, and FWHMχ measurements of plagioclase feldspar grain (spot 2 in Fig. B-22) in breccia clast from sample VG27.

Blue: Anorthite (Ca Al2 Si2 O8) (PDF 03-0505)

Green: Enstatite, ferroan (Fe, Mg) Si O3 (PDF 19-0606)

Appendix C: Clay and Zeolite µXRD data
Supplementary Material

Figure C-1. VA-2017-1E4 thin section showing spots analyzed
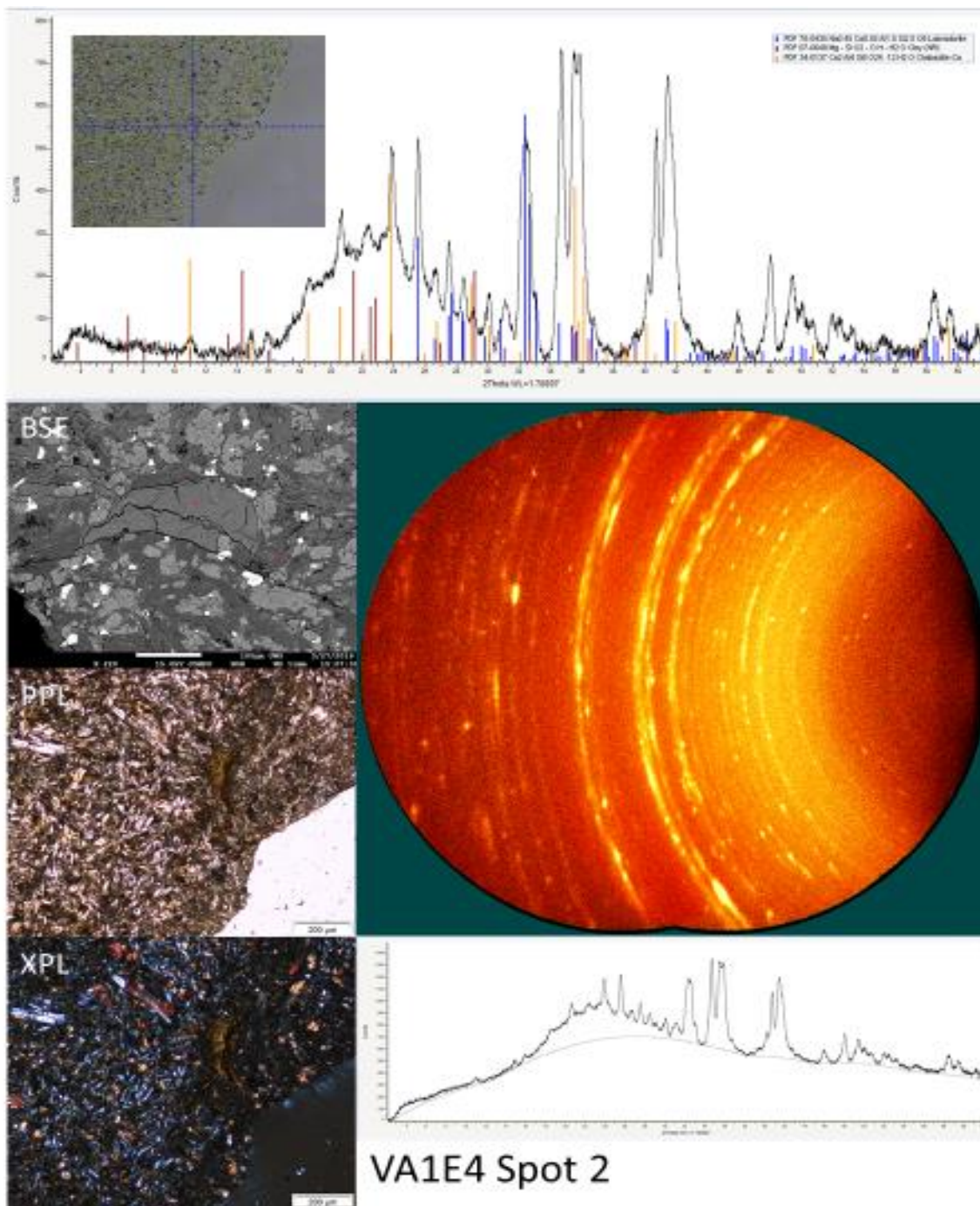
Optical petrography and µXRD analysis using the newly developed method of clays and zeolites (spot 2 in Fig. C-1) in sample VA1E4.

Blue: Labradorite (Na0.45 Ca0.55 Al1.5 Si2.5 O8) (PDF 78-0435)

Maroon: Clay (Mg- Si O2- OH- H2O) (PDF 07-0048)

Orange: Chabazite-Ca (Ca2 Al4 Si8 O24 · 12 H2O) (PDF 34-0137)
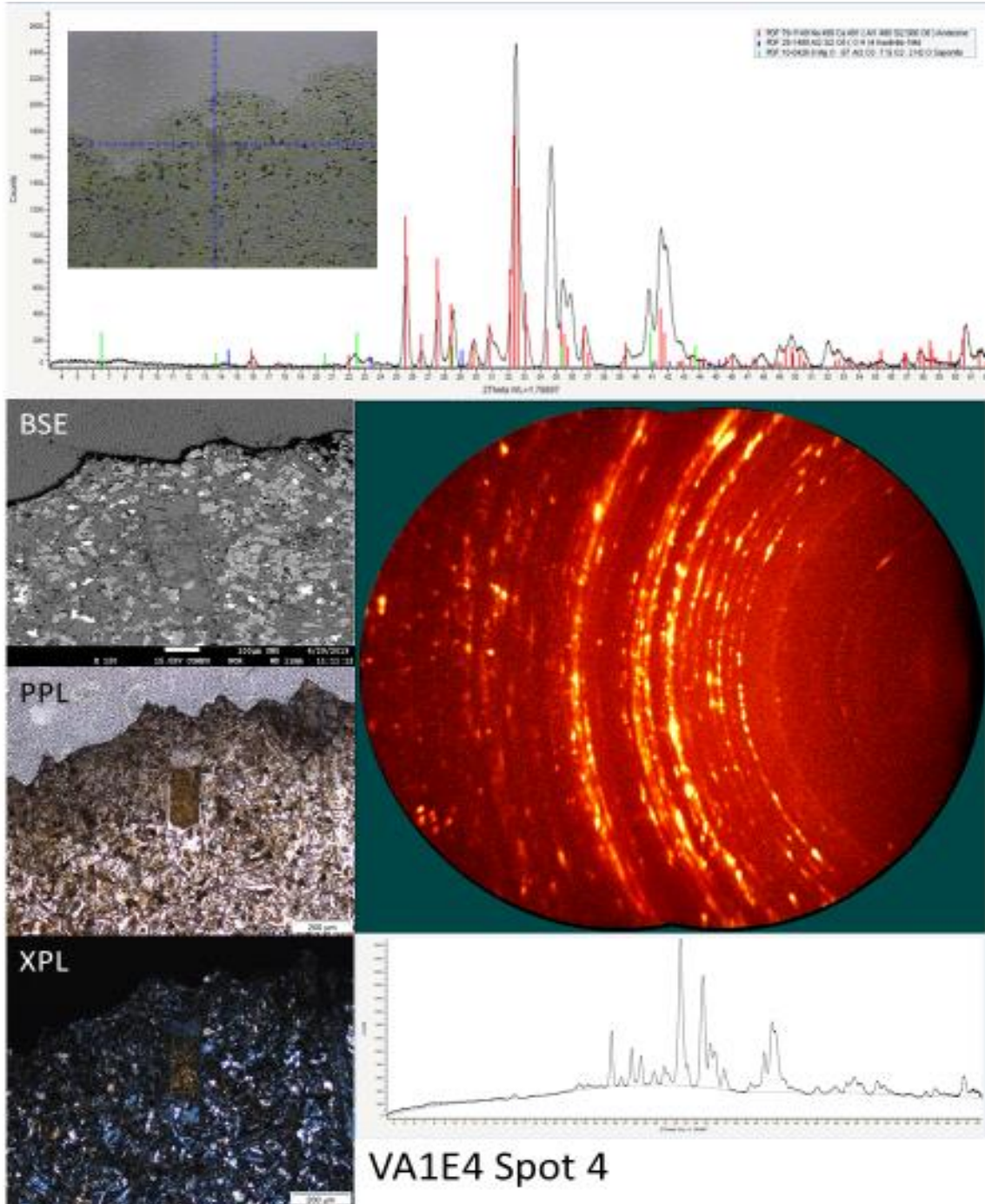
Optical petrography and µXRD analysis using the newly developed method of clays and zeolites (spot 4 in Fig. C-1) in sample VA1E4.

Red: Andesine Na0.499 Ca0.491 (Al1.408 Si2.505 O8) (PDF 79-1149)

Blue: Kaolinite Al2 Si2 O5 (OH)4 (PDF 29-1188)

Green: Saponite (6 Mg O · 0.67 Al2 O3 · 7 Si O2 · 2 H2O) (PDF 10-0426)

Figure C-2. VA-2017-1B thin section showing spots analyzed
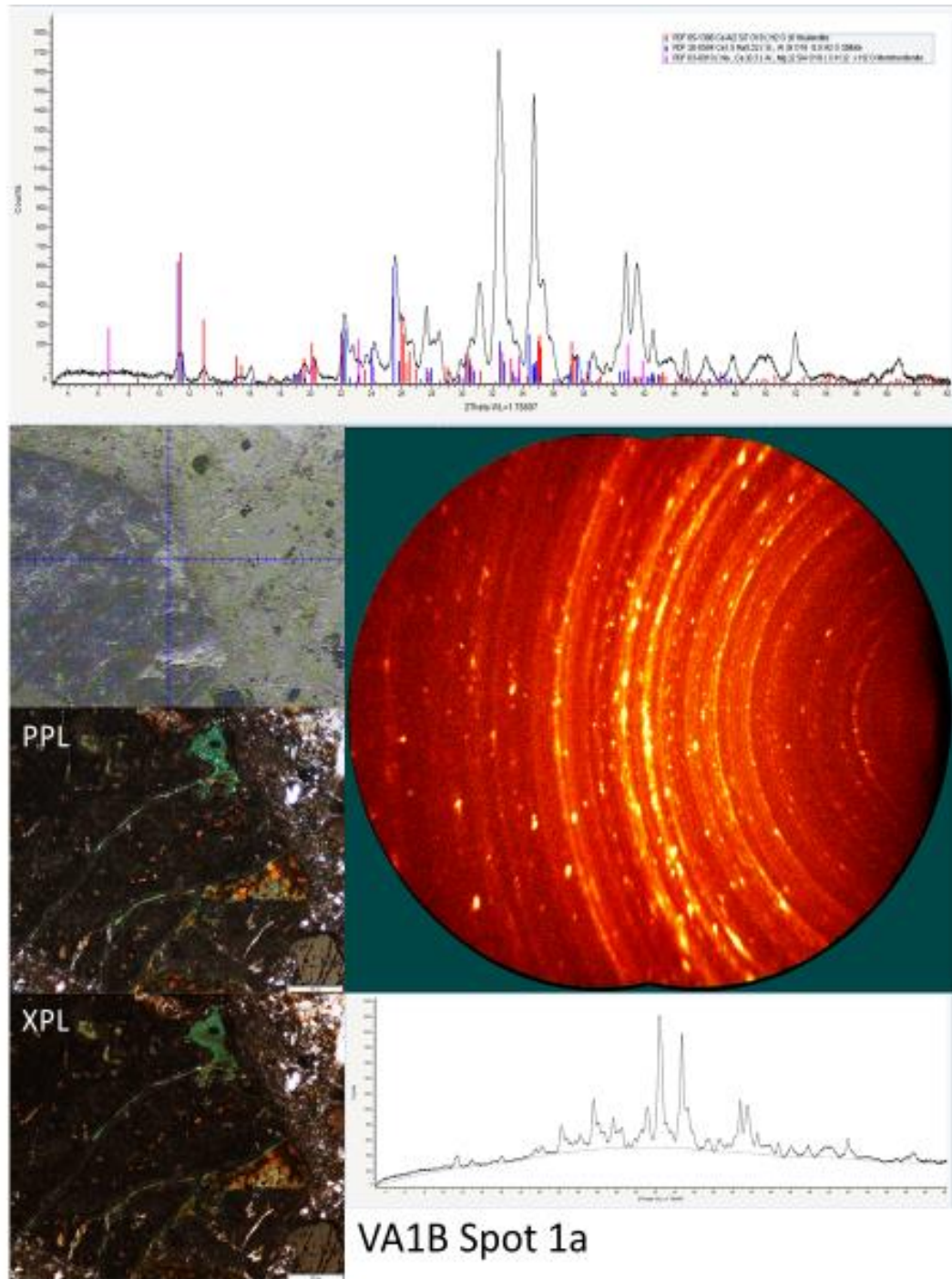
Optical petrography and µXRD analysis using the newly developed method of clays and zeolites (spot 1a in Fig. C-2) in sample VA1B.

Red: Heuladite Ca Al2 Si7 O18 (H2O)6 (PDF 85-1386)

Blue: Stilbite Ca1.5 Na0.32 (Si, Al)9 O18 · 8.5 H2O (PDF 26-0584)

Pink: Montmorillonite (Na, Ca)0.3 (Al, Mg)2 Si4 O10 (OH)2 · H2O (PDF 03-0010)
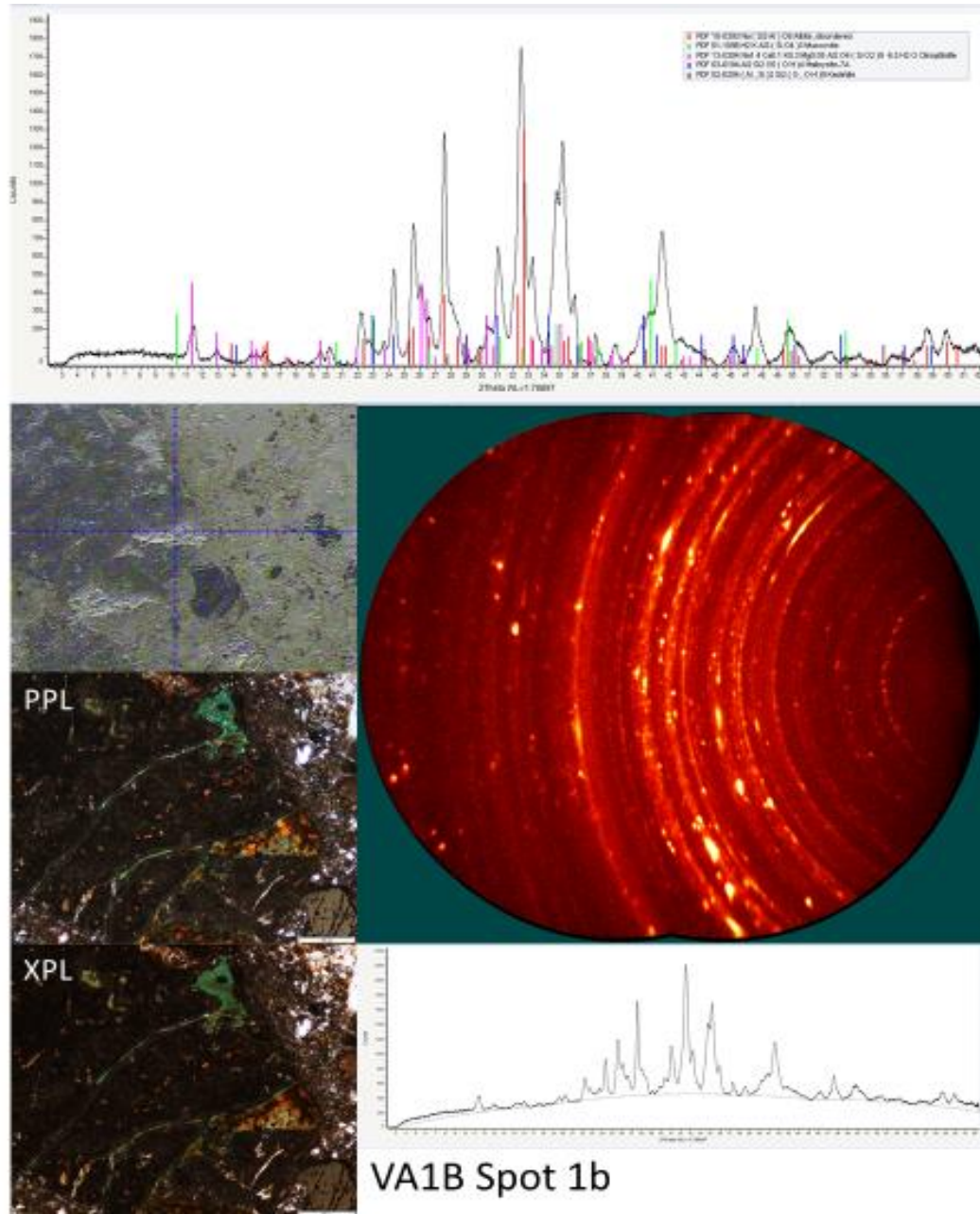
Optical petrography and μXRD analysis using the newly developed method of clays and zeolites (spot 1b in Fig. C-2) in sample VA1B.

Red: Albite Na(Si3 Al) O8 (PDF 10-0393)

Green: Muscovite H2 K Al3 (Si O4)3 (PDF 01-1098)

Pink: Clinoptilolite Na1.4 Ca0.1 K0.3 Mg0.05 Al2 O4 (Si O2)9 · 6.5 H2O (PDF 13-0304)

Blue: Halloysite Al2 Si2 O5 (OH)4 (PDF 03-0184)
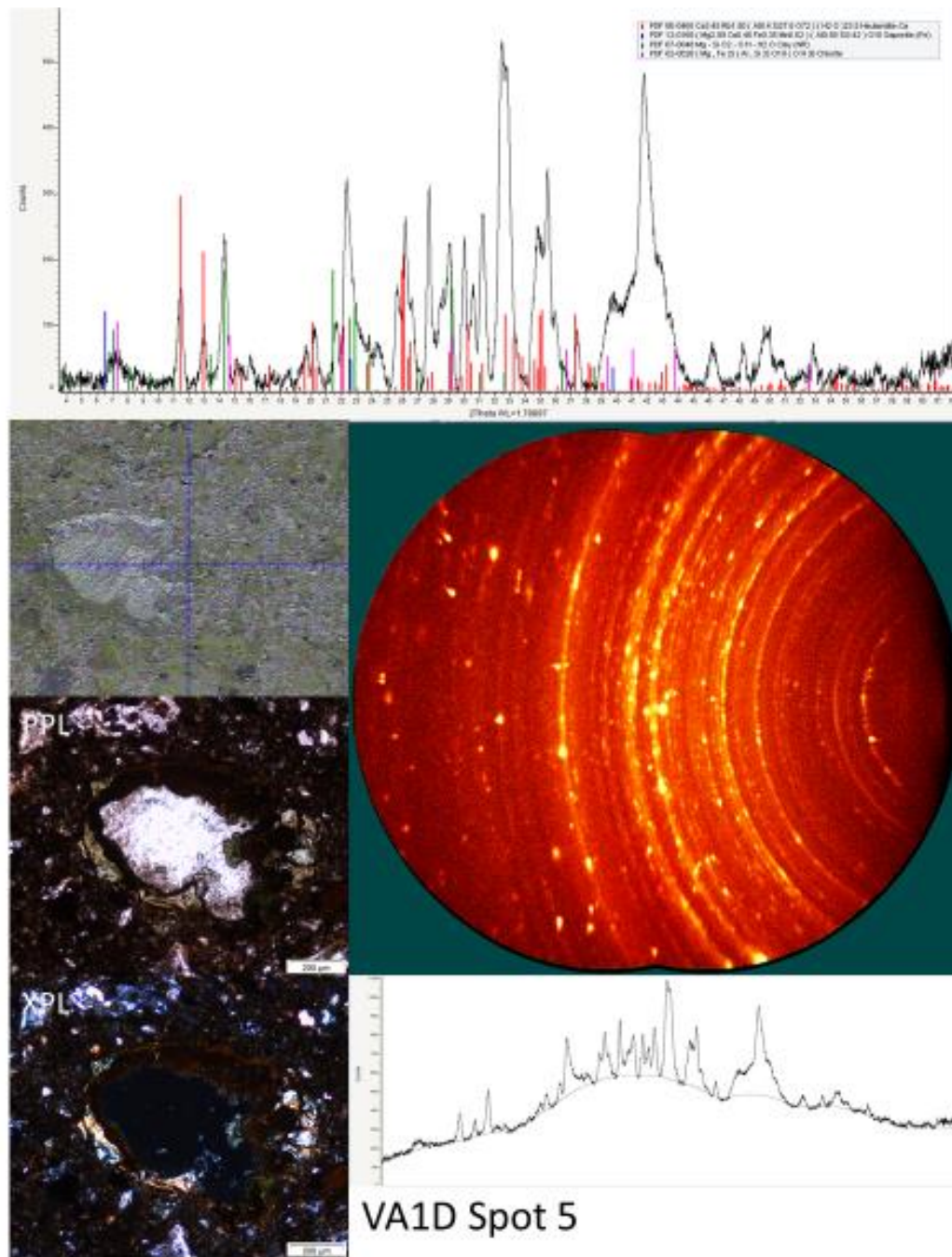
Brown: Kaolinite (Al, Si)2 Si2 (O, OH)9 (PDF 02-0204)
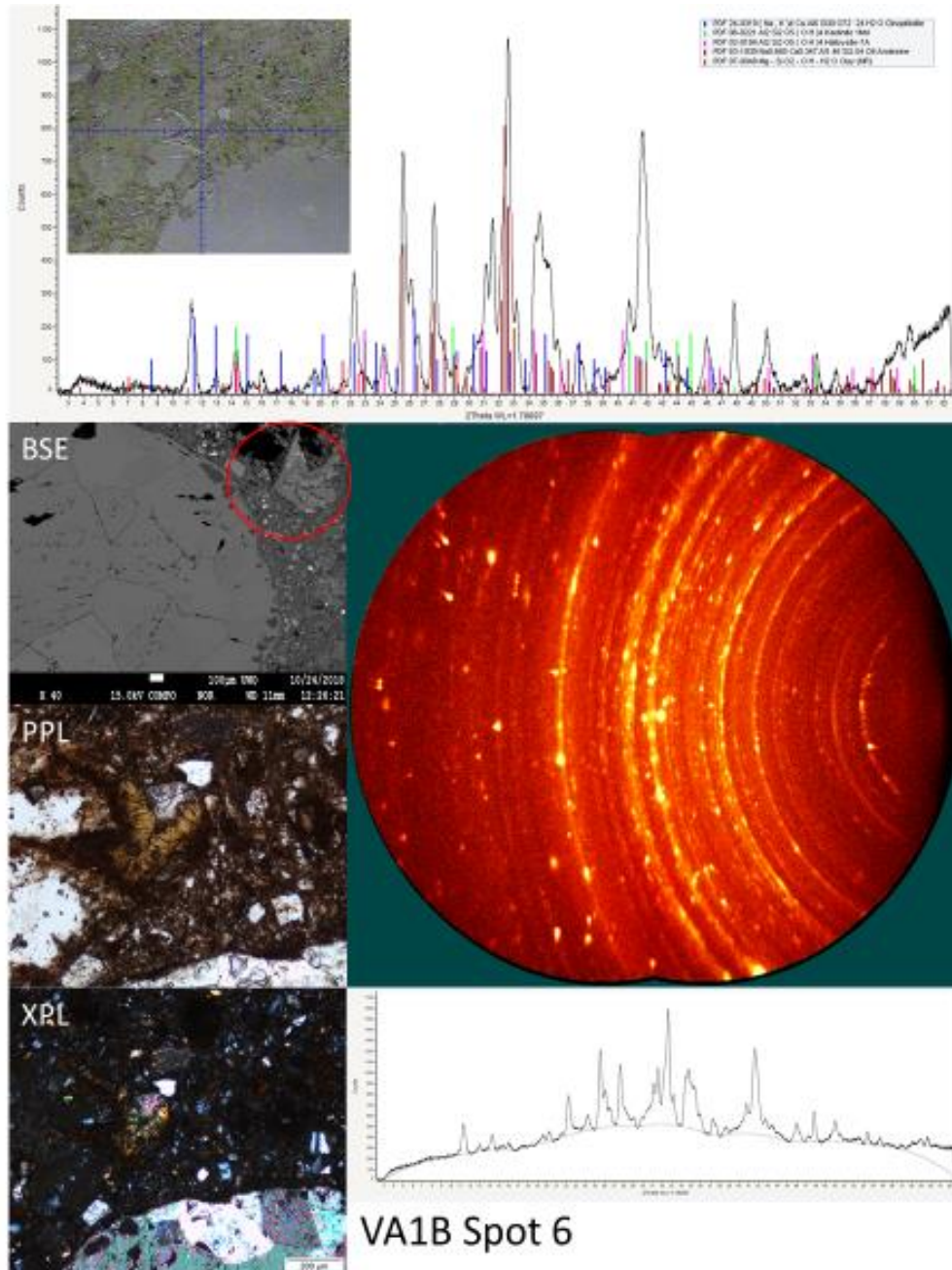
Optical petrography and µXRD analysis using the newly developed method of clays and zeolites (spot 6 in Fig. C-2) in sample VA1B.

Blue: Clinoptilolite (Na, K)4 Ca Al6 Si0 O72 · 24 H2O (PDF 24-0319)

Green: Kaolinite Al2 Si2 O5 (OH)4 (PDF 06-0221)

Pink: Halloysite Al2 Si2 O5 (OH)4 (PDF 03-0184)

Maroon: Andesine (Na0.685 Ca0.347 Al1.46 Si2.54 O8) (PDF 83-1939)

Red: Clay (Mg- Si O2- OH- H2O) (PDF 07-0048)
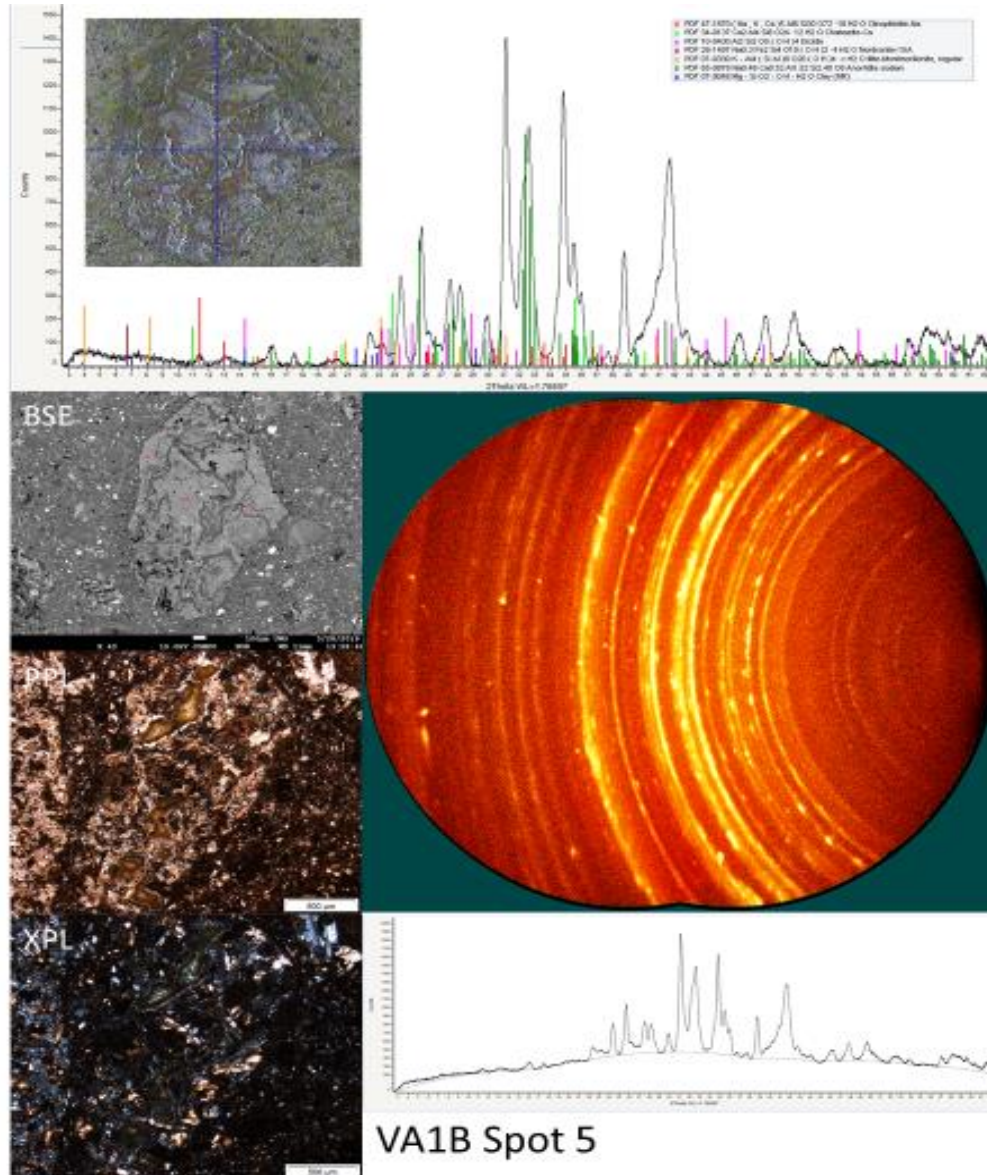
Optical petrography and µXRD analysis using the newly developed method of clays and zeolites (spot 5 in Fig. C-2) in sample VA1B.

Red: Clinoptilolite-Na (Na, K, Ca)5 Al6 Si30 O72 · 18 H2O (PDF 47-1870)

Light Green: Chabazite-Ca (Ca2 Al4 Si8 O24 · 12 H2O) (PDF 34-0137)

Pink: Dickite Al2 Si2 O5 (OH)4 (PDF 10-0430)

Brown: Nontronite Na0.3 Fe2 Si4 O10 (OH)2 · 4 H2O (PDF 29-1497)

Orange: Illite-Montmorillonite K- Al4 (Si Al)8 O20 (OH)4 · H2O (PDF 07-0330)

Dark Green: Anorthite sodian (Na0.48 Ca0.52 Al1.52 Si2.48 O8) (PDF 85-0878)

Blue: Clay (Mg- Si O2- OH- H2O) (PDF 07-0048)

Figure C-3. VA-2017-1D thin section showing spots analyzed
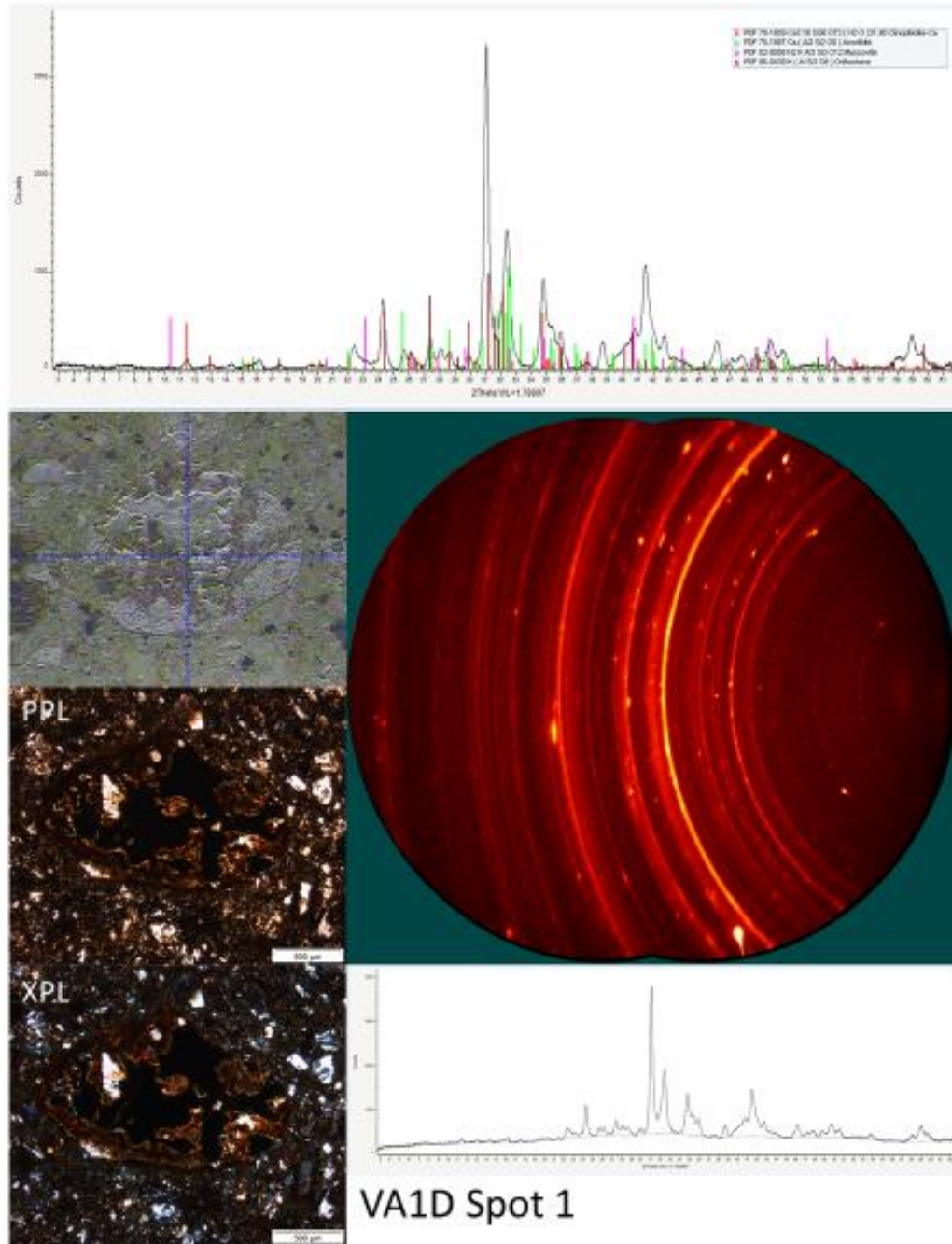
Optical petrography and µXRD analysis using the newly developed method of clays and zeolites (spot 1 in Fig. C-3) in sample VA1D.

Red: Clinoptilolite-Ca Ca3.16 Si36 O72 (H2O)21.80 (PDF 70-1859)

Light Green: Anorthite Ca(Al2 Si2 O8) (PDF 75-1587)

Pink: Muscovite (H2 K Al3 Si3 O12) (PDF 02-0058)

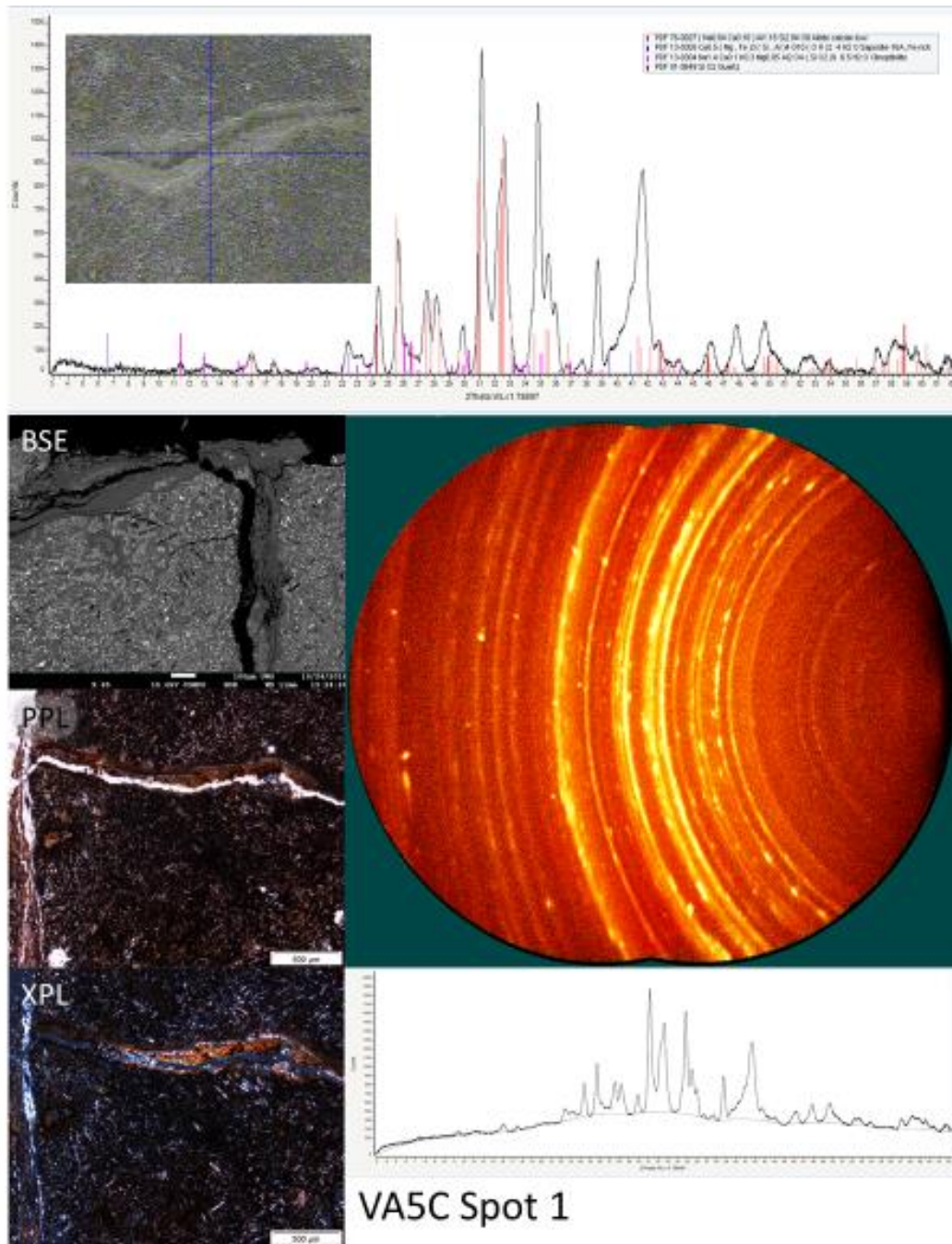**Brown: Orthoclase K (Al Si3 O8) (PDF 86-0439)**
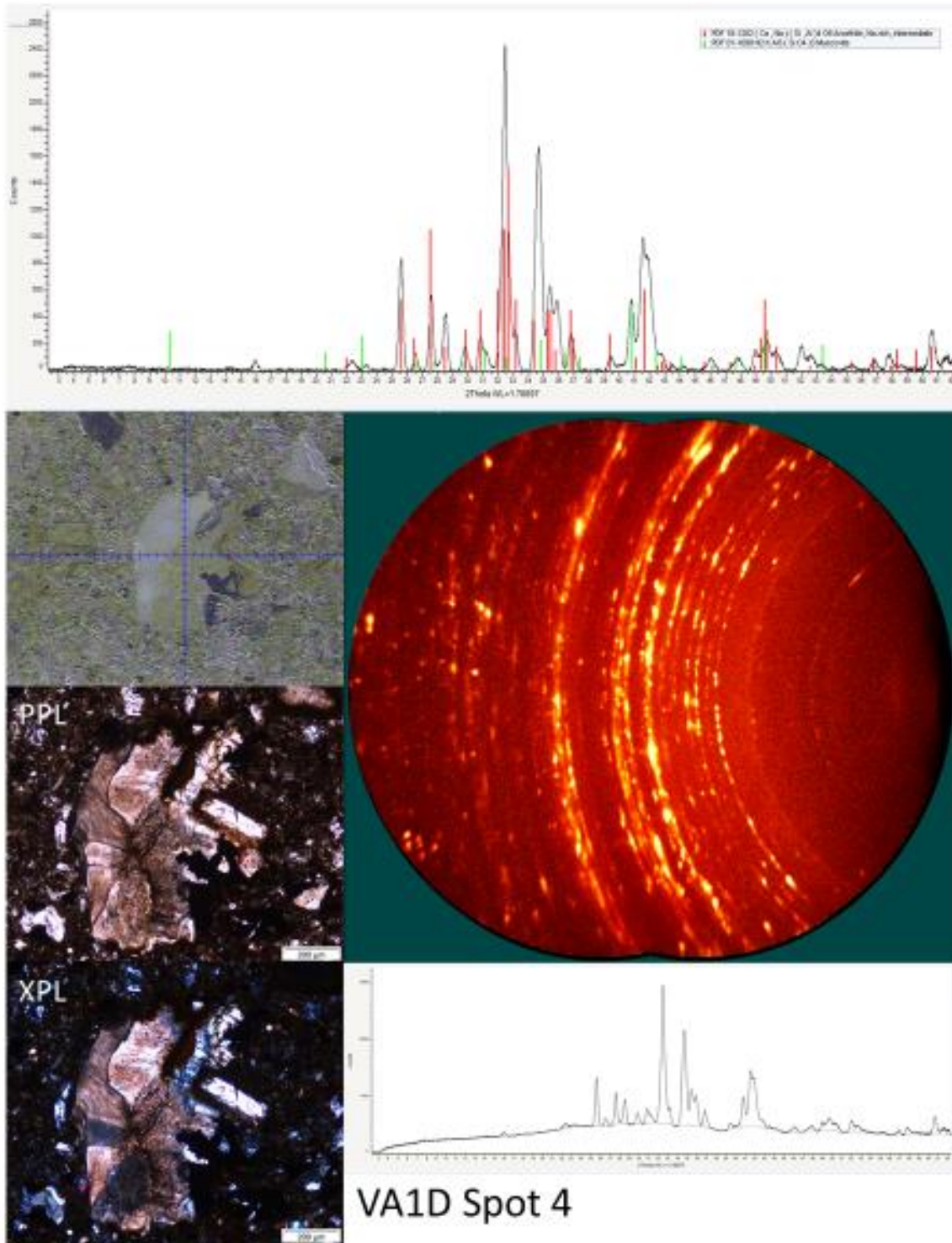
Optical petrography and µXRD analysis using the newly developed method of clays and zeolites (spot 4 in Fig. C-3) in sample VA1D.

Red: Anorthite, Na-rich (Ca, Na) (Si, Al)4 O8 (PDF 18-1202)

Light Green: Muscovite H2 K Al3 (Si O4)3 (PDF 01-1098)
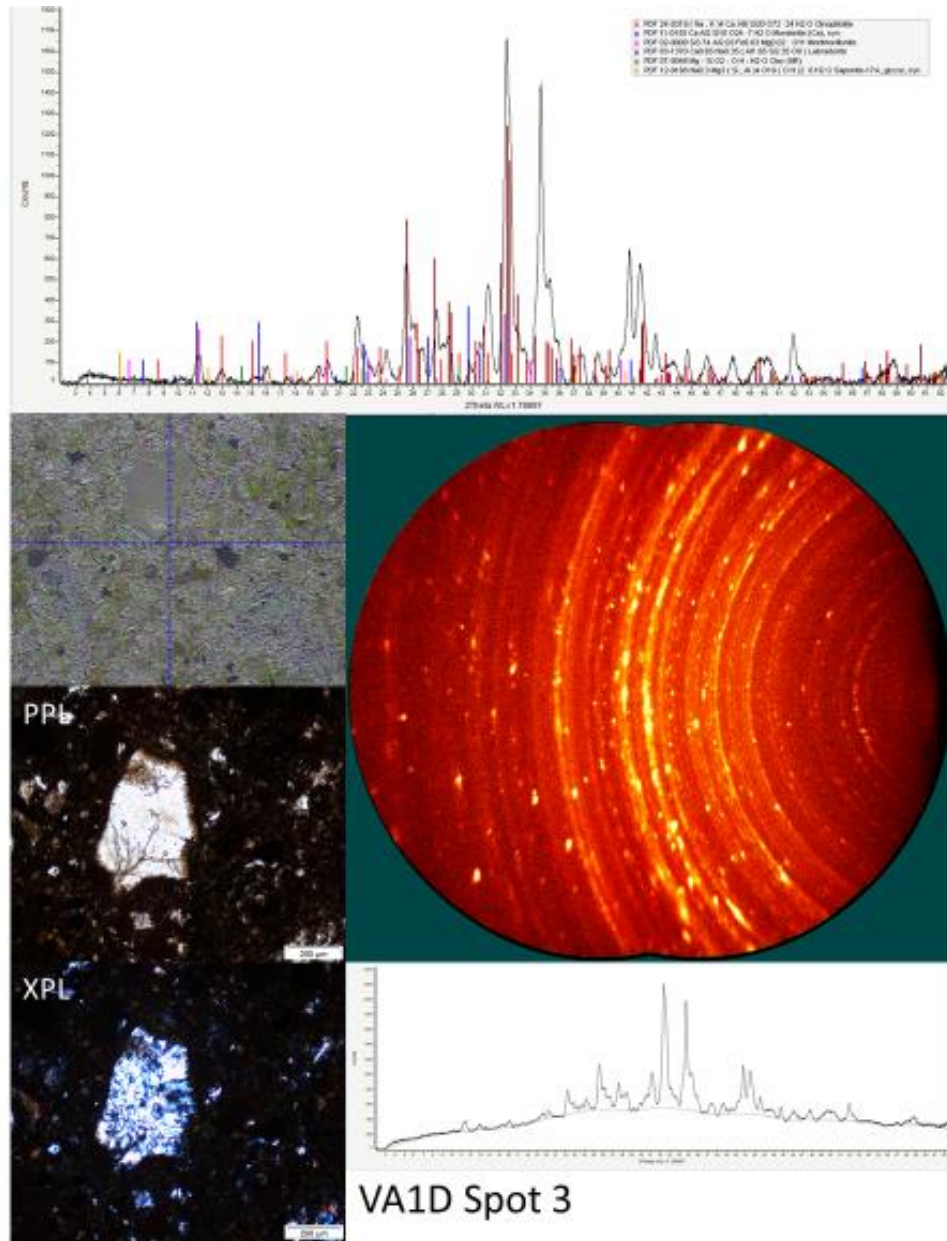
Optical petrography and µXRD analysis using the newly developed method of clays and zeolites (spot 3 in Fig. C-3) in sample VA1D.

Red: Clinoptilolite (Na, K)4 Ca Al6 Si30 O72 · 24 H2O (PDF 24-0319)

Blue: Mordenite-Ca (Ca Al2 Si10 O24 · 7 H2O) (PDF 11-0155)

Pink: Montmorillonite (Si3.74 Al2.03 Fe0.03 Mg0.02 · O11) (PDF 02-0009)

Brown: Labradorite Ca0.65 Na0.35 (Al1.65 Si2.35 O8) (PDF 83-1370)

Dark green: Clay (Si O2- OH – H2O) (PDF 07-0048)

Orange: Saponite Na0.3 Mg3 (Si, Al)4 O10 (OH)2 · 6 H2O (PDF 12-0168)
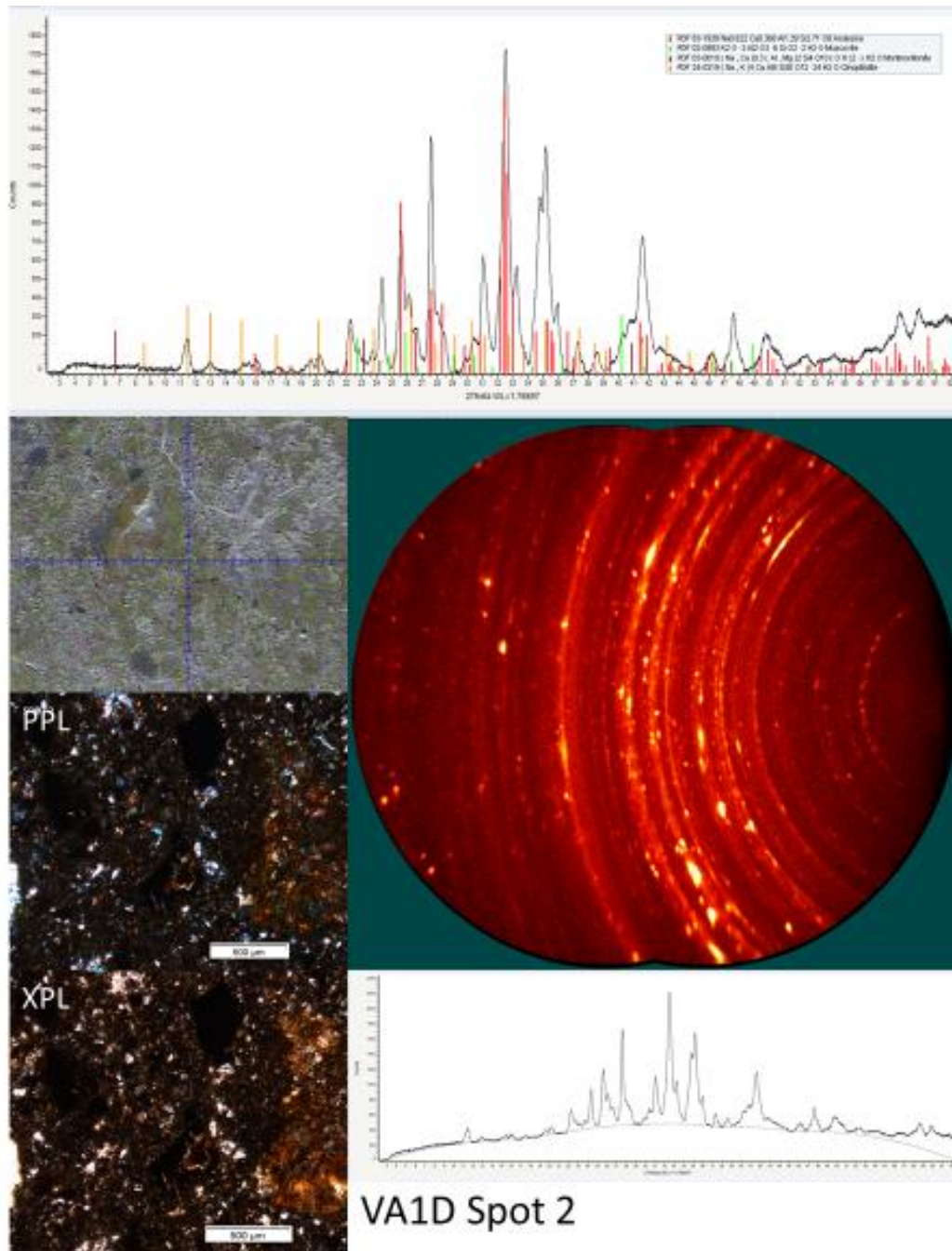
Optical petrography and µXRD analysis using the newly developed method of clays and zeolites (spot 2 in Fig. C-3) in sample VA1D.

Red: Andesine (Na0.622 Ca0.368 Al1.29 Si2.71 O8) (PDF 83-1938)

Light Green: Muscovite (K2 O · 3 Al2 O3 · 6 Si O2 · 2 H2O) (PDF 02-0993)

Brown: Montmorillonite (Na, Ca)0.3 (Al, Mg)2 Si4 O10 (OH)2 · H2O (PDF 03-0010)

Orange: Clinoptilolite (Na, K)4 Al6 Si30 O72 · 24 H2O (PDF 24-0319)

Optical petrography and μXRD analysis using the newly developed method of clays and zeolites (spot 5 in Fig. C-3) in sample VA1D.

Red: Heulandite-Ca Ca3.45 Rb1.50 (Al8.4 Si27.6 O72) (H2O)23.5 (PDF 80-0465)

Blue: Saponite-Fe (Mg2.09 Ca0.46 Fe0.35 Mn0.02) (Al0.58 Si3.42) O10 (PDF 12-0160)

Dark green: Clay (Mg- Si O2- OH- H2O) (PDF 07-0048)

Pink: Chlorite (Mg, Fe)5 (Al, Si)5 O10 (OH)8 (PDF 02-0028)

Figure C-4. VA-2017-5C thin section showing spots analyzed
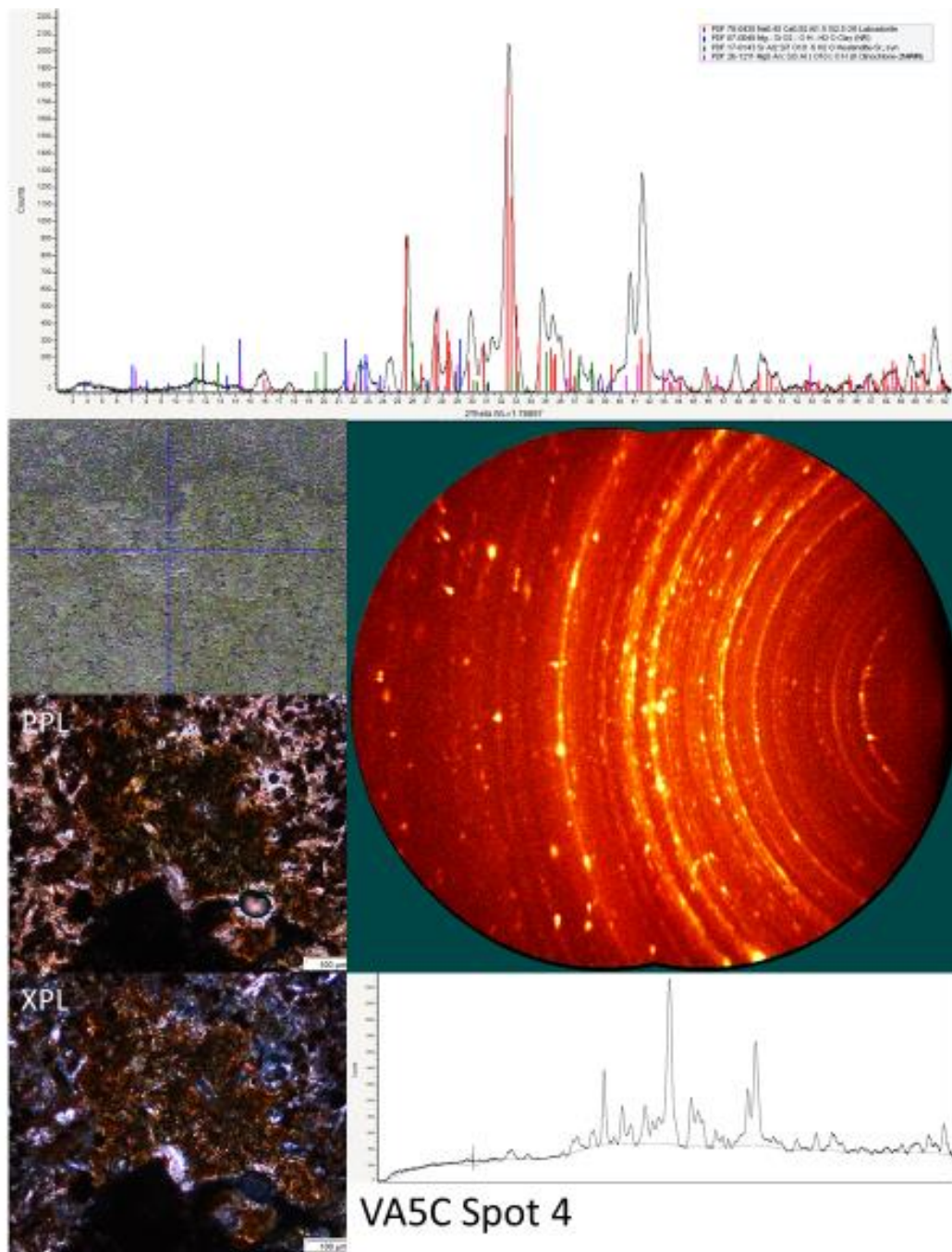
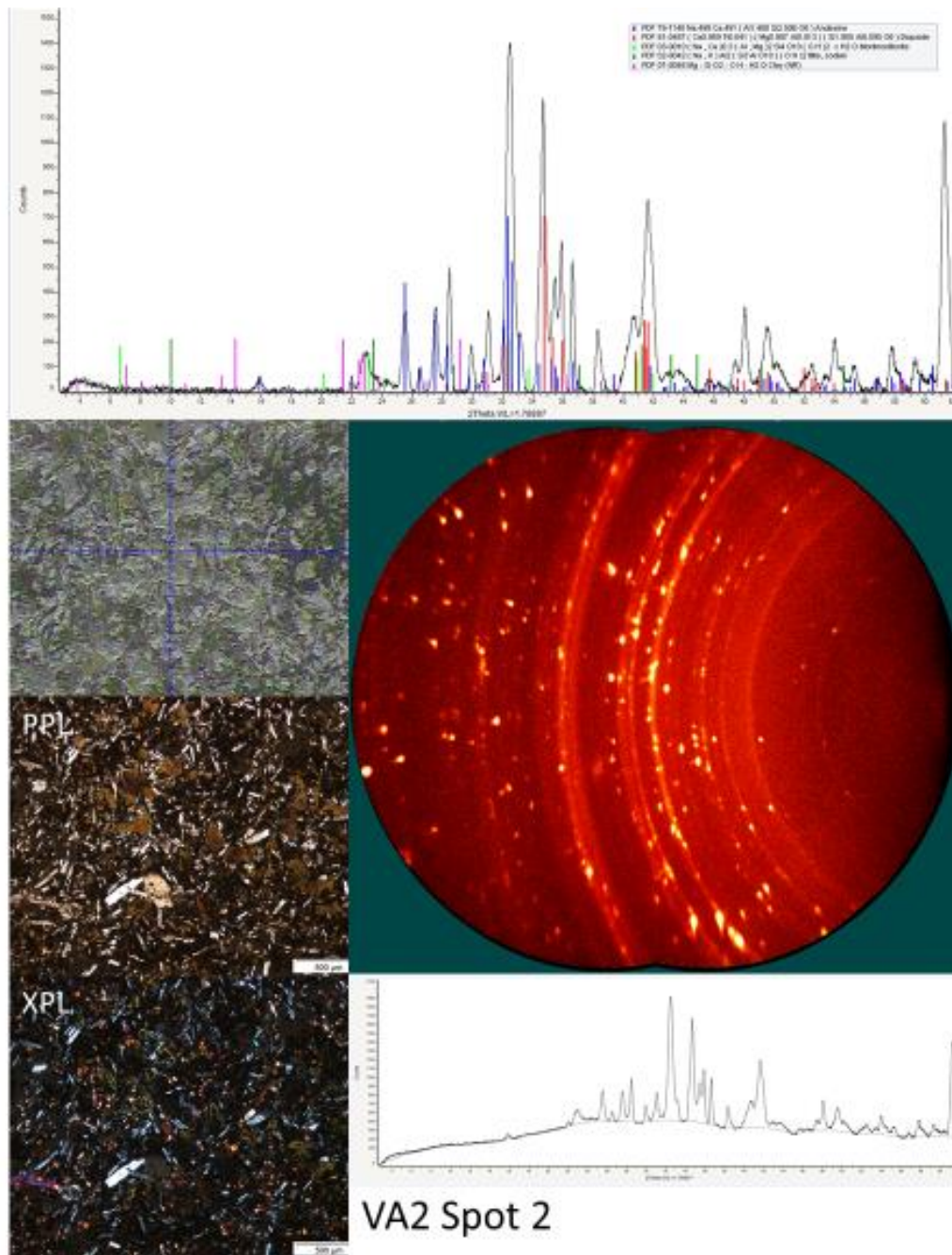**Optical petrography and µXRD analysis using the newly developed method of clays and zeolites (spot 4 in Fig. C-4) in sample VA5C.**

Red: Labradorite (Na0.45 Ca0.55 Al1.5 Si2.5 O8) (PDF 78-0435)

Blue: Clay (Mg- Si O2- OH- H2O) (PDF 07-0048)

Dark green: Heulandite (Sr Al2 Si7 O18 · 6 H2O) (PDF 17-0143

Pink: Clinochlore Mg5 Al (Si3 Al) O10 (OH)8 (PDF 26-1211)

Optical petrography and μXRD analysis using the newly developed method of clays and zeolites (spot 1 in Fig. C-4) in sample VA5C.

Red: Albite calcian low (Na0.84 Ca0.16) Al1.16 Si2.84 O8 (PDF 76-0927)

Blue: Saponite, Fe-rich Ca0.5 (Mg, Fe)3 (Si, Al)4 O10 (OH)2 ·4 H2O (PDF 13-0305)

Pink: Clinoptilolite Na1.4 Ca0.1 K0.3 Mg0.05 Al2 O4 (Si O2)9 ·6.5 H2O (PDF 13-0304)

Brown: Quartz (Si O2) (PDF 01-0649)

Figure C-5. VA-2017-2 thin section showing spots analyzed
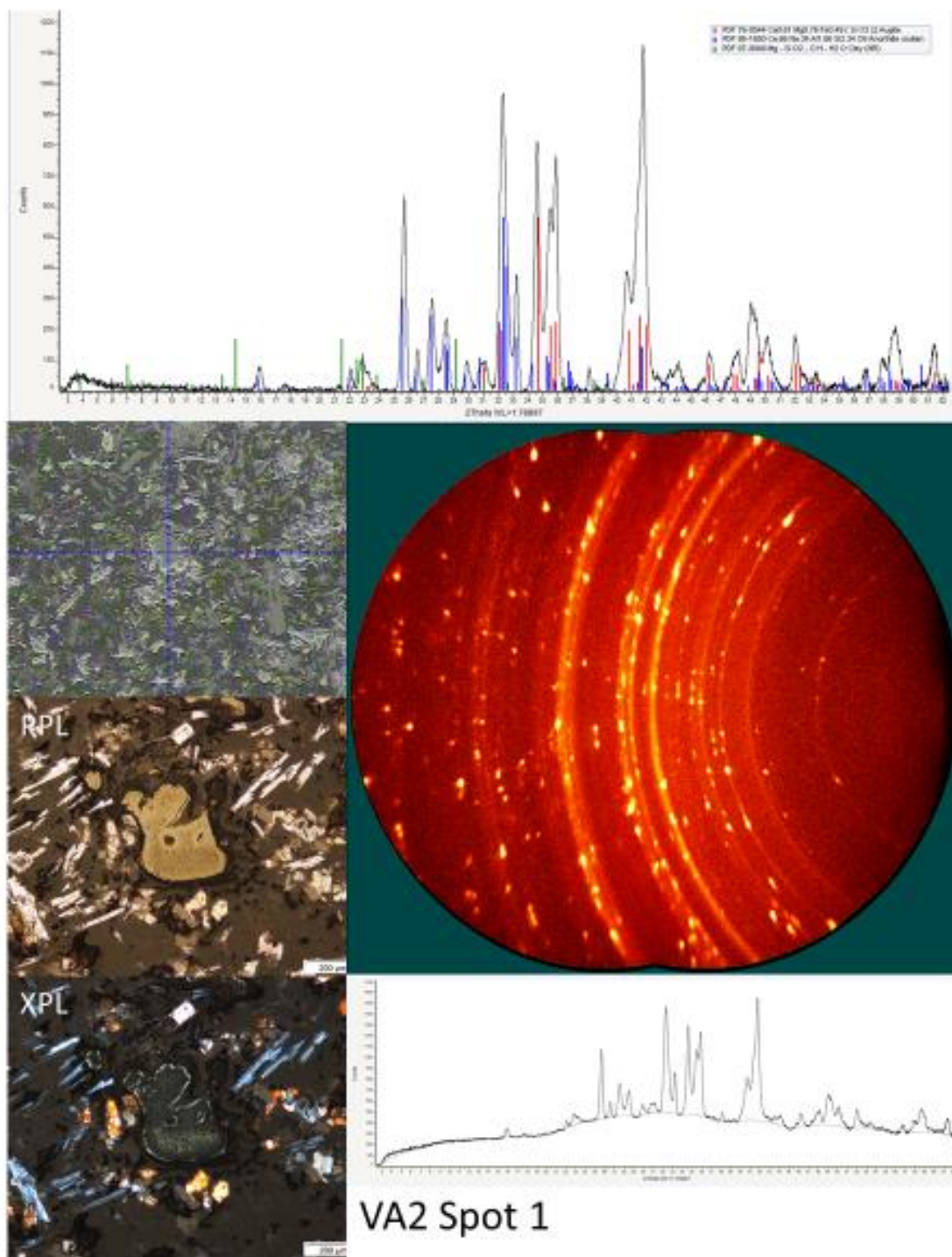
Optical petrography and µXRD analysis using the newly developed method of clays and zeolites (spot 1 in Fig. C-5) in sample VA2.

Red: Augite Ca0.61 Mg0.76 Fe0.49 (Si O3)2 (PDF 76-0544)

Blue: Anorthite sodian (Ca0.66 Na0.34 Al.66 Si2.34 O8) (PDF 86-1650)

Dark green: Clay (Mg- Si O2- OH- H2O) (PDF 86-1650)

Optical petrography and µXRD analysis using the newly developed method of clays and zeolites (spot 2 in Fig. C-5) in sample VA2.

Blue: Andesine Na0.499 Ca0.491 (Al1.488 Si2.506 O8) (PDF 79-1148)

Red: Diopside (Ca0.959 TiO0.042) (Mg0.987 Al0.013) (Si1.905 Al0.095 O6) (PDF 81-0487)

Light green: Montmorillonite (Na, Ca)0.3 (Al, Mg)2 Si4 O10 (OH)2 · H2O (PDF 02-0010)

Dark green: Illite, sodian (Na, K) Al2 (Si3 Al O10) (OH)2 (PDF 02-0042)

Pink: Clay (Mg- Si O2 – OH- H2O) (PDF 07-0048)

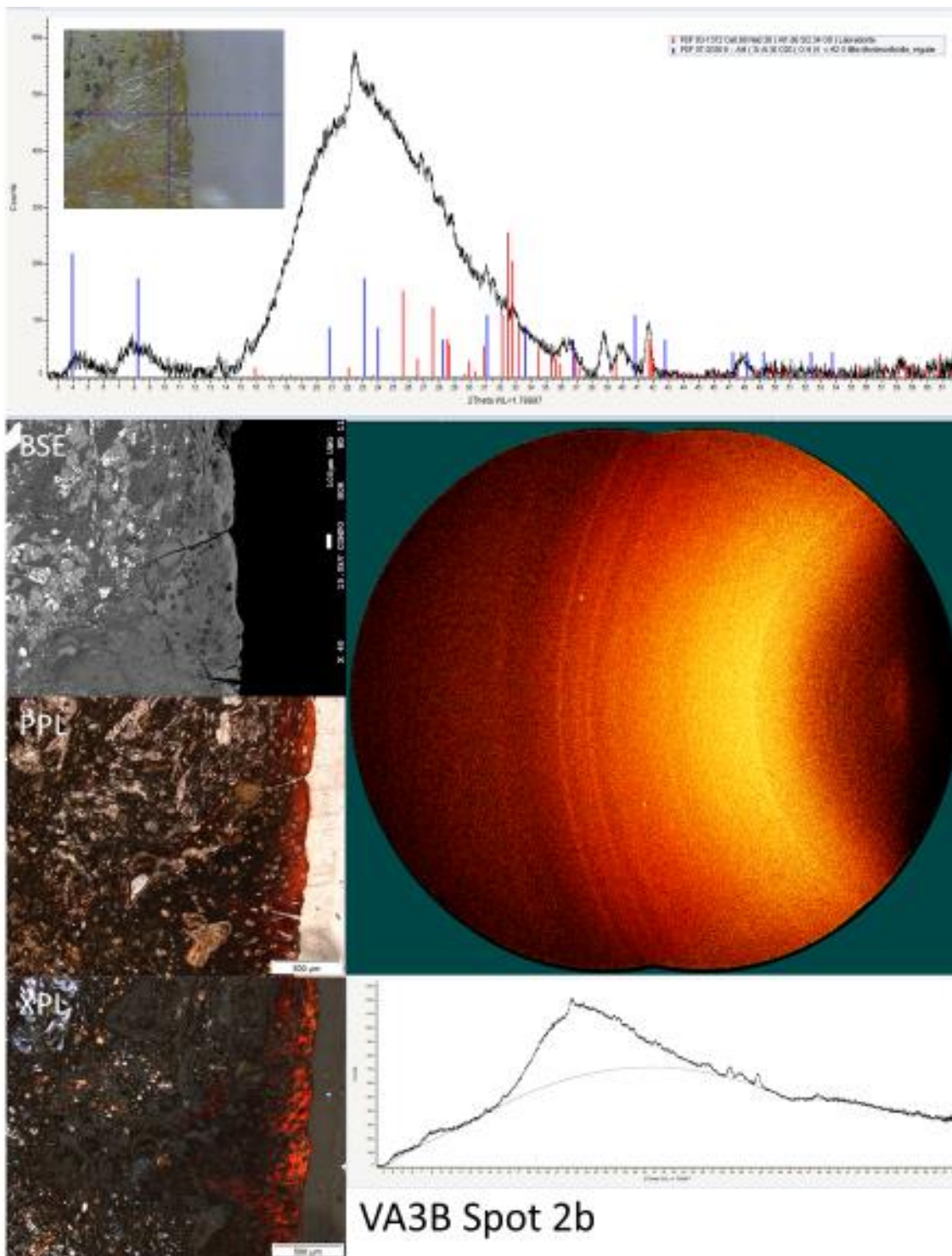**Figure C-6. VA-2017-3B thin section showing spots analyzed**
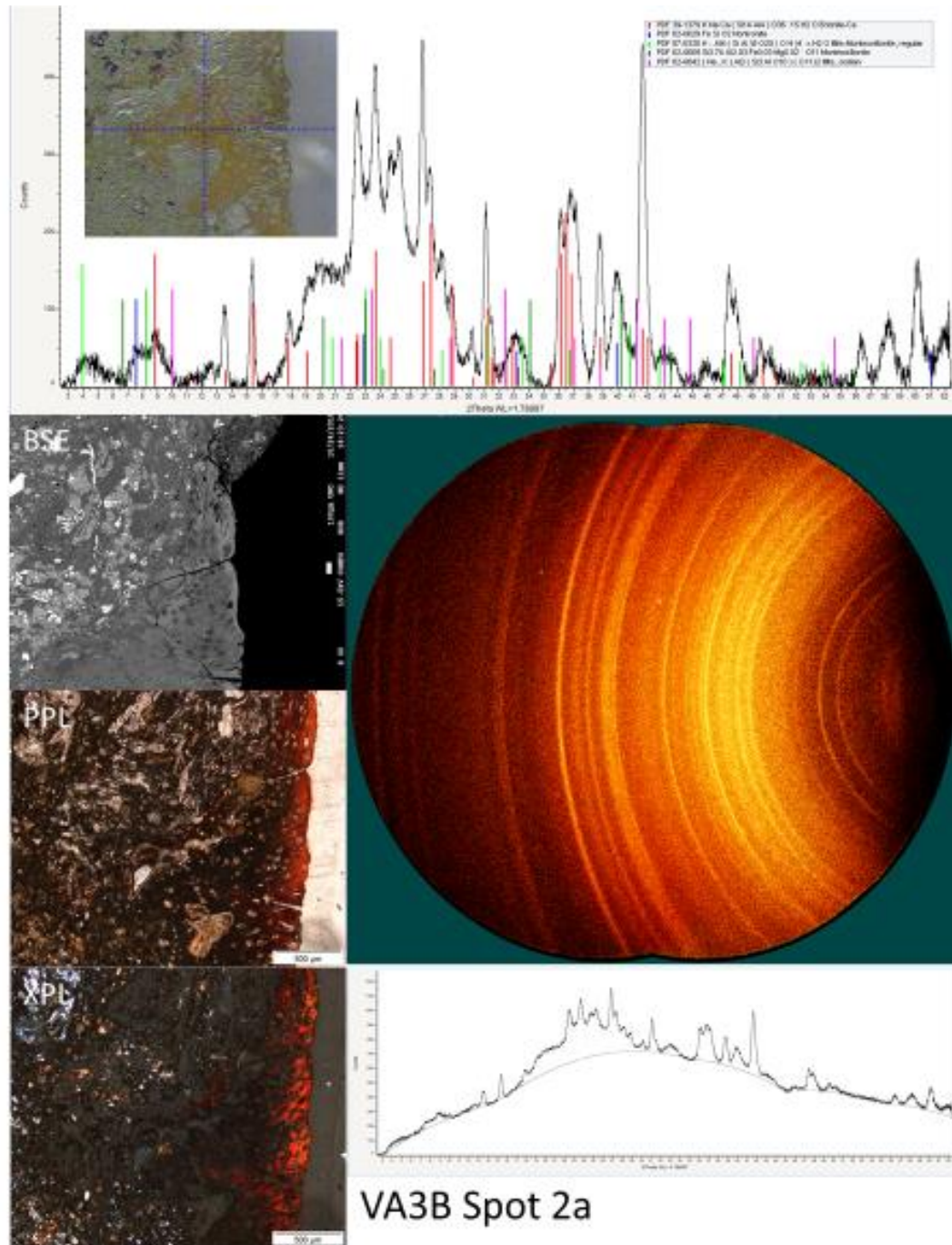
Optical petrography and µXRD analysis using the newly developed method of clays and zeolites (spot 2a in Fig. C-6) in sample VA3B.

Red: Erionite-Ca (K Na Ca [Si14 Al4] O36 · 15 H2O) (PDF 39-1379)

Blue: Nontronite (Fe Si O2) (PDF 02-0029)

Light green: Illite-Montmorillonite Al4 (si, Al)8 O20 (OH)4 · H2O (PDF 02-0009)

Pink: Illite, sodian (Na, K) Al2 (Si3 Al O10) (OH)2 (PDF 02-0042)
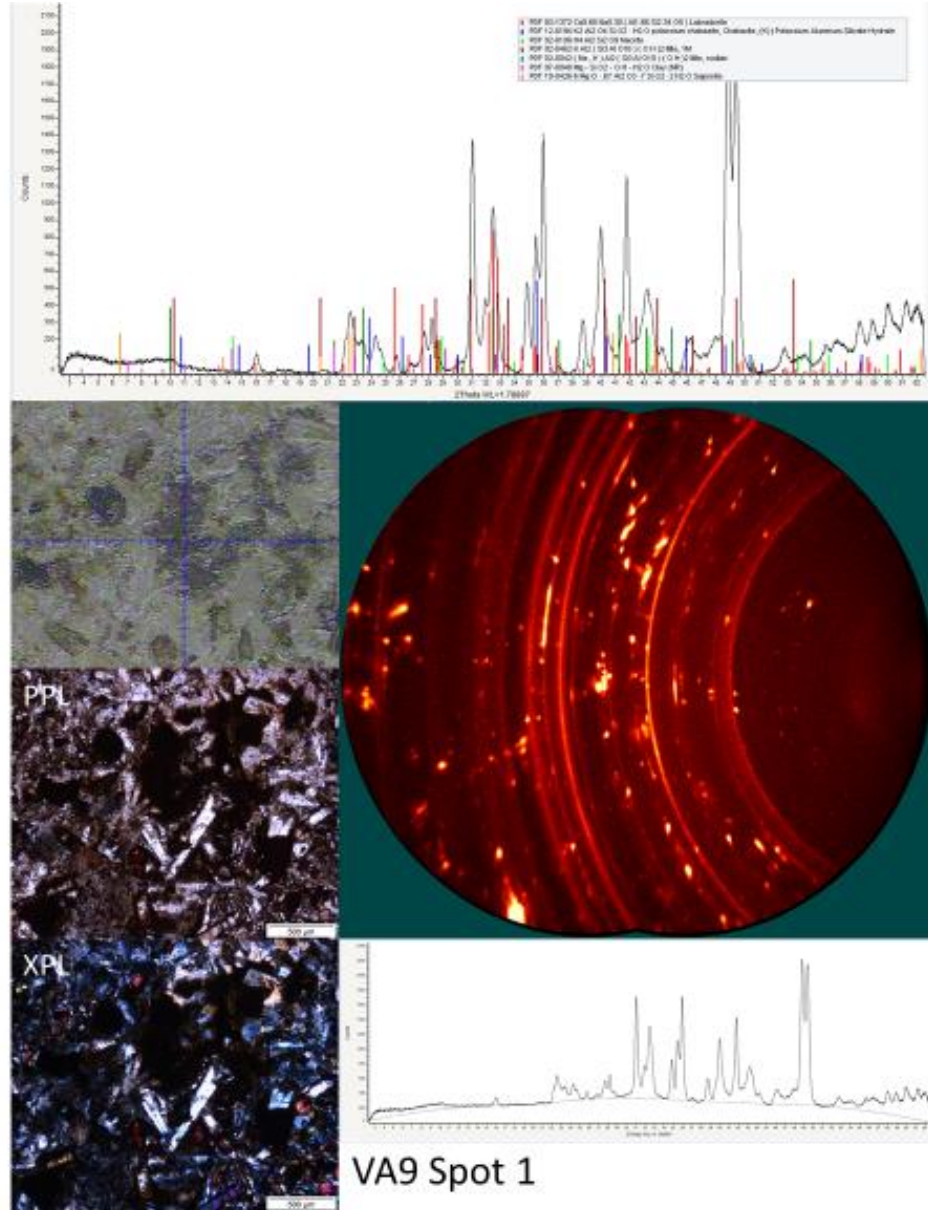
Optical petrography and µXRD analysis using the newly developed method of clays and zeolites (spot 2b in Fig. C-6) in sample VA3B.

Red: Labradorite Ca0.68 Na0.30 (Al1.66 Si2.34 O8) (PDF 83-1372)

Blue: Illite-Montmorillonite K- Al4 (Si Al)8 O20 (OH)4 · H2O (PDF 07-0330)

Figure C-7. VG-2017-9 thin section showing spots analyzed

Optical petrography and μXRD analysis using the newly developed method of clays and zeolites (spot 4 in Fig. C-7) in sample VA5C.

Red: Labradorite Ca0.68 Na0.30 (Al1.66 Si2.3 O8) (PDF 83-1372)

Blue: Potassium Chabazite (K2 Al2 O4 Si O2 · H2O) (PDF 12-0194)

Light green: Nacrite (H4 Al2 Si2 O9) (PDF 02-0106)

Brown: Illite K Al2 (Si3 Al O10) (OH)2 (PDF 02-0462)

Dark green: Illite, sodian (Na, K) Al2 (Si3 Al O10) (OH)2 (PDF 02-0042)

Pink: Clay (Mg- Si O2- OH- H2O) (PDF 07-0048)

Orange: Saponite (6 Mg O · 0.67 Al2 O3 · 7 Si O2 · 2 H2O) (PDF 10-0426)

Curriculum Vitae

Name: Nikol Posnov

Post-secondary Education and Degrees:

The University of Western Ontario
London, Ontario, Canada
2018-2021 M.Sc. Geology and Planetary Science

The University of Western Ontario
London, Ontario, Canada
2020-2022 B.Sc. Nursing

The University of Western Ontario
London, Ontario, Canada
2014-2018 B.Sc. Medical Science

Honours and Awards:

Charles. A. Southworth Memorial Prize in Paleontology
2018

Undergraduate Pre-thesis Award
2018

Mineralogical Association of Canada Undergraduate Student Award
2018

AESRC 2019 Best Student Poster Presentation Award
2019

Robert and Ruth Lumsden Graduate Award in Earth Sciences
2019

Mineralogical Association of Canada Travel/Research Grant
2019

Science International Engagement Fund (SIEF) Award
2019-2020

SEG/Chevron Student Leadership Symposium (SLS) Travel Grant
2019

Robert W. Hodder International Geoscience Field Experience Award
2019

Globalink International Research Award
Held at Georgetown University, Washington DC
2020

Related Work/   Johnson Biosignature Laboratory

Experience   Georgetown University, Washington, DC, USA
01-04, 2020

Teaching Assistant
The University of Western Ontario
2018-2020

David St. Jacques's Exploring Earth Initiative
The University of Western Ontario, CSA, Ingenium and Royal
Canadian Geographical Society
2018

Earth Science Undergraduate Fellowship
The University of Western Ontario
2018

University of Western Ontario Exchange Program
Umeå University, Umeå, Sweden

Publications:

Posnov, N. (2019) University of Western Ontario Geophysics Society: Society of Exploration Geophysicists. *2019 SEG/Chevron Student Leadership Symposium (SLS) and SEG International Exposition and 89th Annual Meeting,* San Antonio, Texas, USA, September 13-17, 2019, Poster Presentation.

Posnov, N., Osinski, G.R., Flemming, R.L., McCausland, P.J.A., Pontefract, A. and Crósta, A. (2019) Colonization of shocked basalt from Vargeão Dome and Vista Alegre: Implication for the search for life on Mars. *Impacts and their role in the evolution of life conference*, Tallberg, Sweden, June 10-13, Oral Presentation

Posnov, N., Osinski, G.R., Flemming, R.L., McCausland, P.J.A., Pontefract, A. and Crósta, A. (2019) Colonization of shocked basalt from Vargeão Dome and Vista Alegre: Implication for the search for life on Mars. *18th Annual Advances in Earth Sciences Research Conference*, Toronto, ON, March 29-31, Poster Presentation

Posnov, N., Osinski, G.R., Flemming, R.L., McCausland, P.J.A., Pontefract, A. and Crósta, A. (2019) Classification of shocked basalt from Vargeão Dome and Vista Alegre: Implication for the search for life on Mars. *50th Lunar and Planetary Science Conference*, Houston, TX, March 18-22, Abs. #2863

Posnov, N., Osinski, G.R., Flemming, R.L., Pontefract, A. and Crósta, A. (2019) Hydrothermal alteration of Vista Alegre basalts: Implication for the search for life on Mars. *50th LPSC*, Houston, TX, March 18-22, Abs. #2856